PONTIFICIA UNIVERSIDAD CATÓLICA DEL PERÚ

ESCUELA DE POSGRADO

OPTICAL AND LUMINESCENT PROPERTIES OF TERBIUM/ YTTERBIUM DOPED ALUMINUM OXYNITRIDE AND TERBIUM DOPED ALUMINUM NITRIDE THIN FILMS

A thesis submitted for the degree of
Doctor in Physics

presented by

Karem Yoli Tucto Salinas

Advisor:

Dr. Rolf Grieseler

Co-Advisor:

Dr. Jorge Andrés Guerra Torres

Lima 2020

Contents

Abstract

In the present thesis the optical and light emission properties of two systems consisting of Tb^{3+} and Yb^{3+} doped amorphous AlO_xN_y thin films and Tb^{3+} doped polycrystalline AlN thin films were analyzed. In the two ions system, to obtain an adequate luminescent emission, commonly a significant effort must be made to find a suitable concentration of dopants and elemental composition of the host material. An interesting and highly efficient method is a combinatorial approach, allowing a high velocity screening of a wider range of properties. In the present work a combinatorial gradient based thin film libraries of amorphous AlO_xN_y:Yb^{3+}, AlO_xN_y:Tb^{3+} and AlO_xN_y:Tb^{3+}:Yb^{3+} have been prepared by radio frequency co-sputtering from more than one target. In the prepared libraries, the Tb and Yb concentration range spreads along with the oxygen to nitrogen ratio of the host matrix all over the substrate area. Concentrations ranges for each ion were established for producing high emission intensity samples, along with an analysis of the light emission features of Yb^{3+} ions with Tb^{3+} ions as sensitizers for cooperative down conversion process. Using different annealing temperatures the activation energy of the rare earth ions and thermal-induced activation mechanisms are evaluated. Here we show that the different oxygen to nitrogen ratios in the host composition affect the light emission intensity. According to experimental results, there is a strong enhancement of the Yb^{3+} related emission intensity over the Tb^{3+} emission in codoped films with Tb:Yb concentration ratios near to 1:2, at 850°C. Thus, suggesting the sensitization of Tb^{3+} ions through an AlO_xN_y matrix and the cooperative energy transfer between Tb^{3+} and Yb^{3+} ions as the driven mechanism for down conversion process with promising applications in silicon solar cells. At the end of this first part, the optimal elemental composition and optimal annealing temperature in the investigated ranges to achieve the highest Yb^{3+} emission intensity upon sensitization of Tb^{3+} ions is reported. The second system studied consists of Tb^{3+} doped AlN layers prepared by reactive magnetron sputtering and analyzed using the conventional one at a time approach. In this work, two types of thermal treatments have been applied: substrate heating during deposition of the films and post deposition rapid thermal annealing, with varying temperature from non intentional heating up to 600°C. The composition, morphology and crystalline structure of the films under different thermal processes and temperatures were investigated along with their optical and light emission properties, with the aim of maximizing the Tb^{3+} emission intensity. The polycrystalline nature of the films was confirmed by X-ray diffraction under grazing incidence, and the influence of substrate temperature on the crystalline structure was reported. Atomic force microscopy and scanning electron microscopy has revealed the smooth grainy surface quality of the AlN:Tb^{3+} films. The highest Tb^{3+} photoluminescence emission intensity was achieved in the film treated with rapid thermal annealing process. For a more detailed study of the post deposition annealing treatments, temperature was further increased up to 900°C, and the

influence of annealing temperature on the emission properties was investigated by photoluminescence and photoluminescence decay measurements. An increase in the photoluminescence intensity and photoluminescence decay time was observed upon annealing for the main transition of Tb^{3+} ions at 545 nm, which was attributed to a decrease of non radiative recombination and increase of the population of excited Tb^{3+} ions upon annealing. Additionally, using the characterized films as active layer, direct current and alternate current thin film electroluminescence devices were designed and investigated.

Resumen

La presente tesis investiga las propiedades ópticas y de emisión de luz de las películas delgadas amorfas de AlO_xN_y codopadas con Tb^{3+} e Yb^{3+} y las películas policristalinas de AlN dopado con Tb^{3+}. En el sistema codopado, la óptima emisión de luz depende de la búsqueda de adecuadas concentraciones del elemento dopante y de la composición de la matríz anfitriona. Para lograrlo se utiliza el moderno método del análisis combinatorio, que ha demostrado ser de mucha eficiencia para la caracterización rápida y avanzada de las propiedades. Se prepararon librerías de películas delgadas amorfas de AlO_xN_y:Yb^{3+}, AlO_xN_y:Tb^{3+} y AlO_xN_y:Tb^{3+}:Yb^{3+}con un gradiente combinatorio de la concentración de los elementos. Para esto se usó la técnica de pulverización catódica de radiofrecuencia con más de un target para la co-deposición de los materiales. En las librerías preparadas las concentraciones de los iones dopantes Tb e Yb se distribuye a lo largo de la superficie de la muestra. También se observa la variación de las concentraciones de oxígeno y nitrógeno en la matrix anfitriona. Se analizaron las concentraciones de los iones de Tb e Yb para producir muestras con una alta intensidad de emisión, y se estudió la emisión del Yb^{3+} codopado con Tb para la producción de capas conversoras de baja energía. La activación de las tierras raras fue inducida por medio de diferentes temperaturas de tratamiento térmico. Se encontró que las razones de oxígeno y nitrógeno en la matrix influyen en la emisión de luz, y que la intensidad de emisión relativa del Yb^{3+} mejora con respecto a la emisión del Tb^{3+} en las películas codopadas con Tb:Yb igual a 1:2 y calentadas a 850°C. Éste resultado sugiere la posible transferencia cooperativa de energía entre el Tb^{3+} y el Yb^{3+} en la matríz de AlO_xN_y, lo cual permitiría la conversión de fotones de energía alta a baja con prometedoras aplicaciones en celdas solares. La óptima concentración de elementos y la óptima temperatura de tratamiento térmico para alcanzar la mayor intensidad de emisión del Yb^{3+} en presencia de iones de Tb^{3+}fueron reportados. El segundo sistema en estudio consiste en películas delgadas de AlN dopado con Tb^{3+}, preparadas por la técnica de pulverización catódica de radiofrecuencia reactiva. Con el objetivo de incrementar la intensidad de la emisión de luz del Tb^{3+}se aplicaron a las muestras dos tipos de tratamiento térmicos con temperaturas que varian desde los 300°C hasta los 600°C. El primer tratamiento se realizó durante la deposición de la película calentando el sustrato y el segundo tratamiento se hizo después de la deposición de la película usando un horno de recocido térmico rápido. La composición elemental, la morfología, la microestructura y las propiedades ópticas y de emisión óptica de las muestras producidas fueron investigadas. La difracción de rayos X de ángulo rasante confirmó la naturaleza policristalina de las películas. La microscopía de fuerza atómica y la microscopía electrónica de barrido demostró que las muestras poseen una superficie granular suave y una rugosidad del orden de pocos nanómetros. Ésto permitiría prevenir las reflexiones internas que disminuyen la cantidad de luz emitida fuera de la película. La máxima luminiscencia del Tb^{3+}se logró para la película calentada en el horno de

recocido térmico rápido a 600°C. Se estudió la influencia del tratamiento térmico rápido midiendo el decaimiento de la luminiscencia en el tiempo. Se observó para la emisión del Tb^{3+} a 545 nm que el incremento en la intensidad de la emisión de luz ocurre junto al incremento del tiempo de decaimiento de la luz emitida después de los tratamientos térmicos. Ésto puede ser atribuido a la disminución de la tasa de recombinación no radiativa y al incremento en la población de iones de Tb^{3+}excitados después del tratamiento térmico. Finalmente, se desarrollaron e investigaron dispositivos electroluminiscentes de corriente directa y de corriente alterna usando como capa activa para la emisión a las películas de AlN:Tb^{3+}caracterizadas.

Dedicatory

To the love of my life, my family: Margarita, Joel, Otilia, Rosario, Vidal, Santiago and Julia.

Acknowledgements

First of all, I would like to express my greatest appreciation to my supervisor, Dr. Rolf Grieseler, for the continuous support of my Ph.D study and related research, for his patience, motivation and extensive knowledge. His friendly guidance and expert advice have been invaluable throughout all the time of research and writing of this thesis. I would also wish to express my gratitude to my co-advisor Dr. Andrés Guerra for extended discussions, insightful comments, valuable suggestions and encouragement, which have contributed greatly to the improvement of this work.

This research was supported by the Peruvian National Fund for Scientific and Technological Development (FONDECYT) on grant 236-2015 and scholarship contract 233-2015. Additional support has been provided by the German Academic Exchange Service (DAAD) in conjunction with FONDECYT and the Pontificia Universidad Católica del Perú (PUCP), under the contract number 035-2016. I express my gratitude to Prof. Dr. Francisco Rumiche, who provided access to the laboratory and research facilities at the Center of Materials Characterization of the Pontificia Universidad Católica del Perú (CAM-PUCP), which holds the characterization equipment. My sincere thanks also goes to Univ.-Prof. Dr. rer. nat. habil. Dr h. c. Peter Schaaf, Head of the Department of Materials for Electronics of the Technische Universität Ilmenau (TUIlm, Germany), for receiving me and allowing to use the laboratory facilities of the Center for Micro- and Nanotechnologies (ZNM) during this research. Special thanks also to Dr. Henry Romanus, Dr. Thomas Kups, Dipl.-Ing. Marcus Hopfeld, M.Sc. Hauke-Lars Honig and Joachim Döll (TUIlm, Germany) for providing me with a great lab training and helping me while I used equipment in the ZNM lab during my experiments. I also thank Dr. Andrés Osvet and Dr. Miroslaw Batentschuk of Friedrich-Alexander-University of Erlangen-Nürnberg, Erlangen (FAU, Germany) for opening their lab in order to perform the PLE and Time-Resolved Spectroscopy measurements and further feedback. My thanks go also to all other colleagues and fellow lab mates for the stimulating discussions, their help and companion in the last three years.

Last but not the least, I would like to thank my family and close friends for their continuous encouragement and understanding throughout writing this thesis and my life in general. They are the most important people in my world and I dedicate this thesis to them.

Chapter 1

Introduction

Rare earth (RE) doped materials are receiving widespread attentions due to their impact on technology fields, such as optoelectronics, optics communications, photovoltaics and biomedical systems [1, 2, 3, 4]. The reason making RE luminescence appealing for several applications arises from the RE sharp optical emission peaks, which covers a wide spectral range from visible to IR with emission wavelengths that hardly depend on temperature and crystal host. This property has its origin in the partially filled inner 4f shell of the RE ion that is screened by the outer 5s and 5p shells. As a consequence, the intra 4f electronic transitions are hardly affected by the surrounding ions and the emitted wavelength is almost independent of the host material. This fact makes RE doped materials suitable candidates for light emission applications as an alternative to band-to-band electronic transition devices [5, 6]. Besides, the RE-host and RE-RE interactions enable energy conversion processes between absorbed and emitted photons which opens the possibility of using RE-doped thin films as spectral converter materials for improving the energy conversion efficiency of solar cells [7, 8, 1].

To cope with the increase in demand for new lighting sources based on more efficient RE luminescence to extend their practical applications, it is important to have a deeper understanding of the RE activation processes, its connection to the thermal activation, the energy transfer mechanisms that can occur in them and the effect of the host matrix in the overall efficiency. In this context, this thesis presents experimental work on developing RE doped aluminum nitride (AlN) and aluminum oxynitride (AlO_xN_y) thin films as a material platform for light emitting devices from the ultraviolet (UV) to the infrared (IR) range. This thesis focuses on the study of the luminescence and structural properties of the aforementioned materials to gain insight into the conditions for boosting the light emission intensity of the embedded RE ions. Herein lies the challenge of understanding the relationship between luminescence properties and structure/composition. This research aims as well to contribute to the efforts being devoted over the past few years to shed some light on the mechanisms responsible for light emission of RE doped wide bandgap semiconductors thin films .

Among the different host materials extensively studied, in earlier studies silicon has been of particular interest and importance due to the overwhelming majority of silicon based microelectronic devices and low cost realization. However, it was shown that thermal quenching of the RE ions emission is a function of bandgap energy [9, 10, 11]. For instance, light emission from silicon is inefficient

due to its indirect and small bandgap energy which generates strong thermal quenching of the luminescence leading to poor performance at room temperature. The wide bandgap semiconductors are known to overcome the latter problem and are recognized to be a more suitable host for RE ions [12, 13, 11]. Amongst them, AlN attracts technological attention as promising material for a broad range of applications due to the better stability at high voltages and higher temperatures compared to silicon, and well-known production techniques [14, 15, 16, 17, 18]. Its direct bandgap of 6.2 eV allows transparency range from deep-UV to IR region, enabling a variety of applications in optoelectronics, displays, photodetectors and solar cells [19, 20]. Apart from the host material, RE luminescent behavior is also a function of two important factors: the dopant concentration and the temperature of annealing treatments. Initially the intensity increases by increasing the RE ion concentration. But as the concentration further increases, it may lead to light intensity loss attributed to an increased probability of energy transfer to centers for non-radiative recombination. Also, the effect of thermal annealing treatments on RE doped wide bandgap semiconductors has shown that the luminescence intensity experiences an improvement as the thermal treatment advances. However, the activation mechanism occurring in this system is still under discussion [21, 22, 23, 24].

During the development of this work, two major challenges have been identified. First, the deposition of high puriy AlN requires the use of considerable energy to reach high purity vacuum conditions, especially to get rid of oxygen (O) atoms which are highly reactive with aluminum (Al) and induce the formation of Al-O bonds. Nonetheless, the risk of oxygen contamination is not only present during the production stage. Reports showed the formation of second phases as aluminum oxide (Al_2O_3) and aluminum oxynitride (AlO_xN_y) at post deposition annealing temperatures above 600°C [25, 26, 27]. The latter temperature range overlaps with the annealing temperatures typically used to enhance the RE emission intensity. On the other hand, it is known that oxygen incorporation has an impact on the RE related light emission intensity [21, 28, 29]. This work tries to shed some light whether the thermal activation mechanism is a pure local effect or if it is promoted by the diffusion of either nitrogen or oxygen atoms towards the RE ion. This can be done by comparing the activation energy values calculated for the light emission with those corresponding to diffusion processes. Hence, it is important to carry out a methodical study of the effect of oxygen incorporation in RE doped AlO_xN_ythin films on the luminescent and structural properties. For the latter, a large number of samples with varying elemental concentration are needed, and can be time consuming if one uses the conventional one-by-one experimental approach. To increase the rate at which RE doped $AlO_xN_y$of different composition concentrations can be grown, annealed and screened for physical properties characterization, this work takes advantage of the benefits of combinatorial experiments. This relatively new combinatorial approach provides high throughput experimental methods to produce a thin film library with varying composition and collect a considerable amount of data, while shortening time and saving energy consumption [30, 31, 32]. The second challenge consists in studying the stoichiometric, structural and luminescence properties of Tb^{3+} doped AlN as active layers for the implementation of electroluminescent devices in order to investigate the ability of this material for opto-electronic applications. For an accurate description of the luminescence behavior, the Judd-Ofelt theory provides the physical and mathematical formalism for the determination of important radiative parameters, such as

the radiative lifetime [33, 34, 35]. Thus, this work aims to complement the experimental measurements with the Judd-Ofelt analysis to evaluate the suitability of Tb^{3+} doped AlN active layers for EL devices.

Finally, in order to help the reader, the introductory chapter outlines the organization of this thesis into five sections. First, Chapter 2 comprises the state of the art knowledge on luminescence of RE doped wide bandgap semiconductors and an overview of the RE luminescence theory. Chapter 3 gives a general experimental part which offers a detailed description of the production techniques used to grow samples as well as thermal annealing procedures. In chapter 4, the experiments, results and discussion concerning the combinatorial approach used to study the luminescence of Tb^{3+}/Yb^{3+} doped AlO_xN_ythin films with a composition gradient is presented. Likewise, Chapter 5 reports the experiments, results and discussion of the analysis performed on Tb^{3+} doped AlN thin films with emphasis on the possibility to use them as active layers in EL devices. Lastly, the conclusions will be presented in chapter 6.

Chapter 2

Fundamentals of luminescence

The first part of this chapter is devoted to a survey of the luminescence and optical properties of wide bandgap semiconductors as host for RE doped luminescent devices. Literature will be reviewed and the state of the art theory and practices regarding the properties of wide bandgap semiconductors such as AlN, SiC and GaN will be examined and compared. The second part presents the basic principles of RE luminescence under the topics of Hamiltonian description, mechanism of energy transfer, radiative and non radiative transitions of RE ions embedded in solids.

2.1 Wide bandgap semiconductors as host for luminescent materials

2.1.1 Overview on the development and applications

Light emission involves electronic transitions from higher to lower energy states. Excitation to higher states may be achieved by a variety of techniques. Up to the nineteenth century, the artificial light generated was of thermal origin and the lighting devices were based on the combustion of gases, liquids and solids as, for instance, propane, oils and lime. As the main principles of electric lighting were discovered, the twentieth century witnessed the devolpment of new lighting devices such as the incandescent filament lamp in 1879. However, the origin of the emission of the incandescent filament lamp was the same as in the limelight, with the difference that now the thermal excitation was due to electric current [36]. The next step came up with the development of the fluorescent lamp, invented in 1938, which produced light using photoluminescence excitation of a phosphor material by UV emission spectrum of mercury. A high input voltage is required to ionize the gas, and once the lamp is switched on lower operating voltages are needed. Because the fluorescent light bulb (CFL) does not produce light through the continual boiling of a metallic filament, it consumes much less electricity than the incandescent bulb (50-60 lm/W cf. 8-10 1m/W) [37]. By 1990s, fluorescent lamps were actively promoted due to its higher efficiency compared to incandescent bulbs and were rapidly employed in most work and home environments.

Luminescence is a phenomenon described as a cold emission of light because it does not involve thermal radiation. This means, the material emits light through electronic transitions caused by the absorption of high energy impinging photons, as in the photoluminescence (PL) phenomenon; or caused by the application of an electric field, as in the electroluminescence (EL) phenomenon. In

1907, Henry Joseph Round reported the effect of the light emission from a semiconductor material: "*During an investigation of the unsymmetrical passage of current through a contact of carborundum an other substances a curious phenomenon was noted. On applying a potential of 10 Volts between two points on a crystal of carborundum, the crystal gave out a yellowish light* [...]" [38]. Based on the EL phenomenon, a new lighting device was born: the light emitting diode (LED). It consists of electrons and holes flowing as majority carriers and injected across the p-n junction after a voltage is applied, when they recombine in the junction it may lead to radiative recombination and the photons emitted have energies closely related to the bandgap of the material (see Fig 2.1). In 1962, General Electrics (GE) produced the first red lighting emitting diode based on the work of Holoynak and Bevacqua using a $Ga(As_{1-x}P_x)$ p-n junction [39], however it produced barely 0.001 lm of red light. Nowadays, LEDs provide efficiency improvements (60-80 lm/W) over the CFL bulb [37]. For the more energy saving and also less negative environmental impacts, white LEDs have been established as breakthrough solutions to replace the existing fluorescent bulbs. [40].

On the other hand, in the last decades, the performance of solid state lighting displays has been growing looking for better brightness and contrast, improvements of color variation and resolution, reduction of cost and power consumption, as well as lower weight and thickness. The rise of EL devices can be understood due to their compliance with all these requirements [41]. Two main systems have evolved for EL displays: LED devices and the thin-film electroluminescent (TFEL) devices [42, 43, 44, 45]. A TFEL device consist of normally three thin films, one active layer (typically a semiconductor) between two dielectric films (typically insulators), all of them sandwiched between electrodes (metal or TCO). It is driven by alternating current AC or direct current DC. The light produced by a TFEL device does not come from electron-hole recombination as in p-n junctions. Instead, the voltage applied inject electrons into the conduction band of the active layer from the electronic states of the insulator/semiconductor interface. Then, a high electric field accelerates the electrons to impact and ionize the crystal lattice and excite the luminescent centers (RE or transition metal ions), which then emit light as they return to the ground state (see Figure 2.1). The first TFEL device was discovered in 1960 by Vlasenko and Popkov using a ZnS:Mn active layer system that emits in the yellow region [46]. One attractive feature of this technology is that color depends uniquely on the active layer material, understood as the combination of a host and dopant.

The need for optically active materials in TFEL and LED devices has experienced great attention, especially the II-VI and III-V compound semiconductors such as phosphides and nitrides have attracted widespread attention in this respect. For instance, a variety of host have been investigated for the incorporation of RE ions or transition metal ions with the aim to increase the capability of emitting a wide range of colors, or to display more than one color. On this matter, ZnS is a extensively used host for multi-color EL display, for orange-red emission (ZnS:Mn) and for green light emission (ZnS:Tb) [48]. For the RE ion Tb emission, the explanation of the green emission was done through the following mechanisms: resonant energy transfer from electron hole pairs, direct intra-shell transitions between the 4f energy levels of trivalent Tb, and indirect excitation via lattice defects or bound excitons around the Tb ion [49]. In the search of a blue LED various materials systems were

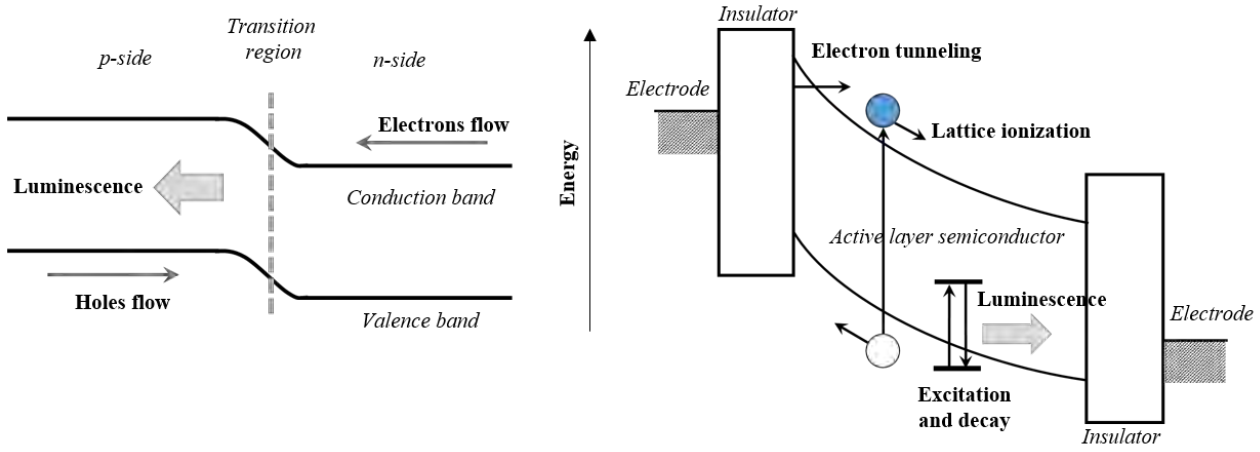

Figure 2.1: Principles of operation of a simple LED p-n junction (left) [47] and a TFEL (right) [41].

investigated, and by 1969, the first blue LED was produced using SiC films in p-n junction devices. But the efficiency was intrinsically poor due to the indirect bandgap of SiC [50, 51]. That means that an electron in the conduction band and a hole in the valence band have different momentums, thus to satisfy the conservation of momentum a phonon must be involved in the recombination process. The probability to fulfill this condition is very low and affects the efficiency of radiative recombinations. At the end, commercial LEDs with GaP and SiC were possible by introducing impurities to relieve the conservation of momentum. As the physical position of the impurity can be specified, the momentum of a carrier in its vicinity becomes unspecified according to the Uncertainty Principle of Heinsenberg. On the other hand, after the reported infrared luminescence from GaAs and the yellow light from GaAsP, many p-n juctions were made of III-V semiconductor compounds. Among them AlN and GaN proved to be the most effective. As better crystal growing techniques were developed, efforts were done to prepare conducting p-type GaN films, and the first blue LED based on GaN came in 1971 [52, 53]. However, it was not until 1994 that a truly bright blue GaN-based LED was demonstrated, after many years of investigation and structure/stoichiometry engineering to move the bandgap energy from the UV 364 nm into the visible spectrum [54]. Following the trend marked by GaN, several works on EL got involved in wide bandgap semiconductors for optical applications. Since then, the major improvements in harnessing EL became possible through the development of wide bandgap sources. For instance, investigation of RE doped GaN led to a new multiple color TFEL system with successful emission of pure red (GaN:Eu), green (GaN:Er) and blue (GaN:Tm) color [55]. Also, white light emission as a result of the combination of orange-red and blue dual color emission has been reported for ZnS:Mn thin films deposited on GaN substrates [56].

As the name suggests, a wide bandgap semiconductor is one having a large bandgap energy or forbidden bandgap, which directly influences the emission and absorption wavelength of the material and their optical properties. The large bandgap allows energy emission and absorption in the green and blue regions of the visible spectrum and in the shorter wavelengths of violet and UV light, being the blue LED a well-known example of its application. Compared to other light sources, the wide bandgap semiconductors can be manufactured in ultra small sizes, have light weight, reach high efficiency and have much longer lifetimes. For all these reasons, the electronic industry has exploited their use as

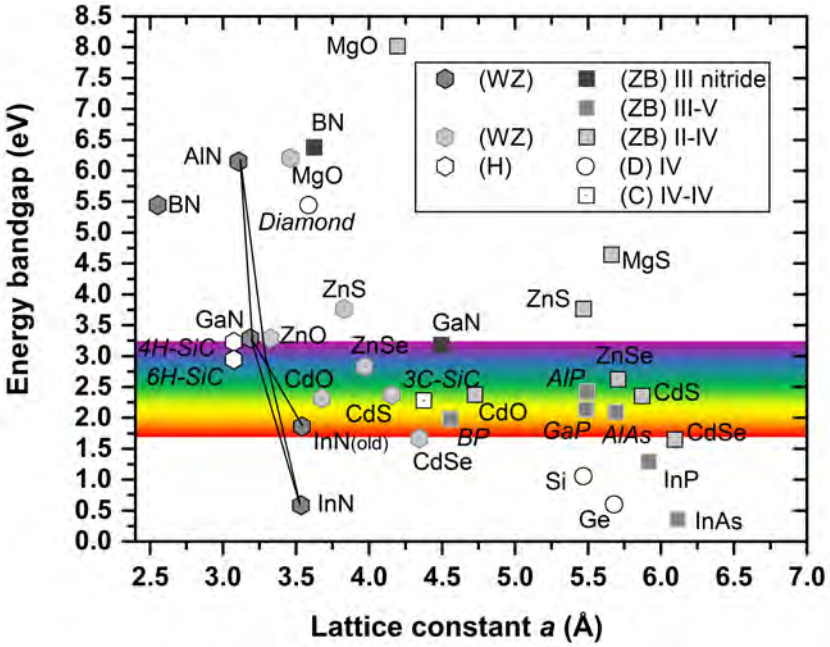

Figure 2.2: Band gap energy versus lattice constant for some technologically important semiconductors. The solid lines show the band gap for some of the ternaries InGaN, AlGaN and AlInN. Source [20].

optical sources for full color displays, white light illumination, blue-violet and UV light sources.

There are three main types of wide bandgap semiconductors: the group III nitrides such as GaN, AlN and InN, the group II oxides such as ZnO and the group II chalcogenides such as ZnSe. Other important wide bandgap semiconductors being studied for electronic device applications are SiC and diamond but their indirect bandgap led to poor emission efficiency which is more than two orders of magnitude less than that of nitride semiconductors. A comparison of the bandgap energies and lattice constants (a) of wide bandgap semiconductors is shown in Figure 2.2, where the hexagons and square symbols represent hexagonal and cubic crystal structures, respectively. The materials name in italicized text are indirect bandgap and those in plain text are direct bandgap semiconductors. When the bandgap energy is larger than 2 eV, the semiconductor is defined as wide bandgap, and optimal for optical applications in the visible-green, blue, violet and UV range of wavelengths. Materials with small lattice constants have shorter interatomic distances and strong binding forces, which strongly bounds the outermost shell electrons or valence electrons to the lattice, as more energy is required to make them free in the conduction band this leads to large bandgap energy. The chemical bonding also determines the bandgap, as the ionicity in bonding increases, the bandgap will also increase due to a reduction in the orbital overlap. The electronegativity difference between the cation and anion of the III-V and II-IV compounds make them partly ionic, whereas diamond has purely covalent bond. Typical crystalline structures of wide bandgap semiconductors are cubic (diamond), hexagonal or wurtzite (AlN) and rock salt (MgO). Many wide bandgap semiconductors exhibit a hexagonal structure, because as the ionic bonding component increases, the interelemental attractive forces also increase. This leads to shorter distances between the ions and resulting in a more compact structure such as the hexagonal close package structure.

2.1.2 Optical properties of wide bandgap semiconductors

Solids can be classified as crystalline and amorphous. While the amorphous materials have a short range order, the crystalline solid has both a long range order and a short range order of atoms, which are placed periodically along the entire material. The crystalline materials can be subdivided in polycrystalline, textured and single or monocrystalline. The polycrystalline structure is one conformed by a set of grains, each of them with a finite-sized regions of periodically arranged atoms with stochastic distribution, thus showing an isotropic behavior. Whereas, the monocrystalline materials might be slightly anisotropic because the distance between neighbor atoms may vary with the crystal direction. On the other hand, amorphous materials have a short range order .

The optical properties of solids are related to their structural and electronic properties, therefore it is important to review the band structure and the electronic density of states of amorphous and crystalline semiconductors. Amorphous semiconductor has broadened electronic states compared to their crystalline counterpart and form band tails at the band edge. The crystalline materials may present band tails with increasing temperature, as a result of phonon interaction and broadened electronic states due to atomic thermal vibrations. Knowing the band structure of a material is extremely useful and important because it led to the calculation of other physical properties such as the optical absorption spectra and the electron density of states

Band structure theory

Crystalline materials have well defined relationship between the energy E and the wavevector k of an electron, usually known as the *energy dispersion* $(E-k)$ relation or the *band structure*. In order to calculate the $(E-k)$ relation of one electron in the crystal, the interactions between different electrons and between electrons and holes are neglected. Only the interaction between the electron and the background of atoms is considered. And the derived $(E-k)$ relation is valid at absolute zero temperature, since the background is assumed to be rigid to avoid worrying about lattice vibrations (phonons). A crystalline solid can be considered as composed of ions placed at the lattice sites with an atomic density on the order of 10^{23}cm^{-3}, with the majority of the electrons tightly bound to the ion core and some less bounded valence electrons participating in the chemical binding. In order to solve the hamiltonian of this huge particle system, it is necessary to use some approximations. First there is the *Born-Oppenheimer approximation*, according to it the electron follows adiabatically any motion of the ions, while the ions reacts slower to changes in the spatial electron distribution. This allows to decouple the core and electron part of the hamiltonian, and further interactions between electrons and phonons can be treated as perturbations. The second simplification is the *Hartree approximation* which considers the Coulomb repulsion from the N-1 electrons as an effective potential influencing one electron. In this manner, our problem has effectively been reduced to a one-particle system [57]. Using these approximation, the hamiltonian of the whole system can be written as a sum of one-electron hamiltonians $\sum_i \left(p_i^2/2m + V(r)\right)$, considering the kinetic energy $p_i^2/2m$ and the potential $V(r)$ of the electron-electron and electron-core interactions. Then, one has to solve the time independent

Schrödinger's equation given in equation 2.1 for a periodic potential and determine $E_n(k)$ and $\psi_n(r)$, where $E_n(k)$ is the electron energy band structure for electrons in band n and state k, and $\psi_n(r)$ are wavefunctions [58].

$$\left[\frac{-\hbar^2}{2m}\nabla^2 + V_L(r)\right]\psi(r) = E\psi(r) \tag{2.1}$$

The potential $V_L(r)$ that an electron experiences inside a crystal is periodic in space due to the periodically order of atoms, however this periodic arrangement is direction dependent, making the band structure anisotropic and different for different crystallographic directions. Solution of the Schrödinger equation gives $\psi_{n,k}(r)$ and $E_n(k)$ which are the wavefunction and the corresponding energy, respectively. Both depend on the wavevector of the electron and the term$E_n(k)$ gives the band structure. Due to the different crystallographic directions in a crystal, the bandstructure typically has a label to indicate the corresponding Miller indices along which it was calculated. In order to solve the Schrödinger equation one has to take advantage of the symmetry properties of the solid, more specifically of the translational symmetry of the lattice. This is done by using the Bloch's theorem and Bloch wavefunctions, which are periodic functions not only in real but also in reciprocal space $\psi_n(k+G,r) = \psi_n(k,r)$, with G as the reciprocal lattice vector.

There are different approximations to calculate the band structure of crystalline materials [59]. The first one is the nearly free electron (NFE) approximation, which considers the outermost electron is very weakly bound to the core and is almost free. This assumption allows to treat the lattice potential $V_L(r)$ as a weak perturbation and apply first order perturbation theory to solve Schrödinger equation and find $E_n(k)$ and $\psi_n(r)$ and calculate the band structure. This approximation is most suitable for a material like sodium which has one electron in the outermost shell, heavily screened from the electrostatic attraction of the nucleus. Following the perturbation theory, a complete orthonormal set of wavefunctions is used as basic functions to expand the perturbed wavefunction, and the Schrodinger's equation is resolved. The calculated band structure is given by:

$$E = \frac{\hbar^2 k^2}{2m_o} + V_o + \sum_{p=1}^{n} \frac{|\gamma_{pG}|^2}{\frac{\hbar^2 —k|^2}{2m_o} - \frac{\hbar^2 —k+pG|^2}{2m_o}} \tag{2.2}$$

where a^3 is the volume of the unit cell (because a is the lattice constant), $G = 2\pi/a$ is the reciprocal lattice vector and γ_{pG} is the component of the spatially periodic lattice pG.

According to equation2.2 the $(E-k)$ relation diverges at $k = -pG/2$, this occurs because the free electron wave with wavevectors k and $k+pG$ are energy degenerate. This degeneracy is resolved by considering latter the effect of spin-orbit interaction. The energy gaps appear at wavevector $k = -pG/2$. In the energy gaps, the wavevector has no real solution and the electron waves with those energies have only imaginary wavevectors. The physical reason of the bandgap in the structure is the periodic lattice potential because the electron wave suffers reflection as it propagates through a periodic array of scattering centers, thus appearing stop bands (frequency/energy which can not transmit or propagate through the array of scatterers) and pass bands (allowed frequency/energy propagation).

The second approximation is the orthogonalized plane wave expansion (OPW) method, which gives good description of realistic band structures because it combines both, the delocalized electron and the tightly bound states to completely describe an electron in an ion. This method considers the case of an electron tightly bound to the ion and where the lattice potential or perturbation is strong. But now the perturbation potential U does not only depend on the local position coordinate, and is much weaker than the lattice potential $V_L(r)$ because it considers not only the attractive but also the repulsive potential terms of the total energy. Since U is weaker than $V_L(r)$, it is possible to solve the Schrödinger equation using first order perturbation theory. On the other hand, the wavefunctions of nearly free electrons are modified to be orthogonal to the atomic core states to consider the screening of the ion Coulomb potential by deep states. The perturbed wavefunction is a linear superposition of the basis functions, and once it is found the complete band structure is resolved. This method is suitable for semiconductors, insulators and metals.

Another powerful approach for calculating band structures is the $k \cdot p$ perturbation theory. This technique used the Bloch Theorem which states that the wavefunction of an electron in a periodic potential can be written as:

$$\psi(r) = \frac{1}{\sqrt{\Omega}} e^{ik \cdot r} u_k(r) \tag{2.3}$$

where Ω is a normalizing volume and $u_k(r)$ is the Bloch periodic function with the same period as the lattice potential so that $u_k(r) = u_k(r + a)$. By substituting equation 2.3 into equation 2.1, one can obtain:

$$\left[\frac{-\hbar^2}{2m_o} \nabla_r^2 + V_L(r) + \frac{\hbar}{m_o} k \cdot p \right] u_k(r) = \epsilon_k u_k(r) \tag{2.4}$$

$$\epsilon_k = E - \frac{\hbar^2 k^2}{2m_o} \tag{2.5}$$

where the term $\frac{-\hbar^2}{2m_o} \nabla_r^2 + V_L(r)$ is the unperturbed Hamiltonian and the last term $\frac{\hbar}{m_o} k \cdot p$ is the perturbation term. One can apply first order perturbation theory to equation 2.4 to find the Bloch wavefunction $u_k(r)$ and the energy ϵ_k. Once the Bloch funtion is found, the Bloch wavefunction can be estimated using equation 2.3 to finally determine the band structure or $(E - k)$ relation.

According to the perturbation theory, one can expand the Bloch functions as a sum of unperturbed states $u_k(r) = C_1 |S\rangle + C_1 |P_x\rangle + C_1 |P_y\rangle + C_1 |P_z\rangle$ ..., where $|S\rangle$ is the s-orbital state and $|P_{i=x,y,z}\rangle$ are the p-orbital states. This means the Bloch function in any band at nonzero wavevector is a mixture of Bloch functions of unperturbed states. For this reason it is important to consider the effect of all the other bands, no matter how far they are in energy, on the wavefunction at nonzero k-state in any band. Otherwise, when one calculates the wavefunctions and energy dispersion relations considering only two bands (conduction and valence bands) the valence band will curve up, instead of bending downwards, in the $(E - k)$ relation plot, leading to quantitatively and qualitatively inaccurate results.

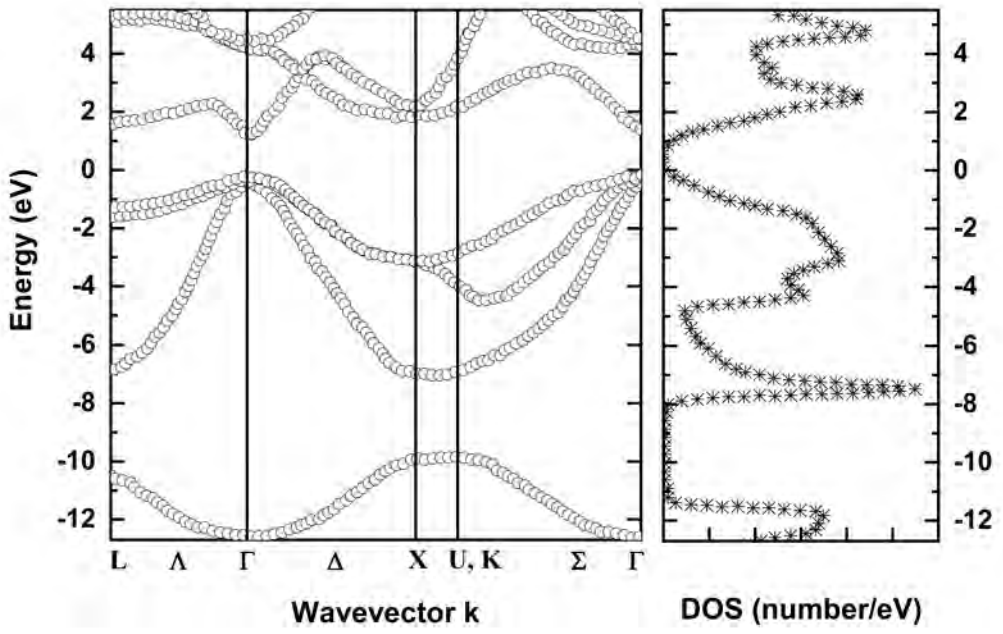

Figure 2.3: Theoretically derived band structure $E(k)$ for GaAs along with directions of high symmetry (right) and the corresponding electronic density of states (left) [60].

In order to illustrate the details of the band structure of III-V semiconductors, the energy dispersion for GaAs is shown in Figure 2.3. This compound has a tetrahedral orientation binding, which is partly ionic. The valence bands of the III-V semiconductors originate from the six atomic p orbitals and the conduction band is originated from the two atomic s orbitals. Also each band has a two-fold degeneracy due to the electron spin. Typically the conduction band has three minima: the Γ-valley, the X-valley and the L-valley. The lowest minimum is known as the primary valley and the others are called satellite valleys. In GaAs, the Γ-valley is the primary valley and the valence band peak usually occurs in the Γ-valley. This configuration corresponds to a direct bandgap semiconductor since the lowest valley in the conduction band occurs at the same wavevector where a maximum valence band point occurs. The other gaps of GaAs, where the valleys occurs at wavevectors different from that of the maximum point in valence band, are called indirect gaps. The optical transition of electrons across indirect gaps is only possible with the assistance of phonon emission or absorption which provides the required momentum.

In semiconductor physics, the bandgap of a semiconductor is always one of two types: a direct bandgap or an indirect band gap. The conduction band minima of a direct bandgap (see Figure 2.4 a) semiconductor occurs in the Γvalley, where the electron momentum is nearly zero. The probability of radiative recombination of electron-hole pairs is highest in the Γvalley of direct gap semiconductors and the conservation laws are full filled with the creation of a photon, emitted in a random direction and with an energy approximately equal to the bandgap. This spontaneous emission in the radiative recombination process is responsible for LEDs producing incoherent radiation. Some examples of this type of direct bandgap LEDs are the high brightness AlGaAs, AlGaInP and InGaN LEDs devices.

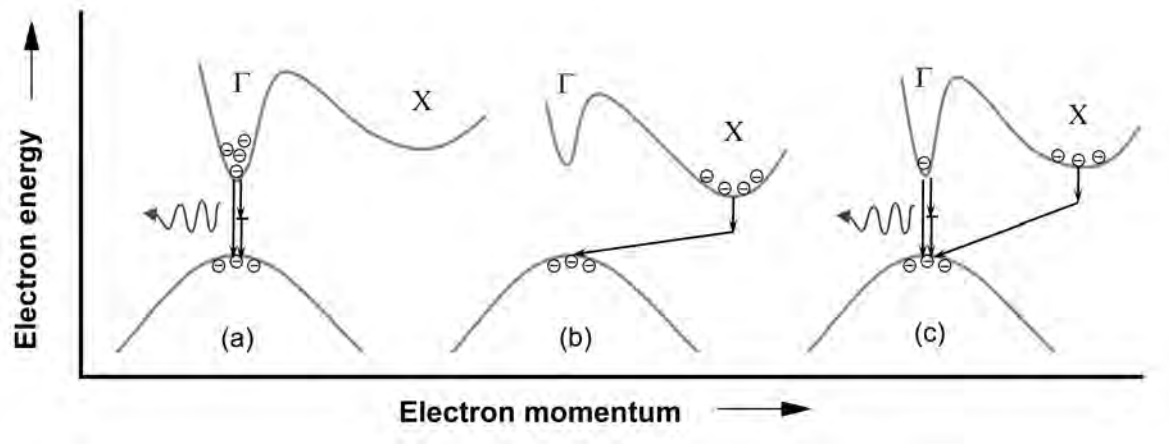

Figure 2.4: Band structure in momentum space (a) Direct bandgap semiconductor. Electron recombines with hole at the Γ valley. (b) Indirect bandgap semiconductor. Electrons occupy the conduction band states of the X valley and the momentum mismatch prevents recombination. (c) Direct-indirect bandgap semiconductor. Recombination probability increases with population of electrons at the Γ valley [61].

The presence of deep levels or defect states within the bandgap is responsible for nonradiative recombinations in the Γvalley. The latter is highly undesired in LEDs, therefore the minimization of impurity and defect concentrations to obtain a high quality layer is extremely critical at all stages of the LED production process. In the case of an indirect bandgap, the conduction band minuma is in the X valley and will be populated of conduction band electrons (see Figure 2.4 b). However, the radiative recombination is very improbable because the conservation of momentum requires the annihilation of a phonon. Therefore, nonradiative recombinations dominates in a typical indirect bandgap semiconductor. The intermediate case is the direct-indirect semiconductor, where both the Γand X valleys have significant electron population (see Figure2.4 c). However, due to the large density of electron states in the indirect minima X relative to the Γdirect minima, the overall radiative efficiency will decrease as the direct-indirect transitions approaches. This type of LEDs such as GaP:Zn:O and GaP:N are much less efficient than direct bandgap devices [61].

To overcome the problem of valence band degeneracy one has to consider the spin-orbit interaction. When an electron moves in an electric field (set by the potential of the background charged ions) and a magnetic field which did not exist in the laboratory frame, appears in the electron's rest frame as a result of Lorentz transformation. The spin orbit interaction arises from the interaction of this magnetic field with the magnetic moment of the electron due to its spin. In order to consider the spin-orbit interaction, one must account the term $H_{so} = \xi \hat{L} \cdot \hat{S}$ in the Schrödinger equation and replacing the scalar wavefunction $\psi(r,t)$ by a 2×1component spinor$[\phi(r,t)]$ which carries information of the spin orientation at any given position r and time t. The spin-orbit interaction resolves the valence band of a crystal, resolving it into three distinct bands: the heavy hole, the light hole and the split-off (see Figure 2.5). Since the valence band states are p-type, with orbital angular momentum quantum number $l = \pm 1$, they experience atomic spin-orbit interation, however, the conduction band does not experience this effect because the atomic orbital states are s-type with $l = 0$.

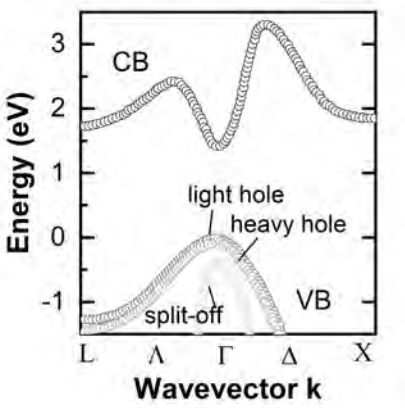

Figure 2.5: Plot of the band structure of GaAs with a zoom on the lifting of the valence band degeneracy by the application of a magnetic field.

Electronic density of states

In the band theory, a solid conformed by a large number of atoms have a large number of energy states that can be considered to be continuous, forming energy bands. Once the $(E-k)$ relation of electronic states is known, it is also important to know how the energy states of the electron system is distributed in a given solid. The density of state (DOS) is defined as the number of available energy states per unit energy per unit volume, and it is obtained by integrating over an energy shell $\{E(k), E(k)+dE\}$ in k-space. The DOS represented by $D(E)$ is given in relation to the total real volume V of the crystal. The units are $eV^{-1}cm^{-3}$.

$$D(E)dE = \frac{1}{8\pi^3}\left(\int\limits_{E(k)=const} \frac{df_E}{|\nabla_k E(k)|}\right) dE \tag{2.6}$$

where df_E is the area element on the energy surface, and $dk_\perp$is the component normal to the energy surface, both related to the volume element dk by $dk = df_E dk_\perp$.

The relationship between the band structure and its corresponding density of states is illustrated in Figure 2.3. The maximum in the DOS is clearly correlated with the flat portions of the $E(k)$ curves along the directions of high symmetry. Also, the zero value in the DOS between the fully occupied valence band states and the unoccupied conduction band states are observed to correspond to the forbidden bandgap of the material.

Electronic states in amorphous materials

The amorphous semiconductor does not possesses a well-defined bandgap. Actually, the band edges of conduction and valence bands are not clear, instead, electronic states are distributed into the gap region forming localized tail states [62, 63]. These tail states arises as a consequence of the disorder and random lattice model of amorphous solids, and are typically associated with variations in the bond length, bond angles, intrinsic defects, dangling bonds and vacancies [64].

The amorphous semiconductors cannot have a $(E-k)$ relation or band structure. The calculation

of electronic states in amorphous materials is more difficult than for crystalline materials. While the atom positions in a crystal are unique, there are infinite number of possible locations of atoms in an amorphous solid, due to this fact the characterization of an amorphous solid is still not well-defined. It is the lack of translational symmetry that prevents from the application of the Bloch theorem. Also, the quasi-momentum conservation for transitions involving reciprocal lattice vectors is invalid. Since the concept of a DOS per energy and volume and of allowed and forbidden bands is independent of translational symmetry with respect to a lattice vector, the DOS can be used in an amorphous solid as long as it exhibits homogeneous composition and structure on a mesoscopic large scale. Therefore, instead of calculating the band structure of amorphous semiconductors, it is preferable to start with the description of the energy-dependent density of states distribution $D(E)$.

The physical origin of the electronic density of states falls into three different energy regions (see Figure 2.6). The first region is the conduction and valence regions, limited by the mobility edges or band edges E_c and E_v respectively. The second region presents band tail states, which are localized electronic states existing near the conduction and valence band edges. The band tail states arise as a consequence of disorder. Thermal, structure, impurity and compositional disorder can all lead to the formation of band tail states. They are also present in a crystalline semiconductor, but they are much more important in determining the electronic properties of an amorphous semiconductor. From Figure 2.6, in the crystalline states the energy band tails are smaller than those of the amorphous counterpart, almost absent. Finally, the third region is the defect state region right inside the forbidden gap. Another important observation from Figure 2.6 is that the well-defined mobility edges of the crystalline solid does not longer appear in the density of states of the amorphous solid. It has been demonstrated that the density of states of the Halperin and Lax type, derived by Sa-yakanit predicts, in three dimensions, an exponential tail of the form $\propto exp\,(-E/E_0)$, with E_0 as a fitting parameter, called the Urbach tail . Also, the localized states in the Urbach tails looks rather continuous. For all these reasons, the limits are not very clear to define the optical bandgap energy value of an amorphous semiconductor. There are several approaches trying to define the energy bandgap, but does not give an absolute bandgap value. These models only represent an expected behavior, similar to that of the real bandgap.

The presence of defects in the crystalline solid introduce energy levels or defect states in the forbidden gap, influencing the electronic properties of the material because the electron occupancy is changed by doping or by trapping charge carriers. In the case of a crystal, any divergence from the periodic and orderly lattice can be considered a defect. However, in the amorphous structure the random lattice and disorder is a normal situation. In an amorphous material, the definition of defect is any departure from the ideal random network [65, 66, 67], which is defined as a continuous and uniform disorderly lattice. By continuous one expects not to have dangling bonds and by uniform, that there is no segregation or clusters formation in order to avoid the formation of a composite instead of a compound. An example of dangling bond is the case of amorphous silicon (a-Si) with its sp^3 hybrid orbital states. When a bond is formed, the sp^3 states split forming a bonding (conduction band) and antibonding (valence band) states. But not all the sp^3 orbitals can find another neighboring orbital

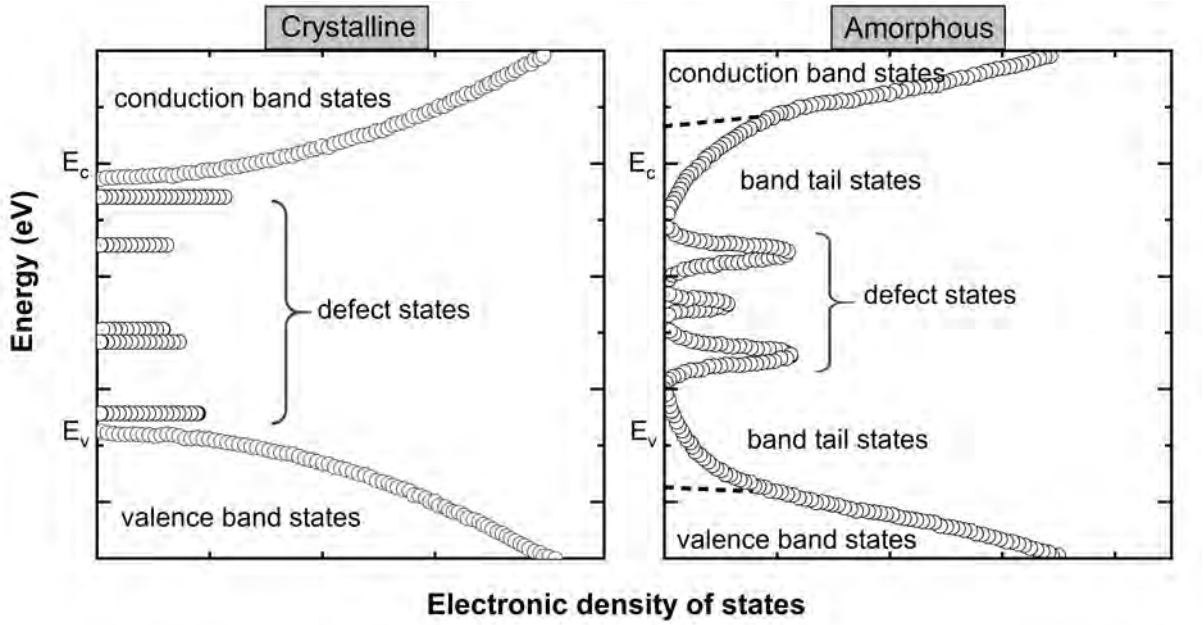

Figure 2.6: Models for the density of states of a crystalline (left) and an amorphous (right) semiconductor.

pair to form a bond in an amorphous solid. Every non-bonding orbital is a dangling bond with an unpaired electron and a net charge, giving rise to localized states in the gap as shown in Figure 2.7.

The net charge of a non-bonding state can have three possible charge states with different energy levels: two electrons D^-, one electron D^0 and no electron D^+. The Coulomb forces between two electrons, repel each other, splitting the energy levels by a correlation energy$\sim 1/r$, where r is the distance between the electrons. The electron-phonon interaction in a semiconductor is the main factor for relaxation of a transferred electron, for instance from the conduction band to a valence bands or defect states. This effect is represented by a configurational coordinate diagram shown in fig. 2.7. To trap an electron from the conduction band, with energy E_c at the bottom of the conduction band, an energy E_T must be released via electronic (optical) transition. At this moment, the optical transition from the upper to lower states is vertical and leaves the lower vibrational state excited. The electron then relaxes to the minimum energy of the defect $E_c - E_T - w$ via electron-phonon coupling. In contrast, thermal excitation requires an energy $E_T - w$, which is the energy difference between the potential minimum of the defect and conduction band, where there is no change of the configuration coordinate q leaving the upper vibrational state excited. Then, further relaxation to the equilibrium state occurs by emitting phonons.

Fundamental optical absorption of semiconductors

The fundamental equation governing all the absorption an emission in solid is the Fermi's golden rule, given by eq. 2.7:

$$W_m = \frac{2\pi}{\hbar} \sum_{final\ states} \delta\left(E_f - E_i \pm \hbar\omega\right) \left|\left\langle f \left| H' \right| i \right\rangle\right|^2 \tag{2.7}$$

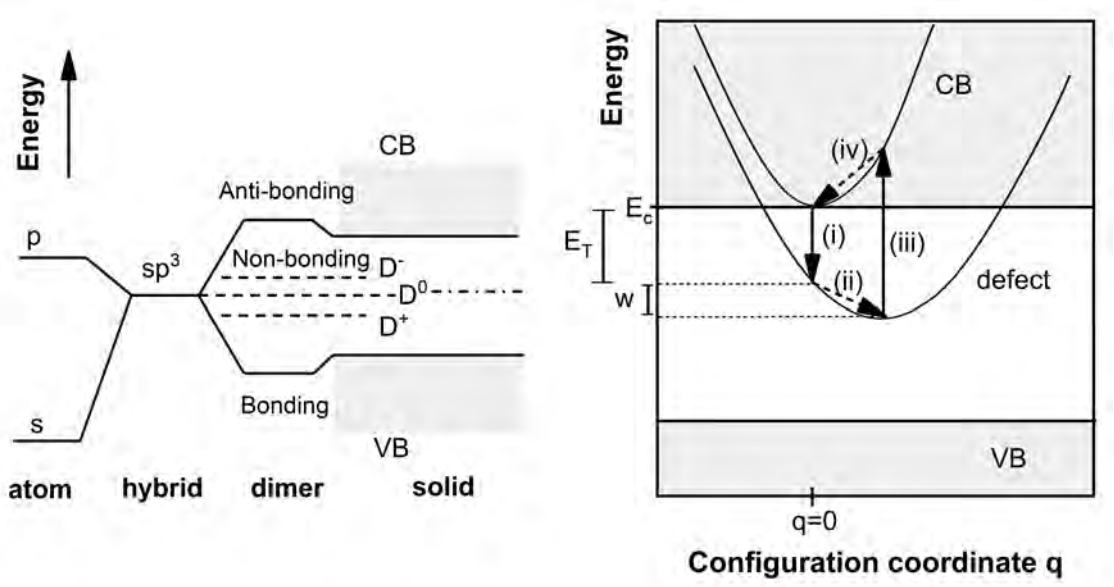

Figure 2.7: Schematic illustration showing the progression of the electronic structure for an sp^3 bonded system and the configuration coordinate diagram describing the (i) capture, (ii) relaxation, (iii) release an (iv) relaxation due to electron-photon interaction.

where $W_m$is the transition rate from the initial state $|i\rangle$ with energy E_i to the final state $|f\rangle$ with energy E_f , $H^{'}$ is the spatial part of the perturbing Hamiltonian, and $\hbar\omega$ is the energy of the photon involved in the interaction. Inside the delta function, the " $+$ " sign accounts for the case of photon emission, and the " $-$" sign, for the absorption. The conservation of energy is represented in the delta function, while the transition strength and selection rule of transitions are determined by the matrix elements given by $\left|\left\langle f\left|H^{'}\right|i\right\rangle\right|^2$. The photon energies of interest ranges from the UV to IR, which means that the momentum of photon in semiconductors is very small compared to the momentum of electron. Therefore it is possible to use the dipole approximation ($k \approx 0$) and simplify the transition matrix to $|\langle u_{v0}|\nabla_i|u_{c0}\rangle|^2$, with $u_{v0}$and u_{c0} represents the valence and conduction band central cell bonding orbitals, and ∇_i is the differential operator in the direction of the light polarization. Thus, the electronic transition rate between the valence and conduction bands in crystals, in the one electron approximation due to the optical excitation of Bloch electrons can be written as:

$$R_{cv} = \frac{2\pi}{\hbar}\left(\frac{\overrightarrow{E}e}{2\omega m_e}\right)^2 \sum \left|M_{cv}^2\right| \delta\left(E_c - E_v - \hbar\omega\right) \delta_{k_c,k_v} \tag{2.8}$$

Here m_e is the electron mass, e the electron charge, ω the photon frequency, $E_{c,v}$ is the electron energy and $k_{c,v}$ is the electron wavevector at the conduction and valence states respectively. The transition matrix element $|M_{cv}|$ in the dipole approximation is given by with the spatial part of the perturbing hamiltonian $H = (e/m_e)\,\nabla \cdot A$ as the operator for the interaction of the electromagnetic radiation with the electrons in the solid [68].

The absorption coefficient α is directly proportional to the electronic transition rate R_{cv} due to optical excitation between the valence states and conduction states. and is given by:

$$\alpha \frac{cn\epsilon_0}{2} |E|^2 = R_{cv}\hbar\omega \tag{2.9}$$

where c is the speed of light, n the refractive index, ϵ_0 the electric permittivity constant in vacuum, and $|E|$ the electric field amplitude [68]. From equations 2.8 and 2.9, one can find an expression for the absorption coefficient in terms of conservation of energy and momentum between the valence and conduction states:

$$\alpha = \frac{\hbar}{4\pi\epsilon_0 nc}\left(\frac{2\pi e}{m_e}\right)^2 \frac{1}{\hbar\omega}\sum |M_{cv}|^2 \, \delta\left(E_c - E_v - \hbar\omega\right) \delta_{k_c,k_v} \tag{2.10}$$

In crystalline materials, depending on the band structure, there are two more probable electronic transition: direct and indirect. Notice that $k_c = k_v$ in case of direct optical transitions, then $\delta_{k_v,k_c} = 1$, also the energy difference between the valence and conduction bands $E_c - E_v$ is exactly the optical bandgap E_g. In contrast, in the case of indirect transition, the energy levels involved in the electronic transition do not share the same wavevectors $k_c \neq k_v$, and the conservation of momentum requires the assistance of another particle, i.e. phonons, here denoted by (k_φ, E_φ). Further calculations for the absorption coefficient use the density of states to represent a summation over the energy-momentum relation and thus, allows discrimination between the direct and indirect bandgap transitions in crystalline solids.

$$^{ind}\alpha = \frac{\alpha_0}{\hbar\omega} \int_{E_c(0)}^{\hbar\omega+E_v(0)} \int_{E_c-\hbar\omega}^{E_v(0)} D_c(E_c) D_v(E_v) \delta(E_c - E_v - \hbar\omega \pm E_\varphi) dE_v dE_c \tag{2.11}$$

$$^{dir}\alpha = \frac{\alpha_0^{'}}{\hbar\omega} \int_{E_{cv}(0)}^{\hbar\omega} D_{cv}(E_{cv}) \delta(E_{cv} - \hbar\omega) dE_{cv} \tag{2.12}$$

Here the indirect absorption coefficient given by equation 2.11 is written as a function of the valence and conduction electronic density of states. In the case of a direct bandgap, eq. gives the absorption coefficient of direct materials, where the is the density of combined states defined from the energy difference. It was assumed for the calculations that the transition matrix elements $|M_{cv}|$ change slowly with the energy E_{cv} in the range of interest, from UV to IR, and therefore it is absorbed with the other constants in the coefficient α_0.

Considering the electronic density of states, in amorphous solids the corresponding absorption coefficient can be written in the form given by:

$$^{amorph}\alpha = \frac{\alpha_0}{\hbar\omega} \int\int D_c(E_c) D_v(E_v) \delta(E_c - E_v - \hbar\omega) dE_v dE_c \tag{2.13}$$

$$D_c(E_c) = \sqrt{2}\frac{m_e^{*3/2}}{\pi^2\hbar^3} \left(E_c - E_c(0)\right)^{1/2} \tag{2.14}$$

$$D_v(E_v) = \sqrt{2}\frac{m_h^{*3/2}}{\pi^2\hbar^3}\left(E_v(0) - E_v\right)^{1/2} \tag{2.15}$$

where $m^*_{e/h}$ is the electron/hole effective mass and $E_{c/v}(0)$ is the free electron energy of the conduction/valence band. Assuming that (1) the valence and conduction bands have a parabolic shape, and (2) the conservation of the wavevector is relaxed, one can solve the integral in equation 2.13and obtain the absorption coefficient written in equation 2.16, which is called the ***Tauc model.***

$$\alpha_{Tauc} = M^2_{Tauc}\frac{(\hbar\omega - E_{Tauc})^2}{\hbar\omega} \tag{2.16}$$

Here M^2_{Tauc} is a constant and E_{Tauc} is the Tauc-energy gap, which can be estimated from the plot of the empirical expression $(\alpha\hbar\omega)^{1/2} = M_{Tauc}(\hbar\omega - E_{tauc})$ versus the photon energy $\hbar\omega$. By extrapolating the linear functional dependence of the expression at large energies. Similarly, by integrating equation 2.12 and equation 2.11 for direct and indirect transitions respectively, the absorption coefficients for each case is given by:

$$^{dir}\alpha = M^2_{ind}\frac{(\hbar\omega - E_g)^{1/2}}{\hbar\omega} \tag{2.17}$$

$$^{ind}\alpha = M^2_{ind}\frac{(\hbar\omega - E_g \pm E_\varphi)^2}{\hbar\omega} \tag{2.18}$$

The optical bandgap calculated from Tauc's model, is strongly affected by the band tails. However, the preceding calculation in the amorphous states did not take into account the mobility edges well into the band tails. Thus, the $E_{Tauc}$is considered a representative value for the true bandgap. For many years, the Tauc's approach has been the standar empirical model to determine the optical band gap of amorphous semiconductors. There are different methods to determine the bandgap [69, 70] which takes into account the localized tail states to enable an accurate calculation of the absorption coefficient in the amorphous case.

On the other hand, the ***Urbach model*** describes empirically the absorption coefficient using an exponential function for the tail absorption with the incident photon energy [71]:

$$\alpha(E) = \alpha_F exp\left(\frac{E - E_F}{E_u}\right) \tag{2.19}$$

Where E_u is the Urbach energy (typically in the range from 10 meV to 200 meV), it reflects the shape of valence band tails so that E_u varies with the structural disorder. On the other hand, E_F and α_F are constants related to the Urbach focus which has been reported already for different materials, e.g. *a*-SiC [72, 73, 74, 75]and *a*-AlN [72, 75]. The exponential shape given to the Urbach tail has been under discussion over the years [76, 77, 66]. One favored explanation for the shape is given by the joint density of states [67], which reflects the natural disorder broadening of the bands. It is considered that the exponential shape of the band tails comes from topological disorder and thermal vibrations [78, 79, 67]. Nevertheless, the exact relation between structural disorder and the band tails shape

is still unclear. Later, O'Leary and his group contributed on modelling the electronic properties of amorphous material, using thermal fluctuations in the band edge and calculated the average absorption coefficient using both the Tauc and Urbach approaches [79].

O´Leary proposed to average the local joint DOS over the conduction and valence bands, using a Gaussian distribution $\hat{W}$ as the weight function, so as to account for the band thermal fluctuations [79]. Using both the average joint DOS and the stimulated relaxation process in the Fermi's Golden rule (eq. 2.8), one can calculate the average electronic transition rate between the conduction and valence bands.

$$\langle R_{cv} \rangle = \frac{2\pi}{\hbar} \left(\frac{\overrightarrow{E} e}{2\omega m_e} \right)^2 \int \left| M_{cv}^2 \right| D_{cv}(E_{cv}) \hat{W}_{(E_{cv}-\hbar\omega)} dE_{cv} \tag{2.20}$$

Note that in the limit for gaussian width $0 \rightarrow \hat{W} \rightarrow \delta(E_{cv} - \hbar\omega)$, recovering the original electronic transition rate for direct transitions presented in equation 2.8.

Motivated by the shape of the Kubo-Greenwood formula [80, 77] for the conductivity of amorphous materials, Guerra proposed to extend $\langle R_{cv} \rangle$ directly to the electronic transition rate R_{cv} by using the derivative of the Fermi distribution $f(\hbar\omega) = 1/(1 + exp(\beta\hbar\omega))$, as weighting function $\hat{W} = -\partial f(\hbar\omega)/\partial(\hbar\omega)$, instead of the Gaussian distribution, for describing structural ***band fluctuations*** [81, 82, 83].

$$\langle R_{cv} \rangle (\hbar\omega, T) = \frac{2\pi}{\hbar} \left(\frac{\tilde{E} e}{2\omega m_e} \right)^2 \int_{E_{cv}(0)}^{\infty} |M_{cv}|^2 D_{cv}(E_{cv}) \left\{ -f^{'}(E_{cv} - \hbar\omega) \right\} dE_{cv} \tag{2.21}$$

The result for the absorption coefficient is shown in equation 2.22 after $\alpha(\hbar\omega) \propto R_{cv}(\hbar\omega)\hbar\omega$.

$$\alpha(\hbar\omega) = -\frac{\pi}{4} \frac{\alpha_0}{\beta^2 \hbar\omega} Li_2 \left(-exp\left\{ \beta(\hbar\omega - E_0) \right\} \right) \tag{2.22}$$

$$\alpha_0 = \frac{2}{cn\epsilon_0} \left(\frac{e}{m_e} \right)^2 \frac{(m_e^* m_h^*)^{3/2}}{\pi^3 \hbar^5} |M_{cv}|^2$$

Where $Li_2(x)$ is the Di-Logarithm function of x, $E_0$is the bandgap in absence of band fluctuations, and β is the Urbach slope defined as $\beta = 1/(k_B T)$ ans is inherited from the Fermi distribution. It defines how large the fluctuations are. Additionally, an asymptotical analysis of equation 2.22 leads to the Urbach and Tauc expressions respectively given in equation 2.23. At zero Kelvin temperature, the first equation in equation 2.23leads to the Tauc expression as expected, while the second equation differs from the original Urbach rule by the factor $\hbar\omega\beta^2$.

$$\alpha(\hbar\omega) = \frac{\pi}{8} \frac{\alpha_0}{\hbar\omega} \begin{cases} (\hbar\omega - E_0)^2 + \dfrac{\pi}{\beta^2} & , \ \hbar\omega \gg E_0 \\ \dfrac{2}{\beta^2} exp\{\beta(\hbar\omega - E_0)\} & , \ \hbar\omega \ll E_0 \end{cases} \tag{2.23}$$

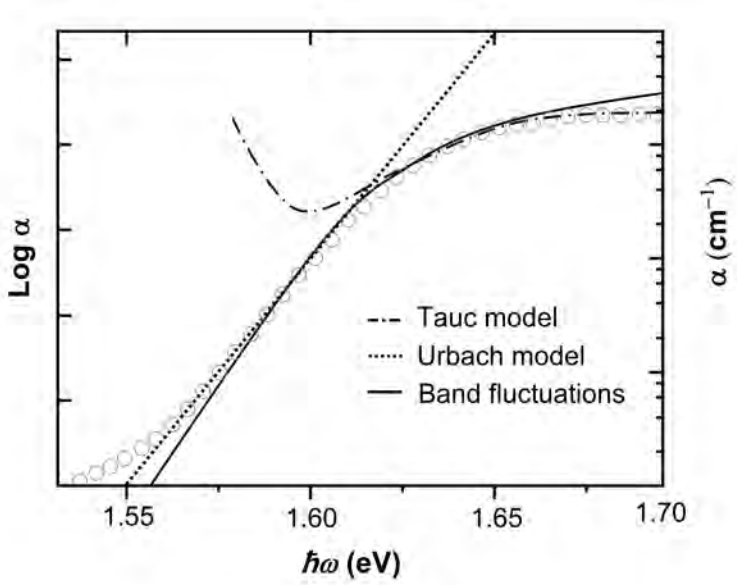

Figure 2.8: Fitted absorption coefficient using the traditional Urbach rule, Tauc model and band fluctuations model. The points correspond to experimental data of Wolf *et. al.* []

For a crystalline structure the absorption equation is as follows:

$$\alpha(\hbar\omega) = -\frac{1}{2}\frac{\alpha_0}{\hbar\omega}\sqrt{\frac{\pi}{\beta}}Li_{1/2}(-e^{\beta(\hbar\omega - E_g)}) \tag{2.24}$$

Until here, two approaches have been used to describe and predict the optical absorption spectrum versus the photon energy: the Urbach tail region and the fundamental absorption or Tauc region. Both approaches are considered into one single analytical expression, achieved by using a band fluctuation average in the free electron approximation, to describe the shape of disorder induced localized and extended states. The expression given by equation 2.22 and its asymptotic behavior by equation 2.23 models the fundamental absorption of amorphous semiconductors and allows to measure the optical bandgap E_0 in the absence of disorder and the Urbach energy E_U independently from a single fit of equation 2.22. It is important to notice from Figure 2.8 that the fits with the conventional Tauc-plot and Urbach rule predict a bandgap that is very susceptible to the selected fitting region. These issues can be overcome when using the band fluctuation model.

2.1.3 Representative wide bandgap semiconductors

III-V nitride semiconductor

The III-V wide bandgap nitrides is a group made up of GaN, AlN, InN, and BN. Nitrogen is the smallest element from group V and has a large difference in electronegativity with elements of group III. In consequence, these compounds have very strong chemical bonds [84]. The nitride semiconductor crystals exhibit wurzite, zinc blende and rock salt structures, depending on the degree of ionicity [85] (see Figure 2.9) . Both covalent bonds and ionic bonds exist between the compound crystal atoms. However, the more the ionic the bonds, the stronger ionicity the crystal has and the easier it is for the wurtzite structure to form. Since all nitrides are strong ionic crystals at room temperature and

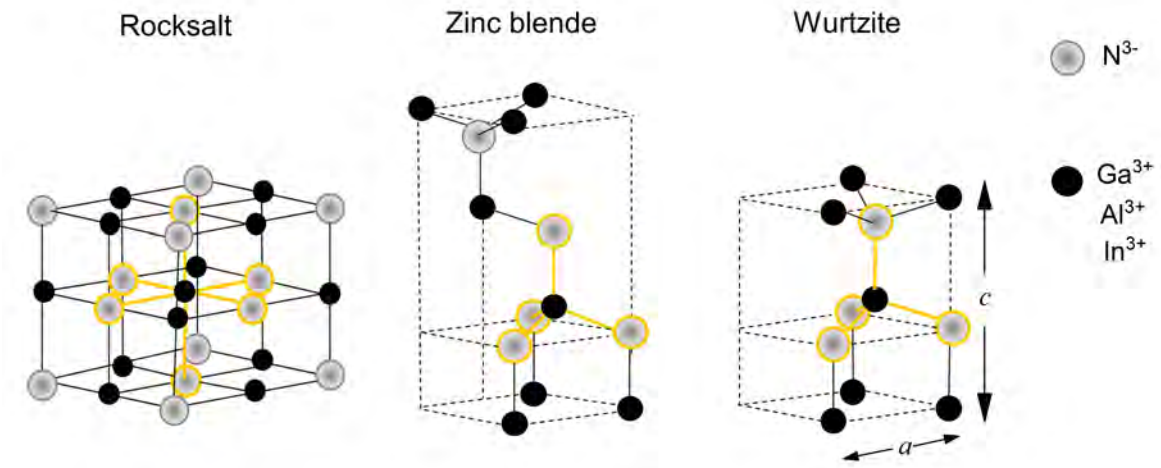

Figure 2.9: Schematic of III nitride crystal structures: cubic rock salt, cubic zinc blende and hexagonal wurtzite.

atmospheric pressure, the wurtzite structure is the dominant and thermodynamically stable phase, whereas, the cubic zinc blende structures is a metastable phase, and the rock salt structure can be induced in AlN and GaN at very high pressures.

The strong bonds and larger direct bandgap of all wurtzite III-V semiconductors is an attractive characteristic for optoelectronic devices that need short wavelength of the visible range (violet and blue regions) and for devices that work at high temperatures or with high powers.

Aluminum nitride

Among all nitrides, when crystallized in the zinc blende phase, AlN present an indirect bandgap (5.4 eV [86]). But when crystallized in the hexagonal wurtzite structure, AlN has the largest direct bandgap (6.2 eV [87, 86]) and thus, is the best material for constructing devices for the violet region. The wurtzite AlN crystal has ideally four equal bonds tetrahedrally connected to atoms of opposite type. This configuration allows to interpret the AlN crystal structure as one built up as a series of interpenetrating hexagonal close-packed (HCP) sublattices, each of which is with one type of atoms. The space group for the wurtzite structure is C_{6v}^4. The height of each tetrahedron is $c/2$ and the length of one side of the base is a. Therefore, the ratio c/a is 1.633 the corresponding to an ideal regular tetrahedron. But commonly, the c axis suffers compression and the departure from the ideal ratio c/a lead to some distortion of the Al-N bonds from a regular tetrahedral arrangement (see fig. 2.9) [88]. Reported lattice parameters range from 3.110 to 3.113 Åfor the a parameter, and from 4.978 to 4.982 Å for the c parameter. The c/a varies between 1.600 and 1.602. This deviation from that of the ideal wurtzite crystal is commonly related to the lattice stability and ionicity.

Comparisons of AlN and other materials are shown in Table 2.1. The optical, mechanical and electrical properties of AlN have been extensively studied [89, 90, 91, 92, 93, 94, 95]. It has been reported that AlN is a "typical dielectric" ceramic material, also AlN has shown high thermal conductivity and low thermal expansion coefficient, as well as good thermal shock resistance. Although AlN has a lower modulus of elasticity than most of other semiconductor, it is compatible with the materials in terms

Material	2H-AlN	2H-GaN	3C-SiC	4H-SiC	6H-SiC	Si	Diamond
Structure	Wurtzite	Wurtzite	Z. Blende	Wurtzite	Wurtzite	Diamond	Diamond
Bandgap (eV)	6.2 (D)	3.47 (D)	2.36 (I)	3.23 (I)	3.0 (I)	1.12 (I)	5.5
Breakdown field($\times 10^6$ V cm^{-1})	1.2−1.8	∼5	∼3	2.4	∼4 [98]	0.2−0.3	1−10 [99, 100]
Resistivity (Ω·cm)	$>10^{13}$	$>10^{10}$	150 [101]	$>10^{12}$		1000	$>10^{13}$
Lattice constant (Å)							
a	3.112	3.189	4.359	3.07	3.073	5.431	3.56[102, 103]
c	4.97	5.186		10.08	15.12		
Index of refraction							
UV (∼3 eV)	2.15	2.3	2.71 [104]	2.72[105]	2.73	4.46−5.03	2.48[106]
IR (1.1 eV)							
Epitaxial (300 K)	2.1−2.2	2.29 [107]					
Crystalline	1.9−2.1	2.3 [108]	2.63	2.57	2.58	3.53 [109]	2.38
Amorphous	1.8−1.9					3.57 [110]	
Thermal expansion coefficient (K^{-1})							
a ($\times 10^{-6}$)	5.27	5.59	3.28	3.30	3.35	2.6	0.8 [103]
c ($\times 10^{-6}$)	4.15	3.17		3.16	3.25		
Thermal conductivity(W cm^{-1}K^{-1})	2.85−3.2	1.3	4.9	3.7	4.9	1.5	22-23[111, 103]
Melting point (K)	3273	2400	3103	3103	3103	1690	1041
Young's modulus (GPa)	308−374	210 -290[112, 113]	448	474[114]	180[112]	75	1003[114]

Table 2.1: Basic properties of AlN, GaN, SiC and Diamond semiconductors in comparison to Si (I: indirect, D:direct band gap) , see references [115][116][87][117][118][118].

of its elastic deformation. It was suggested the possibility of AlN as a refractory material, due to the high melting point (> 2800 °C). However, the main drawback of AlN is the high reactivity of Al with oxygen, which can lead to distortions in the energy gap and lattice constant [96, 97].

Gallium nitride

GaN is a material typically used for all device films which require fast carrier transport with a high breakdown voltage. In particular, GaN presents remarkable electrical and thermal properties (see Table 2.1). The favorable electronic transport characteristics of GaN, makes it ideally suited for high-power and high-frequency electronic devices, and has been extensively examined over the years [119, 120, 121] . GaN usually crystallizes in the hexagonal wurtzite structure. But also, it was reported the growth of GaN films with cubic zinc blende structure on GaAs [122, 123]. Unfortunately, epitaxy layers of GaN are generally difficult to fabricate due to unsuitable lattice-matched substrates [124, 125]. For instance, the thermal expansion mismatch between GaN and Si, which can be as high as 54%, represents a challenge for the growth of GaN on Si substrates for LEDs [126]. The GaN is commonly used in conjunction with other III-V nitride semiconductors to form ternary alloys

of AlGaN and InGaN for bandgap engineering. Indeed, the wide bandgap of GaN offers a range of optical emission wavelengths from red to UV when alloyed with indium or aluminium, whereas GaN based LEDs emit in the blue or UV region and can be used with phosphors to produce white light for solid-state lighting [127, 128, 129].

IV-IV nitride semiconductor

Silicon carbide

SiC is a binary $A^{N}B^{8-N}$compound with eight valence electrons per atom, and the relationship between the Si atoms and C atoms in SiC is such that each Si atom is tetrahedrally bonded to four silicon atoms [111]. The distance between close Si or C atoms is of 3.08 Å, while the distance between close Si and C atom is 1.89 Å. Since the elements in SiC comes from the same group IV, the interatomic bonds posses strong covalency. But, according to Pauling, due to the electronegativity of Si and C, the compound has a 12% of ionicity. There are more than 200 different polytypes of SiC depending on the repetition period of the Si-C bilayer, each of them with diffrent physical properties. The SiC varieties include the cubic β-SiC, which has a zinc blende structure (i.e. 3C-SiC), and α-SiC which is represented as a combination of zinc blende and wurtzite structure (i.e. 2H-,4H-, and 6H-SiC). The band structure of SiC for all main polytypes (3C-, 2H-,4H-, and 6H-SiC) shows valence band maximum at the zone center (Γ-point) and conduction band minimum different from the Γ-point, this means that all versions of SiC are indirect bandgap semiconductors. Indeed, the conduction band minimum is at the X-point for 3C-SiC, near the K-point for 2H-SiC and near the M-point for 4H-, 6H-SiC, and each of them present bandgap values of 2.36 eV, 3.33 eV, 3.23 eV and 3.0 eV, respectively [130].

Because of the indirect band structure of SiC, the absorption coefficient slowly increases even when the photon energy exceeds the bandgap. The wide bandgap of SiC means optical detection capability in the UV range. However, since SiC has an indirect bandgap, its optical emission is inefficient, making it unsuitable for LED applications compared to GaN, which is a direct bandgap semiconductor. Table 2.1 summarizes the major physical properties of most common SiC polytypes. Among them, the 4H-SiC has been almost exclusively employed for power device applications, due to its superior electronic properties such as the high electric breakdown field ranging from 1.5 to 4×10^{6} V/cm, and high electron mobility parallel the c-axis of 4H-SiC. Hence, to realize Schottky barrier diodes with maximum performance, 4H-SiC are generally chosen for work . Also, 3C-SiC has received attention due to the relatively low-voltage applications and high temperature sensors [117].

SiC possesses low thermal expansion coefficient and high thermal conductivity. Therefore, SiC is an attractive semiconductor for high temperature electronic and optoelectronical applications. Its thermal conductivity exceeds that of copper, Al_2O_3 and AlN (around 2.3 to 4 W/cm-K). Its relatively high thermal stability and its strong double bond structure contributes with high decomposition temperature, higher than 2000°C. Although all polytype of SiC are highly resistant to chemical attack, oxides can be formed on the SiC surfaces. When nitrogen is introduced, SiC reacts with nitrogen at temperatures of 1450°C an higher to form a silicon nitride compound (Si_3N_4) [131]. On the other hand, the material is highly resistant to the incorporationand diffusion of impurities, so dopants need

to be implanted or grown into the material. The major mechanical properties of SiC are hardness and fracture strength. The Young's modulus ranges between 330 GPa and 700 GP depending on the polytype and measurement technique used to acquire the data. While fracture strength is as high as 21 GPa at room temperature and around 0.3 GPa at 1000°C [116, 117].

Diamond

From the electronic application point of view, diamond is a wide bandgap semiconductor with highly desirable properties depending on the kind of passivation of the surface dangling bonds. Diamond is an allotrope of carbon in the crystal lattice of which every atom is surrounded by four atoms located in the vertices of a tetrahedron. The crystalline structure of diamond is cubic and metastable at room temperature and atmospheric pressure, as shown in fig. . The sp^3 hybrid orbital bonding of C-C atoms has an interatomic spacing of 1.54 Å, which represents the 66% of the Si-Si interatomic distance. Also, the covalent bonding of diamond is approximately 2.3 times larger than that of silicon [111]. Therefore, diamond crystals are extremely hard (Young's modulus ∼1050 GPa) and presents high melting points (∼4100 K) [132]. Diamond is an indirect bandgap semiconductor, where the lowest minima of the conduction band is located along the Δaxis, and the maximum of valence band is at Γdegenerate axis. The optical bandgap value is 5.50 eV at room temperature and around 5.41 eV at 100 K.

There are four groups of diamonds, depending on their optical and luminescence properties which depend in turn, on quality and quantity of impurities. Type I diamonds are UV absorbent, while type II diamonds are transparent for UV light and in general more pure than the ones of type I. Type IIb diamonds have an appreciable electrical conductivity, whereas the diamonds of type IIa, and type I are insulators. Apparently the high conductivity of type IIb is due to the presence of substitutional boron in the diamond crystal lattice. The most common impurity presented in the diamonds of all types is nitrogen. Moreover, most electrical and optical properties of diamond are of extrinsic nature, i.e. strongly dependent on the impurity content. Diamond possesses extreme thermal conductivity as well as exceptional optical transparency, and chemical inertness. At 300 K, high purity single crystalline diamond has a thermal conductivity of approximately 24-25 W/cm-K, compared with 4 W/cm-K of copper and 1.5 W/cm-K of Si [133]. As temperature decreases, diamonds's thermal conductivity increases reaching the maximum of 42 W/cmacoustooptic-K, but for temperatures lower than 80 K, thermal conductivity decreases. Moreover, impurities such as nitrogen reduce the thermal conductivity. Even more sensitive to impurities than thermal conductivity is the electrical conductivity of diamond. In practice the resistivity of highly pure diamond is in the range of 10^{14}-$10^{16}\,\Omega\times$cm. But, when doped with boron resistivities as low as $0.1\,\Omega\times$cm can be achieved [134]. On the other hand, the optical transmission of pure diamond is the largest of bandwidth from 225 nm into the microwave range. The presence of impurities alters the optical transmission causing diamond to be opaque. The mean value of refractive index of diamond of different types varies negligibly, for instance the reported values for natural and synthetic diamond are 2.41 (λ=547 nm) and 2.42 (λ=547 nm) respectively. However, the quality of the diamond film influences strongly the absolute value of the refractive index, varying from 1.9 for poor quality diamond films, to 2.4 for good-quality films. The

air oxidation of diamond films decrease the refractive index to 1.5 due to the formation of pores, while annealing at 850°C has been reported to increase by ˜ 2 o 7 % the index of refraction of poor qulity diamonds films [135]. Although the variety of interesting properties and potential applications, the market development has not increased substantially mainly due to economic considerations. Thus, continued reduction in the cost of high quality diamond deposition techniques remains a critical area that requires further research.

II-IV semiconductors

The wide bandgap II-IV compounds such as ZnS, ZnO, ZnSe, ZnTe and CdS are being applied to optoelectronic devices, specially LEDs due to their direct bandgap and suitable bandgap energies. In these compounds, the s^2 electrons of the outer orbitals of the group II atoms, which have high positive ionicity, and the s^2p^4 electrons of the group IV atoms, with negative ionicity, rearrange to form sp^3 hybrid orbitals. The adjacent atoms are bonded forming tetrahedral coordination with strong covalency.

Zinc Selenide

Representative semiconductors of this group are ZnSe and ZnS which play an important role in the development of blue-green light emitting optoelectronic devices [136, 137, 138]. The fundamental absorption edge of ZnSe corresponds to direct transitions from the highest valence band to the lowest conduction band at the Γ point. At room temperature ZnSe has a bandgap value of 2.7 eV and ZnS bandgap is 3.68 eV, which makes it suitable for blue emission. The ZnSe crystallizes in cubic zinc blende structure which consists of two interpenetrating face-centered cubic sublattices with one displaced by $a/4$ in each direction from the other sublattice. Each atom is at the center of a regular tetrahedron formed by four atoms of opposite type. However, it is also possible to grow hexagonal wurtzite ZnSe crystals with high ioniciy. High quality ZnSe films can grow on GaAs substrates due to the small lattice mismatch of only 0.26% [111].

Zinc Oxide

Another important II-IV semiconductor is ZnO, with excellent optical, piezoelectric and acousto-optic properties and applications as a photoconducting, and fluorescent material in the VIS-UV wavelength region, gas sensors and solar cell components [139]. This compound crystallizes in the wurtzite structure and has a direct wide bandgap value of nearly 3.4 eV, and similar to GaN it is important for blue and UV optical devices. Also, its lattice constant is nearly the same as GaN, opening the possibility of growing GaN layers on bulk ZnO substrates for optical device applications. However, the advantage of ZnO over GaN lays in its larger exciton binding energy of 60 meV and its ability to grow single crystal substrates. Additional to the wurtzite phase, ZnO also crystallizes in the cubic zinc blende and rock salt structures. The former is stable only when grown on cubic substrates [140], and the latter is a high metastable phase which forms at ˜10 GPa and can not be epitaxially stabilized [141]. The alloying of ZnO with MgO and CdO has been reported to be an effective way for bandgap tunning [142, 143, 144].

2.1.4 Emission of light by impurity atoms

Most luminescent materials are composed of a transparent amorphous or crystalline host and an activator, i.e. a small amount of intentionally added impurity atoms distributed in the host lattice. Therefore, the luminescence process can be divided into two parts: the processes related to the host, and those related to the activator. Section 2.1.2 has a description of the electronic states and fundamental absorption of crystals and amorphous solids. This section deals with the optical absorption and emission by impurity atoms or local defects in a transparent wide band gap semiconductor host, from a macroscopic point of view according to the theory of light interaction with matter[145, 146, 147].

Transition probability

In the quantum theory of radiation, light is emitted or absorbed through electronic transitions between discrete energy levels in an atom, i.e. between two states m and n with energies E_m and E_n respectively, where $E_m > E_n$. To get a quantitative result regarding the discussion on the transition probabilities W_{mn}, it is necessary to describe first the spectrum of radiation and then to characterize the atomic transition. The spectral distribution $\rho(\omega)$ is the number of photons with frequencies between ω and $\omega + \triangle\omega$. The total energy density is obtained by integrating the spectral distribution over the entire frequency range. The atomic transition is described by a lineshape function $\xi(\omega)$ giving the relative probability per unit time that the atom absorbs or emits a photon of frequency ω. The probability that an atom shows a transition $n \to m$ is calculated by:

$$W_{mn} = \int B_{n\to m}\rho(\omega)\xi(\omega)d\omega \tag{2.25}$$

Here $B_{n\to m}$ is a proportionality constant known as Einstein coefficient of optical absorption. To solve the integral, Einstein's treatment assumes that the system of isolated atoms interacts with blackbody radiation at absolute temperature T. The energy spectrum of a black-body source is given by the Plank formula in equation 2.26. Since the spectral density described in equation 2.26 does not vary much across the frequency range of the atomic transition, it is possible to consider a constant value $\rho(\omega_{mn})$ where the angular frequency ω_{mn} of the photon is the center frequency of the lineshape function, and satisfies: $\hbar\omega_{mn} = E_m - E_n$.

$$\rho(\omega) = \frac{\hbar\omega^3}{\pi^2 c^3}(exp\left[\hbar\omega/k_B T\right] - 1)^{-1} \tag{2.26}$$

Considering that the lineshape function is normalized over all the frequencies. The transition probabilities for absorption becomes:

$$W_{mn} = B_{n\to m}\rho(\omega_{mn})\int \xi(\omega)d\omega = B_{n\to m}\rho(\omega_{mn}) \tag{2.27}$$

The energy density $\rho(\omega_{mn})$ is the light intensity $I(\omega)$ divided by c, the speed of light.

Besides the absorption process, there are two possible emission processes: spontaneous emission

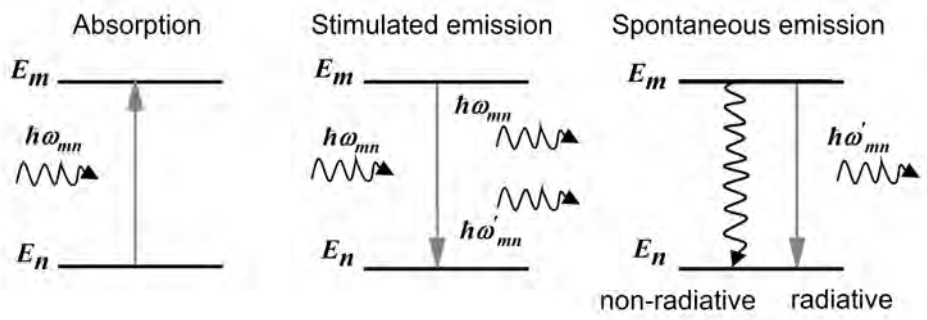

Figure 2.10: Optical transitions between two states n and m in an atom in the presence of inciden light with energy $\hbar\omega_{mn}$. A photon with energy $\hbar\omega'_{mn}$ is emitted after stimulated or spontaneus emission transitions.

and stimulated emission (see Figure 2.10). In the former, the atom in the excited state have a natural tendency to decay and lose the excess of energy, here the transition probability is represented by the Einstein coefficient $A_{n\to m}$. In the latter, the incoming photon field can stimulate de-excitation and produce emission transitions, its probability is represented by the Einstein coefficient $B_{m\to n}\rho(\omega_{nm})$. The three Einstein coefficients introduced above are not independent parameters, instead they are all related to each other. This is deduced by considering the thermal equilibrium of a black body radiation where all the three possible optical transition take place (see equation 2.28).

$$B_{n\to m}N_n\rho(\omega_{mn}) = A_{m\to n}N_m + B_{m\to n}N_m\rho(\omega_{mn}) \tag{2.28}$$

Here N_m is the number of gas atoms in the m state and N_n in the n state. The ratio of N_m to N_n will be given by Boltzmann's law:

$$\frac{N_m}{N_n} = \frac{g_m}{g_n} exp\left(-\frac{\hbar\omega}{k_B T}\right) \tag{2.29}$$

where g_m and g_n are called the degeneracies of the energy levels m and n, respectively.

In the steady state conditions, the rate of absorption transitions must exactly balance the rate of induced and spontaneous emission between the atoms in the states m and n. So that eq. 2.28 can be consistent with the Boltzmann's law and the Plank formula, the Einstein coefficients should be related to each other according to the following equations:

$$g_n B_{n\to m} = g_m B_{m\to n} \tag{2.30}$$

$$A_{m\to n} = \frac{\hbar\omega_{mn}^3}{\pi^2 c^3} B_{m\to n} \tag{2.31}$$

The interrelationship of the Einstein coefficients states the equivalence between the absorption and stimulated emission for a simple atomic system with nondegenerate energy levels. Also it states that a high emission probability will also have a high emission probability for spontaneous and stimulated emission processes.

Radiative transition rates

In a quantum mechanical treatment, the calculation of radiative transition rates is based on time-depended perturbation theory. Therefore, the transition rate, i.e. for the spontaneous emission, can be calculated by using Fermi's golden rule and is given by:

$$W_{mn} = \frac{2\pi}{\hbar} D(\hbar\omega_{mn}) \left|M_{mn}\right|^2 \tag{2.32}$$

$$M_{mn} = \left\langle m \left| H^{'} \right| n \right\rangle = \int \Psi_m^*(\overrightarrow{r}) H^{'}(\overrightarrow{r}) \, \Psi_n(\vec{r}) d^3\overrightarrow{r} \tag{2.33}$$

where M_{mn} is the matrix element for the transition that appears in the Fermi's golden rule dipole moment, and $D(\hbar\omega)$ is the density of photon states. The perturbation of the system causing the transition is represented by $H^{'}$, $\overrightarrow{r}$ is the position vector of the electron and Ψ_m and $\Psi_n$are wavefunctions of the states m and n, respectively. Until now, the atoms are treated as quantum mechanical objects, however it is convenient to treat the light as an electromagnetic wave whose electric dipole moment or magnetic dipole moment varies with time. There are a number of physical mechanisms that cause atoms to absorb and emit light. Among them, the electric dipole interaction is the strongest process. The electric dipole perturbation due to the external electric field $\overrightarrow{E}$, is given by:

$$H^{'} = e\overrightarrow{r} \cdot \overrightarrow{E} \tag{2.34}$$

Considering the electric dipole perturbation in the expression for the matrix elements (eq. 2.33), one can writte the matrix elements in a more succinct form:

$$M_{mn} = -\overrightarrow{\mu}_{mn} \cdot \overrightarrow{E}_0 \tag{2.35}$$

where $\overrightarrow{\mu}_{mn} = -e\left(\langle m|x|n\rangle \hat{i} + \langle m|y|n\rangle \hat{j} + \langle m|z|n\rangle \hat{k}\right)$is the dipole moment of the transition, and a key parameter that determines the transition rate for the electric dipole process.

The energy density is related to the intensity I_0 of the perturbing ligth by $\xi(\omega) = I_0/c$, and thus it is proportional to E^2. Introducing the Fermi's golden rule into the transition probability given by 2.27, the Einstein coefficients for transitions between non-degenerate atomic states are obtained as follows:

$$B_{n\to m} = \frac{\pi}{3\varepsilon_0\hbar^2} \left|M_{mn}\right|^2 \tag{2.36}$$

$$A_{m\to n} = \frac{\omega_{nm}^3}{3\pi\varepsilon_0\hbar c^3} \left|M_{mn}\right|^2 \tag{2.37}$$

The intensity of light is generally defined as the energy transmitted per second through a unit area perpendicular to the direction of light. The intensity of the spontaneous emission of an atom is proportional to the energy of the emitted photon, multiplied by the spontaneous emission transition probability per second given by eq. 2.37.

$$I(\omega_{mn}) \propto \hbar\omega_{mn} A_{m\to n} = \frac{\omega_{mn}^4}{3\pi\varepsilon_0 c^3} |M_{mn}|^2 \tag{2.38}$$

Similarly, the intensity of absorbed light by an atom from an incident intensity is proportional to the energy of the absorbed photon multiplied by the absorption transition probability and the energy density:

$$I(\omega_{mn}) \propto \hbar\omega_{mn} B_{m\to n} (I_0/c) = \frac{\omega_{mn}\pi I_0}{3\varepsilon_0\hbar c} |M_{mn}|^2 \tag{2.39}$$

In the physics of luminescent materials, the emission spectra of atoms in crystalline or amorphous solids is of particular interest. Since the atoms are locked in a lattice, there exists some mechanisms which prevents the radiation emitted in atomic transitions from being perfectly monocromatic or line shaped. At this point, it is convenient to use a parameter known as the radiative lifetime τ_{rad}, which measures the lifetime of an electronic state in the hypothetical situation where only radiative transitions occurs when the excited atom returns to its ground state. If there are N_m atoms in the upper energy state at time t, the decay rate is given by $dN_m/dt = -A_{m\to n}N_m$, with solution $N_m(t) = N_m(0)exp\left[-A_{m\to n}t\right] = N_m(0)exp\left[-t/\tau_{rad}\right]$. This means, the population will decay radiatively due to spontaneous emission with a time constant τ_{rad} defined by:

$$\tau_{rad} = A_{m\to n}^{-1} \tag{2.40}$$

In the case of several possible final states of the transition, controlled only by spontaneous emission processes, the radiative lifetime is determined by the inverse of the sum of the transition probabilities to all final states:

$$\tau_{rad} = \left(\sum_n A_{m\to n}\right)^{-1} \tag{2.41}$$

When the atom decays to the ground state by a non-radiative transition, i.e. by emitting phonons instead of photons, the decay rate becomes $dN_m/dt = -\left(A_{m\to n} - \tau_{NR}^{-1}\right) N_m$ and the total lifetime is given by:

$$\frac{1}{\tau} = \frac{1}{\tau_{rad}} + \frac{1}{\tau_{NR}} \tag{2.42}$$

Where τ_{NR} is the non-radiative transition time. Therefore, the presence of non-radiative transitions

shortens the total lifetime of the excited state and introduces a broadening of the full width at half maximum (FWHM) of the spectral line shape by a factor $1/2\pi\tau$. Indeed, the lifetime of phonon emission is often very fast in solids, and along with the inhomogeneity of the host medium, both cause considerable broadening of the emission lines.

2.2 Luminescence of RE doped materials

Most luminescent materials or phosphors consist of a host lattice usually with embedded impurities which are capable to produce emission of light after suitable excitation. Such impurities are referred to as activator ions or luminescent centers. Generally, these luminescent centers are RE ions or transition metal ion, and the host matrix are wide bandgap solids. The RE elements are highly valued as optically active centers due to their remarkable luminescence features coming from the electronic configuration and electronic transitions within the 4f-shell of trivalent RE ions. The absorption of excitation energy populates the energy levels of the RE ions directly via direct impact on activator ions, or indirectly by energy transfer (via the host lattice). The transparency of wide bandgap hosts enables the transfer of visible light to the surface of the device, and also prevents electrons from bridging the gap thermically. Furthermore, it is the emission of the activator ion the most important light emission-process. An appropriate description of the optical emission within RE ions embedded in a solid, considers them as localized centers and their electronic states are treated with a localized model rather than with a band model [145].

The spectrum of transparent solids containing a small percentage of RE ions exhibits well-resolved groups of lines. Each group of lines corresponds to transitions between the energy levels in the RE ion, such levels are split as a consequence of the interactions with the crystal field of the host ions, which is weaker than the spin-orbit coupling, which in turn is weaker than Coulomb forces interactions. However, the well-resolved spectral lines of REs are only expected if the transitions occur between levels inside the 4f electronic shell, and these transitions are known to be forbidden by the Laporte selection rule. According to Laporte's rule: the electric dipole (ED) character of the RE luminescence transitions [148] requires the change of parity between the initial and final states of the electron system with a spherically symmetric potential. On the other hand, only ED transitions are forbidden within the 4f shell, magnetic dipole (MD) or electric quadrupole radiation are allowed. In 1937, Van Vleck [149] proposed a solution to the selection rule puzzle, by considering a distortion of the electronic motion by a noncentrosymmetric crystalline fields in solids, so that the selection rules for free atoms no longer applies. The lack of a center of symmetry at the equilibrium position forces the wavefunctions to change parity allowing a coupling between odd and even states. This mixing of parity states relaxes Laporte's rule.

The sharp luminescence lines of RE spectra are consequence of the fact that 4f electrons are partially shielded from the surrounding crystal fields by the outer 5s and 5p filled shells. This shielding leaves the energy levels of the 4f electron systems almost unaffected opening up the possibility to have

a spectrum with emission wavelengths almost independent from the host and with spectral line-widths slightly broadened. Nonetheless, the crystal field plays an important role in the dynamical process of radiative transitions between 4f states. Not only by the relaxation of Laporte's selection rules, but also by influencing non radiative transitions and the energy exchange between the host matrix and the ion.

The theoretical calculation of the energy levels of the triply charged RE ions are a necessity for the interpretation of the RE spectra. The methods for dealing with these calculations were developed and described in considerable detail by Condon and Shortley [150] in the Theory of Atomic Spectra published in 1935. However, the approach followed by Condon and Shortly is very laborious compared with the methods developed by Racah in a series of papers entitled Theory of Complex Spectra [151, 152, 153, 154] (1941-1949). In these papers Racah developed a powerful and elegant technique to calculate the energy levels of the states of f^N configurations comprising two or more electrons by defining tensor operators and group theoretical methods, which greatly simplify the problem. This method was further enhanced through the simultaneous developments of new experimental methods and the introduction of electronic computers for the performance of complex calculations.

The following section develops, up to a certain extent, the theory behind the 4f photoemission of RE ions in a solid, in order to be able to understand better the observed RE photoemission spectrum. The first part of this section deals with the energy level structure of RE ions, as affected by their electronic properties and the strengths of the various interactions. The second part develops the luminescence of a localized center, and describes the radiative and non radiative electronic transition processes to take place in RE doped materials. Finally, an overview of the mechanisms responsible for the excitation of optically active RE ions in semiconductors is also provided.

2.2.1 Energy level structure of RE ions in solids

The RE elements, also known as lanthanide atoms, consist of fifteen elements with progressive filling of the 4f shell. The first element of the group is lanthanum (Z=57) and the last one is lutetium (Z=71). In their ground configuration, all RE elements have a xenon like closed shell electronic structure ($1s^2 2s^2 2p^6 3s^2 3p^6 3d^{10} 4s^2 4p^6 4d^{10} 5s^2 5p^6$), and additionally to an unfilled $4f^N$ shell, there are two or three external electrons ($6s^2$ or $5d^1 6s^2$). While the outer shell electrons participates in the band states, the 4f shell remains by far intact in the RE metals. Typically, the band calculations do not include the 4f states, except for the Ce metal because its 4f levels are very close to the Fermi energy. The 4f shell electrons are strongly correlated by the Hund's rule interactions and can not be reliably described in a full band structure. In most RE metals the 4f shells posses a magnetic moment which also complicates the band structure considerably.

In the quantum mechanical framework, it is possible to describe the characteristic RE spectra by the special properties of the 4f eigenfunctions, which in turn are a consequence of the special nature of the 4f effective potential-energy function for these elements. It was demonstratedthat for elements with

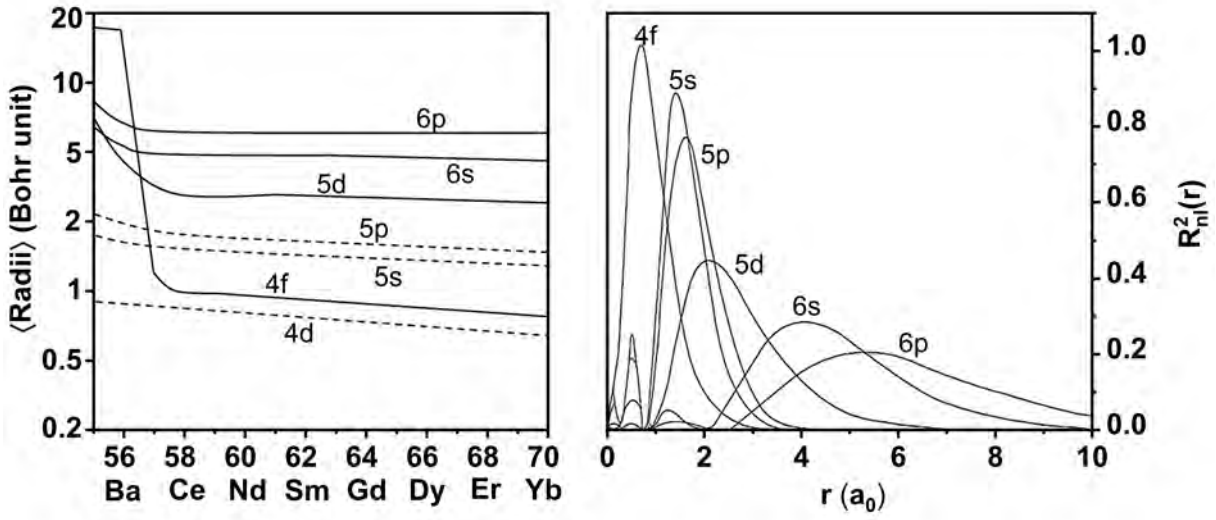

Figure 2.11: Expected radii of the various orbitals in excited $4f^{n-1}5d6s6p$ configurations of neutral atoms (left)[155] . Radial distribution functions of the 4f, 5s, 5p, 5d, 6s and 6p electrons for cerium (right) from reference [156].

small atomic number, the 4f effective potential present a single minimum, thus leading to a large radii orbit with 4f electrons weakly bounded to the atom and essentially external electrons [157, 155]. Up to barium, while the atomic number increases, the 4f effective potential presents a second minimum but the 4f electrons are still outer electrons. A sudden change in the properties of the 4f shell occurs from lanthanum, where the 4f effective potential becomes deeper and wider to that the 4f shell is entirely contained therein. From lanthanum, each consecutive atom has a nuclear charge more positive by one unit, with the corresponding increment in the number of electrons present in the 4f orbitals. Since the 4f electrons can not perfectly shield each other from the increased positive charge of the nucleus, the effective nuclear charge attracts more an more the 4f electron as the atomic number increases. This leads to a successive reduction of the 4f shell radii and binding energies, accompanied also by smaller contraction of the 5d and 6s shells. The described situation is known as the *lanthanide contraction.* Fig. 2.11 illustrates the lanthanide contraction and also shows that the radii of the 4f electrons are appreaciable smaller than those of the n=5 and n=6 electrons. Another property of the RE elements is the so called *competition between electrons*, arising from the fact that the binding energy of the 4f, 5d, 6s and 6p electrons are roughly equal.

When embedded in a solid, the RE ions are no longer free but surrounded by the ligand atoms of the host. These ligand atoms exert a field on the RE ion producing the so called crystal field interaction. The energies associated to this interaction varies between 1 and 1000 meV, competing with the energies associated to the spin-orbit interactions and sometimes the mutual electrostatic repulsion between electrons, whereas the interaction of an electron with the Coulomb field of the nucleus has energies in the order of 10000 meV order. Thus, the crystal field is an additional interaction in a more complicated structure.

In order to solve the energy levels of a triply ionized RE ion in a solid, the Schrödinger equation should considers the Hamiltonian of an optically active RE ion, given by:

$$H = H_0 + H_{ee} + H_{SO} + H_{CF} \tag{2.43}$$

$$H_0 = \sum_i^n \frac{p_i^2}{2m_e} - \sum_i^n \sum_l^N \frac{Ze^2}{4\pi\varepsilon_0 |r_i - X_l|} \tag{2.44}$$

$$H_{ee} = \sum_i^n \sum_{i \neq j}^n \frac{e^2}{4\pi\varepsilon_0 |r_i - r_j|} \tag{2.45}$$

Where r_i and p_i are the position and momentum of the ith electron, X_l is the location of the lth nucleus, Z is the atomic number, the sum on l is over all the N nuclei and the sum on i and j are over all the n electrons. The first term in eq. 2.43 is the free Hamiltonian H_0, given by eq. 2.44, which takes into account the kinetic energy of the electrons in the system and the attractive nuclear potential, respectively. The interaction between the electrons is represented by H_{ee} which takes into account the Coulomb repulsion between the outer electrons. The H_{SO} term accounts for the spin-orbit coupling and the last H_{CF} term represents the static crystal field interaction.

In the absence of external fields, the free ion Hamiltonian H_0 conforms the most relevant interactions and gives a zero-order approximation for the calculation of the energy levels. In this approximation the 4f electrons experience a central field produced by the nucleus and the 54 electrons in the completed xenon-like shell. At first, the electrostatic repulsion between all outer $4f^N$ electrons are disregarded. In this approximation the state of an individual single electron is characterized by four quantum numbers, i.e. n, l, m_l, m_s. The principal quantum number n (orbital size) and the orbital angular momentum l (orbital shape) for each electron are given, but their orientation in space given by m_l and their orienation in spin by m_s are arbitrary. Up to this moment, the degeneracy of a configuration is given by $(4l+2)!/(n!(4l+2-n)!)$, for instance a $4f^{10}$ state, with $l = 3$ and $n = 10$, has a degeneracy of 1001. For a system of N>1 electrons, the free ion problem can not be analytically solved. Several simplifications are made to transform this many body problem into one-body problem. Firstly, the energy is assumed to be constant with time. Secondly, the central field approximation assumes a spherical symmetry function for the potential and kinetic energy exerted on the electron. Therefore, each electron can be considered to be moving independently in the field of the nucleus and feeling a spherical average potential of all the other electrons. This is the Born-Oppenheimer approximation for a system with N electrons. Solving the Schrödinger equation at this point leads to approximate solutions $|n, l, m_l, m_s\rangle$ as shown in equation 2.46 :

$$\psi_{n,l,m_l,m_s}(r, \theta, \phi) = \kappa \cdot R_{n,l}(r) \cdot Y_{l,m_l}(\theta, \phi) \cdot \chi_{m_s} \tag{2.46}$$

The wavefunctions in equation 2.46 are expressed in polar coordinates (r, θ, ϕ) as the product of a normalizing factor κ, the radial function $R_{n,l}$, the angular function Y_{l,m_l} and the spin function χ_{m_s}. However, there are more than one electron in the 4f configuration, and the Hamiltonian H_0 has to be

adjusted to consider the outer electrons and the electrostatic repulsion between them, expressed by H_{ee}. All possible associations of the N electrons with the 4f wavefunctions, considering spin $\pm 1/2$, are called *micro states*, and they are represented with the quantum numbers S, L, M_L and M_S derived from the projections of the sum of the angular momenta, as given by:

$$\overrightarrow{L} = \sum_i^N \overrightarrow{l}_i \,, \quad \overrightarrow{S} = \sum_i^N \overrightarrow{s}_i \,, \quad M_L = \sum_i^N (m_l)_i \,, \quad M_S = \sum_i^N (m_s)_i \tag{2.47}$$

By introducing the electrostatic interaction between the electrons in the zero order Hamiltonian, some of the degeneracy is remove. Initially, the Coulomb interaction in H_0 separates the configuration by the order $10^5\,\mathrm{cm}^{-1}$; but after the introduction of H_{ee} the electronic configuration splits into different *spectroscopic term*s, written as ^{2S+1}L and the SL terms are separated by the order of $10^4\,\mathrm{cm}^{-1}$. This set of micro states have different S and L terms with different energies, but each state is independent of M_s and M_L and the total angular momentum $J = L \pm S$ of the electrons. For the first seven ions (from $La^{3+}$to Eu^{3+}), $J = L - S$; and for the last eight ions (from Gd^{3+} to Lu^{3+}), $J = L + S$. The multiplicity of this term exhibits a degeneracy given by $(2L + 1)(2S + 1)$. Which means that $H_0 + H_{ee}$ is quite limited to describe the fine structure of RE ions because the 4f levels are degenerate. This degeneracy is removed by adding a non-central field interaction to the Hamiltonian, given by the spin-orbit interaction term:

$$H_{SO} = \sum_i \lambda(r_i) \overrightarrow{s}_i \cdot \overrightarrow{l}_i \tag{2.48}$$

$$\lambda(r_i) = \alpha^2 R Z_{eff}/r_i^3$$

Here λ is a constant depending on the position of the electron, with α the fine structure constant, R the Rydberg constant and Z_{eff} the effective nuclear charge. Also, $\overrightarrow{s}_i$ is the spin momentum of ith electron and $\overrightarrow{l}_i$ its angular momentum. The spin-orbit interaction splits the 4f level of RE ions into many different levels called J-multiplets, categorized by the spectral term $^{2S+1}L_J$. The spectral term consists of three quantum numbers L , S and J. The number $2S + 1$ represents the multiplicity of the term and $J = L \pm S$. This interaction allows coupling between states of different S and L but remains dependent on J. In other words, the Coulomb interaction removes degeneracy in S and L, the spin-orbit interaction removes the degeneracy in J and separates the SLJ multiplets by the order of $10^3\mathrm{cm}^{-1}$(see Fig. 2.13). At this point, each level is reduced to $(2J + 1)$ degeneracy. Ordinarily, the effects of the H_{SO} interaction is usually small though not negligible, therefore their influence on energies and wavefunctions is calculated with help of perturbation theory. The remaining degeneracy in M_J is only removed by the crystal field.

Note that since the free ion interactions are independent of the crystalline structure, the position of the multiplets are almost independent of the host. However, when a RE ion is not longer isolated from any other system, but placed into a crystal lattice, the spherical symmetry of its electronic structure is destroyed and the remaining $(2J + 1)$ degeneracy of its spectroscopic levels is partly lifted by the crystal field interaction. The crystal field theory treats the RE ions as isolated atoms placed in a static

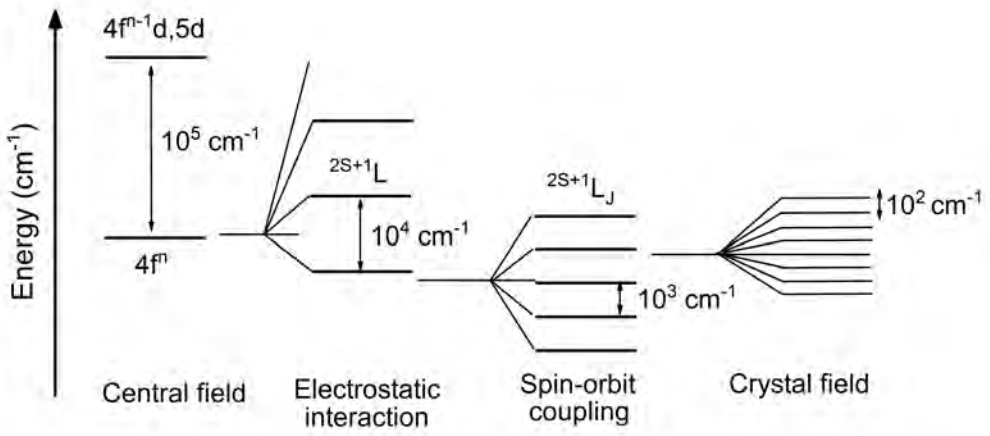

Figure 2.12: Schematic representation of the different potential interactions for the splitting of the electronic energy levels for a RE ion in a solid.

electric field produced by surrounding ions of fixed electrostatic charges, usually known as ligands. The static crystal field does not considers any dynamic interactions with the lattice, with molecular complexes or with individual ions. As the electrons in the outer orbitals and those in the ligand repel each other due to repulsion between like charges, the energy of the orbital electrons will vary depending on the distance to the ligands, which results in the orbital splitting in energy. According to the magnitude of the crystal field, three possible situation may occur. First, when the crystal field interaction is small compared to both the Coulomb interaction and the spin-orbit interaction, one has a weak crystal field. In this case the crystal field is treated as a perturbation on the system that causes the Stark-splitting of the free ion multiplets and determines the selection rules for optical transitions between two energy levels. This is the case of RE ions, because their unfilled 4f shell are shielded from the neighboring ions by the outer orbital electrons. Second, when the crystal field strength is greater than the spin-orbit interaction but less than the Coulomb interaction, it is said to have a medium crystal field case. The effect of this type of crystal field is to split the energy levels of the free ion system into a set of crystal field terms and further apply the spin-orbit interaction to form crystal field multiplets. This is a typical situation of transition metal ions with unshielded active electrons in the 3d shells. Third, there is the strong crystal field case, in which the strength of the crystal field is greater than both the spin-orbit interaction and the Coulomb interaction. Examples of strong crystal field interaction are transition metal ions of the 4d and 5d groups which tend to form strong covalent bonds with neighboring ions .

The presence of the crystal field will modify the energy levels and wavefunctions of the free ions. For the determination of these modifications it is necessary to consider a crystal field Hamiltonian general enough to be applicable to all possible cases, such as the one suggested by Judd [158] and B. G. Wybourne [159]. It is expressed as a series of spherical harmonics and its notation is given by eq. 2.49:

Symmetry	Site symmetry	Crystal field parameters	Example
Monoclinic	C_1, C_s, C_2, C_{2h}	B_0^2, B_0^4, B_0^6, $\Re(B_2^2)$, B_2^4, B_2^6, B_4^4, B_4^6, B_6^6	LaF_3
Rhombic	C_{2v}, D_2, D_{2h}	B_0^2, B_0^4, B_0^6, $\Re(B_2^2, B_2^4, B_2^6, B_4^4, B_4^6, B_6^6)$	$Y_3Al_5O_{12}$
Trigonal	C_3, S_6	B_0^2, B_0^4, B_0^6, $\Re(B_3^4)$, B_3^6, B_6^6	$LiNbO_3$
	C_{3v}, D_3, D_{3d}	B_0^2, B_0^4, B_0^6, $\Re(B_3^4, B_3^6, B_6^6)$	Y_2O_2S
Tetragonal	C_4, S_4, C_{4h}	B_0^2, B_0^4, B_0^6, $\Re(B_4^4)$, B_4^6	$LiYF_4$
	C_{4v}, D_4, D_{2d}, D_{4h}	B_0^2, B_0^4, B_0^6, $\Re(B_4^4, B_4^6)$	YPO_4
Hexagonal	C_{3h}, D_{3h}, C_6, C_{6h}	B_0^2, B_0^4, B_0^6, $\Re(B_6^6)$	$LaCl_3$
	C_{6v}, D_6, D_{6h}		
Cubic	T, T_d, T_h, O, O_h	B_0^4, B_0^6, $\Re(\frac{5}{\sqrt{70}}B_0^4, -\sqrt{\frac{7}{2}}B_0^6)$	CeO_2

Table 2.2: A list of crystal field parameters for f^Nelectronic configurations of different crystal host structures [161].

$$H_{CF} = \sum_i \sum_{k,q} B_q^k C_q^{(k)}(i) \tag{2.49}$$

$$C_q^{(k)}(\theta, \phi) = \sqrt{4\pi/(2l+1)} Y_{lm}(\theta, \phi)$$

In this equation Wybourne use the tensor operators $C_q^{(k)}$ components which transform like the spherical harmonic functions, used for the analytical form of the 4f wavefunctions, to describe the crystal field. Here the summation over i is on all the 4f electrons. The k index can take odd and even values, and together with the q values are related to the site symmetry of the RE ion in the host lattice. The B_q^k are crystal field parameters containing all information about the geometrical arrangement of the ligands around the central ion. Therefore this terms depend on the crystal host, the site symmetry and the nature of the ions in the crystal. The B_q^k can be calculated using the crystallographic data and charges of the host lattice as shown in Table 2.2. The symmetry of the crystal field is that of one of the 32 crystallographic point groups, but the symmetry of interest is that of the electric field at the position of the RE ions. Therefore, it is not sufficient to know only the crystal class, but also a complete x-ray analysis to find the crystal field symmetry. On the other hand, it turns out that only a small number of terms in the infinite sum 2.49 are of significance to determine the crystal field energy levels. For even k values (k =0,2,4,6) the crystal field potential partially lift the degeneracy in J, yielding an energy level separation on the order of $10^2 cm^{-1}$, and the magnitude of this separation depends on the crystal field strength. While, the odd k values (k =1,3,5) play a key role in the induced dipole transitions which will be presented later. It is also important to note that an amorphous host for RE ions presents spectral lines with a large inhomogeneous broadening, typically of the order of $100\,cm^{-1}$. For this reason, instead of investigating the crystal field features in amorphous hosts like glasses, it is preferable to investigate the optical emission properties of RE-doped glasses with the determination of lifetimes and oscillator strength [160].

Finally, although the crystal field interaction is considered in the Hamiltonian, there are still sub-levels in an odd-numbered 4f electronic configuration. Such levels are two-fold degenerate and are referred to as Kramer's doublets or degeneracy. This degeneracy can only be removed by a magnetic field. However, this applied magnetic field produce a net electronic magnetic moment and has an

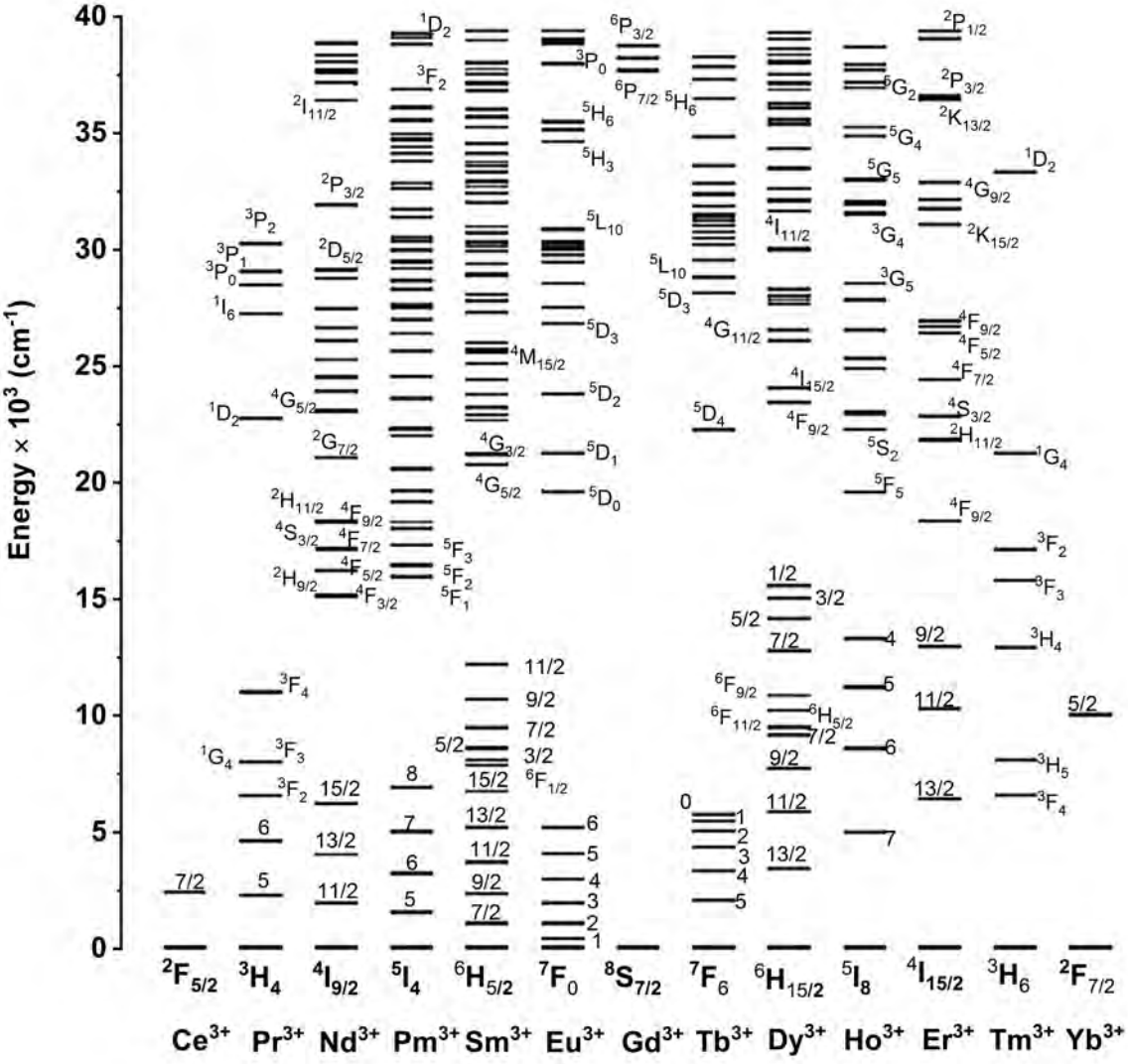

Figure 2.13: Calculated energy levels of trivalent RE ions in a free state. The energy range up to 40000 cm^{-1}, redrawn from [162] .

effect on the spin and radiation polarized photoemission spectra. From this effect, useful information about the magnetic properties of the materials can be obtained [163, 164].

In summary, the energy levels of the trivalent RE ions can be obtained from the analysis of the free ion spectra. The quantum mechanical calculation for the energy levels and wavefunctions starts with a simplified system, omitting the spin-orbit interaction and crystal field interaction, so that the procedure is easy to handle. If the omitted interactions are introduced, most of the degeneracy is removed and these modified states can be calculated using a conventional perturbation theory. In view of the above, the number of energy levels which can appear in the RE spectra are quite complex and numerous. The different energy level configurations for a series of trivalent RE ions in a free state is depicted in fig. 2.12. By considering the crystal symmetry and structure of the spectrum, the well-known *Dieke-Carnall* diagram shows the crystal field splitting of the 4f energy levels configurations for the entire series of trivalent RE ions. This diagram was obtained by Dieke [165] who experimentally measured the optical spectra of RE ions in the $LaCl_3$ host. Later, the results were further extended by Carnall and co-workers [166] for the spectra of trivalent RE ions in LaF_3. A detailed description of the calculations of the $4f^N$ energy levels can be found in references [165][167]. The theoretical calculations of the energy levels of the free ion states are of great importance for guiding the interpretation of the empirical results. Using the energy diagram, it is possible to explain the absorption and emission spectra and assign each spectral line with the corresponding electronic transition from the excited states to the ground state.

2.2.2 Radiative and non radiative transitions in RE ions

Light is comprised of two perpendicular fields, electric and magnetic, oscillating sinusoidally in space and time. When an atom, ion or molecule is bathed in light with wavelength much larger than its size, the spatial variation of the fields over it can be neglected, and assumed to be spatially uniform. In the absence of light, the atom or ion is itself the source of electric and magnetic fields for each electron circulating within it. When light impinges, the electrons in the atom may experience *pushed* strongly by the oscillating electric fields and in some extent by the magnetic fields. This increment in the kinetic and potential energy of the system impulses the electron into a higher energy level state, taking place the absorption process. After this event, the excited atomic system decays the excess of energy by radiative transition (*luminescence*) or by non radiative transition processes.

General considerations:

- A *resonant* interaction is said to occur when the frequency of the light is close to the natural frequency of the perturbed atomic or ionic system. This type of interaction presents the maximal energy transfer from the radiation field to the system (absorption), and a larger induced dipole moment is created through this process.

- *Non resonant* interactions presents typically small energy absorption, due to the unmatch between incident light frequency and the natural frequency of the system. The direction of re-radiation of this energy is not necessarily the same as the direction of the incident ray. The induced dipole moment created in non resonant interaction is smaller than the one in resonant absorption process. The ratio of

Operator	S	L	J	Parity
Electric Dipole	$\Delta S = 0$	$\Delta L = 0, \pm 1$	$\Delta J = 0, \pm 1$	odd/opposite
Magnetic Dipole	$\Delta S = 0$	$\Delta L = 0$	$\Delta L = 0, \pm 1$	even/same
Electric Quadrupole	$\Delta S = 0$	$\Delta L = 0, \pm 1, \pm 2$	$\Delta L = 0, \pm 1, \pm 2$	even/same

Table 2.3: Multipole operators and selection rules [33]

the induced moment to the applied electric field strength is the so called polarizability, which accounts for the degree of response of the electrons.

- Absorption is promoted by *operators* linked to the nature of light: the electric dipole (ED) operator, magnetic dipole (MD) operator and electric quadrupole (EQ) operator. These three mechanisms, shall be considered for the interpretation of the observed: ED transitions, MD transitions and EQ transitions.

There exist many different configurations for a RE element, and various spectral terms and energy levels for each possible configuration so that the 4f electrons can be placed in any 4f orbital except for La^{3+}(empty) and Lu^{3+}(full). For instance, Gadolinium has 3106 energy levels at the $4f^7 5d^1 6s^2$ configuration while its excited state $4f^7 5d^1 6s^1 6p^1$has 36000 energy levels [168]. However, the number of spectral lines observed are much less than the transitions between all existing energy levels. This occurs because many transitions are forbidden by selection rule constrains. According to the quantum mechanical theory, in the Rusell-Saunders coupling ($L-S$ coupling), only the transitions that satisfy the rules given in Table 2.3 are allowed. These rules are derived under several hypothesis and are not completely fulfilled, particularly by the 4f wavefunctions in the presence of a ligand field. Therefore, the term *forbidden* refers to a low probability and the term *allowed* refers to a high probability of occurring. The RE ions with an unfilled 4f shell have around 30 000 observable spectral lines. When compared with the transition metal ions, with an unfilled 5d shell and about 7000 observed spectral lines, the RE ions have more electronic energy levels and spectral lines which can absorb electromagnetic waves from the UV to the IR and emit their characteristic spectra.

In general, the RE ions have three types of possible electronic transitions: the sharp lines of the intraconfigurational 4f-4f transitions, the broader 4f-5d transitions and the broader charge-transfer transitions. The characteristic line-like behavior of RE spectra comes from the 4f-4f transition where 4f electrons exchange between different 4f energy levels. The broad absorption bands observed for example in the case of Ce ($4f^1$) and Yb ($4f^{13}$) ions, originates from configuration transitions $4f^N$ to $4f^{N-1}5d^1$. The 4f-4f transitions of RE ions are comprised mainly of MD transitions and ED transitions. In some cases and EQ or multipole transition are also observed.

Radiative transitions

The intensities of absorption and emission lines can be estimated by the matrix elements of the dipole operators responsible of the transition. As already seen in section 2.1.4, the Einstein coefficients for the transition probability between non-degenerate states (eq. 2.36 and eq. 2.37) are given by:

$$A_{m \to n} = \frac{64\pi^4 v^3}{3hc^3} |\langle m | P | n \rangle|^2 \tag{2.50}$$

Where v is the light frequency and P is the operator for the ED, MD or EQ moment to calculate the squared matrix element $|\langle n\,|P|\,m\rangle|^2$ for the transition. The absorption and luminescence spectroscopy of RE ions shows lines and bands ascribed to electronic transitions inside the 4f shell, between two crystal field levels and two $^{2S+1}L_J$ levels. These 4f shell electronic transitions are called intraconfigurational transitions and are not accompanied by a change in configuration.

ED transitions supposes a linear movement of charge, its operator is given by equation 2.51. When allowed in the visible or near the visible region, the probabilities are of the order of $10^8\,\mathrm{sec}^{-1}$. In this case the ED dipole, strongly predominates over the other dipole and quadrupole contributions. In other words, the majority of the observed optical transitions in RE ions are of ED nature. This transition has odd parity and odd transformation properties under inversion with respect to an inversion center. Therefore, when considering a free RE ion, the intraconfigurational ED transitions between the levels of the $4f^N$ are all forbidden due to Laporte's parity selection rule, because only states with opposite parity can be connected by the ED transitions. This restriction is no longer valid for trivalent RE ions embedded in a solid, because the noncentrosymmetric potential of the crystal field relaxes the parity selection rule by mixing the electronic states of opposite parity into the 4f wavefuncitons. This overcome to the parity selection rule is called an *induced electric dipole transition*. In fact, the noncentral symmetric part of the electric field is quite small, the 4f wavefunctions are predominantly of one parity, and the admixture of opposite parity states is very small. This affects the intensity of the observed transition lines, which are weaker than the ordinary ED transitions. The induced ED transitions are described by the Judd-Ofelt theory which is described in more detail in Appendix A.

$$\overrightarrow{P}_E = -e\sum_i \overrightarrow{r}_i \tag{2.51}$$

Non cero values for the square matrix elements of ED transition probability are obtained if the condition given by eq. 2.52, where the initial $\langle m|$ and final $|n\rangle$ states have opposite parities, is full filled.

$$\left\langle m\left|\overrightarrow{P}_{E,i}\right|n\right\rangle \rightarrow \left\langle 4f^{N-1}SLJM\,|\overrightarrow{r}_i|\,4f^{N-1}S'L'J'M'\right\rangle$$
$$= \sum_{k,q}\sum_{\lambda=even}(2\lambda+1)(-1)^{q+p}A_{kq}\begin{pmatrix}1 & \lambda & k\\ p & -(q+p) & q\end{pmatrix}\left\langle 4f^{N-1}SLJM\left|U^{(\lambda)}_{q+p}\right|4f^{N-1}S'L'J'M'\right\rangle\Theta(k,\,\lambda) \tag{2.52}$$

with

$$\Theta(k,\,\lambda) = 14\sum_{n',l'}(2l'+1)(-1)^{3+l'}\times\begin{Bmatrix}1 & \lambda & k\\ 3 & l' & 3\end{Bmatrix}\begin{pmatrix}3 & 1 & l'\\ 0 & 0 & 0\end{pmatrix}\begin{pmatrix}l' & k & 3\\ 0 & 0 & 0\end{pmatrix}$$
$$\times\frac{\left\langle 4f\,|\overrightarrow{r}|\,n'l'\right\rangle\left\langle 4f\,\left|\overrightarrow{r}^{(k)}\right|\,n'l'\right\rangle}{\Delta(n'l')}$$

Here the A_{kq} term in eq. 2.52 is related to the B^k_q are crystal field parameters as given by:

$$B_q^k = \sum_q \frac{|A_{kq}|^2}{(2k+1)^2} \tag{2.53}$$

The interaction between the magnetic field component of light with the RE ion, through a magnetic dipole gives rise a MD transition. The radiation of this nature can be considered as a rotational displacement of charge in a very small region. MD transitions possess even parity and even transformation properties under inversion, and allows transitions between states of equal parity. Therefore, the wavefunctions in the 4f configuration will not have any problem with intraconfigurational MD transitions, but their intensity is weak in 4f-4f spectra, about one order of magnitude smaller than induced ED transitions. Notwithstanding, very often MD transitions have intensity of the same order of magnitude as induced ED transitions. Eq. 2.50 shows the transition probabilities due to MD contribution for a P_M the magnetic moment given by:

$$\overrightarrow{P}_M = -\frac{eh}{4\pi mc}\sum_i (\overrightarrow{l}_i + 2\overrightarrow{s}_i) \tag{2.54}$$

Similarly to the ED transition calculation, the reduced matrix element for MD transitions are expressed by 2.55, and can be further reduced by splitting the L and S independent terms and g the Landé factor.

$$\left\langle 4f^N SLJM\,|(L+gS)|\,4f^N S'L'J'M' \right\rangle = (-1)^{J-M} \begin{pmatrix} J & J & S \\ J' & L & 1 \end{pmatrix} \left\langle 4f^N SLJ\,|(L+gS)|\,4f^N S'L'J' \right\rangle \tag{2.55}$$

Quadrupolar transitions arise from a displacement of charge of quadrupolar nature. It consists of four point charges with overall zero charge and zero dipole moment. The quadrupole moment tensor is given by eq. 2.56. They are also parity allowed, but they are much weaker than MD and induced ED transitions. Therefore these transitions are not the most intense ones in the optical spectra, and even more they are usually not observed. Minute changes in neighboring of trivalent RE ion has shown hypersensitive induced ED transitions, which are sometimes considered as pseudo-quadrupolar transitions, since they obey the selection rules of EQ transitions. For instance, the Tb related $^5D_4 \rightarrow ^7F_5$ transition shows sometimes ligand-induced pseudo-hypersensitivity. However, the experimental evidence that quadrupole transition plays any role in the crystal spectra is very scarce and thus will not be further discussed.

$$\overrightarrow{Q} = \frac{1}{2}\sum_i (\overrightarrow{k}\cdot\overrightarrow{r}_i)\cdot\overrightarrow{r}_i \tag{2.56}$$

The expression in eq. 2.57 represents the total oscillator strength of 4f-4f transitions including both the ED and MD contributions.

$$f^{abs} = \frac{8\pi^2 m_e v}{3h(2J+1)n}\left[\chi_{ED}^{abs} S^{ED} + n^2 S^{MD}\right] \tag{2.57}$$

Here m and e are the mass and charge of the electron, c is the speed of light and v is the mean transition frequency, n is the index of refraction and h is the Plank constant, all of them givn in SI units. The factor $\chi_{ED}^{abs} = \left[(n^2+2)/3\right]^2$ is the local field correction for an ED-induced absorption in the Lorentz model, given by $[E_{loc}/E]^2$. In the MD oscillator case, there is no need for a local field correction in non magnetic materials because $H_{loc}/H = 1$. These correction factors take into account the local field at the site of the ion undergoing optical transition and its difference from the macroscopic field in the medium. The ED and MD oscillators are defined in eq. 2.58 and eq. 2.59.

$$S_{J\to J'}^{ED} = \sum_{\lambda=2,4,6} \Omega_\lambda \left| \left\langle f^n SLJ \left| U^\lambda \right| f^n S' L' J' \right\rangle \right|^2 \tag{2.58}$$

$$S_{J\to J'}^{MD} = \left(\frac{h}{4\pi m_e c}\right)^2 \left| \left\langle f^n SLJ \left| L + gS \right| f^n SLJ' \right\rangle \right|^2 \tag{2.59}$$

where Ω_λ are the adjustable Judd-Ofelt parameters in units of (m^2) that can be calculated from a fit of eq. 2.58 to the absorption spectrum. The bracket expressions are dimensionless doubly reduced matrix elements, insensitive to the RE ion environment [169] (see Appendix A.1). The summation is over the even-rank doubly reduced matrix elements $\lambda = 2$, 4, 6 of the U^λ tensor operator in the intermediate Russel-Saunders coupling.

The prediction of the oscillator strength transition leads to the calculation of several important quantities such as the spontaneous radiative emission for a transition $|f^n SLJ\rangle \to \left| f^n S' L' J' \right\rangle$ denoted by:

$$A_{J\to J'} = \frac{64\pi^4 v^3 e^2}{(4\pi\varepsilon_0) 3h(2J+1)c^3} \left[\chi_{ED}^{emi} S_{J\to J'}^{ED} + n^3 S_{J\to J'}^{MD} \right] \tag{2.60}$$

Where $\chi_{ED}^{emi} = n^2 \chi_{ED}^{abs}$. For a given transition between an excited initial state to a final state, its radiative emission probability is reproduced by eq. 2.60 and its corresponding transition time is defined as $\tau_{J\to J'} = A_{J\to J'}^{-1}$. However, it usually occurs that an excited state decays to many lower energy final states, therefore the lifetime expression is given by:

$$\tau_{rad}^{-1} = \frac{1}{\sum_{J'} A_{J\to J'}} \tag{2.61}$$

Note that eq. 2.61 only represents the radiative contributions to the transitions $|f^n SLJ\rangle \to \left| f^n S' L' J' \right\rangle$. In fact, experimental lifetimes are smaller than the ones calculated with equation 2.61. This occurs because there are other non-radiative paths that contribute to the transition between energy levels, thus increases the total decay rate and gives an overall shorter lifetime than the one calculated considering only the radiative contribution. The non-radiative contribution comprises mechanisms such as multi-phonon relaxation and a variety of energy transfer processes like cross-relaxation, energy conversion and energy migration.

Non-radiative transitions

Non radiative transitions take place when RE ions in the excited states transfer their energy to the lattice system and relax to lower energy states but no energy is exchanged with electromagnetic field. Such transitions can lead to a decrease of the intensity and to a reduction of the lifetime of the luminescence of the RE ions. Dieke[165] and others attributed this lack of radiative decay to a fast non-radiative decay by phonon emission. Phonons are the quantum of lattice vibrations present in crystals. They are bosons and they commonly interact with the electrons present in crystals, affecting the transport properties of the crystals. Phonons are classified as acoustic and optical branches. Acoustic phonons are those traveling with the velocity of light and do not distort the atomic basis. Optical phonons arise from internal vibrations due to the opposite displacement of atoms in a basis. This results in local change in the dipole momentum that interacts with electromagnetic waves.

Lets assume an ion placed at a specific crystalline site, and its effective ligand is the natural atomic basis attached to each lattice point. If the spacing between two energy levels is smaller than ∼0.05 eV (or ∼400 cm^{-1}), then the transition may be in resonance with acoustic phonons. If the level spacing is approximately between 0.05 and 0.25 eV, then the transition may establish resonance with optical phonons. Both schemes allow emission and absorption of phonons, or in other words the excitation or quenching of lattice vibrations. However, near room temperature, phonon absorptions present smaller probabilities than phonon emissions.

In order to describe the transitions involving acoustic and optical phonons, the Debye approximation is assumed for low-energy phonons. It considers that all mode of vibrations in the crystal lattice have linear dispersion relation between the energy or phonon frequency and the wavevector. The so-called Debye frequency ω_D is the frequency of the maximum allowed value of the wave vector, which never exceed ∼10^{14}rad/s in crystals. In the acoustic case, a degeneracy between the longitudinal and transverse acoustic vibrations are also assumed. Based on the Debye approximation, the volume energy density as a function of the angular frequency ω, is given by:

$$\begin{aligned}\rho_{acoustic}(\omega) &= \frac{3\hbar\omega^3}{2\pi^2 \upsilon_s^3}\frac{1}{exp(\hbar\omega/k_BT)-1}, k(\omega) \leq k_D \\ \rho_{optical}(\omega) &= \frac{k^2(\omega)\cdot\hbar\omega}{2\pi^2\upsilon_g}\frac{1}{exp(\hbar\omega/k_BT)-1}, k(\omega) \leq k_D\end{aligned} \tag{2.62}$$

Here υ_s is the speed of sound, k_D is the wavevector, $k(\omega) = \left(\omega - \omega_{min}^{opt}\right)/\upsilon_g$, $\omega(k)$ is the inverse dispersion function and T is the absolute temperature.

Consider a transition between two adjacent electronic states of the RE ion and the valence electron moving in the ion. When the vicinity of the ion is deviated from its equilibrium position, a perturbing force is exerted on the revolving electron. The relevant ligand vibrations are supposed to be similar to vibrations of a regular atomic basis, with an atomic basis distortion whose normal coordinate $q(x,t)$ exerts a perturbing force on the moving valence electron. For the acoustic case, x represents the equilibrium position coordinate of a given atomic basis. Then, the perturbed force has a form

similar to the electric field q on the electronic charge ε or η represented by $\varepsilon(\vec{r}\cdot\vec{u})q^{'}(0,t)$. Whilst in the optical case, the perturbed force on the moving valence electron is given by $\eta(\vec{r}\cdot\vec{u})q(t)$. Where $\vec{r}$ is the average radius vector of the electron relative to the nucleus of the ion, and $\vec{u}$ is a unit vector in the force direction. The probability per unit time for the resulting stimulated transition $|f^nSLJ\rangle \rightarrow \left|f^nS^{'}L^{'}J^{'}\right\rangle$ averaged over all possible propagation directions of acoustic or optical waves in the volume density, is given by:

$$\begin{aligned} W_{J\rightarrow J^{'}}^{acoustic} &= \frac{2\pi V_C\varepsilon^2}{3\hbar^2\upsilon^2}\left|\left\langle f^nSLJ\left|\vec{r}\right|f^nS^{'}L^{'}J^{'}\right\rangle\right|^2\rho(\omega_0) \\ W_{J\rightarrow J^{'}}^{optical} &= \frac{8\pi V_C\eta^2}{3\hbar^2\omega_0^2}\left|\left\langle f^nSLJ\left|\vec{r}\right|f^nS^{'}L^{'}J^{'}\right\rangle\right|^2\rho(\omega_0) \end{aligned} \tag{2.63}$$

Where V_C is the primitive unit cell volume and $\omega_0 = \left(E_{J^{'}} - E_J\right)/\hbar$ is the angular transition frequency. From eq. 2.63 one can calculate the probability for non-radiative decay per unit time using a treatment close analogous to the Einstein coefficient approach for a two-state atom in an electromagnetic field. Then, the spontaneous non-radiative lifetime is expressed as:

$$\begin{aligned} \tau_{nr}^{acoustic}(\omega_0) &= \left(\frac{\varepsilon^2\omega_0 V_C}{\pi\hbar v_s^5}\left|\left\langle f^nSLJ\left|\vec{r}\right|f^nS^{'}L^{'}J^{'}\right\rangle\right|^2\right)^{-1} \\ \tau_{nr}^{otical}(\omega_0) &= \left(\frac{4\pi^2\eta^2\left(\omega_0-\omega_{min}^{opt}\right)^2}{3\hbar\omega_0\Delta_{opt}^3}\left|\left\langle f^nSLJ\left|\vec{r}\right|f^nS^{'}L^{'}J^{'}\right\rangle\right|^2\right)^{-1} \end{aligned} \tag{2.64}$$

The term in brackets is in fact the electronic transition dipole moment divided by the electronic charge $\left\langle f^nSLJ\left|\vec{r}\right|f^nS^{'}L^{'}J^{'}\right\rangle = \vec{\mu}/e$. The square of the electronic transition dipole is given by $\mu^2 = f\left(e^2\hbar/m_e\omega_0\right)$ with f as the oscillator strength parameter. Also, $\Delta_{opt} = \omega_{max}^{opt} - \omega_{min}^{opt}$. In reality, for all transition frequencies smaller than the Debye frequency, the non-radiative lifetime is in the order of $\sim 10^{-12}s^{-1}$; while radiative lifetimes are typically of the order of $\sim 10^{-5}s^{-1}$ or even longer $\sim 10^{-3}s^{-1}$.

As already seen in a complex level scheme, transitions can be radiative or non-radiative. The formers takes place between well-separated energy states with an energy difference higher than the highest angular frequency of optical vibrations ω_{co} or *cutoff lattice frequency* ($\Delta E > \hbar\omega_{co}$). The latter ones take place between the closely spaced levels. Radiative transitions can be measured for transition energies larger than $\hbar\omega_{co}$ (several tenths of an electron volt).

Mathematical modelling for the luminescence process

The configurational coordinate model is often used to explain the luminescent behavior of luminescence materials, and particularly the effect of lattice vibrations on the optical properties of a localized center. This model provides a basis of normal coordinates for the vibrational modes of the lattice, often called configurational coordinates. In this manner, the huge number of vibrational modes can be approximated by a small combination of specific normal coordinates. For simplicity, the model considers a luminescent ion or molecule and the ions at its nearest neighbor sites, while the effects of other distant ions are neglected. The total energy of the ion in its ground or excited state is represented on

the basis of potential curves as a function of the configurational coordinate Q, which represents the deviation from the equilibrium position of the ions. The curves are assumed parabolic and related to vibrational motion. The bonding force between the luminescent ion and a closest neighbor ion can be expressed with Hook´s law using an harmonic oscillator as expressed in equation 2.65. The total energy of the ground state U_g and the total energy of the excited state U_e are given by the following equations:

$$U_g = K_g \frac{Q^2}{2} \tag{2.65}$$

$$U_e = U_0 + K_e \frac{(Q - Q_0)^2}{2} \tag{2.66}$$

Here K_e and K_g are the force constants of the chemical bond, Q_0 is the interatomic distance from the equilibrium of the groud states, and U_0 is the total energy at $Q = Q_0$. Figure 2.14 represents the energies of the electronic states of the single ion active center along Q. It emphasizes dislocation of ions from the equilibrium and describes the transition and rearrangements of the luminescence ion. These rearrangements during the excitation induces small changes of $\Delta Q(= Q_0^{'} - Q)$, which depends considerably on the size and the charge of the vibrating lattice and the luminescence ion. After excitation of the luminescence center, $E_0 \rightarrow E_1$, the system will be out of thermal equilibrium and will relax from Q_0 towards $Q_0^{'}$. Optical absorption correspond to a transition from the ground to excited state under absorption of electromagnetic radiation. In the adiabatic approximation, such transition is represented by a vertical solid arrow because it must occurs very fast so that the surrounding lattice does not change during the transition, according to the Born-Oppenheimer approximation. At 0 Kelvin, the optical absorption proceeds from the equilibrium position of the ground state Q_0, and ends on the edge of the excited state parabola, where the vibrational states have their highest amplitude. Since the probability for an excited electron to lose energy by emitting phonons ($\sim 10^{12} s^{-1}$) is higher than the probability for light emission ($\sim 10^{5} s^{-1}$), an electron in the excited state will relax to the equilibrium position $Q_0^{'}$ before it emits a photon. When the luminescence ion and its surrounding are in the relaxed excited state, the emission transition takes place ($E_2 \rightarrow E_3$) in the same way as for the absorption transition and the system will again be out of thermal equilibrium. At the end, the system relaxes within the ground parabola to the lowest vibrational level Q_0.

In the high temperature regime, higher vibrational levels can be occupied thermally since the electron states oscillate around the equilibrium position along the configurational coordinate curve up to $k_B T$. This means that the luminescence process does not start form Q_0 but from a higher energy level Q_1. Although the procedure described above does not change, the amplitude of this oscillation leads to a broadening of the absorption and emission bands.

The emission transitions are usually situated at lower energy than the absorption transition. This phenomenon is known as the Stokes shift denoted by $\Delta E_{Stokes} = (E_1 - E_0) - (E_2 - E_3)$. It is a direct consequence of the relaxation processes between the optical transitions. Note that the larger $Q_0^{'} - Q_0$ is, the larger the Stokes shift will be. Assuming that the excited and ground state parabolas have

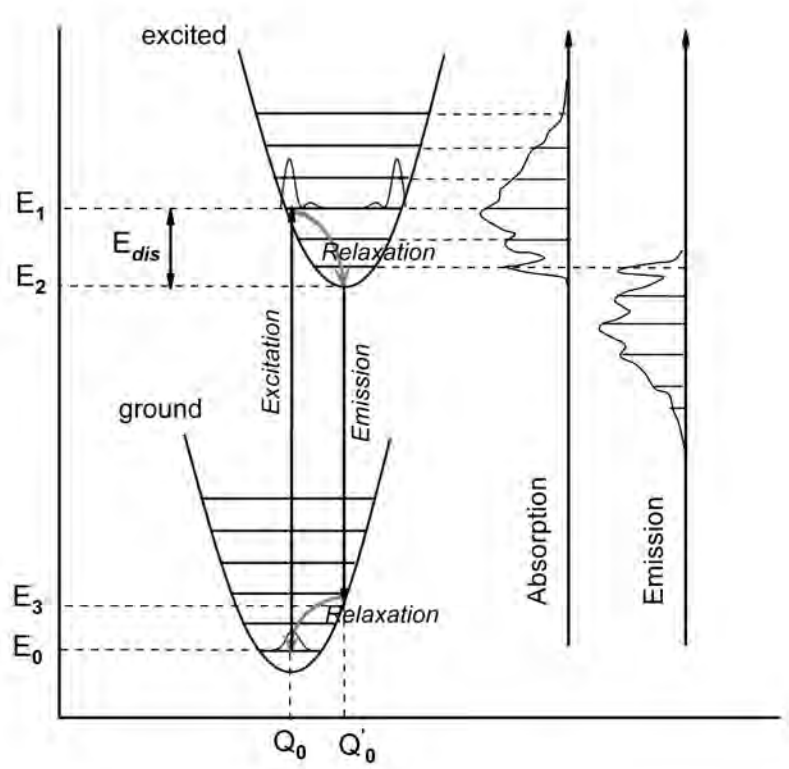

Figure 2.14: Configurational diagram of a system containing RE^{3+} ion in its ground state and in a system containing the RE^{3+} in its first excited state. The assumption of a harmonic approximation is only valid for very small amplitudes of vibration. As temperature increases, the restoring force becomes non-linear destroying the adiabatic separation between the electrons and the nucleus, thus allowing lattice vibrations to cause electronic transitions. In other words, the width of emission peak increases with increasing temperature due to thermal broadening.

the same shape and vibrational frequency, it is possible to define a parameter S called Huang-Rhys parameter given in eq. 2.67. In fact, the two main parameters which describe the electron-phonon coupling are the S parameter and the phonon energy $\hbar\omega$. The parameter S accounts the number of phonons of the energy $\hbar\omega$ excited in the absorption transition [170]. $E_{dis}$is defined in fig. 2.14. To calculate the values of S and $\hbar\omega$, two equations are required. First, the difference between the absorption line and its corresponding emission line given by eq. 2.68. Second, the expression of the emission band full width at half maximum at the absolute temperature T, according to eq. 2.69.

$$S = \frac{E_{dis}}{\hbar\omega} \tag{2.67}$$

$$\Delta E_{Stokes} = (2S - 1)\hbar\omega \tag{2.68}$$

$$\Gamma(T) = 2.35\hbar\omega\sqrt{Scoth\left(\frac{\hbar\omega}{2kT}\right)} \tag{2.69}$$

One can note from eq. 2.68 that the Huang-Rhys parameter is a measure of the Stokes shift, and therefore of the displacement between the ground and excited parabolas. Another important topic to deal with is the shape of the optical absorption and emission bands considering that the luminescence ion is coupled to the vibrating lattice. To accomplish this, lets consider a simplified two electronic energy states center of initial (ground) and final (excited) states described by harmonic oscillators, as the ones shown in fig. 2.14. The Schrödinger equation $H\psi = E\psi$ must consider a Hamiltonian $H = H_0 + H_{CF} + H_L$, where H_L is the Hamiltonian describing the ion-lattice coupling. In the framework of the Born-Oppenheimer approximation and the single configurational coordinate model, the solution to the Schrödinger equation is given by:

$$\psi = f\left(\vec{r}_i, Q\right) \cdot \chi\left(Q\right) \tag{2.70}$$

Where $f(\vec{r}_i, Q)$ are the electronic functions for the static case at the Q coordinates, and the $\chi\left(Q\right)$ are the vibrational wavefunctions with regard to the motion of the ions. For a system at 0 Kelvin, the absorption transition probability from the $n = 0$ state to any m state is given by $\psi\psi^*$ and considering that the ground and excited electronic functions vary very little compared to their values at Q_0, the probability of the transition is given by:

$$P_{if}(n = 0 \rightarrow m) \propto \sum_m \left|\langle f(Q_0)\left|H_{int}\right|i(Q_0)\rangle\right|^2 \times \left|\langle \chi_m(Q) \mid \chi_0(Q)\rangle\right|^2 = \left|\langle f(Q_0)\left|H_{int}\right|i(Q_0)\rangle\right|^2 \tag{2.71}$$

Here H_{int} is the interaction Hamiltonian between the light and the valence electrons of the luminescence ion, $i(Q_0)$ and $f(Q_0)$ and are the ground and excited states respectively. The term $\left|\langle f(Q_0)\left|H_{int}\right|i(Q_0)\rangle\right|^2$ is the squared matrix element as already seen in equation 2.50, and the term $\left|\langle \chi_m(Q) \mid \chi_0(Q)\rangle\right|^2$ gives the relative absorption probability due to the overlap between the $\chi(Q)$ vibrational functions. Since the $\chi(Q)$ form an orthonormal basis, then $\sum_m \left|\langle \chi_m(Q) \mid \chi_0(Q)\rangle\right| = 1$. It is possible to find the analogy between equation 2.71 and equation 2.50. Therefore, if the vibration

modes preserve inversion symmetry, the only effect of the vibrational lattice is to change the band shape, but the full absorption probability remains the same. As shown in Figure 2.14, without the participation of phonons, the zero-phonon emission line coincides with the zero-phonon absorption line. Notice also that the maximum in the emission peak takes place at lower energy than the maximum in absorption. This explains the Stokes shift and it is an important feature to avoid a strong overlap between the absorption and emission bands, which otherwise would cause the reabsorption of the emitted light by the luminescence center.

In order to predict the relative intensity of each $0 \rightarrow m$ absorption or emission band, the square of the overlap functions can be expressed as function of S:

$$|\langle \chi_m(Q) \mid \chi_0(Q) \rangle|^2 = exp(-S) \times \frac{S^m}{m!} \tag{2.72}$$

The factor $exp(-S)$ represents the fraction of the absorption intensity taken by the zero-phonon line, and the factor $S^m/m!$ relates this fraction to the $0 \rightarrow m$ transition. The modelling of the emission and optical absorption bands for parameters of the electron-phonon coupling is given by the expression:

$$I = I_0 \sum_m exp(-S) \frac{S^m}{m!} \delta \left(E_0 \pm m\hbar\omega - E \right) \tag{2.73}$$

Where I is the intensity of the band, E_0 is the zero-phonon energy, E is the photon energy, m is an integer related to the number of phonons involved in the transition. The minus and the plus signs relate to the emission and absorption transition, respectively.

At this point, it is possible to divide the ion-lattice coupling in three classes:

• Weak coupling case (for $S = 0$) , which consists of a zero-phonon line and the spectrum corresponds to a transition between pure electronic states and no appearance of vibrational side bands which can be appreciated for energies $m\hbar\omega$ above the zero-phonon line. As the S values increments, the band becomes broader and structureless.

• Intermediate coupling case (for $1 < S < 5$), so that the zero-phonon line is observable, but not the strongest line in the absorption or emission band.

• Strong coupling case (for $S > 5$), where the ion interacts strongly with the vibrating lattice that the zero-phonon line is so weak that it is not observable in the spectra. This case is also characterized by large Stoke shifts.

It is important to note that most broadband transitions of ions in solids are of ED nature, caused by dynamic lattice distortions of odd symmetry. When the dynamic symmetry, i.e. an odd-parity mode of vibration, destroys the inversion symmetry of the ion in the static lattice, the transitions taking place are called vibronic transitions. In fact, they are forced ED transitions. In this is the case, the intensity of these transitions depends on the strength of the coupling, and it is also influenced by temperatures changes.

2.2.3 Energy transfer processes

In the preceding sections, all the discussion has concerned isolated luminescence ions only. Now, lets consider the interaction between the RE ions and the transfer or sharing of energy between them. This energy transfer can take place between RE ions of the same or different elements, and it may be beneficial or detrimental for the luminescence. First, it is convenient to introduce some frequently used terms such as sensitizer and activator. The ion from which the energy is being transferred is the sensitizer (S) ion, while the ion to which the energy is transferred is the activator (A) ion. There exist many possible energy transfer processes as illustrated in Figure 2.15. The radiative energy transfer process consist of an excited S^* center which relaxes to its ground state by emitting a photon and another A ion gets excited by absorbing that photon. It does not contribute significantly in the radiative lifetime, since the emitted photon is then reabsorbed by another ion before it leaves the matrix. Only in the case of high dopant ion concentrations or large-volume samples, the radiative energy transfer can lead to a distortion of the emission spectrum and to apparent excited-state lifetimes that are artificially long. The non-radiative energy transfer usually dominates the radiative ones, and strongly affect the performance of RE doped materials. Among the non-radiative energy transfer pathways discussed here are the resonant, phonon assisted and cross relaxation.

In general, the probability of non-radiative energy transfer is given by products of the normalized lineshape function of the emission bands of the S and the absorption bands of the A (g_S and g_A, respectively) and their respective Einstein coefficients.

$$P_{SA}(E) = A_{mn,S} g_S(E) \times B_{nm,A} g_A(E) \rho_S(E) \tag{2.74}$$

where $\rho_S(E)$ is the photon at some distance of the activator from the sensitizer.

In the resonance energy transfer, the excited sensitizer transfers its energy to the acceptor, leading to its excited state with no emission and re-absorption of a photon involved. The best know energy transfer of this type is the Förster resonance energy transfer (FRET) which arises from a long-range dipole-dipole interactions between the S and the A. The resonance transfer occurs when the energy levels of the ground and excited states of both S and A systems are separated by nearly equal energies. With a suitable interaction between the systems, the excitation will jump from the S ion to the A ion before any of them is able to emit a photon. The mutual interactions are of Coulomb nature due to the Van der Waals forces between them. Förster assumed that the interaction is strongest if the transitions allowed are of electric-dipole nature. The strength of the interaction depends on the magnitude of a transition dipole interaction, given by the transition matrix elements of the S and the A, and the separation of the dipoles. The transfer probability is given by eq. 2.75, where H_{SA} is the interaction Hamiltonian and ρ_E is the density of states considering the phonon contribution to the line-broadening of the transition. Using a quantum mechanical approach and the classical treatment of the dipole-dipole interaction of a S-A pair [171, 172], Förster derived and expression for the rate of energy transfer from S to A, given by equation 2.76.

$$P_{SA} = \frac{2\pi}{\hbar} |\langle S^* A | H_{SA} | S A^* \rangle|^2 \rho_E \tag{2.75}$$

$$P_{SA}(r) = \frac{1}{\tau_S} \left(\frac{R_0}{r} \right)^6 \tag{2.76}$$

Where R_0 is the Förster radius, r is the distance between S and A, and τ_S is the S photoluminescence decay lifetime in the absence of A. Notice that the rate of energy transfer depends strongly on the ion-ion distance and it is inversely proportional to r^6. Also, when $r = R_0$, the rate of energy transfer is equal to the decay rate of the sensitizer. Typically, the values for the Förster radius ranges from 1 to 10 nm. The efficiency of the energy transfer depends on the distance between the S and the A , but also on the decay rate of the S ion. When the decay rate is much faster than the transfer rate, the energy transfer is inefficient, but for decay rates slower than the transfer rate, the result is an efficient energy transfer.

FRET theory describes the process within the dipole-dipole approximation. However, in the case of multipole Coulomb interactions, such as dipole-quadrupole and quadrupole-quadrupole interaction between the electrons of the S and those of the A, Förster and Dexter [173] developed a more general equation for the resonant energy transfer rate, as given by [174]:

$$P_{SA} = C \frac{Q_A}{R^n \tau_S} \int \frac{g_S(E) g_A(E)}{E^4} dE \tag{2.77}$$

Here, C is a constant and Q_A is the area under the absorption band of the A. The overlap of these two functions is accounted by the integral as a conservation of energy statement. The R^n factor represents the multipole interaction between the S and the A. In the case of a dipole-quadrupole interaction and of quadrupole-quadrupole interaction the FRET rates becomes proportional to higher orders of r^{-8} ($n = 8$) and r^{-10} ($n = 10$), respectively. Clearly, as the distance increases the energy transfer rate decreases for multipole interactions. The dominant term is the dipole-dipole interaction term, and the higher order poles become significant when the S and A ions are very close to each other. In contrast to the Förster mechanism which occurs for larger distances and considers the Coulomb interaction, the Dexter energy transfer considers the collision of electronic orbitals, where the excited S electron is exchanged with an electron from the A. This mechanism can occur in very small S-A distances ($r < 10$ Å) with an interpenetrating orbitals. Also, the Dexter energy transfer changes the spin of the S and the A, which decays exponentially with the distance r between them.

Phonon assisted energy transfer is a process in which the mismatch of energy between the S and the A is compensated by phonon emission and absorption. This type of energy transfer occurs when there is not a well-satisfied spectral overlap between the emission band of the S and the absorption bands of the A. For instance, if two RE ions have different excited states, as indicated in fig. 2.15(c), the energy transfer probability tends to zero because the overlay integral $\int g_S(E) g_A(E) dE$ vanishes. Experiments demostrate that energy transfer can take place without phonon-broadened electronic overlap on the condition that the overall energy is conserved by production or annihilation of phonons with energies approaching the Debye temperature of the host matrix [175]. For small energy mismatch around

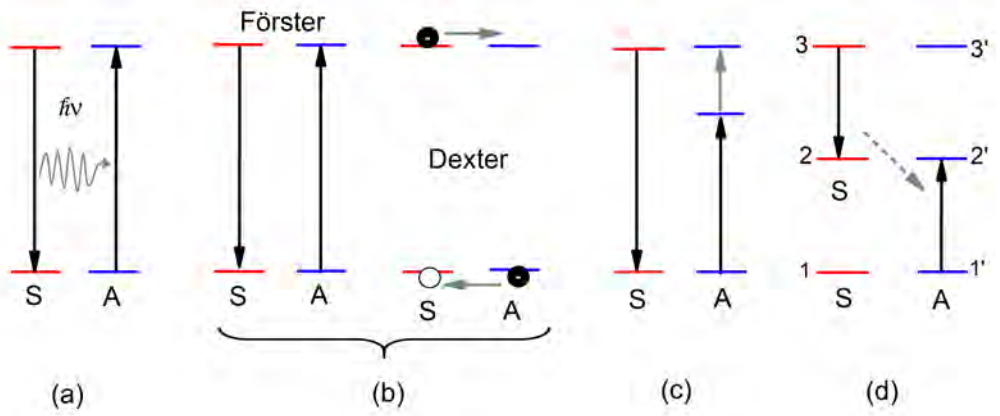

Figure 2.15: Diagrams illustrating the (a) radiative, and non radiative (b) resonant, (c) phonon-assisted and (d) cross relaxation energy transfer processes.

100 cm^{-1}, one or two phonons can assist the energy transfer. But, for energy mismatches as high as several 1000 cm^{-1}, the multiphonon assistance process have to be considered. Miyakawa and Dexter showed that the probability of energy transfer given by equation 2.75, is valid for the multiphonon processes when ρ_E is taken as the overlap the functions for emission of the S and the absorption of the A, including the phonon sidebands in the function. Based on the theory of Miyakawa and Dexter, the probability of phonon-assisted transfer is expressed as:

$$P_{SA}(\Delta E) = P_{SA}(0)exp(-\beta\Delta E) \tag{2.78}$$

Where ΔE represents the energy gap between the electronic levels of S and A ions, $P_{SA}(0)$ is the zero-phonon overlap between S and A for no energy mismatch between them, β is a parameter determined by the strength of the electron-phonon coupling. From equation 2.78 one can note that the energy transfer obeys an exponential energy lap law. Then, if the gap is larger, more than one phonon is required and the transition rate decreases exponentially. This is a common situation in RE ions. On the other hand, if P_{SA} is larger than the decay rate of the excited levels of S and A ions, the two levels become thermalized according to Boltzmann distribution. In the case of RE ions, it has been usually observed that the energy transfer rate may increase or decrease with temperature depending on the energy levels involved [176]. The evidence of the existence of the multiphonon assisted energy transfer for trivalent RE ions doped in yttrium oxide was reported by Yamada et al. [177], even in the case of very small electron-phonon coupling. The probability of phonon-assisted transfer was observed thus the predicted exponential dependence on energy gap could be confirmed. Their results show that phonons of ~400 cm^{-1}contributing to the phonon-assisted process produced the highest intensity in the vibronic side bands of the matrix.

The cross-relaxation is a special case of energy transfer where an ion loses the energy $(E_3 - E_2)$ by reaching the lower state E_2 and another ion gains the energy going to an upper state E_2. A resonance between the transition energies of the involved ions is required for this process to take place. The cross-relaxation transfer is a common process in RE ions due to their complicated energy level

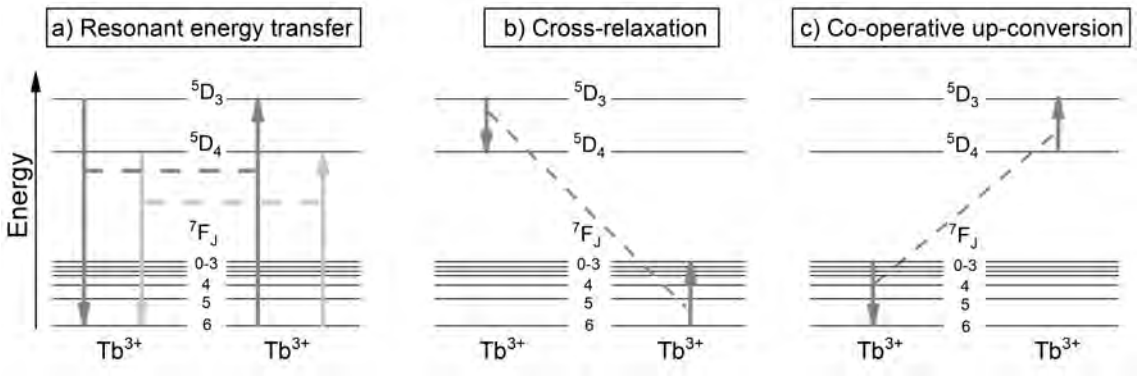

Figure 2.16: Energy transfer processes in Tb^{3+} . Among them, the cooperative upconversion process is very unlikely to take place for Tb^{3+} , instead the cross-relaxation by emitting phonons is more probable.

structure. This process has been observed in a variety of RE ions and it is a governing factor in non-radiative relaxations at high concentration. For the same RE ions, meaning that the S and A are identical ions, cross-relaxation is a columbic interaction phenomenon. In this case, it becomes a major challenge for luminescence quenching at higher concentrations. Also, cross-relaxation can occur between two different RE ions, which happens to have two pairs of electronic levels separated by the same amount of energy gaps or energy gaps matched by one or two phonons. In this case, the interactions of different RE ions cause the dopant quenching and sensitizing.

The energy transfer processes between two active ions could be of any of the mechanisms reviewed above. For instance, some possible processes for two Tb^{3+} ions are depicted in Figure 2.16. In this case, the energy difference between the $^5D_3$ and $^5D_4$ excited states matches more or less the energy difference between the ground state $^7F_6$ and the upper ^7F_j levels. Since the energy gap between the excited and ground states is adequate to avoid multiphonon emission, the resonant energy transfer is very likely to occur first. Another possible process to occur is cross-relaxation. It consists on the energy transitions $^5D_3 \rightarrow ^5D_4$ in one Tb ion, and $^7F_6 \rightarrow {}^7F_0$ in the other Tb ion, where the energy differences are approximately 0.72 eV. At large Tb^{3+}-Tb^{3+} distances, or low Tb^{3+} concentration, the cross-relaxation process has a low rate. When this is the case, emission from both the $^5D_3$ and $^5D_4$ excited states is observed unless the gap between both levels is bridged by emission of high-energy phonons. The resulting emission spectrum shows transition bands from the near UV into the red part of the visible spectrum. In contrast, at high Tb^{3+} concentration, cross-relaxation quenches the emission from the $^5D_3$ level to the advantage of $^5D_4 \rightarrow ^7F_j$ emission lines. Therefore, at higher Tb^{3+} concentrations, no blue light is observed in the emission spectrum. There is also another process known as cooperative up-conversion, which is opposite to the cross-relaxation, but it is pretty unlikely to occur in Tb^{3+} ions because the energy gap between the ^7F_j levels is in the order of 100 meV. For energy gaps of this size, from the$^7F_6$ to the $^7F_0$ states, the multiphonon relaxation is the dominant process.

A consequence of the various energy migration mechanisms is the so-called concentration quenching effect, which is directly related to the ion-ion interaction and the subsequent energy back transfer

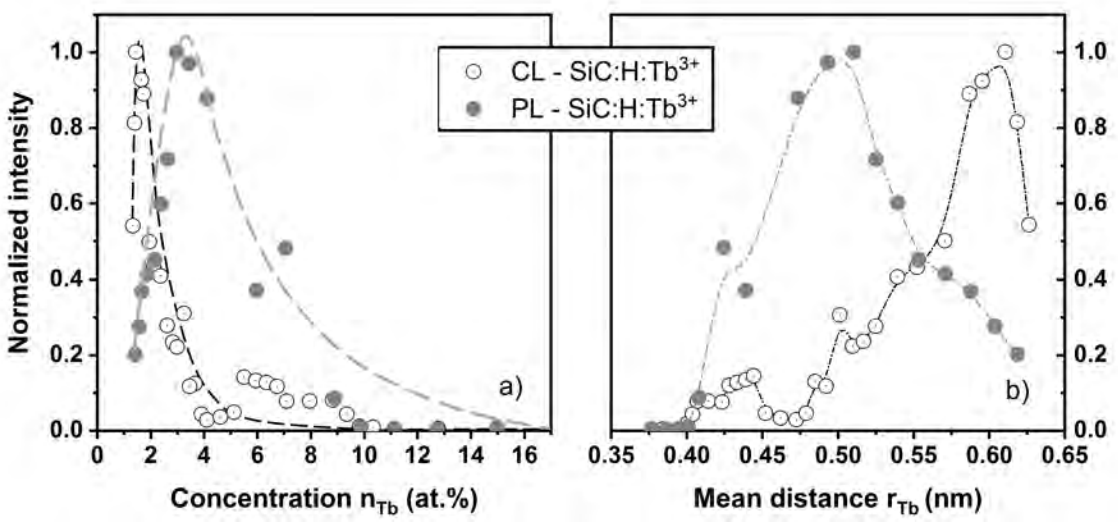

Figure 2.17: (a) Normalized integrated intensity CL and PL intensities of Tb doped SiC:H versus the Tb concentration. Dashed lines are fits using the equation 2.86 with $P_i = exp\,(n_{RE}/n_0)$ for simplicity. (b) Mean ion interdistance. The data was taken from reference [178].

to the host. The possible interactions depends on the distances between ions. As the RE concentration increases above a critical concentration, the distance between activators and sensitizers becomes smaller and the probability of energy transfer between them increases. When the probability of energy migration exceeds that for emission, then the excitation energy continuously goes from one ion to another and eventually to the host lattice. In the lattice, the excitation energy will eventually reach a *killer* site from where it can be lost non-radiatively. These killer sites may be impurities, defects, surface sites, dangling bonds, and so on. Due to this effect, up to a certain concentration the emitted light intensity increases no more and the light emission efficiency starts to decrease.

Figure 2.17 shows a manifestation of concentration quenching for the green emission of Tb^{3+} ($\sim$545 nm). In this figure, the emission intensity of Tb^{3+} ions in SiC:H thin films is shown as a function of the Tb content, and also as a function of the calculated Tb ions mean distance [178]. The maximum emission intensity is observed at the critical concentration, which occurs between 1.2 at.% and 3.0 at.% for the PL and CL excitation energy, respectively. The critical concentration divides the emission intensity in two regions. First, there is the low concentration region where the light emission intensity increases linearly with Tb content. Second, there is the high concentration regime, where the intensity drops exponentially. Another observable feature is the change of the exponential decay rate for different excitation sources (electron and photons).

It is possible to model the variation of the emission intensity as a function of concentration by phenomenological rate equations, which describe the time dynamics of population densities of RE ions excited in different energy levels.

To accomplish this, we must consider first that the total number of active ions remains constant and second, that the variation of the excited state population N_{exc} equals the variation of the ground state population N_{grd} , expressed as:

$$N = N_{exc} + N_{grd} \tag{2.79}$$

$$\frac{d}{dt}N_{exc} = -\frac{d}{dt}N_{grd} \tag{2.80}$$

Let k_{exc} be the excitation rate. Then, the ground state reduces its population by $-k_{exc}N_{grd}$. But at the same time the ground state increases its population due to the relaxation of ions in the excited state, which can occur by radiative and non radiative transitions. The radiative transition rate is equivalent to the Einstein coefficient and is represented by k_{rad}. The non-radiative transition rates, responsible for the light emission quenching, are given by $k_{non-rad}$ and $k_{ET-loss}$. The former accounts for the energy migration from the excited RE ion to a killer center, the latter accounts for the migration of energy about various RE ions before being trapped by a killer center. Therefore, the population of the ground state is give by:

$$\frac{d}{dt}N_{grd} = -k_{exc}N_{grd} + k_{rad}N_{exc} + \left(k_{non-rad} + k_{ET-loss}\right)N_{exc} \tag{2.81}$$

Using equation 2.80 and 2.81, one obtains:

$$\frac{d}{dt}N_{exc} = k_{exc}N - \left(k_{exc} + k_{rad} + k_{non-rad} + k_{ET-loss}\right)N_{exc} \tag{2.82}$$

Solving the last equation, one gets:

$$N_{exc} = \frac{k_{exc}N}{k_{exc} + k_{rad} + k_{non-rad} + k_{ET-loss}} + Cexp(-t\sum_i k_i) \tag{2.83}$$

Here, C is an integration constant and the sum on k_i represents the addition of all transition rates. The second term in equation 2.83 vanishes for a sufficient long time. Since the light emission intensity I is proportional to $k_{rad}N_{exc}$, the expression for I is proportional to equation 2.83 multiplied by k_{rad}.

$$I \propto \frac{k_{rad}k_{exc}N}{k_{exc} + k_{rad} + k_{non-rad} + k_{ET-loss}} \tag{2.84}$$

The rate $k_{ET-loss}$ depends on the distance between the RE ions, just as the energy transfer probability given by Förster (electric dipole interaction) and Dexter (electric multipole interaction).

To model the distance dependent luminescence intensity, the averaged interspace distance $\langle r \rangle$ can be considered in the probability function p_{ET}, so that the non-radiative rate due to energy transfer migration is expressed as:

$$k_{ET-loss} = k_{loss} \times p_{ET}\left(\langle r \rangle\right) \tag{2.85}$$

Since N is the total number of active centers, it can be linked to the RE concentration values. Therefore, one can rewrite equation 2.84 as a function the RE concentration η_{RE} and the mean RE interdistance r_{RE}.

$$I\left(\eta_{RE}\right) = \frac{A\eta_{RE}}{1 + B \times P_{ET}\left(r_{ET}\right)} \tag{2.86}$$

Equation 2.86 has the shape similar to a sigmoidal function multiplied by a line with the intercept in the origin. This equation describes the two regions of the light emission intensity versus RE concentration: the linear regime of increasing intensity at low RE concentration and the exponential quenching of light emission at higher concentrations.

Chapter 3

Experimental details of the preparation and thermal activation RE doped thin films

This chapter will outline the general methodology used to perform the research in this thesis. For specific experimental details and the experimental details regarding the characterization of the films, see the Methods sections of Chapters 4, 5, and 6.

3.1 Magnetron sputtering

The sputtering of solid materials in glow discharges has become one of the most functional and extensively used methods of thin film preparation. From the use of magnets to enhance the discharge flow in 1939 [179], to the invention of the planar magnetron in 1974 [180], and to more modern developments using high-power pulsed DC sputtering [181], the sputtering technique has grown to the point where it has become established as the process of choice for the deposition of a broad variety of industrially important coatings.

In general terms, the sputtering process takes place in a chamber with 10^{-2}- 10^{-3}mbar pressure, with a continuous flow of gases (argon and/or nitrogen). Inside the chamber, the target (cathode) is held at a negative potential relative to the charged ions from the ionized gas. The bombarding of ions from the plasma towards the surface of the target, with an accelerating voltage in the range 1 - 7 kV, eject the atoms of the target by momentum transfer. The released material settles on any surface in the chamber. The process is schematically shown in Figure 3.1(a). When the ions collide with the target material, different events can occur. Some of the bombarding ions are reflected back and neutralized, but the majority of the colliding ions produce the sputtered atoms which are subsequently thrown to the substrate surface to form the film. The plasma is ignited between the cathode and the anode due to a high voltage input from a direct current (DC) or alternate current (RF) source. An optimum gas density not only maintains the plasma but also gives the electrons the correct energy to ionize argon atoms. The emitted secondary electrons may join the oscillating plasma gas and cause an avalanche effect to sustain it, otherwise they can liberate their energy in the form of heat on colliding with the

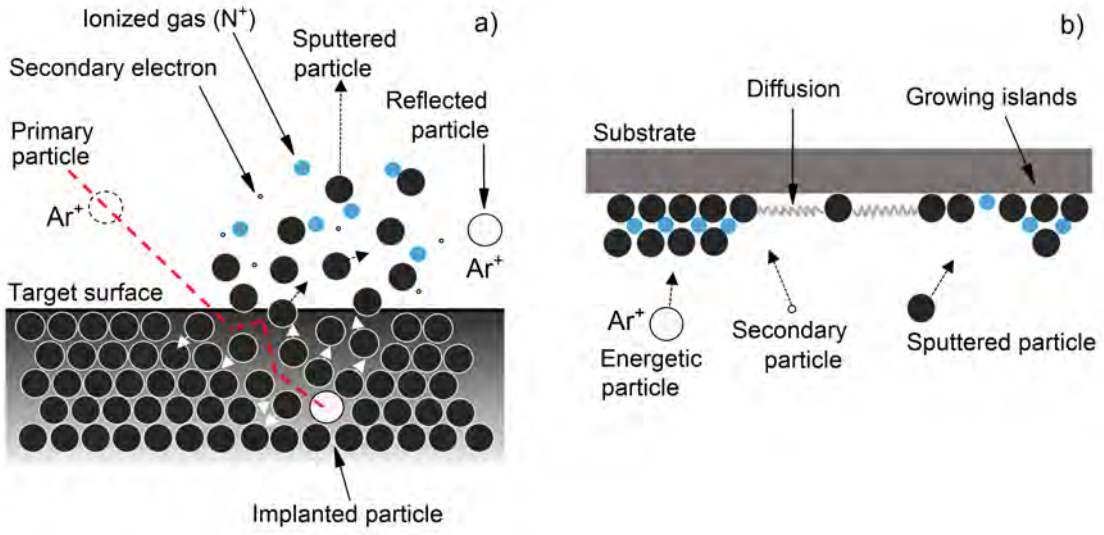

Figure 3.1: An illustrative diagram showing the sputtering process. (a) An accelerated Ar^+ ion impact the target and releases material by momentum transfer. In a reactive sputtering process, an ionized gas bonds to the sputtered atoms and form a different compound. (b) Film formation at the substrate.

substrate or other parts inside the chamber. In the RF sputtering, the positive charge built up on insulating targets can be avoided by the alternating potential, whereas in DC sputtering the charge build up strongly reduces the sputtering rate unless metallic conductive and semiconducting targets with small bandgap (e.g. Carbon, Si and others nonmetals) are used. The use of a magnetron allows the plasma technique utilizing magnetic fields to enhance and confine the plasma close to the target. The magnetic field forms a race track from where the bigger fraction of the material is sputtered. The drawback of this is that the target erodes at a much higher rate in these regions, while the majority part of the target is poorly used. Most importantly, the growth rate depends mainly on the pressure and power at which the films are deposited. However, increasing the power brings the problem of raising the temperature, and increasing the pressure has a limited effect because at higher pressures the sputtered atoms are slowed down by inelastic collisions that can decrease the rate.

The process of film formation is shown in Figure 3.1(b). The growing process of sputtered films initiates with the nucleation stage. It consists in the adsorption of sputtered atoms on the surface. If the adatoms have enough energy to overcome the diffusion barrier, they will move until they find a place energetically more favorable. The dynamics of nucleation are important since this stage influences the grain structure of the film [182]. The mobility of the adatoms depends strongly on the sputtering parameters of pressure, power, target-substrate distance, substrate temperature and substrate surface. The substrate temperature has direct correlation with the resultant microstructure and properties of the thin film [183, 184]. An advantage of using high temperature substrate for thin film deposition is that residual stress produced in the film is minimized. Additionally, the thin film quality can be improved due to the desorption of contaminants from the surface. Another factor to consider is the surface of the substrate. For instance, the presence of surface defects or texturing influences the mobility of the incident atoms which is reflected in the resulting properties of the film. If the atoms in the surface are energetic enough they can diffuse over the substrate to join other incident atoms to

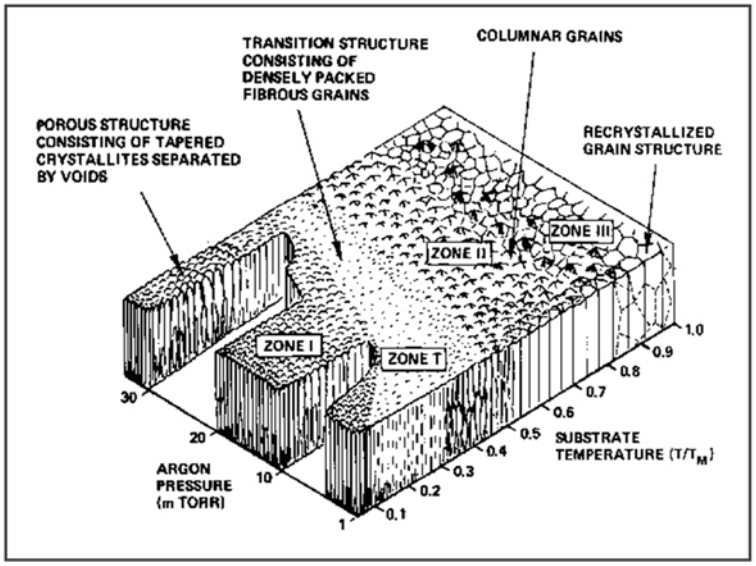

Figure 3.2: Schematic representation of the Thornton growth zone model of sputtered layers. (T) is the deposition temperature and (T_M) is the melting temperature of the sputtered material. Image from [185].

form islands which will continue to grow until they coalesce to become a continuous film that grows vertically. On the other hand, the neutral reflected atoms and gas particles can not be controlled easily by electric or magnetic fields. If they posses enough energy they can reach the substrate and react with the atoms from the target and get incorporated into the film. The working pressure can help to control these events by promoting a smaller mean free path of the atoms relative to the distance between the substrate and the target. Nonetheless, any impinging particle on the substrate, even the electrons, will liberate energy in the form of heat and increase the substrate temperature which also affects the mobility of the incident atoms and the growth of the film.

The mobility of the adatoms during growth influences on the morphology and microstructure of thin films. This mobility is provided by the following mechanisms such as the thermal effect, ionic bombarding and chemical reactions at the substrate. According to the structure zone model, the parameters describing these mechanisms are basically the substrate temperature, the final working pressure, the bias voltage applied to the substrate, and the thermal characteristics of the target. Movchan and Demchishin [186], established a normalized temperature parameter T_s/T_m (where T_s is the temperature of the substrate and T_m is the melting temperature of the target) to describe the microstructure of the thin films of Ti, Ni, $ZrO_2$and Al_2O_3. In this model, there are three well-defined zones. The first zone, T_s/T_m <0.3, exhibits a small and elongated grains forming a columnar structure, with porous morphology and weakly binding grains. Due to the low mobility of the adatoms and the various incidence angles at which the atoms arrive at the surface of the substrate. In the second zone, $0.3 \leq T_s/T_m \leq 0.45$, the substrate temperature increases and leads to the higher diffusion of the adatoms, which enables the formation of bigger grains extended in equiaxed form, from the substrate-film interface to the film substrate. In this zone, a dense structure with a strong binding of the columns and the borders between columns takes place. Finally, in the third zone, $T_s/T_m \leq$ 0.45, the thermal energy allows a great mobility of the adatoms which increases the volumetric dif-

fusion size, produces the growth of equiaxed grain and re-crystallization that gives rise to a greater crystalline structure. Further correlation of the sputter parameters to describe the growth of thin films are described in the Thornton model [187, 185] (see Figure), which considers not only the substrate temperature but also the sputter pressure. According to Thorton, the final working pressure influences both the kinetic energy of the ions that arrive at the substrate and the mean free path of the particles. This defines a transitional T zone between first and second zone with grains defined by the limits of the low porosity, and a denser and less rough surface than the others surfaces around them.

3.1.1 Single target sputtering

The equipment LA 440S Von Ardenne Anlagentechnik GMBH was used to deposit thin film layers of different materials. Figures 3.3(a) and (b) show images of the LA 440S sputtering equipment. This equipment can be used in sputtering deposition of thin films using various modes such as DC magnetron sputtering and RF magnetron sputtering. The property of sputtered thin film quality is enhanced to larger extent with the use of substrate heating. Figure 3.3(b) shows the schematic drawing of the circular magnetrons inside the chamber: PM1 and PM3 are the magnetrons of the DC mode, PM2 corresponds to the RF mode and ISE is reserved for inverse sputter etching. The four substrate are mounted on a rotatable carousel suspended above the magnetrons. The equipment possesses also a rotatable shutters to provide shielding for the substrate from the plasma, specially this allows the substrate to be sputter-cleaned prior to the deposition of the film. This provided the facility to sputter different layers on different substrates separately and therefore allowed the deposition on multi-layered films. This setup allows high deposition rates. In order to achieve high vacuum, the system counts with two types of vacuum pumps, a mechanical pump for low vacuum and a diffusion pump for high vacuum. A vacuum range of about 10^{-3} mbar is achieved through the use of mechanical pump. An improved vacuum around 10^{-6} mbar is obtained by using the diffusion pump. When no sputtering process is occurring, the vacuum chamber is maintained at 60°C to keep a water vapor free atmosphere at high vacuums. Further enhancement in vacuum around 10^{-7} mbar is obtained when the chamber is water cooled for 30 min.

In this study, part of the sample preparation experiments were performed using the LA 440S equipment in DC magnetron sputtering mode. The positions PM1 and PM3 were used to deposit the films using a DC power supply. Three sputtering target materials were used: aluminum (Al), molybdenum (Mo) and indium tin oxide (ITO) in order to grow AlN, Mo and ITO thin films, respectively. In the case of ITO, a special copper plate under the target was used to improve the electrical and thermal contact. The rare earth doping was achieved by placing Tb flakes on the surface of AlN target. The diameter of all targets is 90 mm with a thickness between 5 mm and 8 mm. The targets are parallel to the substrates with a distance around 50 mm. Silicon and sapphire squared substrates of 10 mm x 10 mm with thicknesses of 500 µm and 1 mm, respectively, were used. In order to promote the quality of the deposited films, the substrates were cleaned in acetone, then isopropyl alcohol and then distilled water for 3 minutes in each solution in a ultrasonic bath at room temperature. Then, they were dried by a stream of dry nitrogen (N_2) gas to remove any surface dust particles. The

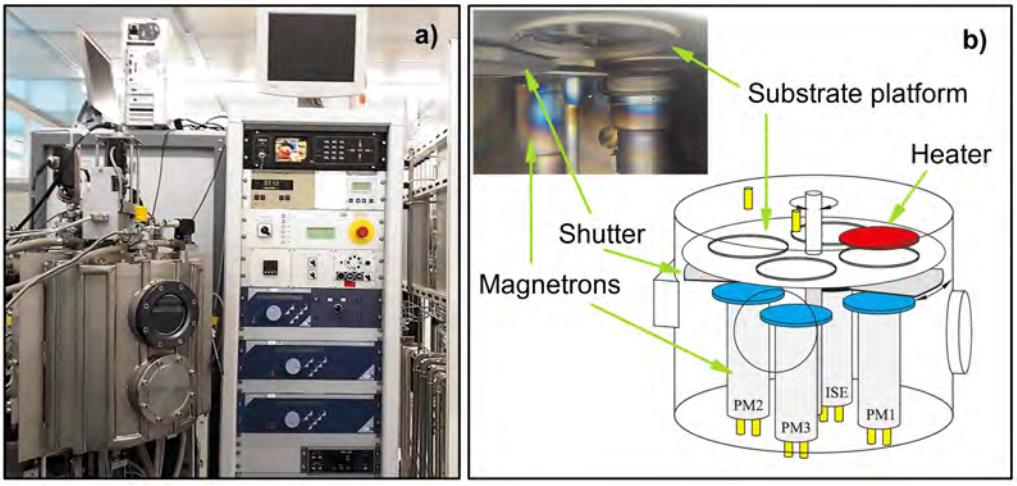

Figure 3.3: (a) The sputtering chamber system LA 440S installed at the Center for Micro- and Nanotechnologies at Technische Universität Ilmenau. (b) Scheme of configuration of the sputter chamber used for this work from reference [188].

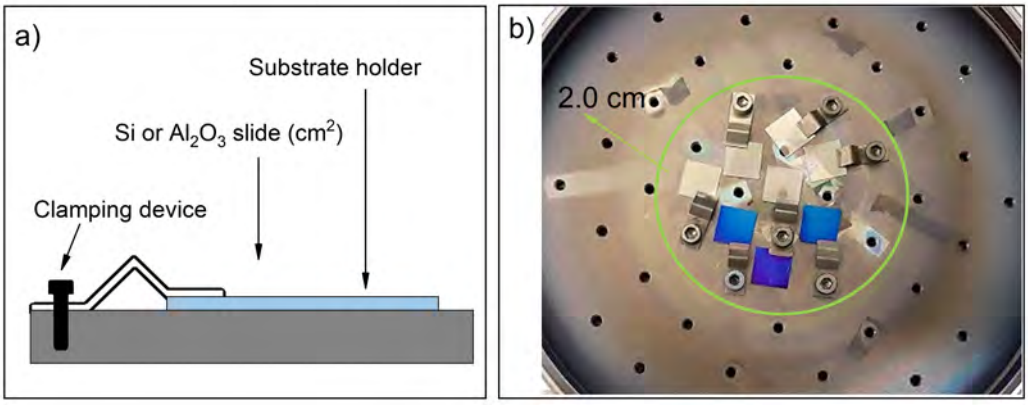

Figure 3.4: (a) Scheme of the substrates holders used during the sputter deposition of the films. (b) As deposited samples of Tb doped AlN after 9 min sputtering and no subtsrate heating. The uniform color of the films reveals thickness controllability within an area of 2.0 cm in radius from the center of the substrate holder.

substrates were then clamped to the substrate holder as shown in Figure 3.4. A sputtering power of 200 W was used in each deposition procedure. An inert working gas of high purity argon (99.99%) was introduced with a flux of 80 sccm, and served as the medium in which the plasma is initiated and sustained. For the deposition of Mo and ITO thin films only the Ar gas was introduced into the chamber. Whereas, for the deposition of AlN films, a flux of N_2 gas was introduced up to 20 sccm. Before each deposition, a pre-sputtering of 5 min was regularly performed to remove the contaminated surface of the target. During the pre-sputtering a shutter plate protected the substrate from the adherence of any pre-sputtered atoms. The deposition conditions for each material are listed in Table 3.1.

All in situ deposition annealing experiments were conducted over the position of PM1, as here, at the backside of the substrate holder a boron nitrite heater was installed. Temperatures of 300°C, 400°C, 500°C and 600°C have been applied to the substrate during deposition. Upon completion of the deposition, the substrates were shielded from the plasma using the shutter, and the power was

Sample	Target	Ar (sccm)	N_2 (sccm)	Substrate heating (°C)	Power (W)	Working pressure (mbar)	Time (min:s)	Sputter rate (nm/W•s)
AlN	Al	80	20	-	200	1.0×10^{-2}	4:36	0.0023
AlN:Tb	Al	80	20	-	200	1.1×10^{-2}	3:30, 6, 9	0.0023
AlN:Tb	Al	80	20	300	200	1.0×10^{-2}	6	0.0023
AlN:Tb	Al	80	20	400	200	1.0×10^{-2}	6	0.0023
AlN:Tb	Al	80	20	500	200	1.0×10^{-2}	6	0.0023
AlN:Tb	Al	80	20	600	200	1.0×10^{-2}	6	0.0023
Mo	Mo	80	-	-	200	8.4×10^{-3}	2:05	0.0040
ITO	ITO	80	-	-	200	8.7×10^{-3}	1:52	0.0106

Table 3.1: Deposition conditions of sputtered thin films using a single target DC magnetron sputtering system.

turned off. The continuous flow of argon and/or nitrogen was then turned off and the chamber was maintained in high vacuum for 10 minutes. Before venting the chamber to atmospheric pressure, it was warmed-up for 30 min. After that, the chamber is vented to atmospheric pressure using dry nitrogen gas which reduces the risk of contamination, and the substrates were removed.

3.1.2 Co-sputtering from different targets

Figure 3.5 shows a schematic of the RF combinatorial magnetron sputtering system in the Materials Science Laboratory at Physics Section of PUCP. This system was designed and fabricated in-house, and allows to create compositions spreads across a large substrate area (i.e.ϕ=10mm) by simultaneous sputtering of different materials which leads to a natural atomic mixing of elements. The system is equipped with 3 magnetron sputtering guns arranged in confocal geometry which locates the magnetrons at the corners of an equilateral triangle, equidistant to the substrate rotation axis and each having in situ tilt of 30°, as shown in Figure 3.5. This technique of arranging the magnetrons enhances film thickness uniformity (±5% error with a rotating substrate) and allows to co-sputter different materials to grow a complex film during a single process. Each gun uses a 50.8 mm diameter target and can be used simultaneously using radio frequency (RF) power supply whose power can range from 5 to 150 W. The substrate can be held static or it can be rotated. Since in this work we are interested in compositional gradients, samples are prepared using the static mode of the substrate holder. This enables the natural composition spreads to be fabricated without the use of a masking system. For deposition of binary composition spreads, only two magnetron guns were used, but for ternary spreads the three magnetron gun orientation shown above was used. Before each process, the vacuum chamber is bake out at 60°C in high vacuum for a long period of time so as to accelerate outgassing and desorption to reduce contamination and water vapor. The mechanical pump of the system creates lowers the pressure around 10^{-3} mbar, while the diffusion pump creates a base pressure lower than 2×10^{-6} mbar.

In this study, thin film libraries of undoped, Tb-doped, Yb-doped and Tb/Yb co-doped amorphous AlO_xN_y thin films have been prepared by RF combinatorial magnetron sputtering. The libraries were

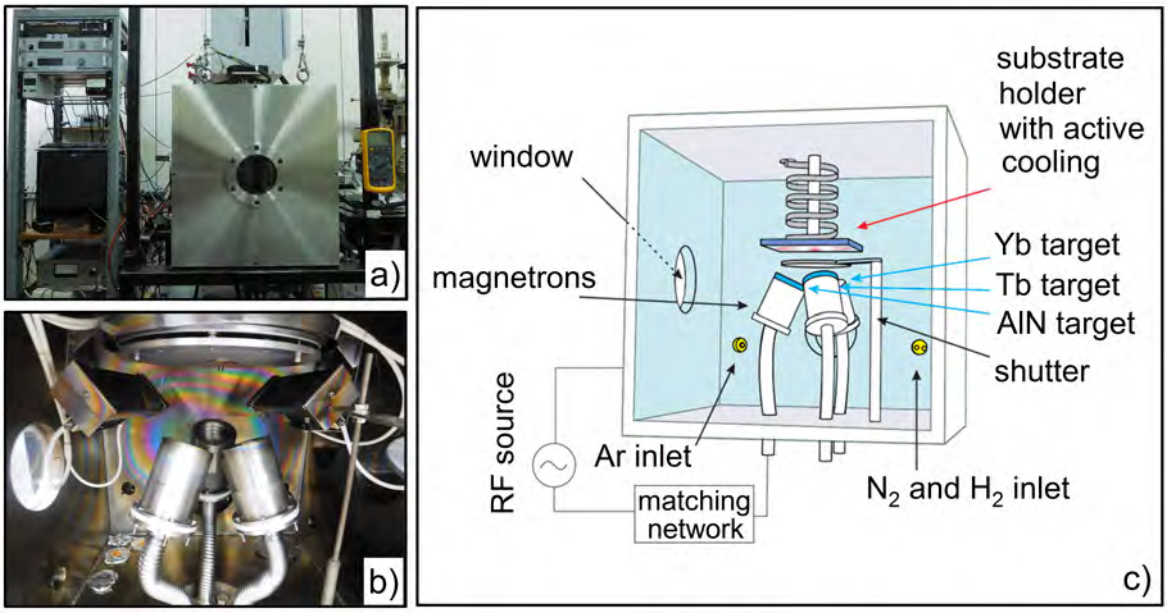

Figure 3.5: (a) RF combinatorial magnetron sputtering system at PUCP. (b) View inside the deposition chamber showing three magnetrons and the substrate holder. (c) Diagram of the setup of RF combinatorial magnetron sputtering deposition.

Sample	Power (W)			Ar	N	H	Base pressure	Working pressure	Time
	AlN	Tb	Yb	(sccm)	(sccm)	(sccm)	(mbar)	(mbar)	(min)
AlN:Tb:Yb	100	15	20	23	4	3	1.7×10^{-6}	1.5×10^{-2}	360
AlN:Tb	100	15	20	23	4	3	9.4×10^{-7}	1.5×10^{-2}	360
AlN:Tb	100	15	-	23	4	-	1.1×10^{-6}	1.5×10^{-2}	420
AlN:Yb	100	-	15	25	5	-	1.4×10^{-6}	1.5×10^{-2}	480
AlN	100	-	-	23	4	3	1.1×10^{-6}	1.5×10^{-2}	420

Table 3.2: Deposition parameters of thin film libraries prepared by RF magnetron sputtering.

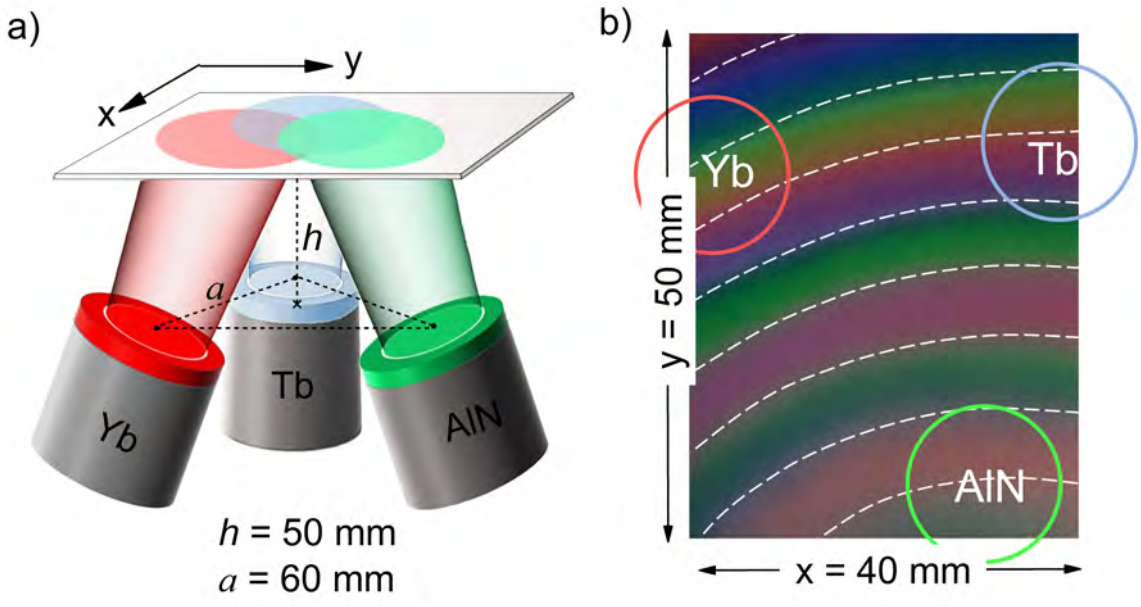

Figure 3.6: (a) Target-substrate geometry durign deposition and (b) as deposited library of Tb, Yb co-doped AlN:H with target positions.

deposited onto one single side polished Si <100>-oriented substrates of 60 mm×40 mm and 500 µm thickness, especially to measure optical properties. Additionally, some films were deposited onto double-side polished fused silica (SiO_2) substrates of 10 mm×10 mm and 500 µm thickness. All substrates were previously cleaned with acetone in the ultrasonic bath for 5 min. The target-substrate distance was fixed at 50 mm and the target-substrate geometry is shown in Figure 3.6 (a). Before deposition, the system is pumped down to a high vacuum of 2.9×10^{-6} mbar. However, the presence of oxygen was still detected inside the chamber at high vacuum by the mass spectrometer. This remaining oxygen content will be used to include it on film growth. The targets used were AlN (99.99% purity) which was grown by physical vapor transport in [189], Tb (Alfa Aesar, 99.95% purity) and Yb (Alfa Aesar, 90.90% purity). The working pressure was 1.5×10^{-2} mbar in all processes; and a mix of Ar, N_2 and H_2 atmospheres of 5N purity was used. The targets were pre-sputtered for 15 minutes at the same target powers used during deposition (see Table 3.2). The deposition conditions were chosen after the deposition rates of the targets had been matched, and deposition conditions for all samples can be found in table 3.2. The resulting thickness gradients over the substrate surface led to the formation of a materials library in the form of a thin film composition spread. The macro trend of thickness gradient is shown in Figure 3.6(b).

3.2 Annealing treatments

In-situ and post-deposition thermal annealing has been investigated as a required method to enhance the optical properties of Tb doped AlN semiconductors. This annealing process enables the migration or rearrangement of atoms and eliminates some defects which appear in the material during the growth. It also influences the energy migration processes that activates or quenches RE luminescence.

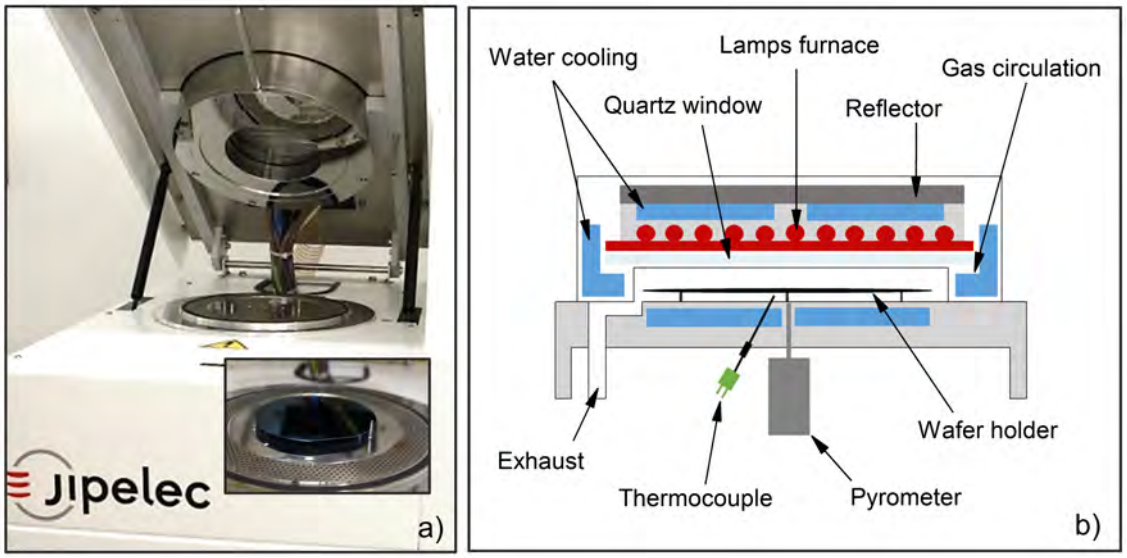

Figure 3.7: (a) Open lid of the Jipelec JetFirst RTA furnace. (b) Cross section of the RTA tool.

Typically, annealing of RE doped samples lead to a better emission intensity, a higher quenching temperature and a narrowing in the full width half maximum (FWHM) of the emission peaks. The magnitudee of these effects depends on annealing parameters such as time, temperature and atmosphere. More insight and discussion on how annealing affects the optical emission of RE doped AlN and AlON thin films will be proposed in the following chapters. In this study, the post-deposition annealing experiments have been performed using a rapid thermal annealer (RTA) system and a rather slower quartz tube furnace (QTF).

3.2.1 Rapid thermal annealer

The instrument used was a Jipelec JetFirst RTA furnace. The radiative power of halogen lamps assures the fast increment of temperature for a short time and then rapidly cool down the sample using cold heating chamber walls to stop the annealing. Figure 3.7 illustrates the open lid of the heating chamber and shows the main parts of the inner structure. During the entire treatment, in situ monitoring of the temperature induced in the sample is achieved by a three-term controller with two thermocouples and a pyrometer.

All the annealing experiments using the RTA system were carried out at different temperatures (300, 400, 500, 600, 700, 800 and 900°C). The annealing process is divided into three phases: the heating ramp, the isothermal step and the cooling ramp (see fig. 3.8). Before annealing the RTA chamber was pumped and purged with 1000 sccm N_2 flow several times in order to ensure adequate purity. Further conditioning uses a pre-heat step to heat the entire Si/SiN wafer holder up to 200°C prior to the heating ramp. This preheating stage suppresses the thermal stress that may appear on the wafer surface at high annealing temperature processes. During thermal treatments, a 1000 sccm gas flow of N_2 at ambient pressure was maintained to prevent samples from contamination. In all processess the operating temperature was reached using a heating rate of 5 K/s and the samples were maintained at the operating temperature for 5 min. After annealing, samples were cooled down to room temperature in the furnace with a cooling rate of 5 K/s.

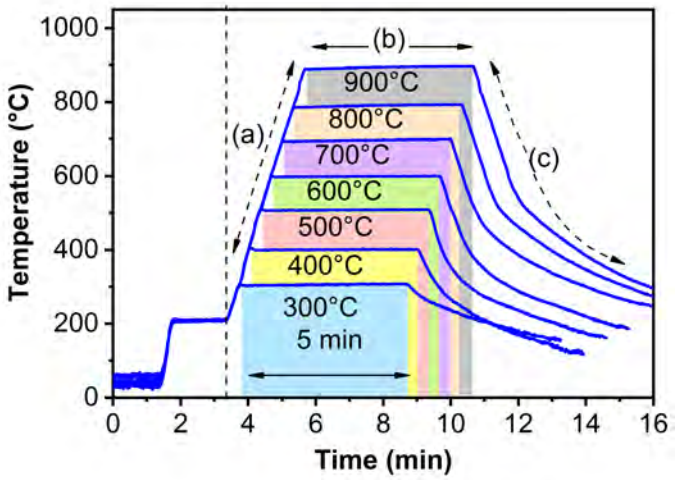

Figure 3.8: RTA thermal cycle at different annealing temperatures comprising (a) heating ramp, (b) isothermal step at the operating temperature for 5 min and (c) cooling ramp. The heating rate and the cooling ramps were kept constant.

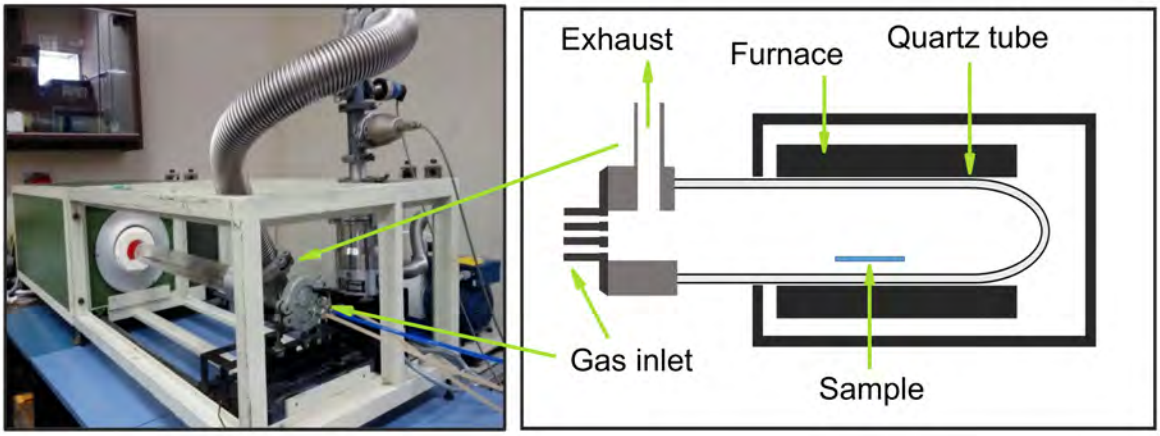

Figure 3.9: Illustration of the quartz tube furnace.

3.2.2 Quartz tube furnace

Isochronal annealing experiments have been performed on the RE (Tb, Yb and Tb:Yb) doped AlON thin film libraries at different temperatures (550, 650, 750 and 850 °C) using a quartz tube with one end necked to allow both the entrance of experimental samples and fittings for the atmosphere gases. The furnace, vacuum pump and gas delivery system is illustrated in fig. 3.9. After the samples were placed inside the quartz tube, an end cap made of stainless steel fits over the end of the tube, completely sealing the system. At each annealing step the tube was first evacuated down to 10^{-5} mbar and then filled with a constant flux of high purity (5N) nitrogen and/or argon up to a pressure of 4×10^{-2} mbar. Once the operating temperature was reached, the quartz tube with the samples was rapidly introduced inside the resistance heated furnace (shock tempering) and left there for an annealing time of 30 minutes. The same samples after analyzing all the properties at one temperature, the same sample was annealed to the next higher temperature step.

Chapter 4

Combinatorial co-deposition and characterization of luminescent Tb^{+3}-Yb^{+3} codoped AlO_xN_y:H thin film library

4.1 Introduction

The wide bandgap materials, and in particular AlN, are known to be a favorable host for the intense luminescence of RE ions at room temperature, due to an efficient excitation of the dopants [11]. However, AlN, like any semiconductor material can not be formed without defects in its structure. The functional properties and the electronic structure rely on the type of these defects. Regarding the impurity defects, the oxygen-related defects are the dominant intrinsic defects in AlN thin films and ceramics. Indeed, the deposition of high purity AlN requires the use of considerable energy to reach high vacuum conditions in specialized equipment. Otherwise, the presence of gas impurities, especially oxygen (O), induces the formation of Al-O bonds by substitution of nitrogen (N) atoms. Also, it was experimentally demonstrated that high temperature thermal treatment, typically above 600°C [25, 27, 26], is required for the activation of the optical centers to improve the light intensity of RE doped wide band gap semiconductors. These temperatures of annealing treatment affect the oxidation state and structure of AlN, easily forming second phases such as aluminum oxide (Al_2O_3) and aluminum oxynitride (AlO_xN_y) [190].

Although it is known that oxygen incorporation has an impact on the RE related light emission intensity, this influence is not solely detrimental for the RE emission intensity. Some investigations have reported that the presence of oxygen to a certain content can boost the emission intensity of rare earth ions [21, 191, 192, 193, 194]. Furthermore, the optical properties of (oxy)nitrides (i.e., transmittance, absorption edge, photoluminescence) are connected with the composition of materials, and more precisely the O/N ratio. Moreover, these properties become tunable with the O/N ratio in most cases, and enables the oxynitrides different applications such as antireflection coatings [195],

solar absorbers [195, 196] and spectral conversion phosphors [197, 198]. Indeed, AlO_xN_y has recently attracted researcher's attention due to its excellent thermomechanical properties and high transmission in the visible range [199, 200, 201], which make of it a promising material for RE doping with applications in white LEDs. Therefore, a better understanding of the optical response of oxygen rich phases such as AlO_xN_y is essential to manipulate the host properties and to tune the the luminescence properties of RE doped AlO_xN_y films.

Based on the above, this chapter is dedicated to investigate the optical behavior of amorphous Tb^{3+} doped AlO_xN_y:H, Yb^{3+} doped AlO_xN_y and Tb^{3+}/Yb^{3+}codoped AlO_xN_y:H thin films prepared by RF magnetron sputtering. The reason of combining Tb^{3+} and Yb^{3+} ions arises from the technological interest and potential applications in the fields of solar cells due to the energy conversion processes that may take place between them, which can provide better exploitation of the solar spectrum. In fact, in silicon solar cells, the mismatch between the incident solar spectrum and the spectral absorption frequencies results in an inefficient use of sun energy: not every photon has enough energy to produce an electron-hole pair in the solar cell. Photons with energies just above the bandgap are useful for the production of electron-hole pairs. The lower energy photons just pass through the cells as if it were transparent, while high energy photons produce an excess of energy that dissipates in the lattice as thermalization losses. In order to enhance the Si solar cell efficiency and reduce thermalization losses, a material co-activated with Tb^{3+} and Yb^{3+} ions could be used as a down-converter layer, see Figure 4.1. High energy photons can excite the $Tb^{3+}$to higher energy levels and then undergo fast intra-ion thermal relaxation to the $^5D_4$ level, from which emission transitions to the lower ^7F_J (J=6, 5, 3) levels can occur. If there are two or more Yb^{3+} ions in the vicinity of the Tb^{3+}, the latter can transfer its energy via cooperative energy transfer to excite two or more Yb^{3+} ions, since the $^5D_4$ energy level of Tb^{3+} has approximately twice the energy between the $^2F_{7/2}$ ground state and the $^2F_{5/2}$ excited state of Yb^{3+}. Finally, the excited Yb^{3+} ion emits its characteristic NIR emission around 980 nm-1100 nm, conveniently closer to the silicon bandgap energy.

The Tb^{3+} an Yb^{3+} ions are luminescent centers with appropriate energy difference between their related levels to promote quantum cutting (QC) processes such as down conversion (DC) and down shifting (DS). The interaction between Tb^{3+} and Yb^{3+} ions can promote DC events by which a high energy photon is converted into two or more energy photons. Theoretically, it is possible to achieve two NIR emission photons for every incident visible photon with quantum efficiency of up to 200%. In this way, DC is a more efficient process compared to the simple DS, which converts one high energy photon to another one with lower energy and therefore the conversion efficiency does not exceed 100 %. However, most transitions results in simple DS process.

There are two possible mechanisms in the NIR QC process: the first-order energy transfer and the second-order energy transfer. The first-order energy transfer is of resonance nature and requires that the emission spectrum of the donor (i.e. Tb^{3+}) should overlap with the excitation spectrum of the acceptor (i.e. Yb^{3+}). If this overlap is absent, second-order energy transfer may become the dominant relaxation process by which, one Tb^{3+} ion excites two Yb^{3+} ions simultaneously. The reso-

nance condition is satisfied when the energy of the absorption transitions from $^2F_{5/2}$ to $^2F_{7/2}$ levels of the two Yb^{3+} ions (1.26 eV or 980 nm) equals the energy of the emission transition from $^5D_4$ to $^6F_7$ energy levels of the Tb^{3+} ion (2.53 eV or 490 nm). NIR QC was achieved first in Tb^{3+} - Yb^{3+} doped YPO_4 [202]. An efficient energy transfer to Yb^{3+} upon excitation of the $^5D_4$ level of Tb^{3+} was found experimentally and combined with Monte Carlo simulations, it was demonstrated that the second-order CET was the dominant mechanism in the system. In subsequent publications, the mechanism responsible for the observed DC was assumed to be a cooperative energy transfer (CET) process from Tb^{3+} to Yb^{3+}, however, no solid evidence was presented. [203, 204, 205, 206]. There are many reports about second-order CET, but there are also reports that considers the first-order energy transfer more favorable, due to the presence of intermediate energy level of donor ion to resonantly excite the acceptor ion in a two-step process.

The energy transfer processes between Tb^{3+} and Yb^{3+} ions can face limitations of non-radiative decays, which usually occurs by multi-phonon deactivation. The host matrix plays an important role in the optical energy transfer because the phonon energy of the host is associated with the probability of non-radiative depopulations of the energy states. A low phonon energy is related to low probability of non-radiative transitions [207, 208, 209]. Along with low phonon energy, the choice of a suitable host must consider not only a large bandgap to avoid the absorption of the converted light, but also high RE solubility and high efficiency of light conversion, which depends on the RE ion concentration and enhanced energy transfer processes between host and dopant ions. Among the typical host materials used for up-/down-conversion applications of REs, the wide bandgap semiconductors (AlN, SiC, GaN) have shown the ability to meet the most of these requirements. They possess transparency for photonic applications, high thermal and electrical properties for optoelectronic devices, and intermediate phonon energy values. In fact, SiC, AlN and GaN show lower phonon energies than borates, phosphates and silicates but higher than fluorides and halides [210, 211, 212]. However, fluorides need charge compensation for the introduction of trivalent RE ions into the divalent lattice, which leads to the formation of solid solutions [213]. Whereas the RE solubility is enhanced in wide bandgap semiconductors by promoting the amorphous phase, which enables to incorporate higher concentration of dopants [214]. Moreover, the growth of amorphous or polycrystalline semiconductors is cheaper in comparison with the expensive cost of production of large halide single crystals.

During this work the optical and luminescence properties of RE (Tb^{3+}, Yb^{3+}, Tb^{3+}/Yb^{3+}) doped and undoped AlO_xN_y:H thin films have been systematically investigated at different oxygen concentrations, in particular O/N ratios. Other important factors that can affect the optical emission intensity are concentration and temperature of thermal activation of the RE dopants. In order to proof the influence of each factor on the optical and emission properties of the film and to face the problem of optimizing a material property by tuning its composition, a large number of samples have to be prepared and characterized such that all the factors are kept constant and changed only the one under investigation. Such dedicated study would require a lot of time and effort without the techniques of high throughput combinatorial thin film library growth and characterization [31, 32, 215]. This new tool has been developed over the past twenty years, mainly to speed up materials discovery in

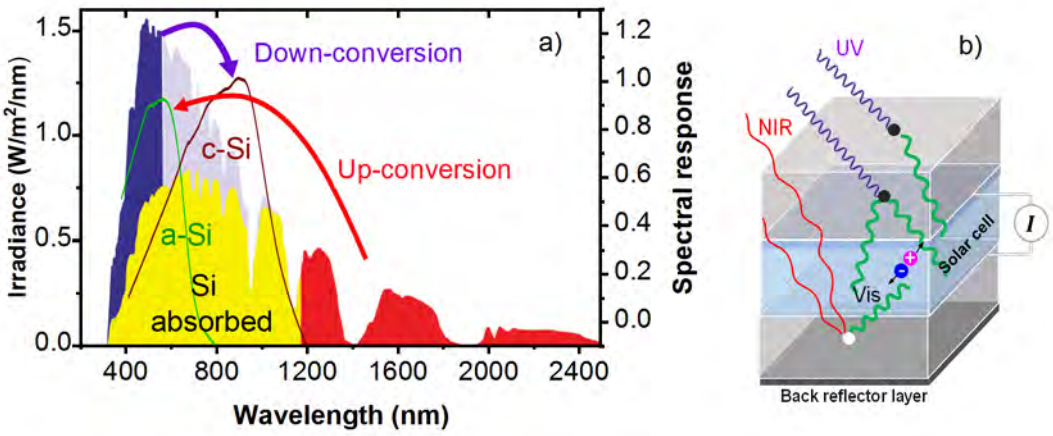

Figure 4.1: (a) AM 1.5 solar spectrum with available fractions for up and down-conversion processes. The fraction absorbed by a thick solar silicon device is shown in yellow. Relative spectral response of amorphous silicon and polycrystalline silicon is overlaid on the solar spectrum. (b) Representation of an arrangement of up-/down-conversion layers in a semiconductor based solar cell to boost solar cell efficiency.

comparison with the time consuming conventional one-at-a-time experiments [216]. The combinatorial approach is featured by the fabrication of a library of samples that contains variations of the material parameters of interest, commonly composition. After deposition of such a thin film combinatorial library, the properties of interest can be evaluated as a function of position within the library and hence as a function of composition of the deposited material, thus producing and collecting a large data set.

4.2 Experimental details

The samples in this work were prepared in a home-built co-sputtering deposition system, which allowed the deposition of thin film libraries with a continuous compositional gradient. In this way, a single deposition experiment results in the availability of a combinatorial sample, which comprises a binary or ternary compound deposited as a thin film onto a wafer substrate. The behavior of the Tb^{3+} and Yb^{3+} emission is investigated by PL and PLE experiments. The codeposition of Tb and Yb resulted in a rapid quenching of Tb^{3+} emission with annealing temperature in contrast to the increment of Yb^{3+} emission observed. The effect of oxygen concentration is investigated by mapping the composition with EDX and the crystalline structure analysis by mapping XRD. The results are complemented by an optical characterization of the RE doped and undoped AlO_xN_y:H matrix, achieved by transmittance measurements.

All the undoped and RE-doped AlO_xN_y:H samples were been grown using a combinatorial method in a RF magnetron co-sputtering system. Details of the materials synthesis are discussed in section 3.2.1. In order to enhance the RE-related light emission intensity, the Tb^{3+} and Yb^{3+} ions were

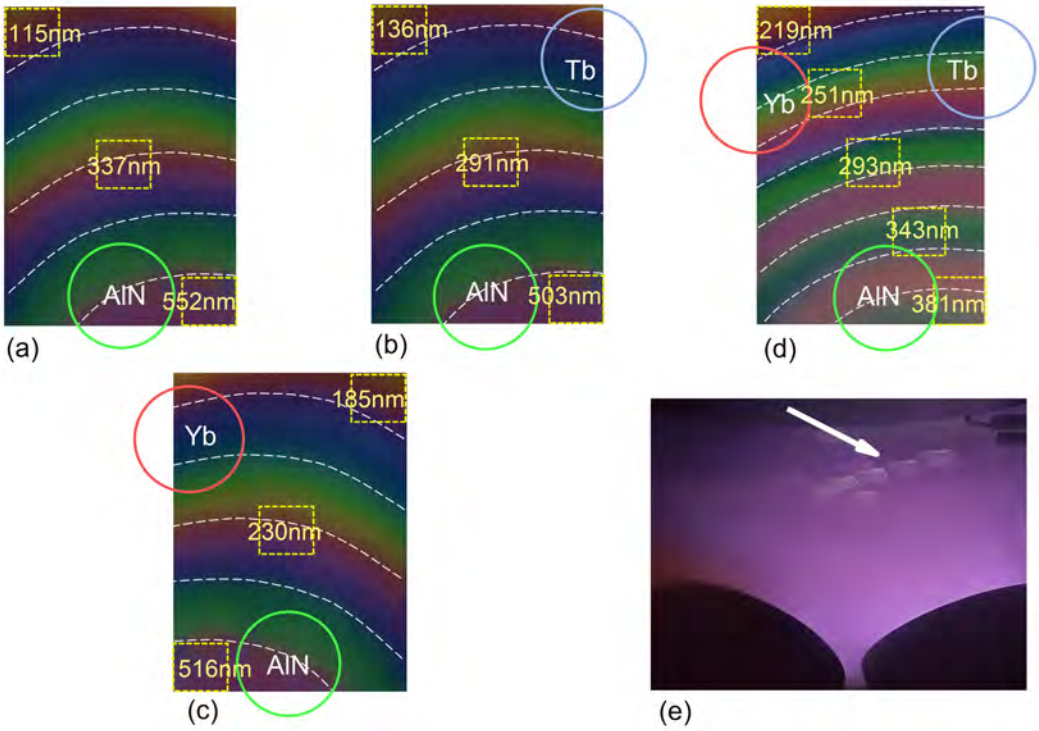

Figure 4.2: Photo of as deposited thin film libraries with target positions detailed in solid circles. The dotted lines are drawn to guide the eye through the gradient colors changing with thickness. The dotted squares denote the position of (a) undoped AlO_xN_y, (b) Tb-doped AlO_xN_y, (c) Yb-doped AlO_xN_y and (d) AlO_xN_y:Yb^{3+}:Tb^{3+} thin films deposited on transparent fused silica substrates and their respective thicknesses.

thermally activated by post-deposition annealing treatments using a quartz tube furnace at 550°C, 650°C, 750 °C and 850°C, as indicated in section 3.2.2. The prepared thin film libraries were grown onto silicon wafers of $4\times5\,cm^2$ and onto fused silica substrates, as shown in Figure 4.2. The target-substrate distance has been around 50 mm and the films thickness are in the range from 110 to 550 nm.

Optical characterization

The thicknesses of the undoped and RE-doped AlO_xN_y:H layers were determined following a modified envelope method made by means of transmittance measurements using a Perkin Elmer Lambda 950 spectrophotometer in the wavelength range from 190 to 1100 nm with a resolution of 1 nm at normal incidence angle. This method helps to establish the optical parameters and the thickness of layers with high accuracy and from a single transmittance measurements. More details on the fitting curves and the fitting parameters are provided in the Results and Discussion section. By modeling the refractive index with few fitting parameters only, it is possible to determine the absorption coefficient from the transmittance spectrum. The modified envelope method has the advantage to be more suitable for the calculation of the refractive index and the absorption coefficient from spectra that have few interference fringes. For more details concerning this methods please see references [217, 218].

Photoluminescence characterization

Photoluminescence measurements were taken in reflection geometry using a Renishaw inVia Reflex

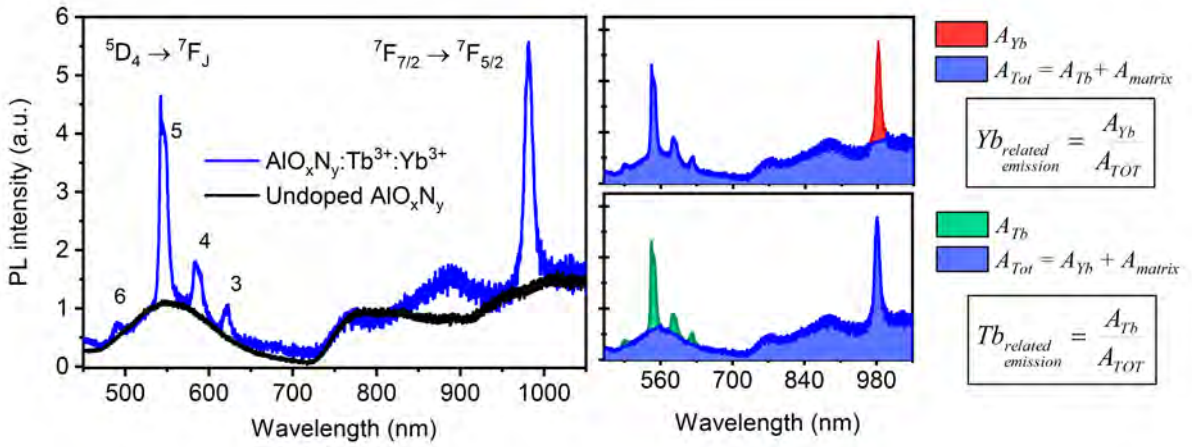

Figure 4.3: PL spectra of Tb/Yb codoped AlO_xN_y and undoped AlO_xN_y thin films in as deposited state.

spectrometer system for Raman and PL spectroscopy. By this technique, the electron in the transition band of each RE luminescent center moves from the ground state to the excited state under 325 nm wavelength excitation from a laser source of He-Cd. The laser power density at the sample was less than 16.6 mW/mm^2. After a characteristic time, the excited electrons decay to the ground state by emitting a characteristic luminescent spectra (radiative process) and or by heat dissipation (non-radiative process). The emission spectra of Tb^{3+} doped, Yb^{3+} doped and Tb^{3+}/Yb^{3+} codoped samples were recorded from 450 to 1050 nm.

In order to calculate the emission yield of one RE ion (Tb or Yb), its contribution to the total light emission have to be separated from the AlO_xN_y:H matrix and the other RE ion embedded in the thin film. This means, to normalize the integrated RE^{3+}- related light emission intensity with respect to the total integrated light emission (see Fig. 4.3). In this way, additional thickness normalization is avoided since the excitation volume at photoluminescence is already considered in the total sum of emission intensities. Additionally, room temperature PLE spectra were measured with a fluorescence lifetime spectrometer FluoTime 300 (PicoQuant GmbH), using a Xe-lamp as the light source with a spectral resolution of 8 nm. The photons were detected using a PMA 192 photomultiplier detector in a single-photon-counting mode.

Structural characterization

The chemical composition of layers was determined using Energy-Dispersive X-ray Spectroscopy (EDS), which uses the X-ray energies caused by electrons jump between energy shells as a result of the primary electron beam interaction. The EDS analysis was carried out inside a scanning electron microscope FEI Quanta 650 at the accelerating voltage of 4.5 kV and a working distance of about 10 mm. A relative small electron beam voltage was used to limit the electron penetration into the sample to avoid strong silicon substrate contribution during measurements. In order to average the results obtained for the surface chemical composition as well as establish possible material heterogeneity, an area of $320 \times 125\,\mu m^2$ was examined. Because the excitation energy must always be slightly higher than the energy of a given X-ray emission line of the elemental composition, reliable measurements

require a voltage excitation value so that the beam energy is at least 1.5 times greater than the value of the emission line energy. From the measurements, it was observed also a weak signal coming from silicon and, sometimes, from carbon. The carbon and the silicon signals were not taken into account in the quantification analysis.

It is important to remark that the elemental concentration quantification by EDX face some limitations, especially for light elements such as oxygen and nitrogen. Nonetheless, in this work the EDX quantification was done taking into account three important considerations. First, an optimum accelerating voltage (4.5 kV) was used in order to obtain a strong oxygen and nitrogen peak. This reduced considerably the self-absorption of low energy X-rays and enhances the relative intensities of the elements. Secondly, there is no overlap between the peaks of nitrogen and oxygen in the EDX spectrum. Last but no least, when running the quantitative analysis, we make sure the software used the correct value for the incident energy beam. The voltage control was of 4.5 kV and the actual accelerating voltage was of 4.504 kV. Due to the rough estimate of the composition, the values of elemental concentrations are reported with no digits after the comma.

X-ray diffraction (XRD) was employed to verify the amorphous state of the thin film libraries and to determine any change in the film microstructure with temperature. The XRD patterns were measured using a Bruker D8 Discover system at U=40 kV and I=40 mA with a Cu-kα radiation (lambda = 0.15406 nm). The grazing incidence set up was used to limit the incidence of the X-ray beam to the surface of the film, and therefore enhance the sensitivity to obtain a better signal from the film while minimizing the interference effect of the silicon substrate. An automated X-Y table was used for high throughput measurements. There was no observable diffraction peaks in the XRD patterns for both the as deposited samples and after each annealing treatment step. Further discussion on the results are shown in the following section.

4.3 Results and discussion

a) Optical properties

The first part of the experimental results presented here deals with the optical characterization of the prepared materials by means of optical transmittance spectroscopy, which let us measure the optical parameters such as the index of refraction and the absorption coefficient. The knowledge of the wavelength dependent absorption coefficient in the fundamental region is very important, especially for amorphous semiconductors, for the determination of the optical bandgap. However, this region can only be observed in sufficiently thin samples [217]. The method applied to calculate the aforementioned optical parameters is a modified envelope method, based on the work of Swanepoel [219], which takes advantage from the interference fringes of thin film transmission spectra to extract the optical parameters and thickness of the film. Another technique used for the determination of the optical constants from single optical transmittance spectra is PUMA [220]. More details concerning the modified method and a confidence analysis of its accuracy with respect to PUMA and Swanepoel

can be found in references [217, 178].

For a short description, it is worth to mention that this method models the refractive index by a Cauchy series $n(\lambda) = A_0 + A_1/\lambda^2$ and retrieves the absorption coefficient behavior by a fit of the transmittance spectrum using equation 4.1 for the transmittance curve.

$$T(\lambda) = \frac{Ax}{B - Ccos(\phi)\, x + Dx^2} \tag{4.1}$$

The expressions for the coefficients *A, B, C, D* are functions of the wavelength dependent refractive index of the film $n(\lambda)$ and substrate s. The phase shift ϕ depends on the film thickness and the wavelength λ [221, 219]. The free transmittance curve T_α, defined as the geometric mean $T_\alpha = \sqrt{T_m T_M}$ of the upper T_M and lower T_m envelopes, is a useful result because the absorbance x_α can be expressed as a function of the T_α, according to equation 4.2. This approach of describing the absorbance with the T_α curve depends less on the number of fringes and the right position of the extremes, compared to the upper and lower envelopes.

$$x_\alpha = \frac{\sqrt{E_\alpha - \sqrt{E_\alpha^2 - (n^2-1)^6 - (n^2 - s^4)^2}}}{(n-1)^3 (n - s^2)} \tag{4.2}$$

$$E_\alpha = \frac{128 n^4 s^2}{T_\alpha^2} + n^2 \left(n^2-1\right)^2 \left(s^2-1\right)^2 + \left(n^2-1\right)^2 \left(n^2 - s^2\right)^2$$

By replacing the absorbance expression in equation 4.1, one obtains an expression for the transmittance curve $T_{fit} = T_{fit}(\lambda, A_0, A_1, d)$ as a function of the wavelength λ. This expression can be fitted to the measured spectrum by adjusting the fitting parameters A_0, A_1 and d. Once the refractive index and the thickness are calculated, the absorption coefficient can be found by solving $\alpha = -log(x_\alpha)/d$. It is important to remark that there is actually no proper model for an accurate determination of the optical bandgap of amorphous semiconductors from their fundamental absorption spectrum. Nonetheless, the relative behavior of the bandgap can be unraveled by applying the existing models. In this work, the band fluctuation (B.F) model, the Tauc model (E_{Tauc}) and the Urbach energy (E_U) are used as representative values of the bandgaps and of the tail states of our amorphous samples, respectively [222, 223, 224, 82].

Figures 4.4 (a)-(d) depict the UV/VIS/NIR transmittance spectra of as deposited films and its corresponding absorption coefficients (e)-(h) in a Tauc plot. The position of each thin film sample during sputtering is depicted in Figure 4.2 and here represented by their respective calculated thickness. From transmittance spectra, it seems that the doped and undoped AlO_xN_y:H films show relative high transmittance in the visible and near IR region. All transmittance spectra showed a quite sharp absorption edge near 200 nm, which is attributed to the fundamental absorption of AlO_xN_y:H. A blue shift of the absorption edge is observed for thinner layers. Also the absorption edge becomes severe in the case of undoped films. On the other hand, the red shift of the optical absorption edge is more obvious for the RE doped samples. This shift may be explained on the basis of band tailing due to

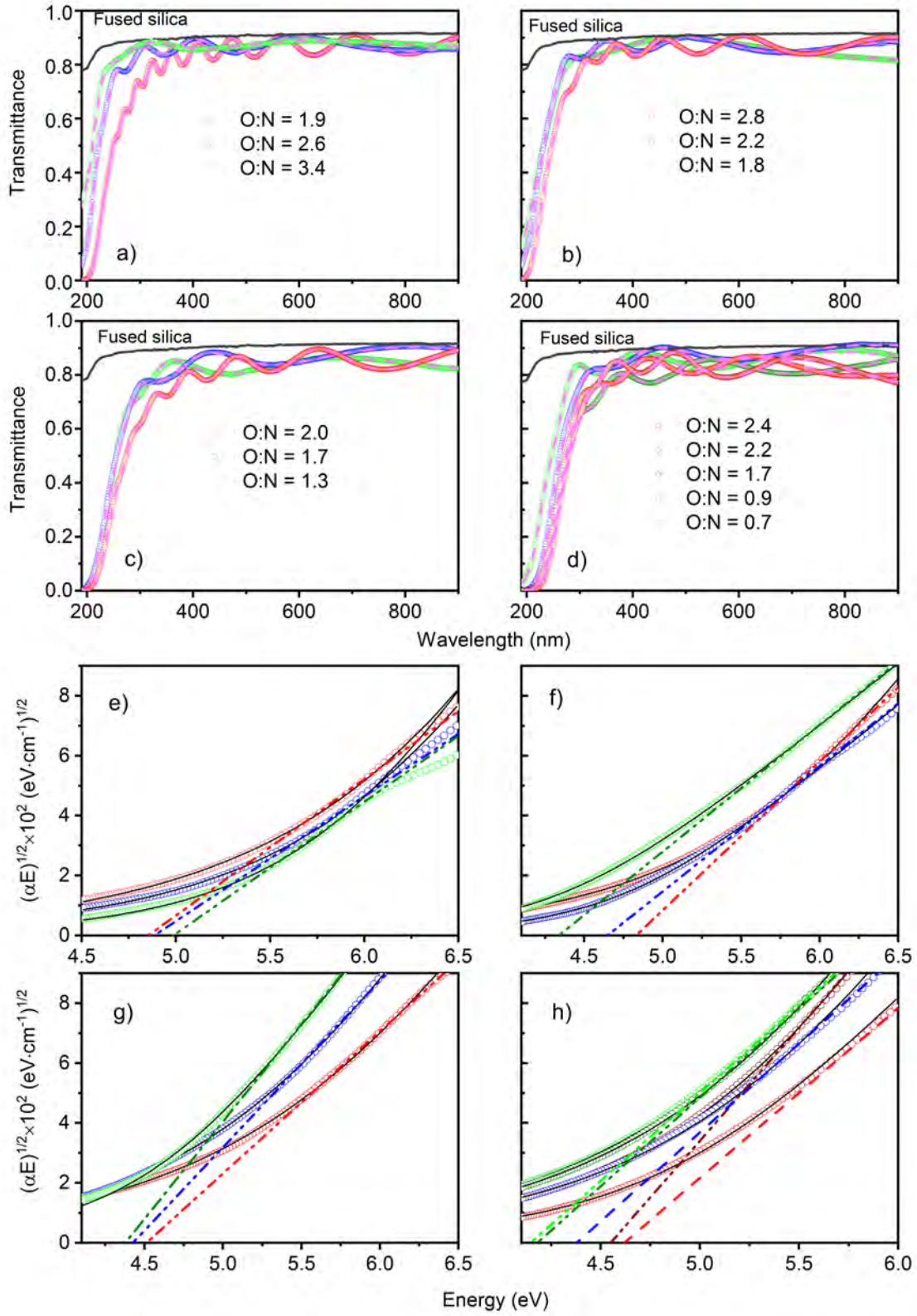

Figure 4.4: Transmittance spectra of amorphous (a) undoped (b) Tb-doped (c) Yb-doped and (d) Tb/Yb codoped AlO_xN_y thin films onto fused silica substrates and their respective fits (dashed lines) in as deposited state. Fitted absorption coefficient using the Tauc model $(aE)^{1/2}$(dashed-dotted lines) and the band fluctuations model (BF) (solid lines).

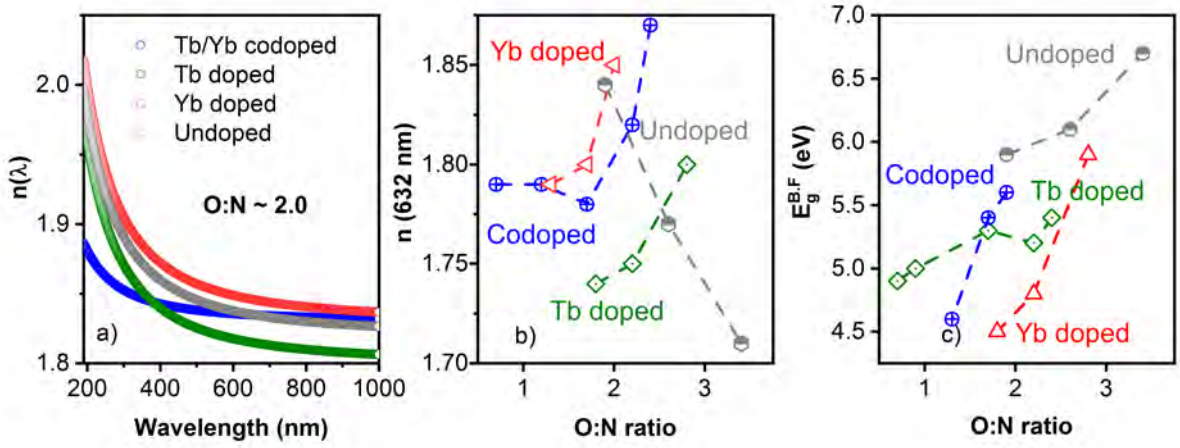

Figure 4.5: (a) Refractive index of doped and Tb, Yb singly doped and codoped AlO_xN_y thin films as a function of wavelength. (b) Variation of refractive index of thin films with O:N ratio. (c) Variation of the bandgap versus O:N ratio. All reported values correspond to the films in as deposited state.

creation of disorder related localized states. The optical bandgap energy and Urbach energy of all the films has been analyzed by a fit of the wavelength dependent calculated absorption coefficient. Three different fits were performed according to the region being considered for the analysis: the Tauc model (fundamental absorption region), the Urbach rule (band tails region) and the Band fluctuation model (from the fundamental region to the band tails). Among the three fits, the band fluctuation model is the more accurate since it considers the whole absorption coefficient curve and thus, avoid the bias of the other models. Table 4.1 shows the fitting parameters values obtained after applying the modified Swanepoel method of the transmittance curve, as well as the retrieved optical bandgap and Urbach energies using Tauc, Urbach and Band fluctuation models for a fit of the absorption coefficient. Along with these values, the composition analysis of each sample is also reported to evidence some clear trends.

In Figure 4.5(a), the calculated index of refraction values n in the VIS-NIR spectral region for an undoped, Tb^{3+} doped, Yb^{3+} doped and, Tb^{3+}/Yb^{3+} codoped AlO_xN_y:H layers are shown. Although there is no relation between thickness and refractive index, it is known that thin film material properties can change with thickness. Moreover, the observed thickness gradient varies along with the concentration of oxygen an nitrogen in the sample. The closer the sample is to the AlN target, the thicker the film and the higher the concentration of oxygen found in the sample. This behavior is observed for all Tb^{3+} and Yb^{3+} doped samples, but not for the undoped samples. It might be a result of the oxidation of the film surface, especially in the critical case of thinner films, where the surface oxidation can severely change the O:N ratio of the film. The results shown in Figure 4.5(b) indicate that the values of refractive index decreases with increasing film thickness. With respective to the sample composition, the refractive index of all samples has shown to decrease with increasing O:N ratio. Similar behavior has been observed in Eu_2O_3 doped lead fluoroborate glass [225] and in amorphous Ge-Sb-Te films where the index of refraction varies inversely with the oxygen concentration [226].

By fitting a band fluctuations (BF) model in every $(\alpha E)^{1/2}$ spectra [194] from the calculated

Sample: AlO_xN_y	Al (at.%)	O (at.%)	N (at.%)	Tb (at.%)	Yb (at.%)	O:N	d (nm)	A_0	A_1 (nm^2)	$E_g^{B.F}$(eV)	E_g^{Tauc}(eV)	$E_U^{B.F}$(eV)	E_U(eV)
Undoped	39	47	14	-	-	3.4	110.5	1.69	6372.2	6.7	5.0	502.5	528.8
	39	44	17	-	-	2.6	337.9	1.75	7265.7	6.1	4.9	535.6	479.4
	35	43	22	-	-	1.9	553.8	1.82	6372.2	5.9	4.9	591.3	407.3
Tb/Yb codoped	29	27	37	~ 2	~ 5	0.7	219.6	1.75	14718.6	4.9	4.1	389.5	512.1
	27	31	34	~ 2	~ 6	0.9	251.2	1.76	15397.2	5.0	4.2	420.2	421.9
	32	41	23	~ 1	~ 3	1.7	293.3	1.76	9388.9	5.3	4.4	409.4	452.9
	34	43	20	~ 1	~ 2	2.2	343.1	1.83	2030.6	5.2	4.6	448.6	498.2
	33	45	19	< 1	~ 2	2.4	381.2	1.86	4905.4	5.4	4.7	465.1	565.2
Tb doped	26	45	25	~ 4	-	1.8	136.8	1.72	6864.7	4.5	4.3	481.9	478.6
	29	47	21	~ 3	-	2.2	299.2	1.72	10356.7	4.8	4.7	298.9	135.4
	35	48	17	< 1	-	2.8	503.1	1.79	4268.8	5.9	4.8	287.9	142.2
Yb doped	27	39	29	-	~ 5	1.3	186.7	1.75	17430.9	4.6	4.4	549.8	456.4
	31	41	24	-	~ 4	1.7	309.5	1.77	12042.2	5.4	4.4	480.5	421.5
	30	45	23	-	~ 2	2.0	516.4	1.83	6764.7	5.6	4.5	309.8	347.8
Tb/Yb codoped	As deposited sample with O:N = 2.4 and d = 219.6 nm												
550°C	31	44	17	~ 3	~ 5	2.6	181.4	1.8	124.4	5.5	4.9	701.9	474.1
650°C	34	46	13	~2	~5	3.5	192.5	1.73	5819.3	4.9	4.5	859.4	464.2
750°C	34	49	9	~ 3	~ 5	5.4	189.5	1.68	5493.2	4.5	4.1	913.7	563.4
850°C	33	48	10	~ 3	~ 6	4.8	214.0	1.63	14289.9	4.6	4.4	915.7	778.3
Undoped	As deposited sample with O:N = 2.6 and d = 337.9 nm												
550°C	40	48	12	-	-	4	297.7	1.65	1578.2	6.3	4.8	524.2	603.4
650°C	42	48	10	-	-	4.8	226.9	1.68	2341.6	6.4	4.9	481.7	520.4
750°C	40	52	10	-	-	5.2	218.5	1.63	5826.7	6.5	5.1	452.9	424.2
850°C	41	51	8	-	-	6.4	227.1	1.56	13141.3	6.7	5.2	462.8	435.7

Table 4.1: Optical parameter values of as deposited thin films on fused silica substrates. Each thin film is characterized by its elemental composition and corresponding thickness d. The Cauchy fitting parameters A_0a and A_1 are determined from the fitting of UV-VIS spectra with Eq. 4.1. $E_g^{B.F}$ and $E_U^{B.F}$ are the bandgap and Urbach energy values obtained after the fitting procedures depicted in Fig. 4.4. $E_g^{Tauc}$is the bandgap calculated by extrapolation from the linear region in the $(\alpha E)^{1/2}$-plot and E_U is the slope in Urbach region found by independent fitting. The reported errors are retrieved from the fits. Errors associated with the thickness are around 1 to 2 nm due to the employed fitting method, equations and additional film inhomogeneities.

absorption coefficient, the optical bandgap E_g and the Urbach energy E_U were determined. For comparison, E_g and E_U were also calculated. The former by an extrapolation of the linear region in the $(\alpha E)^{1/2}$- plot with the Tauc model, and the latter by the use of the Urbach rule in the $Log(\alpha)$ plot. Note that both, the BF fit and the Tauc model fit, resolve bandgap values that follow the trend observed in Figure 4.4(e)-(h) (also see Table 4.1). However, the BF fit retrieves reliable higher bandgap energy values due to the consideration of the Urbach tail and absorption edge regions in the model for an accurate reproduction of the absorption coefficient.

Figure 4.5(c) shows the optical bandgap of all undoped and RE-doped samples in as deposited state as a function of the O:N ratio. The bandgap energy values obtained for the case of undoped AlO_xN_y:H is around 6.4 eV which is consistent with corresponding literature [227] and lies between the optical bandgap values of Al_2O_3 [228] (7.0 - 7.6 eV) and AlN [229, 230] (6.1 - 6.2 eV). From Figure 4.5(c) one can note that the RE doping produced an overall reduction of the bandgap compared to the values observed in the case of undoped AlO_xN_y matrix. A lot of factors can influence the optical bandgap of any material such as the average particle size distribution, lattice parameter, phase state, degree of structural order-disorder and dopant concentration. Here, the observed increase of bandgap is attributed to the dominant effect of oxygen concentration in the amorphous matrix, and its reduction at some degree is related to the incorporation of RE elements. In fact, the variation of optical bandgap can be useful to extract information regarding the structural arrangement and the nature of bonds [231]. As the RE ion enters in the matrix structure, it changes the coordination number and the oxygen bonding in the host. Also the formation of non-bridging oxygen alters the absorption characteristics and decreases the optical bandgap. For instance, when Er_2O_3 is replaced by Gd_2O_3 the increase in optical band gap is due to the replacement of Er-O bond by Gd-O bond which decreases the number of non-bridging oxygens [232, 233].

In order to activate the RE ions in the host, annealing treatments are typically performed at temperatures above 600°C. The thermal treatment change the optical transmittance curves due to impact of annealing on the host properties that may undergo diffusion, rearrangements and second phase formation processes. The UV-VIS spectra of the undoped samples (4.6(a)) shows a reduction of the thickness with annealing temperature. The samples become more compact, which means a smaller mean bond distance or bond length. The latter has also an impact on the bandgap value which shows an increment with annealing temperature. It is also noteworthy the strong increment of the O:N ratio which should also contribute to the observed increase of the bandgap energy.

According to Table 4.1, the behavior of both Tauc and B.F energy bandgap is similar. Nevertheless, the former is always smaller than the latter, mainly due to the fact that it does not take in to account the tails. The defects and disorder of amorphous semiconductors result in the band tails with localized states in the energy gap. A representative parameter of this disorder is the Urbach energy. Annealing treatments also induces a change of the internal arrangement of the atoms and reduces structural defects. Therefore, in Figure4.6 (c) it is observed for the undoped matrix that an increase of the annealing temperature leads to a reduction of the Urbach energy. This is caused by a reduction

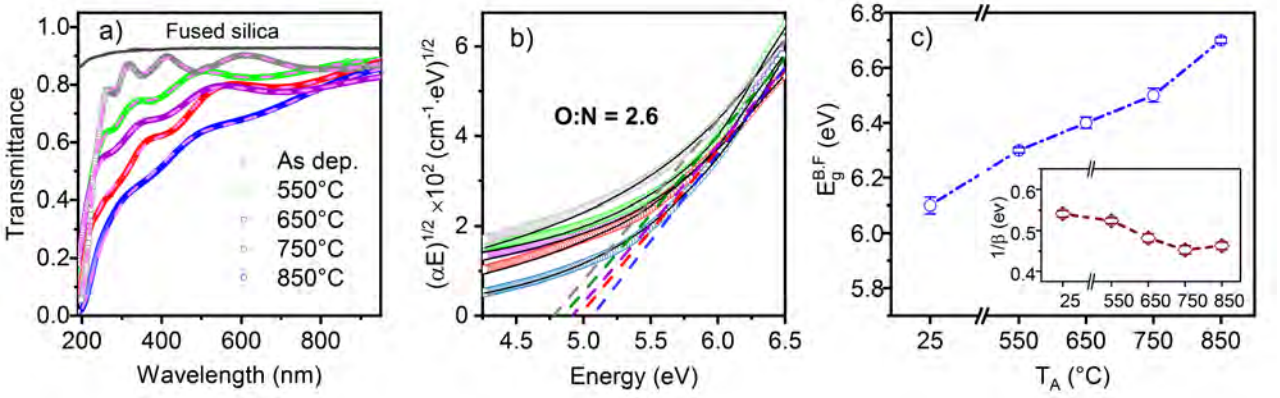

Figure 4.6: (a) Transmittance spectra of undoped AlO_xN_y:H (O:N ratio of 2.6 and thickness of 337.9 nm) after annealing treatments at 550°C, 650°C, 750°C and 850°C. (b) Fitted absorption coefficient using the Tauc model $(aE)^{1/2}$(dashed-dotted lines) and the band fluctuations model (BF) (solid lines). (c) Energy bandgap and Urbach energy values versus annealing temperature.

of the disorder which clean the tails and increase the estimated Tauc energy bandgap.

In the case of Tb^{3+} and Yb^{3+} codoped films, a different behavior is observed. Figure 4.7(a) shows the measured transmittance curves after different annealing temperatures. The transmittance has also been reduced with thermal treatments, but instead of reducing the thicknesses as in the undoped matrix, the codoped sample had an increment of the thickness with temperature. This is followed with a reduction of the estimated optical bandgap energy and a strong increment of the O:N ratio. The two latter observations seems to be quite contradictory. However, the sample under study contains Tb^{3+} and Yb^{3+} ions and therefore one can infer that second processes are taking place due to the presence of RE impurities, for instance the formation of RE oxides clusters of smaller energy bandgaps.

Figure 4.7(c) shows a reduced bandgap energy and increased Urbach energy at higher annealing temperature, in the case of Tb^{3+} and Yb^{3+} codoped sample. While the reduced bandgap can be related to the formation of RE oxides, the increment of the Urbach energy reveals the introduction of energy states in the matrix bandgap when embedding the host with isovalent RE ions. In fact, the RE ions are luminescent impurities that increments the disorder of the amorphous host, leading to a greater number of band to tail and tail to tail transitions, thus narrowing the Tauc bandgap. Although the disorder degree has been reduced in the undoped matrix with higher annealing temperatures, the opposite behavior is obtained in the codoped matrix. This can be a consequence of the the formation of the RE-O solid solutions with increasing annealing temperature.

The effect of annealing treatments on the bandgap of undoped AlO_xN_y:H film has been examined. A reduction of the disorder with the annealing temperature is observed by the decrease of the Urbach energy, see fig. 4.6(c). The observed increase of the Tauc bandgap can be understood as a consequence of thermally induced structural relaxation and a decrease of the defect related and band tail states[234, 235]. Simultaneously, oxygen concentration was found to increase while nitrogen

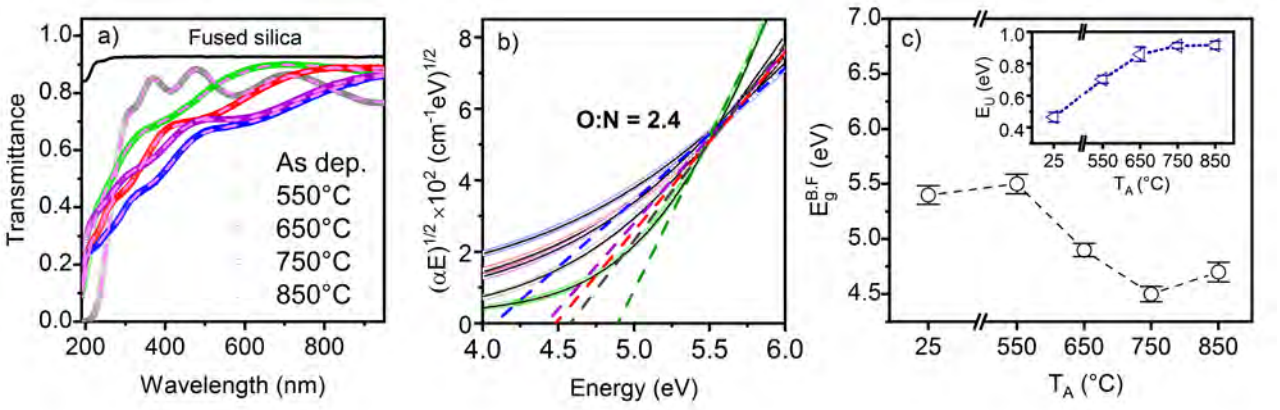

Figure 4.7: (a) Transmittance spectra of Tb/Yb codoped AlO_xN_y:H (O:N ratio of 2.4 and thickness of 381 nm) after annealing treatments at 550°C, 650°C, 750°C and 850°C. (b) Fitted absorption coefficient using the Tauc model $(aE)^{1/2}$(dashed-dotted lines) and the band fluctuations model (BF) (solid lines). (c) Energy bandgap and Urbach energy values versus annealing temperature.

concentration decreases with the rise in the annealing temperature. The increase in the Al-O/Al-N intensity ratio after annealing can be attributed to the breakage of Al-N bonds which are metastable with respect to oxygen. In order to understand the oxidation of AlO_xN_y film, the atomic ratio of N:Al was calculated to be 0.44, 0.30, 0.24, 0.25 and 0.19 for the as deposited, 550, 650, 750, and 850 °C annealed sample, respectively. It suggests that the breakage of Al-N bonds is more intense with the increasing annealing temperature. Another possibility is the presence of oxidation in the furnace. This is in good agreement with reported results in literature, where a strong nitrogen loss from N-rich AlN film was observed after annealing treatments [236]. With the increase in annealing temperature, one would expect that the bandgap of AlO_xN_y increases owing to the increment of oxygen concentration into the film due to surface oxidation.

The observed reduction of the optical bandgap from 5.5 eV (without annealing) to 4.6 eV (at 850°C) in the case of Tb^{3+} and Yb^{3+} codoped films, can be a consequence of the coordination between RE ions and oxygen atoms with increasing annealing temperatures, which may induce the formation of RE oxides and RE clusterization. Indeed, the occurrence of Tb-oxide clusterization (TbO_2, Tb_2O_3) has been reported in silicon oxide [237] and silicon oxynitride [238] matrices upon annealing at 900°C and 1200°C, respectively. According to Labbé et al, the nitride based host matrix has a higher thermal threshold of RE cluster formation compared to the silicon oxide host. A similar result was early observed for Er ions embedded in both silicon oxide and silicon nitride matrices [239]. Moreover, the reported optical bandgap of Tb_2O_3 (3.82 eV) [240], TbO_2 (1.51 eV) [241] and Yb_2O_3 (4.9 eV) [242] are smaller than the values observed for the AlO_xN_y matrix in this study. Therefore, an increasing number of RE oxide clusters can induce a variation of the optical bandgap due to its dependence on composition. There exist a variety of crystal defects owning to the RE doping of AlO_xN_y:H films related to the formation of crystalline clusters in the matrix with the thermal annealing treatments, [243, 244, 245] which may induce intermediate energy levels within the conduction and valence bands, and lower the bandgap.

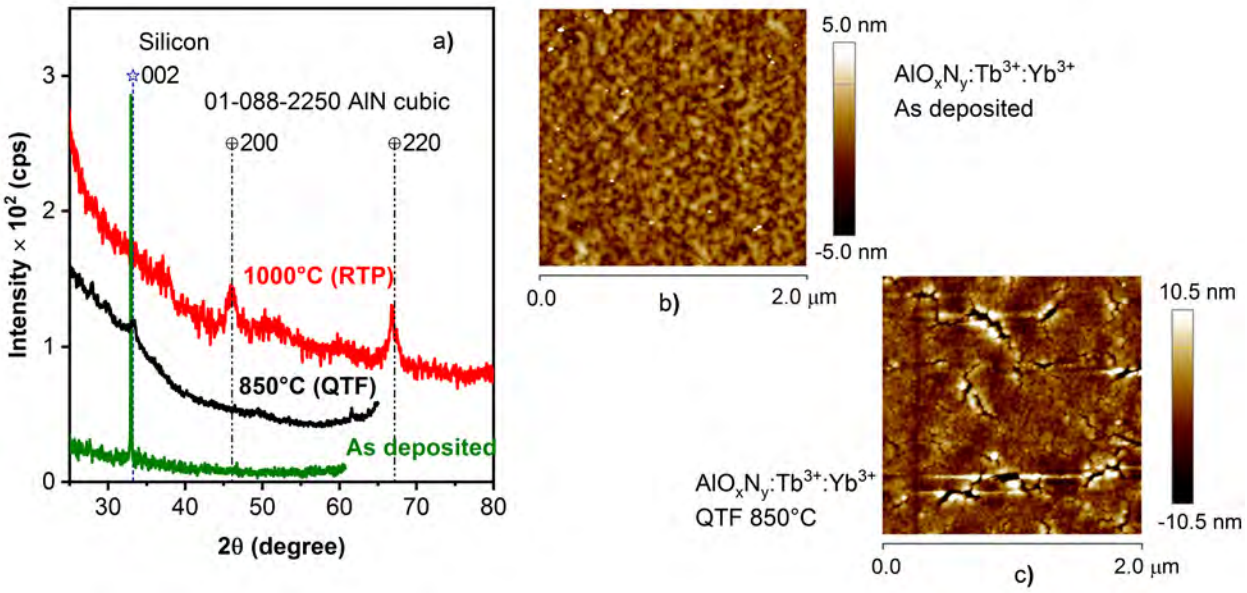

Figure 4.8: (a) XRD pattern for Tb/Yb codoped AlO_xN_y in as deposited state and after annealing treatments at 850°C using a quartz tube furnace procedure and at 1000°C using a rapid thermal processing system. XRD peaks corresponding to (002) of Silicon and, (200) and (220) of cubic aluminum nitride samples. The surface roughness is observed in AFM images of a Tb/Yb codoped AlO_xN_y (a) in as deposited state and (c) after annealing at 850°C using a quartz tube furnace.

In order to characterize the possible formation of second phases due to higher annealing temperatures, X-ray diffraction experiments were performed. However, the X-ray diffractogram at room temperature before and after annealing indicate that the matrix remains predominantly amorphous up to 850°C anneling using the quartz tube furnace (QTF). Nonetheless, it was verified that it is possible to induce the formation of polycrystalline phases by annealing the amorphous matrix at 1000°C using a rapid thermal processing (RTP) as shown in Figure 4.8(a). Complementary atomic force microscopy (AFM) images has been obtained to investigate the effect of high temperature annealing on the surface roughness of the samples in Figure 4.8(b) and (c). Although the mean roughness value after annealing at 850°C (Ra = 2.29 nm) has been found to increase with respect to the as deposited sample (Ra=0.92 nm), the overall roughness of the film had not been severely changed after annealing at that high temperature. It is important to note that there is a microstation creep damage at the surface due to cracks formation which may be a consequence of thermal stress effects at higher annealing temperatures.

b) Luminescent properties of Tb and Yb doped AlO_xN_y:H layers

This work has systematically investigated the optical properties and light emission features of Tb^{3+} doped, Yb^{3+} doped, Tb^{3+}/Yb^{3+} codoped and undoped AlO_xN_y:H thin films. The effect of the dopant concentration was studied as well as O:N ratio and thermal annealing treatments on the optical properties and light emission features. First, a description of the luminescent properties of the singly doped and the codoped amorphous AlO_xN_y:H layers at room temperature under band-to-band electron excitation (325 nm) is presented. In order to verify which possible excitation pathways can

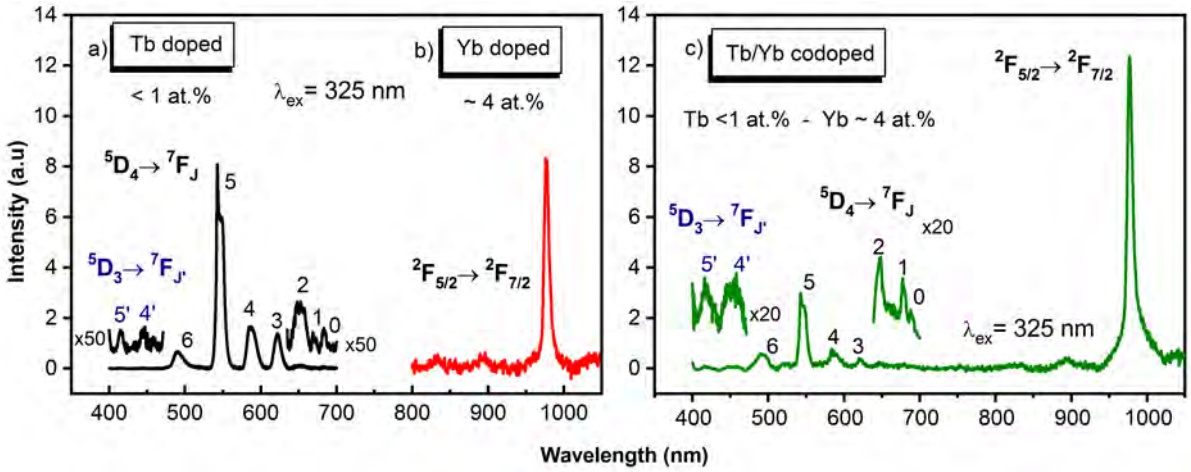

Figure 4.9: UV excited emission spectrum of (a) Tb doped, (b) Yb doped and (c) Tb/Yb codoped AlO_xN_y thin films with the visual and NIR emission intensities of Tb^{3+} and Yb^{3+} ions respectively. The numbers indicate the different transition bands discussed in detail in the text.

occur in the Tb^{3+}/Yb^{3+} codoped amorphous AlO_xN_y:H samples, PLE spectroscopy measurements were performed. The role of the matrix on the overall emission intensity will be discussed, in order to explain the normalization used to compare the different Tb^{3+} and Yb^{3+} related emission intensities. Also, it will be shown that the matrix emission, and therefore the RE emission, are deeply influenced by the annealing temperature.

Figure 4.9 show the emission transitions of Tb^{3+} and Yb^{3+} ions in the singly doped and codoped samples for a 325 nm excitation wavelength at room temperature. The Tb^{3+} doped sample presents four main transition bands related to the radiative transitions from the $^5D_4$ state to ^7F_J (J = 6, 5, 4, 3) states of Tb^{3+} at 490, 541, 586, 621 nm, respectively. The $^5D_4$ to $^7F_5$ transition is the most intense line and corresponds to the green color. The Yb^{3+} doped sample emits a PL signal around 980 nm attributed to the transition between the energy levels from $^2F_{5/2}$ to $^2F_{7/2}$. Although the emission wavelength of Tb, Yb and other RE ions are characteristic features that depends very little on the host and excitation source, the intensity of the emission bands are strongly affected by the host chemical environment, lattice vibrations and the concentration of luminescent centers [246, 247, 248, 249]. Take for instance, the blue transitions of Tb^{3+} from the $^5D_3$ state to ^7F_J (J = 6, 5, 4) states at 384, 416 and 446 nm, respectively. These bands show lower intensities compared to the green ones. However, by adjusting the Tb^{3+} doping concentration and increasing the excitation intensity, the emission colors can be tuned between green and blue with considerable increase in intensity [250, 251].

The photoluminescence spectra shown in Figure 4.9 are host background substrated, with the aim to focus on the Tb^{3+} and Yb^{3+} emission lines in the singly doped and codoped film with similar concentration of dopants. Nonetheless, in order to discuss the optical emission properties, it is important to consider first the matrix emission in the calculations. Figure 4.3 shows the PL spectra of as deposited Tb^{3+}/Yb^{3+} codoped AlO_xN_y:H thin film with the matrix emission under excitation at 325 nm at room temperature. Since the excitation energy (E = 3.81 eV) is below the bandgap energy value ($E_g \sim 5$ eV), it is possible to be actually exciting electronic defects directly. If the excitation source

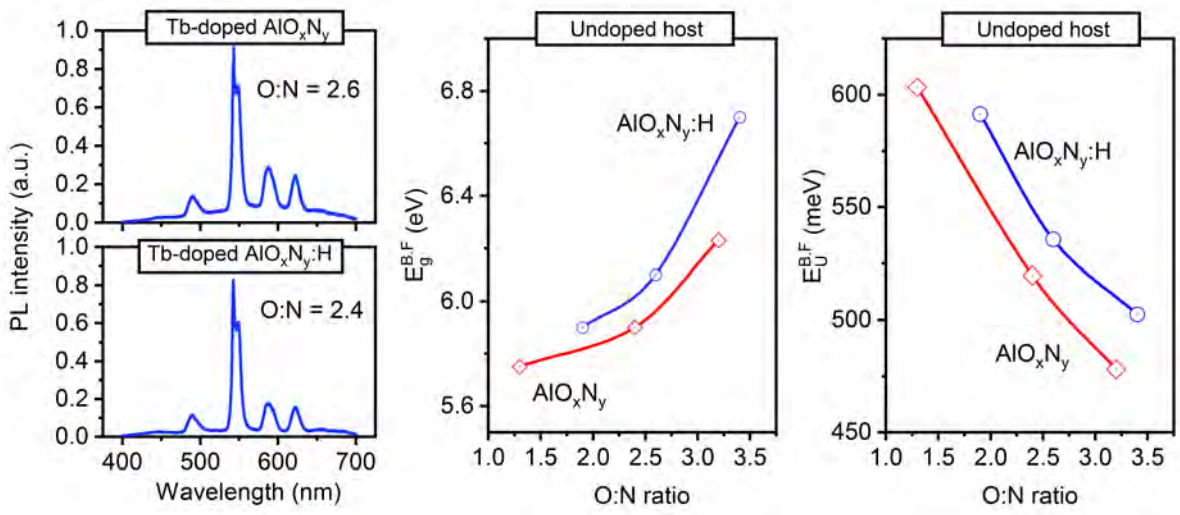

Figure 4.10: Room temperature PL spectra of AlO_xN_ythin films with and without hydrogen passivation under the excitation of 325 nm.

is an electron beam, for example in cathodoluminescence experiments, a lower matrix background emission would occur because the impinging of electrons is a more efficient excitation path through the RE ions than photon excitation.

In general one can reduce the matrix emission following two approaches. First by hydrogen dilution on AlO_xN_y during film deposition in order to passivate dangling bonds and thus decrease the density of localized defect states. The previous work of Guerra [178, 246, 75] has demonstrated that hydrogen dilution on SiC effectively passivates dangling bonds causing the increment of the bandgap and the reduction the Urbach energy due to the energy separation of the mobility edges. The passivation increases the transparency, and reduces the chance to excite electrons in the bandtails of the passivated matrix compared to the non passivated one. This effect lowers the background matrix emission of the passivated host, as can be appreciated in Figure 4.10 in the case of Tb^{3+} doped AlO_xN_y:H samples. This matrix emission reveals the presence of defect related recombination processes, energy back transfer mechanisms between the RE ions and electronic defects may take place enhancing the nonradiative transition rate, and thus quenching the luminescence and the efficiency [21, 252].

The second approach is the reduction of matrix emission due to succesive annealing of the sample at higher temperatures. Fig. 4.11 shows the increase of Tb^{3+} and Yb^{3+} related emission intensities with annealing temperature and the decrease of host related emission intensity. Noteworthy is the connection between the increase of Tb^{3+} and Yb^{3+} related intensity with the decrease of undoped host related emission through successive thermal treatments increasing the temperature. This may indicate the quenching of radiative recombination in host related states and the improvement of other energy transfer channels from the matrix to the RE ion.

The behavior observed in Fig. 4.11 suggests that the excitation of Tb^{3+} and Yb^{3+} related emissions in an amorphous AlO_xN_y:H matrix is a result of energy transfer processes from the host to the REs mediated by intrinsic defect states in the bandgap. This indirect excitation of the RE ions

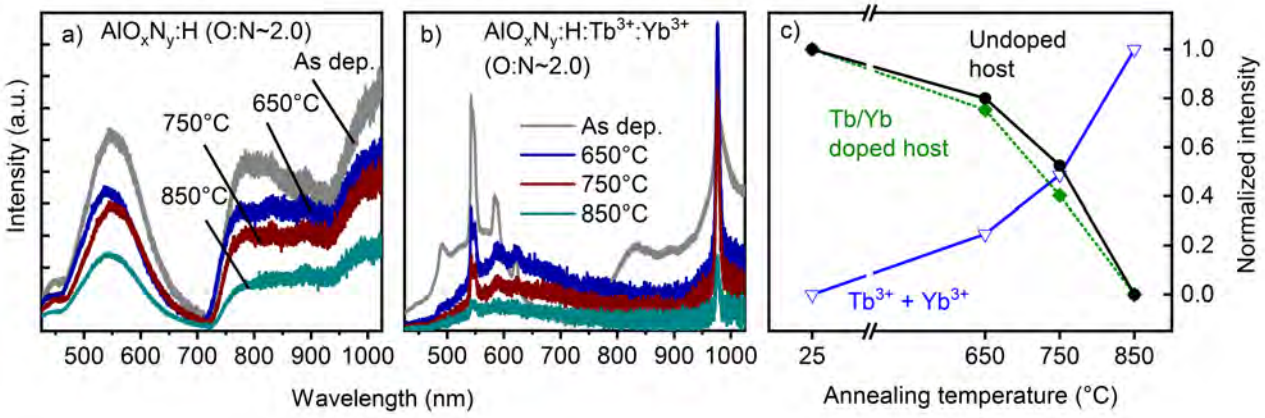

Figure 4.11: PL spectra for (a) undoped AlO_xN_y:H host and (b) Tb^{3+}/Yb^{3+}codoped AlO_xN_y:H before and after annealing treatments. The sample depicted had an O:N ratio of 1.2 in as deposited state. Spectra are offset for clarity. (c) Normalized $Tb^{3+}+ Yb^{3+}$ related emission (blue solid line) with its reciprocal codoped host related emission (green dotted line), and the undoped host related emission (black solid line) at different annealing temperatures.

is much more probable than the occurrence of a direct excitation. Generally speaking, the host is excited first and produces an electron hole pair which recombines transferring the energy to a nearby RE ion. The emission of the RE originates in the excited states of the 4f electrons, and they do not hybridize with the sp^3 orbitals of III-V semiconductor host, therefore no overlap between the electron wavefunctions of the matrix and the RE ion occurs. This means that the recombination of an optically excited electron hole pair can not transfer its energy to the RE ion core by exchange interaction. The excitation process in this case relies on dipole-dipole interactions which are less efficient. However, the presence of an impurity state due to RE doping can enhance the energy transfer process. Because the energy released by nonradiative recombination of an electron hole pair via an impurity state, within the bandgap of the host, is closer to the RE related level, making it easier for the 4f electrons to take over the energy released. In other words, the gap states bridge the extended host states to the localizes states of a RE ion.

Other possible paths for indirect nonradiative excitation of RE ions is the ligand-to-metal charge transfer (LMCT) [253]. It involves the promotion of an electron from the valence band to a RE ion producing a divalent RE [254], with the aim to form a charge transfer state closer to the 4f energy levels of the trivalent RE. This is not the case of AlN and other wide bandgap semiconductors where the ground state of divalent Tb^{2+} lies within the conduction band, resulting in the immediate autoionization of the electron charges transfer state in the conduction band [255]. Also, there is the 4f - 5d transitions which involves an electron promoted into the 5d sub-shell [256]. Such transitions are broader than 4f – 4f transitions, also they are allowed by Laporte selection rules, whereas the 4f – 4f transitions are forbidden. In the 4f – 5d transitions, the color of the emission severely changes with different hosts due to the larger interaction of the 5d electron with its environment. As these transitions require high energies only those of the easily oxidized ions Ce^{3+}, Pr^{3+}, and Tb^{3+} are commonly observed [161].

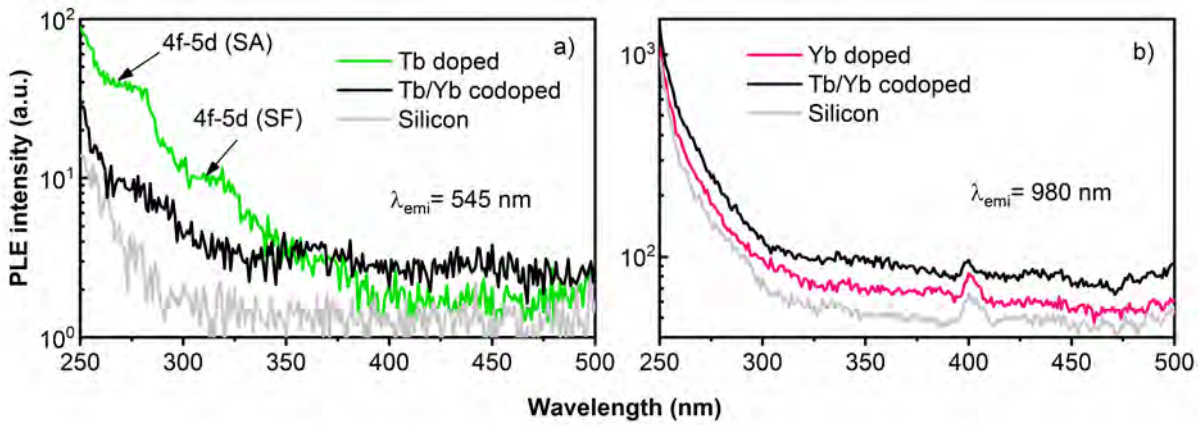

Figure 4.12: Excitation PL spectra recorded at room temperature of Tb/Yb codoped AlO_xN_y:H sample compared with singly doped sample and silicon alone monitoring the (a) Tb^{3+}main transition emission at 545 nm for spin allowed (SA) and spin forbidden (SF) contributions, and the (b) Yb^{3+}NIR emission at 980 nm.

Figure 4.12 shows the PLE spectra of Tb^{3+} doped and Tb^{3+}/Yb^{3+} codoped AlO_xN_y:H thin films which exhibit two broad peaks: one observed from 250 to 300 nm, and the other from 300 to 325 nm. They correspond to the matrix contribution to the excitation of the Tb ions via energy transfer processes. In the literature, a similar PLE spectra was reported in the case of Tb^{3+} doped AlN at 491 nm [257] and at 545 nm emission wavelength [178]. According to [257] the broad peaks observed could be caused by structured isovalent (RESI) trap clusters or due to the energy transfer from excited electronic defects. Also, PLE spectra of Yb^{3+} doped AlO_xN_y was monitored at 980 nm but only host related bands ($\lambda <$ 250 nm) are observed. The absence of a direct photon resonant excitation of the $^7F_6 \rightarrow {}^5D_{4,3}$ transition could be a consequence of non radiative recombinations via energy back transfer to deep localized band tail states, via energy migration from ion to ion, or even simply the lack of host mediated centers that could effectively transfer the energy to the Tb^{3+} ions.

Nonetheless, matrix mediated nonradiative excitation is not a one way process because the energy absorbed by the RE ion can also migrate to other gap states enabling nonradiative recombinations of the optically excited RE ion. Among the different processes here, two are the most relevant: the Auger energy transfer to free carriers and the energy back-transfer. The first one involves a free carrier or electron associated with a RE related donors or other impurity, which is promoted for example to the conduction band by consuming the energy of the excited RE ion. In the second one, the energy of the 4f electrons decays nonradiatively by promoting an electron from the valence band to a level of a RE related donor or impurity center. It is an exact reversal of excitation. Back transfer has been recognized as the most important decay process for the PL quenching of Er-luminescence at high temperature [258, 259].

c) Composition gradient of Tb and Yb doped AlO_xN_y:H thin film libraries

Figures 4.13 and 4.14 depict the normalized integrated PL intensities, respectively of the $Tb^{3+}$and Yb^{3+} singly doped AlO_xN_y thin film libraries in as deposited state, as well as the concentration

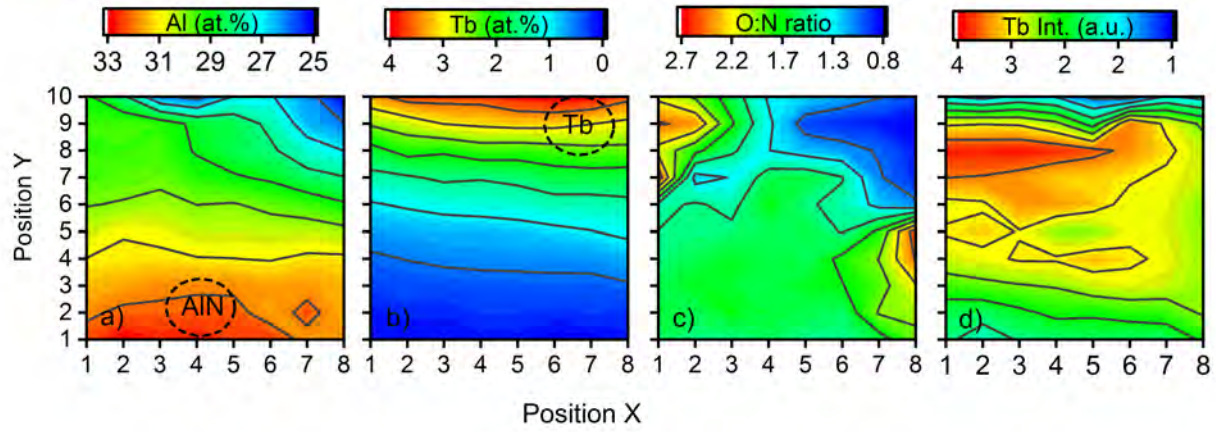

Figure 4.13: As deposited EDS combinatorial screening of (a) Al concentration, (b) Tb concentration, (c) O:N ratio and (d) the corresponding Tb-related PL intensity of AlO_xN_y:H:Tb^{3+} thin films are shown as a function of position.

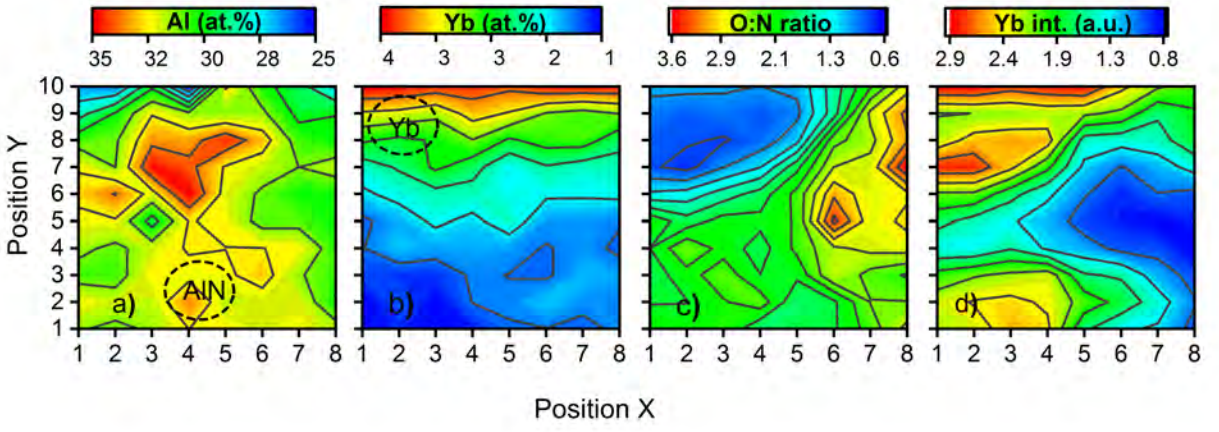

Figure 4.14: As deposited EDS combinatorial screening of (a) Al concentration, (b) Yb concentration, (c) O:N ratio and (d) the corresponding Yb-related PL intensity of AlO_xN_y:Yb^{3+} thin films are shown as a function of position.

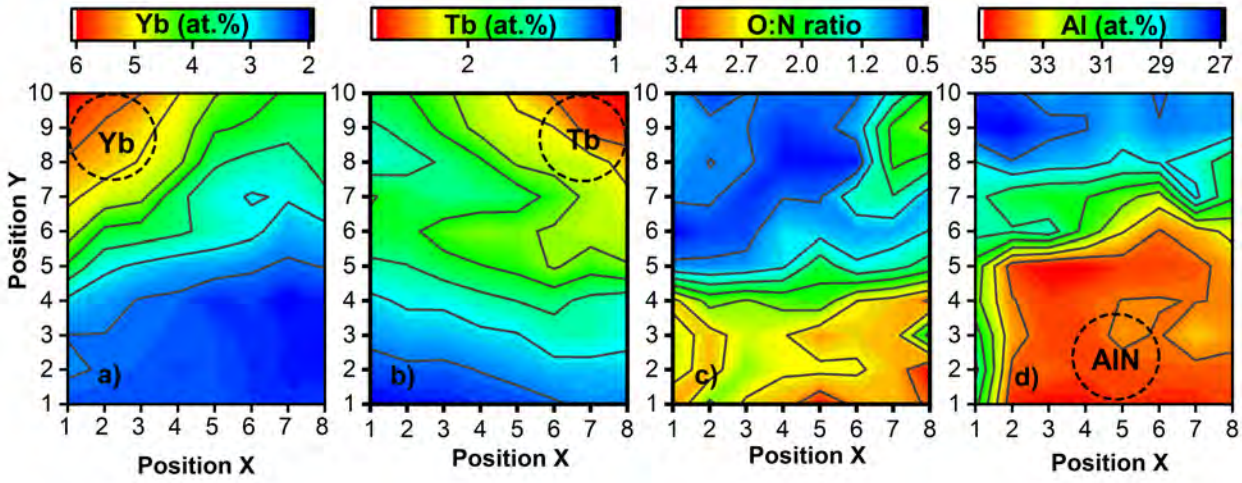

Figure 4.15: Combinatorial EDS result for as deposited (a) Yb concentration, (b) Tb concentration, (c) O:N ratio and (d) Al concentration of Tb/Yb codoped AlO_xN_ythin film library.

variation of their respective elemental composition. From the EDS analysis, the elemental composition can be observed in the thin film library. In both, the Tb^{3+} and Yb^{3+} singly doped AlO_xN_y samples, the concentration gradient follows a radial distance distribution from the RE and host target. The concentration of RE dopants varies from ˜ 1 to 4 at.% and the Al concentration ranges between 25 and 35 at.% with most of concentration values above 30 at.%. Also, the EDS analysis shows occurrence of low O:N ratio values next to the RE target proximity, which increases approaching the AlN target periphery. It is widely know that RE metals commonly react with the oxygen of the air. A glance at the free energy of formation reported by Borzone [260] demonstrates the high stability of RE oxides and RE nitrides in comparison to the oxides and nitrides of metals such as Ti, Al, Fe. In addition, the reported enthalpy of formation of nitrides of RE metals and aluminum are 5-6 times lower than that of their oxides [261] (i.e. $\triangle_{form}H$ = -319.6 kJ/mol for AlN, -326 kJ/mol for CeN, -1676 kJ/mol for Al_2O_3 and -970 kJ/mol for TbO_2 [262], at 300K and 1bar pressure), indicating a tendency of RE metal to actively reacts with oxygen present in the atmosphere. At first hand, one would expect to observe higher O:N ratios in the Tb and Yb target proximity, because the more negative free energy of formation, then the more spontaneously a reaction can occur. However, the results show greater oxygen concentration close to the AlN target and increasing nitrogen content with radial distance. This may be a consequence of competing oxidation and nitridation processes since their rates depend on several variables such as the level of N_2 and O_2 gases, the temperature, the concentration of metals and the atomic number of the RE element. It can be assumed that the nitride formation process may be caused by the deficiency of oxygen in the chemical reaction zone near the RE target and its enrichment in nitrogen. Note that during oxidation, the local heat released increases the temperature. The variation in the oxidation spread is related to the formation of oxide products during film growth which influences the coordination of the oxygen ions in the presence of RE ions. In fact, the RE dopant concentration may influence the formation of different oxide phases. For instance, the increase of Eu and Ce concentration (> 3 at.%) has been reported to cause the formation of AlO_xN_y phase prevailing over the amorphous Al_2O_3 phase in the synthesis of AlO_xN_y:Eu^{2+} and AlO_xN_y:Ce^{3+} [263].

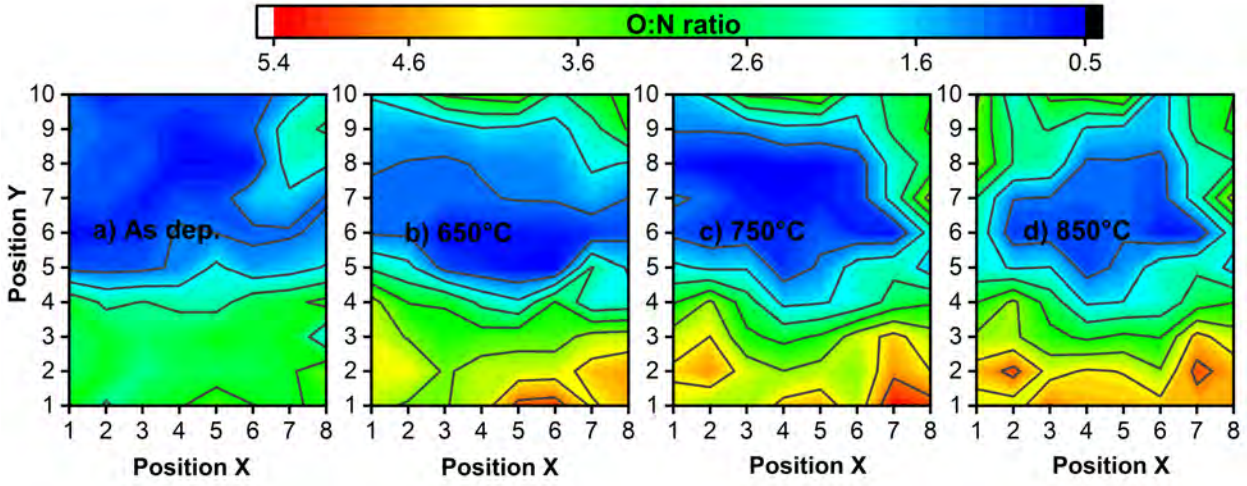

Figure 4.16: Evolution of the O:N ratio of Tb/Yb codoped AlO_xN_y:H thin film library from the (a) as deposited state, and after annealing at (b) 650°C, (c) 750°C and (d) 850°C.

The variation of elemental concentration in the case of Tb^{3+}/Yb^{3+} codoped AlO_xN_y:H is depicted in Figure 4.15. The Tb^{3+}/Yb^{3+} codoped library shows the same trend observed in the O:N ratio versus sample position of singly doped samples: the oxygen concentration increases close to the proximity of AlN target, being approximately 4 times higher than the values around the RE targets. In order to understand this result, one should consider the factors influencing the competition between oxidation and nitridation rates, such as the level of N_2 and O_2 gases, the temperature, the concentration of metals an the atomic number of the RE element.

Figures 4.16(a) - (d) depict the variation of the O:N ratios versus sample position, of the Tb^{3+}/Yb^{3+} codoped AlO_xN_y:H samples after each annealing step at 650, 750 and 850°C. In as deposited state the AlO_xN_y film presents two regions: one of low oxygen concentration, around the position of RE targets, and the other of higher oxygen concentration in the AlN target vicinity. It is worth noting the increment of oxygen concentration throughout the thickness of the film. These results clearly exhibit that the oxygen can incorporate effectively into the film at high temperature of annealing process. Indeed, the highest observed O:N ratio without annealing has increased by ∼50, 55 and 60 % of its value after successive annealing at 650, 750 and 850 °C respectively. Note that the increase of oxygen is more accentuated in a nitrogen rich region (O:N < 1.0) at the second temperature of annealing process. For further annealing temperatures the increment is less prominent. This initial sudden increase could be tentatively attributed to the break of the metastable Al-N bonds, which releases a mobile nitrogen inducing a desorption phenomena, while the immobile Al atom react with oxygen atoms from the film or from the gas phase [236, 264]. Note also that, after heating at 650°C, the increment of oxygen content takes place around the zone of higher Tb concentration, and just after heating at 850°C the oxygen content increases around the zone of greater Yb content (see Figure 4.16). This behavior may be a consequence of the relatively inert Yb with respect to Tb. In fact, the former present only one YbO phase with $\triangle_{form}H$ = -16 kJ/mol [265] while there exist several possible Tb_nO_m phases with reported $\triangle_{form}H$ values ranging from -930 to -970 kJ/mol [265], revealing a most stable and stronger bonds for Tb oxide phases.

d) Concentration quenching and thermal activation

There is strong evidence that the mechanisms behind RE ions activation and energy migration are highly susceptible to variations in the host atomic composition and/or structure [22, 23, 12]. Furthermore, the embedded RE ion can form pairs and clusters with other RE ions and impurities such as oxygen or transition metals [21, 257]. Regarding the composition of the luminescent layer, two factors are directly related to the optical emission intensity and should be addressed. First, the concentration of RE ions that influences the interactions responsible for the concentration quenching of the light emission; and second, the oxygen content in the matrix which may induce formation of RE-O complexes and clusters, at times favorable on the structural arrangement for the emission of RE ions [21, 266].

To systematically study the effect of RE (Tb, Yb) concentration and oxygen content (using the O:N ratio) on the emission spectra of Tb^{3+}/Yb^{3+} codoped AlO_xN_y:H thin films, a combinatorial screening of PL intensity and EDS measurements were performed throughout 80 positions on the sample. As a result, large data sets of O:N values, RE concentration and RE-related intensity areas has been obtained at each position. To cope with the very large data sets, Figures 4.17 were constructed to show the RE-related intensity as a function of the O:N ratio and RE concentration. The advantage of this approach is the possibility to then analyze how the RE-related emission intensity behaves at the variation of one parameter (i.e. the O:N ratio) while the other parameter (i.e. Tb concentration) is maintained. Along with the concentration quenching analysis, the ability of the material to activate emitting RE centers is also studied based on the evolution of the RE-related intensity at different temperatures. The results obtained in the case of Tb^{3+}/Yb^{3+} codoped films are compared with those obtained for the singly doped AlO_xN_y :H films, in order to differentiate the effect of codoping on the luminescence behavior of Tb^{3+} and Yb^{3+}. The PL spectra of the Tb^{3+} and Yb^{3+} doped AlO_xN_y:H thin film libraries were measured in a reflection setup using 325 nm excitation wavelength from a monochromatized He-Cd lamp. The elemental concentrations were measured by means of EDS inside a SEM chamber, using a 4.5 kV electron beam to avoid the substrate.

Figure 4.18 shows the normalized integrated PL intensities of each RE-related emission as a function of their respective RE concentration for both singly doped and copoded thin films with an O:N ratio approximately constant. In this type of plot two regions can be identified: (1) a low RE concentration region where the intensity of emitted light increases linearly with the amount of RE ions, and (2) a high RE concentration region where takes place the exponential decay of emitted light intensity with more RE ion concentration. In the first part, the probability of light emission increments with more luminescent centers, but this behavior can not be further sustained. As the amount of RE ion continues to increase, the mean ion interdistance is reduced and the interaction between them becomes more probable, leading to nonradiative energy transfer process. The theoretical sustain for these interactions are based on Förster and Dexter's interpretation of the phenomenon. According to Förster, the energy transfer is a dipole-dipole resonant interaction between closely located atoms [171] and its strength rapidly vanishes with increasing distance between the ions. Meanwhile, Dexter

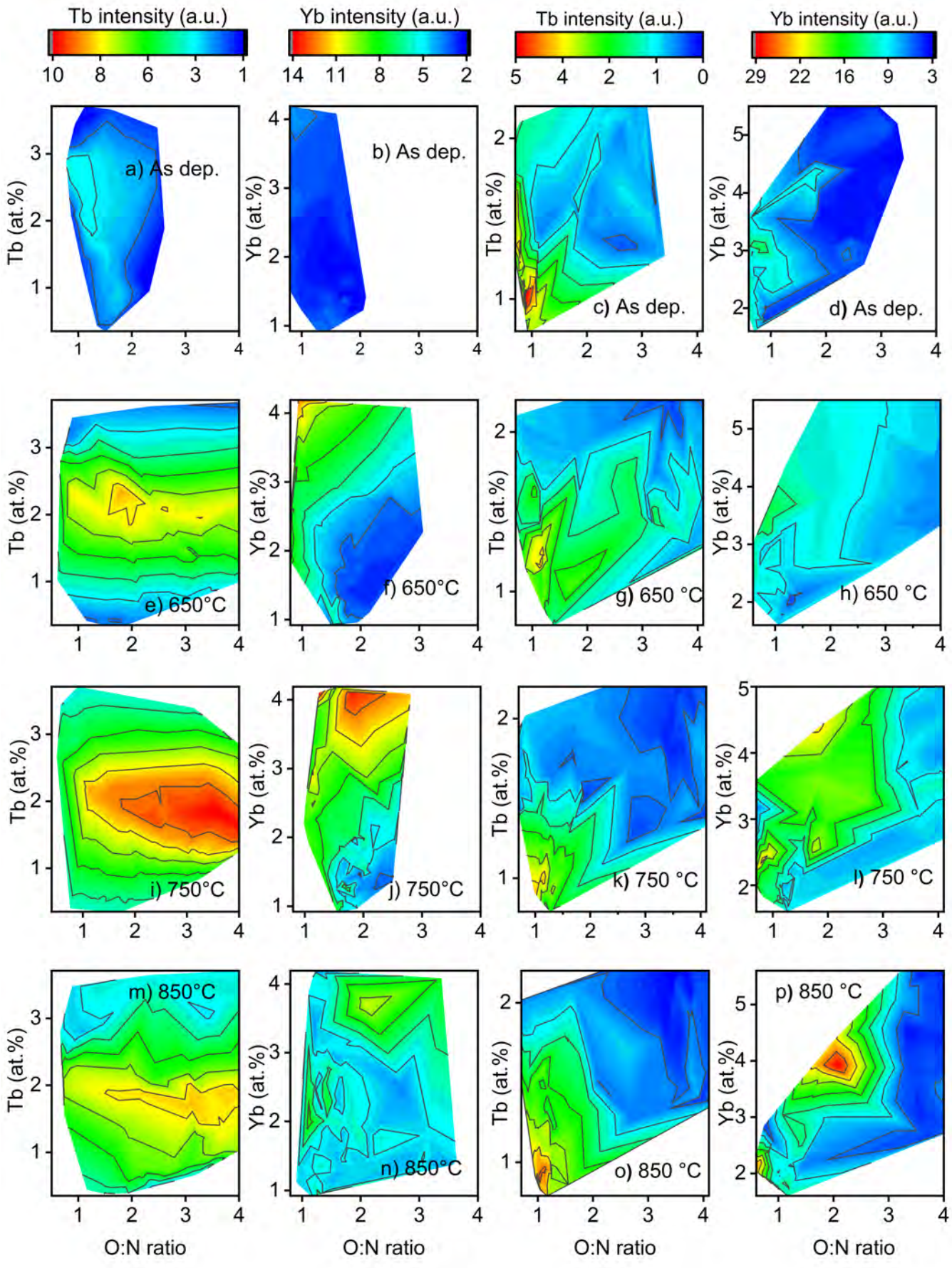

Figure 4.17: Evolution of the integrated PL intensities of $Tb^{3+}$and Yb^{3+} related emission of singly doped and codoped amorphous AlO_xN_y:H host versus O:N ratio at different Tb and Yb concentration in as deposited state and after annealing at 650 °C, 750 °C, and 850 °C.

explain the exnergy transfer process as a short range interaction that involves quantum mechanical electronic exchanges between ions [173]. More details about each energy transfer rate model can be found in section 2.2.3.

The integrated PL intensity below the emission spectrum is a measure of the relative probability that the excitation will relax via a radiative decay versus the nonradiative pathways. The RE ion concentration is one factor, however not the only one as will be discussed later, that strongly influences this probability. From the curves depicted in Figure 4.18, the differences in the optical emission properties of Tb^{3+} related and Yb^{3+} related emissions in singly doped codoped AlO_xN_y:H will be highlighted regarding the effect of RE ion concentration. The first difference observed is the change in the behavior of Tb concentration quenching in the presence of Yb codoping ions compared with the Tb^{3+} singly doped samples. When no Yb is codoping the AlO_xN_y:H matrix, the integrated intensity of the Tb^{3+} related emission increases linearly in the low concentration region of up to 2 at.% of Tb^{3+} ions. At this point the maximum integrated PL emission is obtained and beyond this concentration the luminescence quenchesexponentially. For the codoped Tb^{3+} related intensity, no linear increase is observed in the low concentration region. Instead, the exponential decay of Tb^{3+} intensity occurs earlier at around 1 at.% of Tb. By fitting an exponential function Exp(-x / x_0) in the concentration quenching region, the exponential decay rate (x_0) to the Tb^{3+}related emission without the presence of Yb codoping was of 0.81, whereas with Yb codoping the value was reduced to 0.46 indicating a faster decay of Tb^{3+} related intensity. This result evidences the interaction of Tb^{3+} and Yb^{3+} ions and the occurrence of nonradiative energy transfers that are detrimental for the Tb^{3+} related emission.

In contrast to the Tb-related emission in the codoped sample, whose light decay exponentially with increasing concentration, the Yb-related emission intensity increases linearly and yet no quenching is observed up to 4 - 5 at.% of Yb. However, the integrated PL intensity related to Yb^{3+} increases linearly not only in the codoped AlO_xN_y:H matrix but also in the Yb^{3+} singly doped matrix. Since no concentration for a maximum intensity has been reached during thin film deposition, the present study can not indicate the critical Yb concentration at which luminescence quenches. Besides this, the intensity of Yb^{3+} related emission in the codoped sample is appreciably stronger, approximately 2 times, than the intensity of Yb^{3+} related emission in the singly doped sample. Notice that in the codoped sample the improved intensity of Yb^{3+} related emission, is connected with a strongly reduced intensity of Tb^{3+} related emission. This behavior may suggest the boost of energy transfer processes from the Tb^{3+} ion to Yb^{3+} ion, enhancing the Yb^{3+} light intensity emission at the expense of total quenching of Tb^{3+} related emission intensity.

The integrated PL intensities presented in Figure 4.18 corresponds to thin film areas where the matrix is maintained at a constant O:N ratio although the RE concentration varies. In the singly doped matrix, there is just one type of RE ion, and therefore the reported PL intensity depends only on its respective RE concentration. However, in the codoped matrix there are two RE ion concentrations and the overall concentration increases. For this reason, Figure 4.19 plots the integrated PL intensity versus dopant concentration maintaining constant the concentration of one of both types

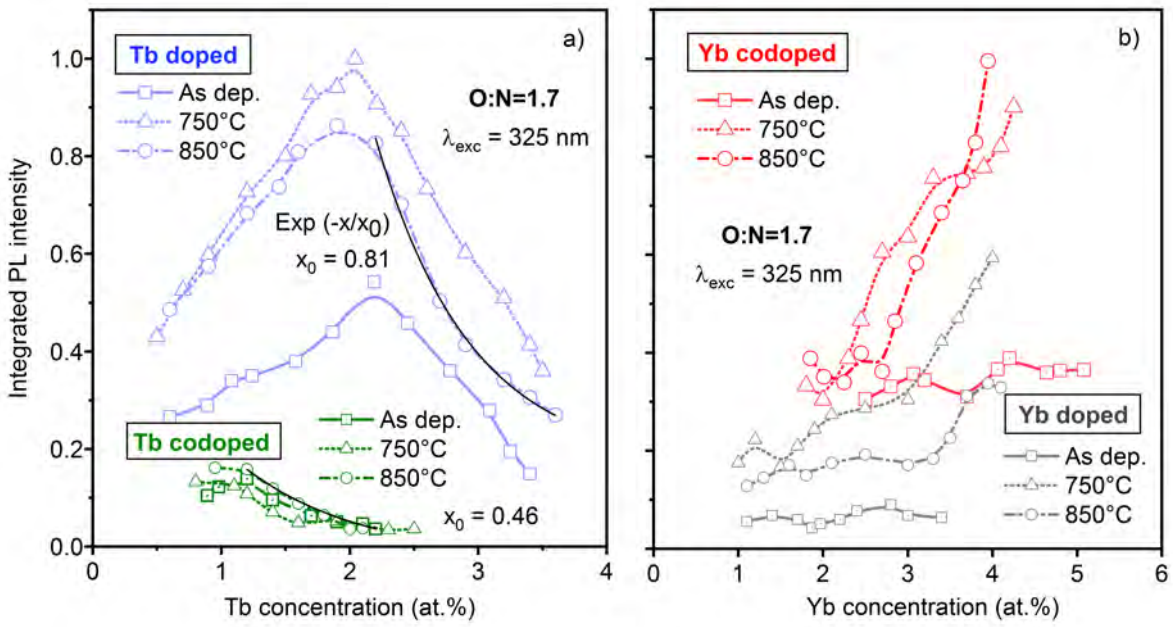

Figure 4.18: Normalized integrated PL intensity of (a) Tb related emission versus Tb concentration and (b) Yb related emission versus Yb concentration of the corresponding of singly doped and codoped AlO_xN_y:H matrix with an O:N ratio of 1.7. The thicknesses of Tb doped, Yb doped and Tb/Yb codoped thin films are 299.2 nm, 309.5 nm and 381.2 nm, respectively. The solid lines are simple exponential decay fits with decay rates x_0 of the integrated PL intensity of Tb related emissions after thermal treatment at 850°C.

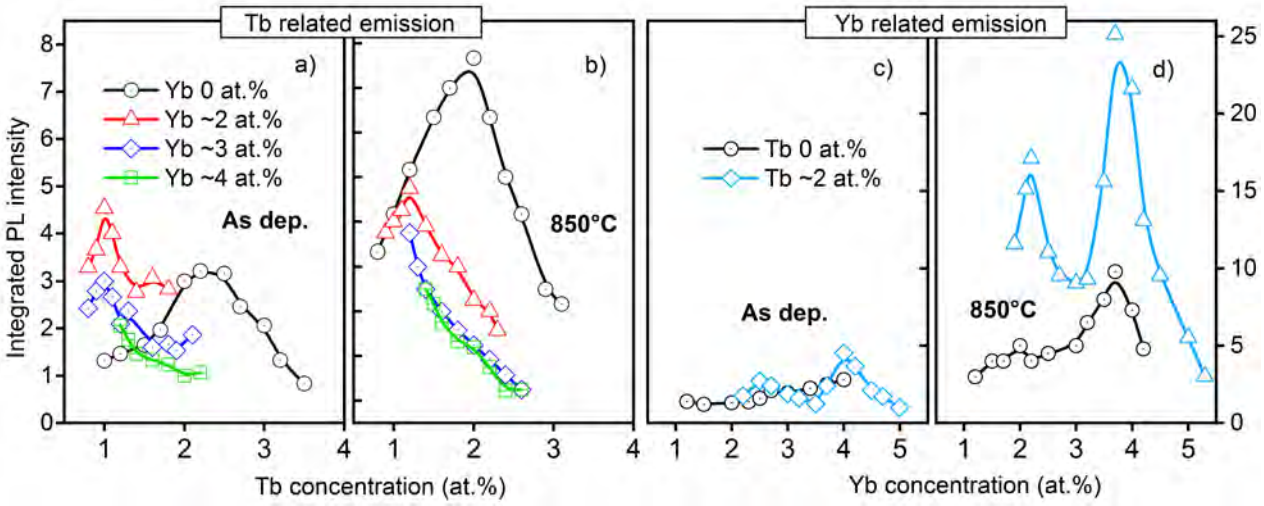

Figure 4.19: Integrated PL intensity versus concentration of Tb related emission in the AlO_xN_y:H matrix in (a) as deposited state and (b) after annealing at 850°C, for different Yb concentrations and without Yb doping. Similarly, the Yb related emission in the AlO_xN_y:H matrix in (b) as deposited state and (b) after annealing at 850°C, for 2 at.% of Tb and withoutTb doping.

of RE ions. In order to distinguish the changes of integrated intensities, the original scale is shown. The Tb concentration quenching is shifted to lower Tb concentration (from ∼2 at.% to ∼1 at.%) by adding Yb ions in the matrix. The increase of Yb concentration does not accentuates the shift, instead it reduces the Tb^{3+} related intensity. Instead, the Tb^{3+} related intensity decreases with increasing Yb concentration. Without annealing treatment, the Yb emission intensity is almost the same in the codoped and the singly doped matrix. After annealing at 850°C, the effect of codoping is more accentuated. The highly enhanced Yb^{3+} related emission intensity has a peak around 4 at.% of Yb^{3+} ions with a Tb concentration around 2 at.%. This gives a relation of one Tb^{3+} ion for each pair of Yb^{3+} ions, which matches the Tb^{3+}/Yb^{3+} ratio required for a CET process.

It is well known that thermal treatments can activate RE ions that are not active for light emission. This activation is appreciated in the singly doped and codoped Yb^{3+} related emission intensity, and the singly doped Tb^{3+} emission intensity depicted in Figure 4.18. The mechanisms behind this activation is controversy discussed [23]. One possible explanation is the reduction of electronic defects upon annealing treatments which may reduce the nonradiative recombination centers and boost the light emission of RE ions. Another mechanism could be the improvement of the atomic environment surrounding the RE ion in the host. For instance, it has been suggested that RE activation can be promoted by an optimum coordination of the RE center with oxygen atoms [21], or by the modification of the local structure around the RE ion (symmetry of the RE site) [248, 22]. According to previous researches, the highest intensities for Tb^{3+} doped amorphous AlO_xN_y:H, AlN, SiOC:H and SiC [190, 22, 248, 267] thin films has been found at annealing temperatures between 400°C and 900°C. This behavior has also been reported in the case of Yb^{3+} doped amorphous AlO_xN_y:H and SiOC:H [267, 194] thin films. To simplify the large dataset to be treated in this study, this work focuses on the critical annealing temperatures of 650, 750 and 850°C.

Figure 4.20 shows the variation of the integrated intensity of Tb^{3+} and Yb^{3+} related emissions for similar stoichiometric samples ∼2 at.% Tb, ∼4 at.% Yb and O:N ratio around 2.0. The emission intensities of singly doped samples exhibits an increase of the light emission intensity with annealing temperature. The optical emission of Tb^{3+} doped AlO_xN_y:H and Yb^{3+} doped AlON layers present a maximum increment at 750°C before intensity decays. If both Tb^{3+} and Yb^{3+} ions are embedded in AlO_xN_y:H, the Yb^{3+} related emission increases monotonically up to 850°C, while the Tb^{3+} related emission remains almost constant. It is noteworthy that the enhanced RE related emission occurs simultaneously with the reduction of the undoped matrix related emission with increasing annealing temperature. This behavior is accompanied by the increase of the optical bandgap and the reduction of the Urbach energy in the undoped matrix. Since the Urbach energy is representative of the amount of electronic defects, this demonstrates that thermal annealing treatments clean out the defect related localized electronic states in the matrix gap which are responsible for the increase of sub-bandgap host emission intensity. In contrast, for a doping concentration of ∼1 at% Tb and ∼2 at.% Yb, the optical properties of the film has been significantly altered (see Figure 4.7), decreasing the bandgap and increasing the Urbach energy at higher annealing temperatures. This has been tentatively attributed to the formation of RE oxide clusters which lowers the bandgap and increases the degree of disorder

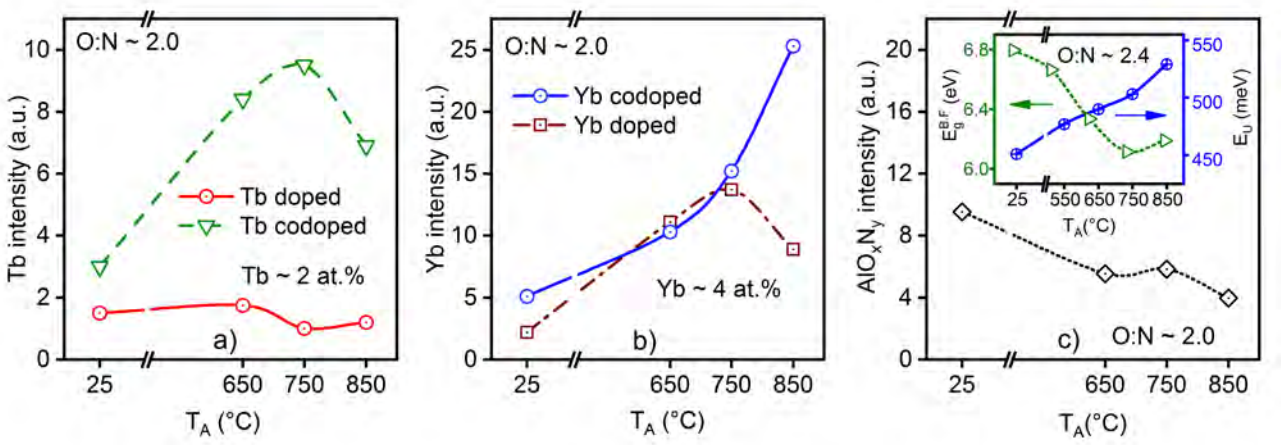

Figure 4.20: Effect of annealing temperature on the integrated PLintensity of (a) Tb related emission (b) Yb related emission and (c) undoped matrix emission. The inset shows the optical bandgap and Urbach energy of undoped AlO_xN_y:H versus annealing temperature.

degree in the film [243, 244, 245] .

Also, the increased Urbach energy of the RE doped matrix responds to the fact that the RE doping creates localized electronic states. However, these defects are luminescent centers whose gradual increment of concentration gives a greater emission intensity, but this is true up to some critical point after which the strong ion-ion interaction quenchs the luminescence. On the other hand, not every embedded RE ion is an active center for light emission. A way to improve the light intensity is to increase the amount of more active RE centers by thermally induced optical activation mechanisms. By comparing the intensity behavior of $\sim$ 2 at.% Tb and/or $\sim$ 4 at.% Yb doped samples with O:N ratio ˜ 2.0 with the variation of the optical properties of undoped and codoped matrix with annealing temperature, a superposition of two possible activation mechanisms can be noted. First, the reduction of localized electronic defects in the matrix, which means that less non-radiative paths are left inside the host. This effect is appreciated in the decrease of undoped matrix related emission with increasing annealing temperature. Second, there is the decrease of the optical bandgap, possibly due to RE oxides cluster formation and the formation of nanostructures that modifies the RE site influencing the activation degree.

The rate equation model derived in the previous section 2.2.3 allows the description of the curves shown in Figures 4.18 and 4.19, that is, processes involving excitation, radiative transitions, non-radiative transitions, ion-ion interactions and energy transfer. The expression in the numerator of equation 4.3 describes the linear regime of increasing radiative transitions which are exponentially quenched in the presence of several non-radiative transition pathways, represented with a sigmoidal function. Here, η_{RE} denotes the atomic concentration of the RE ion. P_{ET}, is the interaction probability between the RE centers. A and B are fitting constants that depend on the excitation probability, the Einstein coefficients and the non-radiative transition pathways.

$$I\left(\eta_{RE}\right) = \frac{A\eta_{RE}}{1 + B \times P_{ET}\left(\eta_{RE}\right)} \tag{4.3}$$

In the present study, the Tb^{3+} related curves of singly doped samples present both the enhance and the quench of the intensity emitted up to a maximum concentration and activation temperature and the quenching at higher Tb^{3+} concentrations. This situation does not occur for the Tb^{3+} related emission of codoped samples, where almost no increment of Tb^{3+} emission intensity is observed. The presence of Yb^{3+} codoping in the same matrix has suppressed the enhancement of Tb^{3+} intensity with increasing concentration. It has also caused an early quenching of Tb^{3+} luminescence, and the diminution of the intensities of Tb^{3+} related emission compared with those obtained in the singly Tb^{3+} doped film. Furthermore, this strong decay of Tb^{3+} intensity occurs simultaneously with the increment of Yb^{3+} related intensity, which is higher than the Yb^{3+} intensity obatined fron the Yb^{3+} singly doped film. This behavior strongly suggest the occurrence of energy transfer processes from Tb^{3+} to Yb^{3+} in favor of higher Yb^{3+} emission intensity in the Tb/Yb codoped AlO_xN_y:H matrix.

After the thermal annealing treatments, the integrated PL curves shown in Figure 4.18 exhibits an increasing intensity with temperature. In the Yb^{3+} related emission no falling intensity is observed with increasing Yb concentration up to 4 at.% . In this regime of low concentration, the inter ionic interactions are found to be negligibly small because the RE ions are separated by a large distance, therefore the linear increment of Yb^{3+} related intensity is mainly driven by the term $A\eta_{RE}$. The slope A is representative of the RE activation degree and directly proportional to the fraction of thermally activated ions [23]. Consequently, a steeper slope with annealing temperature means that the amount of optically active RE ions has increased. For the sake of simplicity, the slope A can be calculated using a direct linear fit in the low concentration region. The curves are fitted using $I_{PL} \propto M_A\eta_{RE}$, and the corresponding slope M_A versus annealing temperature are shown in figure 4.21. The advantage of using M_A instead of A relies on the smaller error that M_A exhibits due to the simplicity of the linear equation, which does not require a large number of fitting points and a large linear region, compared to the more complicated equation 4.3 [23].

Figure 4.22 depicts the Arrhenius plot of the slopes M_A for the different annealing temperatures. From the slope of the Arrhenius plot, an activation energy E_A associated to the thermal activation process can be found. Thermal treatments cause morphological changes of the local environment around the RE ion, which influences on the optical activity of the RE center by enhancing or quenching the light emitted. The thermal activation of RE centers is typically associated to the reordering of atoms in the surrounding of the RE ions, thus allowing a sufficient low symmetry to enhance the electronic transition probability for light emission. Beside the rearrangements of atoms, annealing treatments can also induce RE clustering [268, 257] and formation of nanocrystals as it has been shown in AlN [248] and Si based hosts [268]. This effect has an impact on the energy transfer mechanisms from the host to the RE ions. Particularly, nanocrystals could work as sensitizers, whilst

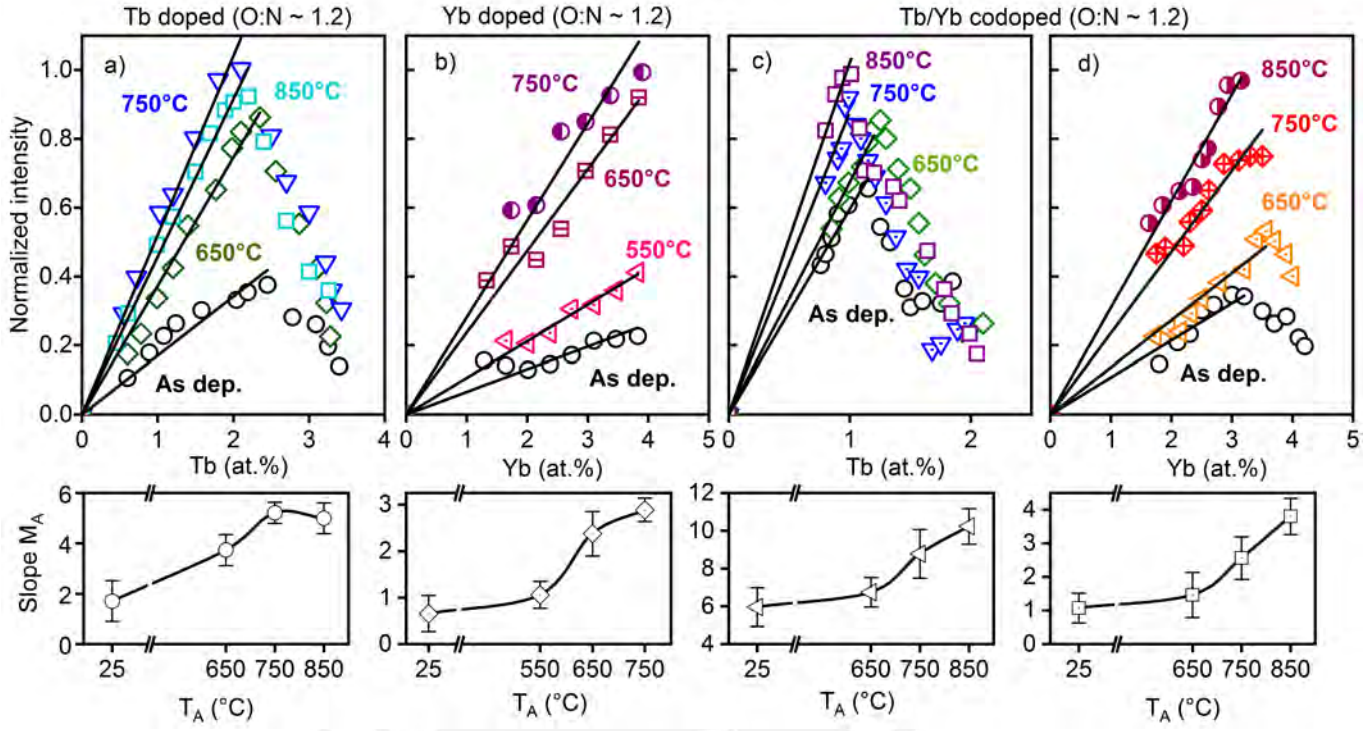

Figure 4.21: Integrated PL intensity of (a) Tb doped, (b) Yb doped, (c) Tb related of codoped and (d) Yb related of codoped AlO_xN_y:H films (O:N = 1.2) for different annealing temperatures. The solid lines are linear fits and the graph below corresponds to the slope M_A versus annealing temperature T_A.

the RE clustering may have a key role on the light emission yield [268]. The energy required to form such systems depends on the host. For instance, the density of defects mainly represented by dangling bonds in the amorphous AlO_xN_y:H matrix are expected to be modified, or more importantly, reduced after each annealing step. It may occur through some structural ordering and/or diffusion of oxygen or nitrogen atoms in the amorphous matrix. This may possibly induce a considerable reduction of the number of non-radiative channels, and improve the RE emission intensity.

To explore the effect of oxygen concentration on the luminescent properties, the E_A values of each Tb^{3+} and Yb^{3+} related emission have been estimated for different O:N ratios in the AlO_xN_y:H matrix. Figure 4.23 (a) plots the E_A values as a function of the O:N ratios. The results, with respect to the Tb^{3+} singly doped AlO_xN_y:H films, indicate that to thermally activate the Tb^{3+} ion emission less energy is needed as the oxygen concentration increases in the host matrix. In fact, the curves of Tb^{3+} related intensity versus O:N ratio, depicted in Figure 4.23(b), shows that oxygen favors the occurrence of higher Tb^{3+} related emission intensities at high annealing temperature. The underlying mechanisms behind the evolution of the Tb photoluminescence, upon the temperature range from 650 to 850°C, can be tentatively attributed to the clusterization of Tb oxide systems or the formation of nanocrystals in the host matrix [268, 248]. The reduction of the energy bandgap of the Tb^{3+}/Yb^{3+} codoped AlO_xN_y:H film, with annealing temperature (see Figure 4.7), compared to the increment of the bandgap of the undoped AlO_xN_y:H film (see Figure 4.7), strengthens the idea that Tb oxide and/or Yb oxide clusterization is taking place at high temperatures [238, 237]. It is also possible that

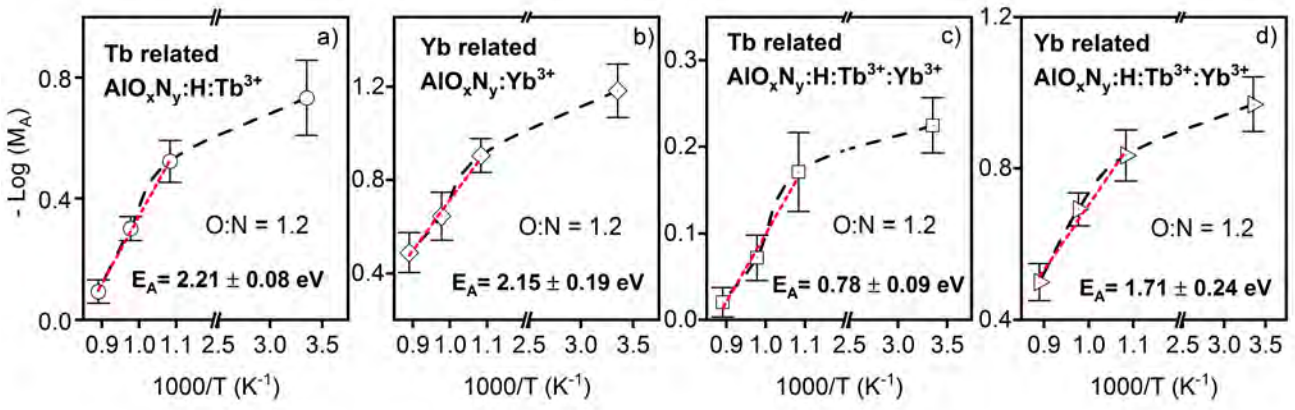

Figure 4.22: Arrhenius plot of the slopes M_A of (a) Tb doped , (b) Yb doped, (c) Tb related and (d) Yb related of codoped AlO_xN_y:H films for (O:N = 1.2), and their corresponding activation energy values.

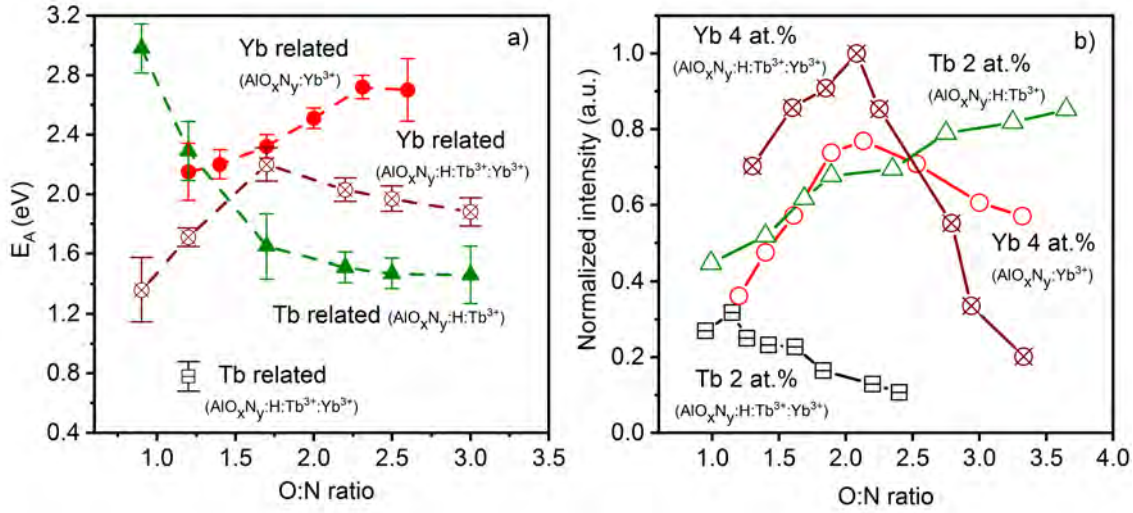

Figure 4.23: (a) Variation of the activation energy for films with different O:N ratios. (b) Normalized PL integrated intensity of Tb doped, Yb doped, Tb/Yb codoped AlO_xN_y:H films versus O:N ratios for samples annealed at 850°C.

Tb oxide systems are more likely to occur than Yb oxides. Note that oxidation processes are more easily started in those parts of the film library with high Tb content as shown in figure 4.16.

Maqbool [269] and Caldwell [270] showed that thermal activation, the oxygen effect, and the co-dopants are the key factors for better efficiency and enhanced luminescence from rare earth ions. E_A can be used to evaluate the difficulty of RE activation in the matrix. In the case of Yb^{3+} related emission from the Tb^{3+}/Yb^{3+} codoped AlO_xN_y:H film, the results presented in figure 4.23 (a) show an E_A that first increases and then decreases with the increase of O:N ratio. According to the result, the addition of oxygen increases the difficulty of Yb^{3+} activation up to an O:N < 2. However, with the further increment of oxygen (O:N >2), the activation of Yb^{3+} becomes easier. This is not the case of Yb^{3+} singly doped AlO_xN_y:H film, for which the E_A monotonically increases with O:N ratio. Therefore, if the oxygen concentration increases in the Yb^{3+} doped film, more energy is required to thermally activate Yb ions. Note that the average E_A of Yb emission in the Tb/Yb codoped sample

is higher than that obtained in Yb^{3+} singly doped sample. Moreover, due to the direct quench of Tb^{3+} related emission in the case of Tb^{3+}/Yb^{3+} codoped AlO_xN_y:H films, most E_A values could not be calculated. In fact, the linear fit in the activation region of Tb^{3+} intensity was only possible for an O:N ratio of 1.2, with an obtained $E_A = 0.65\,eV$ obtained. This evidence suggest that Tb acts as an efficient luminescence sensitizer of Yb^{3+} in the codoped AlO_xN_y:H films. Thus, the Tb concentration and the different O:N ratios in the Tb^{3+}/Yb^{3+} codoped AlO_xN_y: H matrix are the different kinetic parameters that under thermal treatment conditions can optimize the DC luminescence and increase the emission intensity of Yb^{3+}.

If the thermal activation is a pure local effect or if it is mainly promoted by the diffusion of either nitrogen or oxygen atoms towards the RE ion, can be examined by comparing the E_A values calculated for the light emission with the ones that correspond to diffusion processes. In earlier works, the reported activation energies of oxygen diffusion in AlN and Al_2O_3 have values between 4.43 to 6.37 eV [271, 272, 273], and the activation energy of nitrogen diffusion in AlN is approximately 1.7 eV or less [274]. In this thesis, the E_A values for the luminescence obtained from the Arrhenius plot are lower than 2.8 eV for either Tb^{3+} and Yb^{3+} ions in singly doped and codoped AlO_xN_y:H films, with the lowest E_A value at 0.65 eV for the Tb^{3+} related emission of Tb^{3+}/Yb^{3+} codoped film. The activation energies reported for diffusion of oxygen in AlN and Al_2O_3 hosts are higher than the E_A values for luminescence of Tb^{3+} and Yb^{3+} ions, but the activation energy for the diffusion of nitrogen are in the range of estimated E_A values for luminescence. Therefore, the activation is more likely attributed to a local phenomenon where the diffusion of nitrogen might play a more important role than oxygen diffusion. In addition, the E_A values ranging from 0.65 to 2.8 eV are higher than those reported for the optical phonons energy of the AlN matrix (from 0.04 eV to 0.102 eV in both polycrystalline and amorphous AlN [2]) and the Al_2O_3 matrix (0.05 eV for amorphous Al_2O_3[275] and 0.1 eV for single crystal Al_2O_3(0001) [276]), thus suggesting that the transition process might be multiphonon-assisted.

In summary, the thermal activation of Tb^{3+} doped, Yb^{3+} doped and Tb^{3+}/Yb^{3+} codoped amorphous AlO_xN_y:H was reported for different O:N ratios and Tb concentrations around 1 and 2 at.% revealing the close relation between the light emission intensity and the Urbach energy. The influence of thermal annealing treatments on the behavior of the concentration quenching curves was also reported for the singly doped and the codoped amorphous AlO_xN_y:H films. The slope M_A of the linear increase in the low concentration region was recovered to study the variation of the light emission intensity with thermal annealing treatments. The slope M_A was constituted as proportional to the RE activation degree, and depends on the changes in the microstructure of the host and the surrounding of the RE ion. Hence, for each Tb^{3+} and Yb^{3+} related emission in all samples, the activation energies were obtained from an Arrhenius plot of the slope M_A for different O:N ratios. The calculated activation energies for luminescence were compared with the reported activation energies for diffusion of oxygen and nitrogen atoms in AlN and Al_2O_3 matrix in order to shed some light on the possible mechanisms behind the enhanced intensities of Tb^{3+} and Yb^{3+} emission after annealing treatments. Finally, the decrease of Tb^{3+} related emission in favor of Yb^{3+} related emission in the Tb^{3+}/Yb^{3+} codoped matrix could be possibly attributed to an energy transfer probability from Tb^{3+} ions to Yb^{3+}

ions upon cooperative energy transfer from the $^5D_4$ energy level of Tb^{3+} to the $^2F_{5/2}$ level of Yb^{3+}, however this behavior requires additional confirmation.

4.4 Conclusions

In this chapter it was presented the combinatorial study of the luminescence features and the optical properties of amorphous AlO_xN_y:H thin film libraries doped with Tb^{3+}, Yb^{3+}, and both Tb^{3+}/Yb^{3+}. Using co-deposition radio frequency magnetron sputtering, thickness-gradient film libraries were prepared on large Si (100) substrates. The combinatorial samples have not only greatly speeded up the deposition process, but also allowed the high-throughput characterizations to measure the samples. After deposition, the films were submitted to cumulative thermal treatments up to 850°C with the purpose to investigate the RE thermal activation process and the effect of annealing temperature on the light emission intensity. The concentration quenching effect of Tb^{3+} and Yb^{3+} codoped AlO_xN_y:H has been examined upon different annealing temperatures. Its behavior was compared with those obtained in the case of Tb^{3+} and Yb^{3+} singly doped samples, with the aim to discriminate the effect of the Tb codoping in the activation of Yb^{3+} related light emission intensity due to possible cooperative energy transfer mechanisms.

The optical characteristics were investigated by means of UV-VIS spectroscopy. For this purpose, undoped a- AlO_xN_y:H and Tb^{3+}/Yb^{3+} codoped a- AlO_xN_y:H films have been grown on fused silica substrates and their transmittance curves have been measured. Due to the amorphous state of the films before and after thermal treatments, the Tauc-model and the band fluctuation model have been applied to calculate the optical bandgap and the Urbach energy from the optical absorption coefficient. The annealing treatments used to activate the Tb^{3+} and Yb^{3+} ions have an impact on the host properties, and thus on the localized band tail states, which is reflected in the energy gap and the Urbach energy. This fact is shown for the case of a- AlO_xN_y:H host in which the bandgap energy increases and the Urbach energy decreases with the annealing temperature. This behavior shows a reduction of the disorder, represented in the Urbach energy parameter, while the strong increase of the oxygen content has contributed to the increase of the bandgap energy. When embedding Tb^{3+} and Yb^{3+}into the host matrix, lower bandgap energies and higher Urbach energies have been obtained in as deposited state samples. The addition of luminescent impurities increases the disorder of the amorphous matrix and creates more intermediate energy levels which lead to a more narrow optical bandgap. A further reduction of the bandgap is observed with annealing temperature which can be attributed to the formation of Tb and/or Yb oxide clusters. Although the amorphous state of the films has been demonstrated by XRD experiments before and after thermal treatments, the nanocrystalline clusterization around the RE ion is yet feasible and may explain optical absorption behavior.

With the aim to investigate the cooperative energy transfer between Tb^{3+} and Yb^{3+} in the codoped AlO_xN_y:H host, the rare earth thermal activation and the concentration quenching have been studied by means of EDX analysis and PL measurements. For a better understanding of the process the optical

activation of the luminescent centers was examined in two distinct types of samples: the singly doped and the codoped host matrix. In both samples the annealing process leads to the conclusion that increasing annealing temperatures up to 850°C leads to higher RE related emission intensity while the undoped AlO_xN_y:H host related emission drops. This behavior not only obeys the increase of luminescence centers by activating more Tb^{3+} and Yb^{3+} ions in the host matrix, but the reduction of non radiative recombination paths which enhances the RE luminescence at the expense of host related emission by energy migration between the RE ions and the host matrix, an indirect excitation. The effect of thermal annealing treatments regarding the behavior similar to the concentration quenching has been evaluated. The concentration quenching related to Tb^{3+} emission in the Tb^{3+} singly doped sample behaves completely different than in the Tb^{3+}/Yb^{3+} codoped sample. In the former, the integrated light emission intensity is 5 times higher and the quenching starts at Tb concentrations around 2 at.%. In the latter the intensity quenches much earlier around 1 at.% and almost no linear increase of light emission is observed in the low Tb concentration regime. Whilst the Tb^{3+} related emission diminishes in the presence of Yb codoping, the Yb^{3+} PL emission was found to have an almost 2 times higher integrated emission intensity in the Tb^{3+}/Yb^{3+} codoped AlO_xN_y:H sample than in the Yb singly doped layer. These facts suggest a possible cooperative energy transfer from one excited Tb^{3+}ion to two nearby active Yb^{3+}ions. Also, the codoped samples with Tb concentrations around 2 at.% showed that the highest Yb^{3+} related intensity occurred for an Yb concentration around 4 at.%. This concentration ratio (Tb:Yb $\sim$ 1/2) is similar to that required for the cooperative energy transfer from one Tb^{3+} ion to two Yb^{3+} ions.

Along with the increment of the RE related emission intensity, EDX analyses of the thin film library showed an evolution of the O:N ratio with annealing temperature and an overall increase of oxygen concentration. This result shed some light on the thermal activation process and the impact of oxygen content in the energy transfer from the host to the RE ions, mediated by intrinsic defect states in the bandgap. Although the annealing temperature activates the RE ions, the further increase in oxygen diminishes the RE emission, except in the case of singly doped Tb^{3+} samples. A simple linear fit was used to describe the increasing intensity in the low RE concentration regime, and to obtain the slope M_A parameter related to the RE activation degree. From the Arrhenius plot of the slopes M_A, the thermal activation energy E_A related to the light emission was calculated. The E_A interpretations are typically twofold: the reordering of atoms in the surrounding of the RE ions with sufficient low symmetry to enhance the optical transitions, and the electronic enhancement of the material reducing the number of possible non radiative pathways intensity of light emitted.

Since the E_A values are below the required for oxygen diffusion, the RE activation can be tentatively attributed to the diffusion of nitrogen atoms, the reordering of the local structure and/or the formation of host-related sensitizer-activator systems that may enhance the excitation rate. However, these processes are sensitive to the oxygen content. The E_A values, calculated for Yb^{3+} in the Tb^{3+}/Yb^{3+} codoped a- AlO_xN_y:H, first increases from 1.4 eV to 2.2 eV and then decreases from 2.2 eV to 1.9 eV with the increase of O:N ratio. In contrast, the E_A values of Yb^{3+} doped a- AlO_xN_y increases monotonically from 2.1 eV to 2.7 eV, and the average E_A of Yb^{3+} singly doped film is higher than in

the Tb^{3+}/Yb^{3+} codoped film. This result can be a reference for the heat treatment and the O:N ratio to improve down conversion luminescence of Tb^{3+}/Yb^{3+} codoped a- AlO_xN_y:H in the future. Finally, this work reports an optimal emission intensity of Yb^{3+} in the case of Tb^{3+}/Yb^{3+} codoped film at 850°C, Yb concentration $\sim$ 4 at.%, Tb concentration $\sim$ 2 at.% and O:N $\sim$ 1.7. From the evolution of Yb^{3+} related PL integrated intensity, the higher Yb^{3+} related emission in the codoped sample compared to the singly doped sample, can be tentatively attributed to cooperative down conversion processes.

Chapter 5

Characterization of Tb^{3+} doped AlN thin films for electroluminescent devices

5.1 Introduction

Electroluminescence (EL) comprises the production of light by an electric field. This phenomenon is widely applied in display devices, and its categories are twofold: low field devices which are known as light emitting diodes (LEDs) and high field devices which are better represented by the thin film electroluminescent (TFEL) devices. In LEDs the light is generated by electron-hole pair recombination at p-n junction, while in TFEL devices the impact of the high energy electrons excites the luminescent centers in the host material, and generates an EL emission when the luminescent center relax from the excited state [277]. Also, LEDs are essentially low impedance, high current devices and are made from relatively expensive single crystal layers of semiconductor materials. For large area displays, these factors are the major drawbacks of LEDs. The low impedance and high current causes difficulties in the driving circuitry of complex displays with great size since it shall supply many tens of amperes of current with switching speeds of ∼100 μs or less.

Considering the high cost of production and material for large area displays using LEDs, the pursuit of alternative forms of active displays that are better suited to large area formats is necessary. The TFEL devices are a good choice to fulfil the requirements on the driving circuitry by ensuring a better proportion between the current and voltage. In fact, the TFEL devices have a solid position in the flat panel display market where their properties and advantages are appreciated. With the suitable materials combination of the deposited layers electroluminescent devices can have a high impact on the optical quality of wide screen applications, especially when it comes to color brilliance to the very specific optical spectrum emitted by rear earth doped materials. Since the first TFEL structure based on zinc sulfide doped with manganese (ZnS:Mn) which was fabricated by Russ and Kennedy in the late 1950's [278], continuous efforts have beed made in the progress of EL technology. For example, considerable work has been done mainly on GaN doped with a variety of RE elements to observe strong visible room temperature EL emission [279]. In comparison, AlN has received much

less attention, although it is successfully in use as a buffer layer for the growth of GaN.

Currently, TFEL devices are further classified into AC driven and DC driven devices. In the former, the thin active element is sandwiched between thinner high dielectric insulating layers which are used to prevent the breakdown of the active layer due to high voltage applied. Although the passage of a DC through an insulator may cause breakdown voltage drift with time, the DC-TFEL device has potential advantages compared to their respective AC-TFEL counterparts due to the simplicity of the device structure and application. Both types of TFEL devices require the investigation of the conduction mechanisms to overcome the obstacles related to the ohmic or schottky like behavior of the electrical contact. The fundamental research has put a lot of effort in exploring new structures, new material and new process routes in order to reduce the driving forces and the degradation mechanisms in EL devices [280].

In previous works the green PL and CL emission of Tb^{3+} doped AlN layers have been demonstrated [190, 23, 246, 248]. However, few works reported EL emission from Tb^{3+}doped AlN based DC-TFEL [8] and AC-TFEL [281, 282] devices at room temperature. While in PL the electron hole pairs responsible for the light emission are photo excited by exposure to a sufficiently intense light source, in EL the electron hole pairs are produced by current injection through the application of bias voltage to electrical contacts on the AlN layer. Herein the correct choice of boundary layers are critical to improve the login behavior of the devices, especially regarding the energy input to obtain electroluminescence. For this, the charge carrier energy shall be transferred from the matrix to the Tb^{3+} dopants by direct impact excitation or by nearby electron-hole recombination. In order to optimize the energy transfer from the matrix to the luminescent centers, thermal treatments can be applied to enhance the AlN host around the Tb^{3+} ion (i.e. quench of non radiative relaxation pathways and rearrangement of the local structure around the ion).

Inspired by the above scenario, the purposes of this chapter are the production and characterization of Tb^{3+} doped polycrystalline AlN films and a viability study regarding their implementation as active layer materials in an AC-TFEL and DC-TFEL devices. The first part of this work comprises the study of the stoichiometry, structural and luminescent properties of the Tb doped AlN films prepared by DC reactive magnetron sputtering. During the second part of this work, DC-TFEL and AC-TFEL devices have been designed and produced using Tb^{3+} doped AlN as active layers. Although AlN is highly resistive ($\sim 10^7$ - 10^{13} Ωcm), it posseses outstanding physical properties such as wide bandgap (6.2 eV), high thermal conductivity, high melting temperature and reasonable match of the thermal expansion coefficient of AlN to a Si substrate. The latter factor results the implementation of a simple DC-TFEL device using a system of ITO/AlN:Tb^{3+} thin films deposited onto Si substrates. While in the AC-TFEL devices, the former factor ensues the use of dielectric AlN layers on the top and the bottom of the AlN:Tb^{3+} film with the aim to lower the driving voltage and enhance the electron-hole injection in the active layer.

With the aim to systematically investigate the influence of thermal treatments on the optical prop-

erties and Tb^{3+} related luminescence features, some Tb^{3+} doped AlN samples were prepared using in situ deposition annealing treatments, as well as post deposition treatment for a second set of samples. Additionally, the Tb^{3+} ions are subjected to a crystal field from the chemical environment of the AlN host, leading to several optical spectral properties that can be analyzed on the basis of the Judd-Ofelt (J-O) theory [35, 34]. Part of this chapter is devoted to the development and application of a modified J-O method to extract from the emission spectra of Tb^{3+} the J-O parameters. With them a quantitative measure for the influence of AlN host structure on the Tb^{3+} emission can be established. Here the radiative lifetimes or decay rates for each Tb^{3+} related transition were calculated, and compared with the decay times measured by time resolve spectroscopy. Finally, the luminescence quantum efficiencies were determined for samples treated with different annealing temperatures.

5.2 Experimental procedure

Tb doped AlN thin film deposition details

The experimental procedures for sputter deposition of Tb^{3+} doped AlN films and for fabrication of EL devices have been described in detail in section 3.1.1. Briefly, prior to the fabrication of the TFEL device structures, Tb^{3+} doped AlN thin films were grown onto 1cmx1cm p-type Si <100> substrates and sapphire substrates by dc reactive magnetron sputtering of an Al target with Tb flakes in mixed nitrogen (20 sccm) and argon atmosphere (80 sccm). The films were grown at room temperature and at in-situ annealing temperatures from 300°C to 600°C in steps of 100°C. The growth rate was approximately 0.46 nm/s and the total thickness of the films, as determined from the transmission UV-VIS spectrum of AlN:Tb^{3+} films, was around 100 - 200 nm. Also, to optimize the luminescence intensity of AlN:Tb^{3+} film deposited at room temperature, the samples were annealed using a rapid thermal process (RTP) for 5 min from 300°C to 900°C in steps of 100°C in a nitrogen atmosphere. In all samples, the Tb concentration in the films was set to be around 2 at.%, as determined by EDS analysis. The polycrystalline structure of the as deposited film was determined by XRD analysis.

Schematic drawings of the DC-TFEL and AC-TFEL device structures are depicted in figure 5.1. In general, a TFEL device consists of an active layer with electrodes. Typical transparent and metal electrodes used are indium thin oxide (ITO) and molybdenum (Mo). The former allows the light output from the device, and the metallic ones contribute with low resistivity, good adhesion to the large bandgap active layer and low cost. Although Al has lower cost than Mo, the advantage of Mo over Al is its high melting point of 2623°C, which opens the possibility of annealing at high temperatures to promote the optical emission intensity of the active layer. The active layer shall posseses a large bandgap for transparency in the visible region and UV. Also, semiconductor active layer materials are advantageous for a better match of the work functions between the active layers, the electrodes and/or the carrier transport layers.

Regarding the working principles, in the AC-driven device, when an electric field is applied through the electrodes, the electrons from the interface AlN/AlN:Tb^{3+} shall tunnel into the conduction band

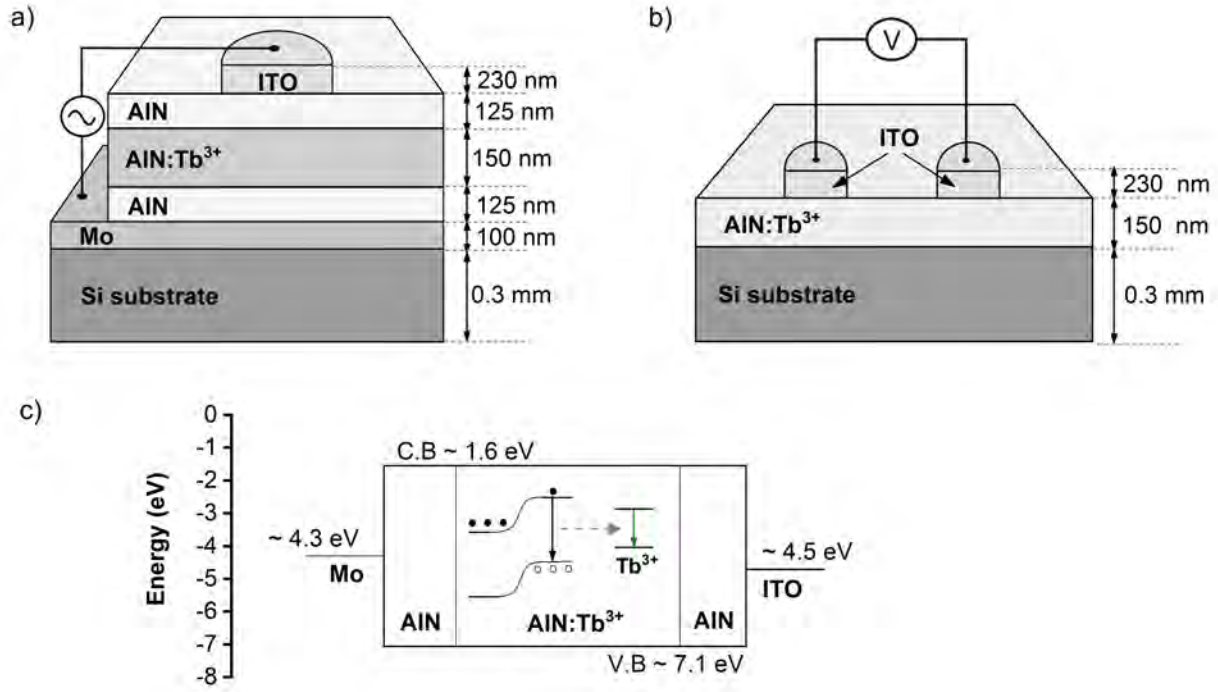

Figure 5.1: Cross-section schematic of the (a) a.c.-TFEL device structures, consisting of an AlN:Tb^{3+} film sandwiched between two dielectric AlN layers, the conducting Mo and ITO are the bottom and top electrodes, and the (b) DC-TFEL consisting of AlN:Tb^{3+}layer and transparent ITO electrodes on the top. (c) Energy band diagram of the AC-TFEL device detailing the working fuctions of the Mo [286], ITO [287] and the respective band energies of AlN [288].

of the active layer. The electric field accelerates the electrons across the active layer, creating electron hole pairs which can recombine radiatively through a Tb dopant impurity, or exciting the Tb centers by direct impact of hot carriers [277]. In the DC-driven device, a DC-current is applied through the electrodes, thus injecting holes/electrons from the anode/cathode electrode to the conduction/valence band of the active layer, respectively. Then, the electron hole pairs can recombine radiatively by exciting the Tb ions for light output. In some literature references, in DC-TFEL devices, carrier transport layers are used for assisting the injection of holes and electrons through the active layer. Such transport layers must have work function and band offsets that are closer to that of the respective active layer. Also, since the DC-TFEL devices operates at a lower voltage than AC-TFEL devices, the formers do not require insulating layers. For example, threshold voltages between 10 and 45 V have been reported for the ZnS:Mn based DC-TFEL device [283, 284, 285], and around 30 V for the AlN:Tb^{3+} based TFEL device [281]. However, the problem with the DC-TFEL devices is short lifetime caused by the overheating from excess current. To avoid this problem, a resistive layer can be used but at expenses of raising the threshold voltage to about 100 V.

Due to higher voltages and lower current operation of AC-TFEL devices, the active layer is in the form of a sandwich between insulating layers to prevent the direct flow of electrons from the electrode/active layer interface. Moreover, due to the capacitive characteristics of the device, the insulating dielectric layers can ensure the uniform distribution of the electric field across the active

layer and lower the required external driving voltage for light generation and improve the breakdown voltage. In fact in AC-TFEL devices, before the breakdown of voltage, the charge is uniformly distributed across each layer and if the voltage drops across each layer, the operating voltage lowers. The capacitive characteristic can be increased not only using a higher dielectric constant insulator but also by thickness reduction, which will reduce even more the voltage drop across the layers and the resultant operating voltage. Nonetheless, the reduction of the thickness may cause the undesired effect of higher density of pinhole defects which effectively might form a short circuit across the layer. For an AC-TFEL device, the maximum applied voltage is determined by the electrical insulating strength of the most dielectric layer. The turn-on voltage for light emission will occur when the active layer is exposed to an electrical field beyond its electrical breakdown, thus allowing current flow.

Fabrication of AC- and DC-TFEL device structures

The AC-TFEL devices, the Tb^{3+} doped active layers were deposited onto 1cmx1cm p-type Si <100> substrates coated with a layer of molybdenum (Mo), $\sim$ 100 nm thick, which served as the bottom metallic electrode. Then, a layer of aluminum nitride (AlN), $\sim$ 125 nm thick, was grown on both sides of the active layer to prevent breakdown. The AlN:Tb^{3+} layers were deposited by controlling the sputtering parameters such that thicknesses between 150 and 200 nm were obtained. To complete the AC-TFEL device structure, ITO dots, $\sim$230 nm thick, were deposited using a patterning mask on the top of the AlN layer. All electrode layers were deposited by using dc magnetron sputtering chamber depicted in Figure 3.2. The choice of the AlN semiconductor as the insulator layer was made not only to prevent the breakdown of the active layer due to the high voltage applied (i.e. for AlN:Er^{3+} and AlON:Tb^{3+} are around 70 V and 170 V respectively under frequency of 1 MHz [289, 6]), but also to reduce the mismatch of work functions and band offset with respect to the active layer (AlN) host. Its wide bandgap and relatively high resistivity has been reported to withstand high electric field of around 100 V/m without electric breakdown [289].

The fabrication of the DC-TFEL devices was done in the following form: (1) Tb^{3+} doped AlN films were deposited onto 1 cm x 1 cm p-type Si <100> substrates with a thickness around 150 nm, and (2) to complete the device structure, indium thin oxide (ITO) dots of $\sim$230 nm thick, which served as the transparent electrode, were deposited by DC magnetron sputtering. The choice of ITO as both the emitting and ground contact was made for reasons of practical convenience: its use in both electrodes enabled for single mask device patterning. It offers good transparency in the visible region and its conductivity is nearly independent of temperature. In fact, ITO has been reported a transmission between 90 and 95% for green light [290, 291]. But, since AlN:Tb^{3+} is basically semi-insulating, the ITO/AlN:Tb^{3+} system on Si forms a schottky diode and when a voltage is applied to the contacts, the charge would flows through the AlN film, and perhaps also through the semiconducting substrate.

Morphology and composition characterization

Scanning electron microscopy (SEM) and electron dispersive X-ray spectroscopy (EDS) were used a SEM Hitachi S4800 with secondary electron detector at an acceleration voltage of 20 kV for imaging and 4.5 kV for spectroscopy. All micrographs and measurements were performed at 0° tilt with

a normal incidence of the electron beam. EDS signal was collected during 100 seconds and the low voltage prevented from further penetration to the silicon substrate. The atomic force microscopy measurements were done using a Dimension Icon AFM device from Bruker Co. Billerica. All of the AFM images were obtained at room temperature with a ScanAsyst air cantilever probe in a peak force tapping mode with a set point value of 0.2 V, scan size of 2 x 2 μm, scan angle 0° and scan speed of 1 Hz. The fast scan direction in all images was set to horizontal and the scan was from the top to the bottom. The images were post-edited by a third-order polynomial flattening procedure by Nanoscope Analysis software (Bruker Co. Billerica) to remove tilt and curvature. For comparison purposes, the height scales were set at the same range.

Crystallographic structure characterization

The crystal structure was identified with a Theta-Theta X-ray diffractometer (XRD) D 5000 with a Goebel mirror in grazing incidence geometry (angle of incidence was 3°) with Cu Ka radiation (0.15418 nm). The operation voltage and current were 40 kV and 40 mA respectively. The small angle of incidence and the parallel beam characteristics are used to limit the incidence of the X-ray beam to the film surface, and therefore enhance the sensitivity to obtain a better signal and less interference from the substrate. The scanning angle 2ϑ varied in the range from 20 to 80 degrees. The step size was 0.020° and the time per step was 1.3 seconds. Qualitative analysis of the diffraction patterns were carried out using the EVA (Bruker) software for phase identification procedure.

Optical and luminescence characterization

Transmittance spectra were carried out at room temperature using a Varian Cary 5000 spectrometer. The transmission spectra were recorded in the spectral range of 190 to 1100 nm under normal incidence. For the characterization of the optical emission intensity of Tb^{3+} doped AlN films both cathodoluminescence (CL) and photoluminescence (PL) measurements were performed. The CL spectra were obtained using a FEI Quanta 650 SEM equipped with a parabolic mirror allowing for electrons to pass through. The CL signal collected by the mirror is focused on the entrance slit of a spectrometer Horiba H-CLUE-p. The emission spectra were recorded from 400 to 700 nm on an area of 100 μm x 100 μm, using a beam current with spot number 7 and an acceleration voltage of 10 kV. Also, room temperature PL spectra were measured in reflection geometry with a Renishaw inVia Reflex spectrometer system for Raman and PL spectroscopy. The visible emission of Tb^{3+} was recorded from 400 to 700 nm after excitation with a He-Cd laser at 325 nm wavelength. The laser power density at the sample was less than 16.6 $mW/\mu m^2$. Complementary PL lifetime measurements were done on the Tb doped AlN samples using a FluoTime 300, PicoQuant GmbH fluorescence lifetime spectrometer, using a Xe lamp as excitation source with 100 Hz repetition rate for 375 nm wavelength excitation.

Electrical transport measurements

For recording the current-voltage (I-V) curves of the prepared TFEL devices, a Keithley 2004 system source-meter was used as a current generator and for the voltage measurement. The source-meter is controlled by a Labview program. For the DC-TFEL device, the ITO contacts were connected to the positive electrode and to the negative electrodes. Whilst, for the AC-TFEL device, the ITO contact

was connected to the positive electrode and Mo contact to the negative. In all I-V measurements, the DC current from the source was applied between points 2 and 3, and the voltage is measured between the points 1 and 4. The curves are recorded by continuously sweeping from –20 mV to +20 mV and recording data points in 2 mV steps at a fixed 10 mA.

5.3 Results and discussion

This section shows the study of the composition, structural, morphological and luminescent properties of the Tb^{3+} doped AlN thin film. The time resolve pholuminescence was complemented with Judd-Ofelt analysis of the PL spectra measured, in order to calculate the radiative lifetime and quantum efficiency. The electrical properties and the luminescence characteristics of prepared AC-TFEL and DC-TFEL devices are also presented and studied througth I-V curves and PL measurements. However, no successful EL measurements were obtained from the devices produced yet. Throughout the chapter, the effect of the thermal treatments during film deposition and post film deposition is discussed. For this, the samples were heated at 300, 400, 500 and 600°C using in situ substrate heating and an RTA furnace in a nitrogen atmosphere.

Elemental composition analysis

To estimate the chemical composition of samples, EDS measurements on Tb^{3+} doped and non-doped AlN were done and the results are listed in Table 5.1. In the case of doped samples, it was obtained an almost constant 2 at. % of Tb. Although lower Tb concentrations around 1.0 - 1.5 at.% have been reported to cause the highest luminescent intensity [23, 178], the concentration obtained was low enough for a relatively high Tb emission intensity as shown in the PL and CL spectra. The low concentration is required to prevent concentration quenching effect which reduces the light emission intensity due to non-radiative Tb - Tb ion interactions. In the case of doped samples, the stoichiometry related only to the AlN_x matrix showed a presence of nearly 56 % of Al, 36 % of N and 5 % of O, which gives an Al/N ratio of 1:0.63 and x value of 0.64 in AlN_x. In the case of non-doped AlN, the observed stoichiometry (54 at.% of Al, 36% of N and 10% of O) showed a relation of Al:N = 1: 0.69 which gives an x value of 0.69 in AlN_x. In both the doped and non doped samples, the value of x is higher than 0.34, related to Al-rich composition layers, and closer to 0.74 for stoichiometric 1:1 compositions. The x value in AlN_x can be tuned by controlling the sputtering process parameters, but more importantly it can effectively control the work function of the material. In fact, a study on the AlN interfacial layer in a dual metal gate stack reported lower work function values ∼4.42 eV for the Al-rich AlN layer but, the work function increased to ∼4.89 eV as the composition moved closer towards stoichiometry [292].

A low quantity oxygen impurity was observed in all samples. But more importantly, the EDS analysis result revealed the reduction of oxygen content for samples deposited with in situ substrate heating. In fact, the high temperature can favor rapid and defect free crystal growth. A similar effect of substrate temperature on oxygen concentration and oxygen vacancy has been reported on sputtered NiO [293], ZnO [294] and ITO [295] thin films. In contrast, post deposition annealing in

	Sample	T (°C)	Tb (at.%)	Al (at.%)	N (at.%)	O (at.%)	O:N	x (N:Al)
RT	AlN	25	-	55	37	10	0.27	0.66
RT	AlN:Tb^{3+}	25	2	56	36	6	0.17	0.64
In situ	AlN:Tb^{3+}	300	2	56	37	5	0.14	0.66
		400	2	55	38	5	0.13	0.69
		500	2	55	38	5	0.13	0.69
		600	2	56	38	4	0.10	0.68
RTA	AlN:Tb^{3+}	300	2	55	37	6	0.16	0.67
		400	2	55	36	7	0.20	0.65
		500	2	54	37	7	0.19	0.69
		600	2	53	37	8	0.22	0.67

Table 5.1: Elemental composition for the non doped AlN grown at room temperature (RT) and the effect of in situ deposition substrate temperature and post annealing temperature on the stoichiometric composition of Tb^{3+} doped AlN thin films at different annealing temperatures. The O:N ratio and the Al:N are also included.

an RTA furnace using nitrogen atmosphere, has slightly increased the oxygen concentration from the as deposited state with increasing annealing temperature. This increment is better observed with the O:N ratio.

Structural and surface morphology properties

The crystal structure of the Tb^{3+} doped AlN films was identified to be polycrystalline wurtzite phase as shown in Figure 5.2. The thicknesses of the films under investigation were consistently around 150 nm. The analysis of XRD patterns of samples deposited at room temperature demonstrate a wurtzite phase structure which exhibited a $(10\bar{1}1)$ preferred orientation in as deposited state. After RTA treatments from 300 to 600°C the same preferred orientation have been maintained but an overall increase of the peaks intensity was observed with increasing annealing temperature due to possible thermal activation processes. When the substrate temperature was increased above 500°C, the crystalline planes changes slowly from $(10\bar{1}1)$ to (0002) with respect to the behavior observed in the RTA processing. The peak intensity showed also an increase with increasing substrate temperature. As shown in Figure 5.2 the substrate temperature has a profound influence on the preferred diffraction peaks of the AlN:Tb^{3+} films. However, the dependence of these preferred peaks on the substrate temperature exhibits no simple rule.

To understand the change observed in the XRD peaks of samples produced using in situ annealing, it is important to recall the crystallographic lattice unit of hexagonal wurtzite AlN. In this unit lattice, each Al atom is bonded with four N atoms forming a distorted tetrahedron as shown in Figure 5.3 a) [296]. There are two types of Al-N bonds. The first, denoted by B_1, has a length of 0.1885 nm and occurs in the plane perpendicular to the c-axis, where the Al-N bonds are equivalent with respect to the central Al atom. The second Al-N bond, denoted by B_2, is formed in the direction parallel to the c-axis, with a bond length of 0.1917 nm. Since the length of B_1 is shorter than B_2, the energy required for their formation is higher. According to the crystallographic planes in the hexagonal AlN

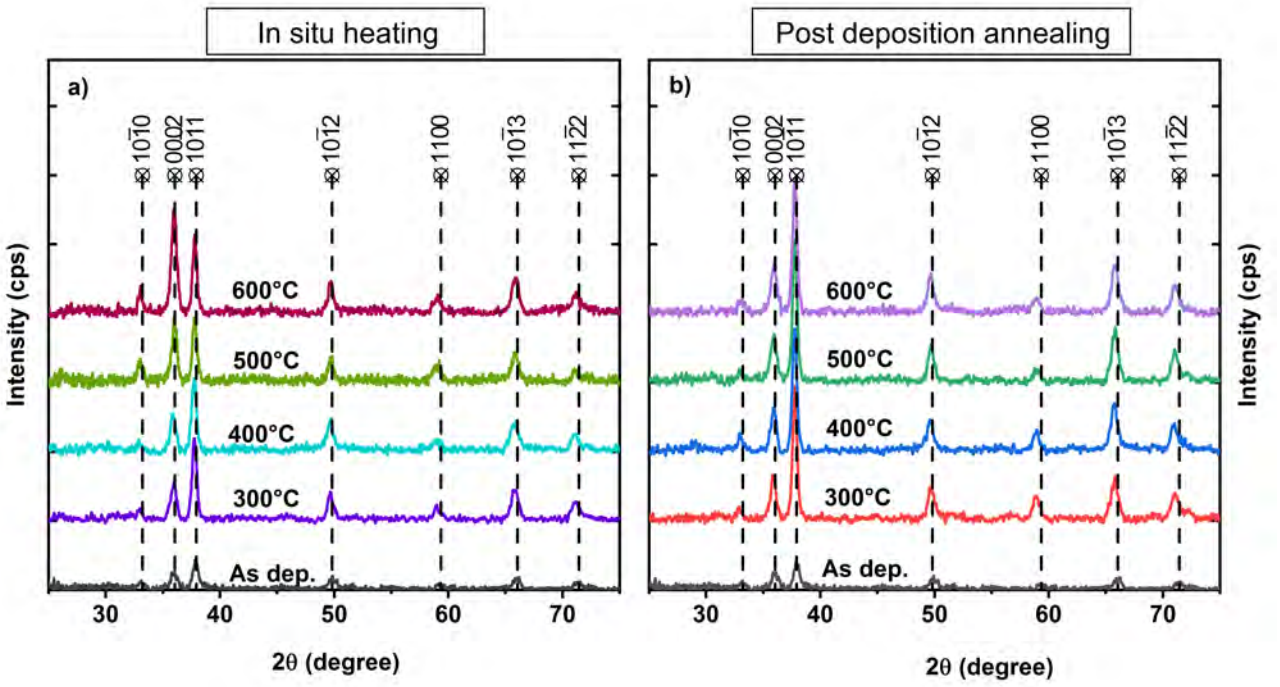

Figure 5.2: Grazing incidence X-ray diffraction pattern of AlN:Tb films prepared with in situ annealing at (a) various substrate temperatures and (b) after RTA process. The as deposited sample XRD pattern is shown for comparison. The hexagonal wurtzite structure of AlN corresponds to the Power Diffraction File (PDF) 25-3311. The cascade style has been used for better visualization of the peaks in each pattern.

lattice, the B_1 bond is only contained in the (0002) plane, while the B_2 bond is only contained in the $(10\bar{1}0)$ and $(10\bar{1}1)$ planes. Therefore, the (0002) plane has a higher formation energy compared to the $(10\bar{1}0)$ and $(10\bar{1}1)$ planes.

In the light of the above, the XRD patterns shown in Figure 5.2 can be understood as follows: in the non heated substrate the sputtered adatoms on the substrate did not have enough kinetic energy, and only a low formation of (0002) planes took place compared with the major presence of $(10\bar{1}1)$ planes. As the substrate temperature increases to 500°C, the thermal energy in the substrate give the adatoms enough surface mobility to form the closely packed (0002) crystallographic planes. With further increase in temperature up to 600°C, the (0002) plane has become the most prominent orientation in the AlN structure. Additionally, at substrate temperatures higher than 500°C an increase in the intensity of the $(10\bar{1}0)$ planes was evidenced. Thus demonstrating that also the high kinetic energy adatoms can rearrange to the second low energy plane $(10\bar{1}0)$.

Hence, the substrate temperature has a profound influence on the preferred orientation peaks of the AlN:Tb^{3+} films and therefore it can exert a strong effect on their optical and mechanical properties. For example, EDS has revealed that substrate temperature has reduced the oxygen content in the films. It is well established that the number of oxygen vacancies strongly depends on the substrate temperature, and its presence in the film composition may have an important effect on optical properties such as the energy bandgap and refractive index of the films. It has also been well established the

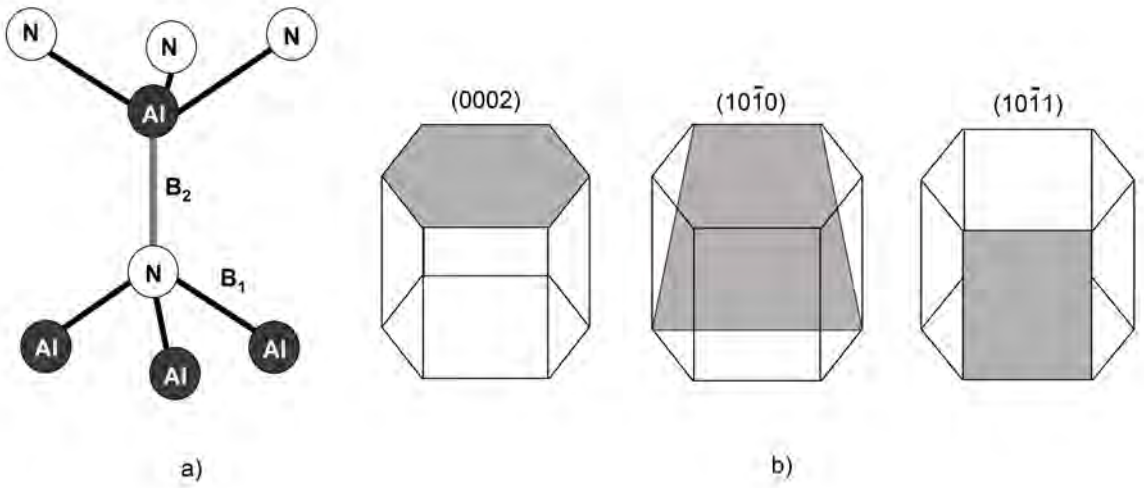

Figure 5.3: (a) Arrangement of Al-N bonds in the formed tetrahedron and (b) geometry of crystallographic planes for the (0002), (10$\bar{1}$0), (10$\bar{1}$1) in hexagonal wurtzite AlN lattice. [296]

surface roughness dependence on the substrate temperature, since at higher substrate temperature, the rearrangements of the adatoms could fill the gap between the columnar crystalline structures, thus smoothing the film surface.

The comparison of films surface quality is presented in Figure 5.4, where SEM micrographs of AlN:Tb^{3+} films grown at different substrate temperatures and subjected to post deposition annealing, are shown. The samples present a grainy morphology with an apparent surface quality, uniformity and smoothing of the films that is slightly enhanced with increasing temperature, as seen in Figures 5.4(a)-(e). In samples heated using an RTA process, the small grains in the clusters coalesced together to form bigger grains. Complementary, to quantify the effect of thermal treatments in the surface quality, the root mean square (RMS) roughness of AlN:Tb^{3+} was investigated in all samples via AFM measurements. The substrate temperature influence on the surface roughness of the AlN:Tb^{3+} film sample deposited at 300 and 600°C are shown in Figure 5.5, and calculated from the entire scanned region.

The RMS surface roughness of the deposited Tb^{3+} doped AlN films was plotted versus the substrate temperature in Figure 5.5(f). It is demonstrated that, generally, higher substrate temperature leads to lower surface roughness. The AlN:Tb^{3+} sample deposited without intentional heating presented larger RMS roughness of 3.3 nm, whereas the AlN:Tb^{3+} sample deposited at 300°C and 600°C have lower RMS roughness from 2.6 nm to 1.8 nm. Similarly, the AFM micrographs of samples annealed at 300°C and 600°C leads to RMS roughness from 2.3 nm to 1.9 nm respectively. This result confirms the surface quality and smoothing observed in SEM images for films subjected to both: post deposition annealing and in situ annealing with substrate temperature. Additionally, it was observed that film thickness influences the RMS roughness, which increased from 2.8 to 4.5 nm in as deposited samples, as shown in Figure 5.6. The reasons for the RMS roughness behavior with temperature could be attributed to the crystalline structure evolution process observed in Figure 5.2. Furthermore, surface

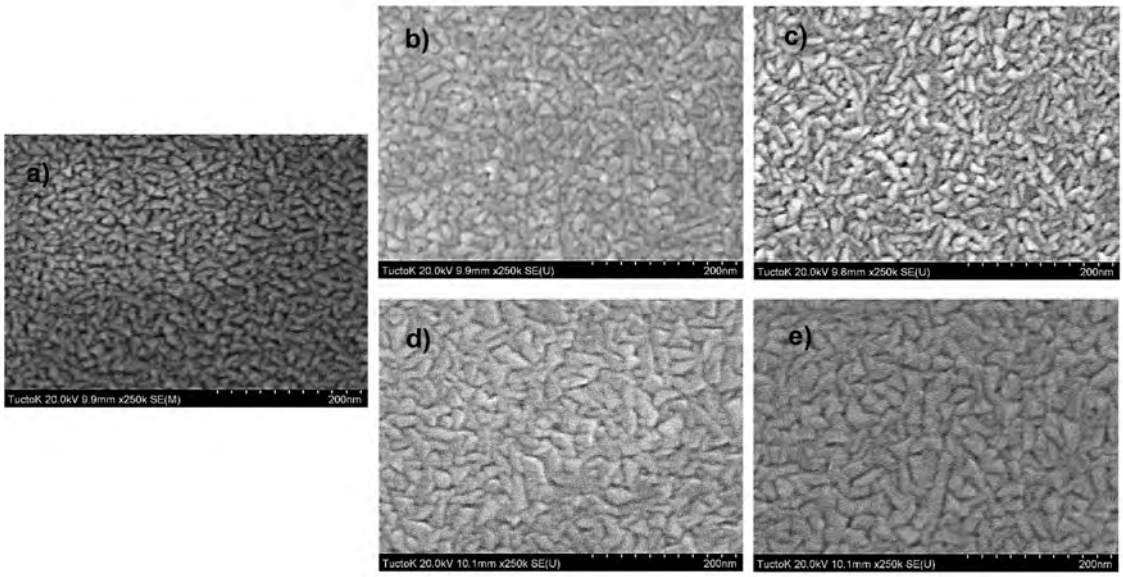

Figure 5.4: SEM images of AlN:Tb^{3+} films: (a) as deposited state without substrate heating, (b) grown at 300°C, (c) grown at 600°C, (d) annealed at 300°C and (e) annealed at 600°C. The images were taken at 250 k of magnification.

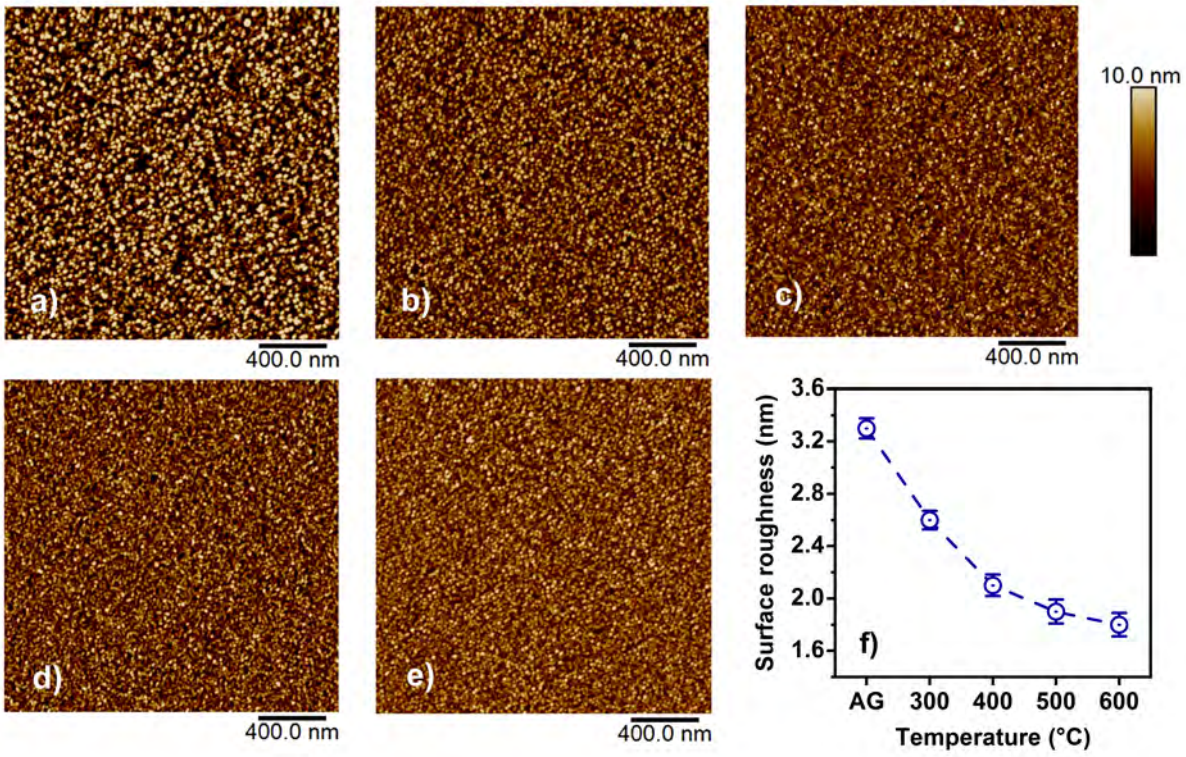

Figure 5.5: AFM images of AlN:Tb films consistently around 200 nm: (a) as deposited state, (b) deposited at 300 °C , (c) deposited at 600°C, (d) annealed at 300°C and (e) annealed at 600°C. (f) Dependence of AlN film surface roughness on substrate temperature (AG = as grown).

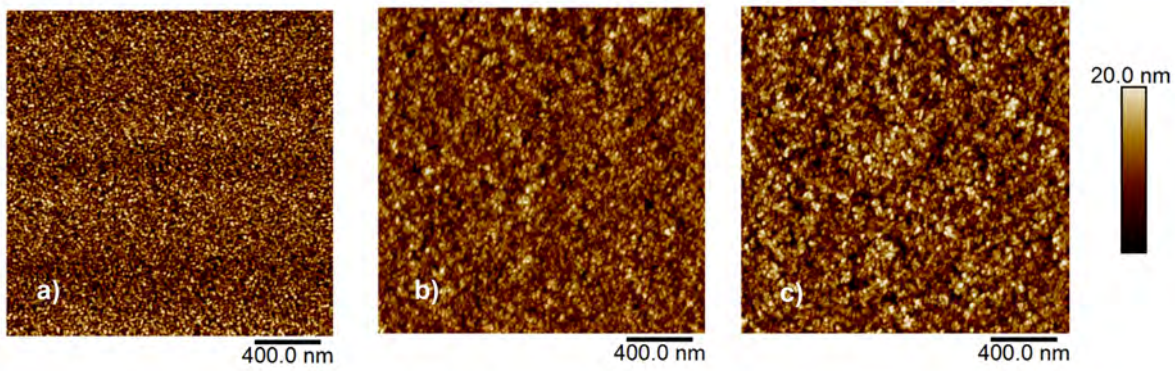

Figure 5.6: AFM micrographs of AlN:Tb^{3+} films deposited with different thicknesses on a silicon substrate: (a) ∼105 nm (RMS = 2.8 nm), (b) ∼150 nm (RMS = 3.3 nm), and (c) ∼200 nm (RMS = 4.5 nm).

roughness could also be one of the reasons for lower PL intensity from the samples deposited at lower substrate and post deposition annealing temperature.

Optical properties and light emission analysis

The transmittance spectra of the Tb^{3+} doped AlN thin films are depicted in Figure 5.7. In order to determine the film thickness and the optical properties of the films from the transmittance curves, a modified Swanepoel's method [217, 178] is used. By fitting the transmittance curves, the film index of refraction and the film absorption coefficient were calculated. Due to the polycrystalline structure of the samples, the optical bandgap E_g and the Urbach energy E_U are determined by plotting $(\alpha h\nu)^2$-versus photon energy $(h\nu)$, and fitting the curve with a band fluctuation (B.F) model for direct band gap materials, as depicted in Figure 5.8. For comparison the Tauc gap is determined by plotting the $(\alpha h\nu)^2$ as a function of the photon energy and performing a linear fit of the fundamental absorption region. The intercept of this linear fit with the energy axis is the Tauc-gap [75]. Additionally, E_U was extracted in our experiments from the low energy tail of the absorption spectrum for a range of temperatures, by plotting the natural logarithm of the absorption coefficient as a function of the photon energy. A detailed report of the optical properties can be found in Table 5.2.

The band gap values were calculated from the $(\alpha h\nu)^2$-plot using the B.F model and the conventional Tauc model as shown in Figure 5.8. Both types of calculated bandgaps have a relatively large difference between them, owning that their definition is model-dependent. However, the BF fit retrieves reliable higher bandgap energy values because the model include the Urbach tail and absorption edge regions for an accurate reproduction of the absorption coefficient. Here, the interest lies on the relative changes of the bandgap due to the the two types of thermal treatment applied.

In both applied thermal treatments, it is observed that band gap energy rises with increase in temperature (see inset graphs in Figure 5.8). The samples annealed with RTA present higher bandgap values. In contrast, the samples prepared using substrate heating show bandgap values closer to the reported wurtzite AlN direct bandgao of 6.12 eV [297, 298], which can be related to lower oxygen

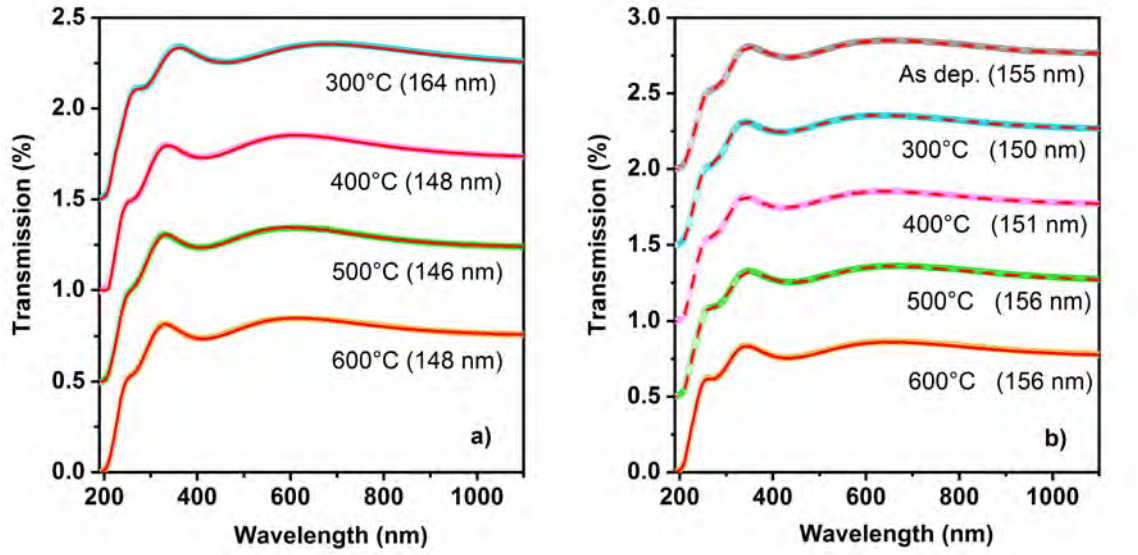

Figure 5.7: Measured transmittance spectra in the wavelength range 190 - 1100 nm of the Tb doped AlN samples grown on sapphire substrates: (a) with in situ annealing using substrate temperature during deposition, and (b) with post deposition RTA processing. The layers thicknesses are around 150 nm for all the samples.

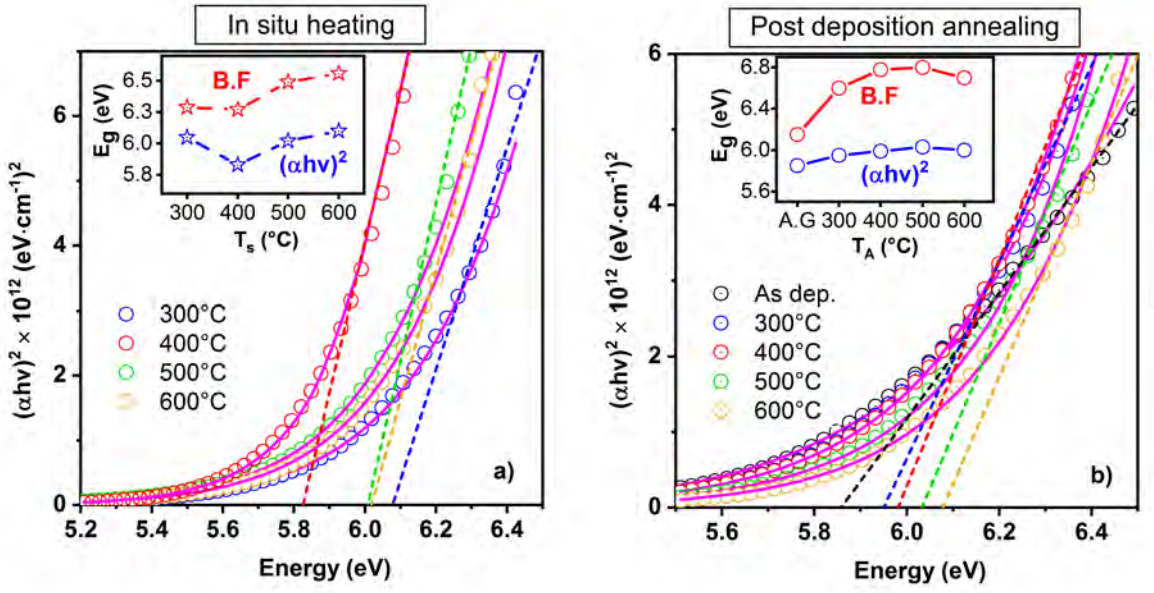

Figure 5.8: Plot of $(\alpha hv)^2$ versus photon energy hv to estimate the optical bandgap of Tb doped AlN films grown: (a) with in situ annealing using substrate temperature and (b) with post deposition RTA processing. The conventional Tauc linear fit (dashed lines) and the band fluctuatations model fit (solid lines) are shown. The inset graphs depict the variation of the optical bandgap versus the annealing temperatures.

AlN:Tb^{3+}		d (nm)	A_0	$A_1(10^4 nm^2)$	n (545 nm)	$E_g^{B.F}$(eV)	$E_U^{B.F}$(eV)	E_g^{Tauc}(eV)	E_U^{Log}(eV)
	As dep.	155.2	2.04±0.02	1.88± 0.23	2.04	6.1±0.2	478.4±0.2	5.7 ±0.1	564.9±0.2
RTA	300°C	150.5	2.04±0.03	1.86±0.17	2.04	6.6±0.3	485.8±0.2	5.8±0.2	549.4±0.2
	400°C	151.4	2.03±0.01	2.18±0.28	2.03	6.8±0.1	468.2±0.6	5.9±0.1	534.7±0.7
	500°C	156.2	2.07±0.01	1.39±0.42	2.07	6.8±0.2	452.2±1.0	6.0±0.1	542.9±1.0
	600°C	155.6	2.03±0.03	1.56±0.39	2.03	6.7±0.4	394.5±0.9	6.0±0.2	449.9±0.7
In situ	300°C	163.7	2.07±0.01	0.79±0.34	2.09	6.3±0.2	399.2±0.3	6.1±0.2	504.3±0.4
	400°C	148.1	2.10±0.02	1.65±0.29	2.16	6.2±0.1	379.1±0.3	5.8±0.1	458.7±0.9
	500°C	146.5	2.08±0.03	2.09±0.54	2.15	6.5±0.1	407.2±0.4	6.0±0.1	451.2±0.9
	600°C	148.7	2.05±0.03	1.99±0.25	2.11	6.5±0.2	415.1±0.4	6.1±0.2	494.3±1.1

Table 5.2: The film thickness d and the Cauchy fitting parameters $n(\lambda) = A_0 + A_1/\lambda^2$ obtained by a fit of the transmittance curves with eq.4.1 [219, 178], the index of refraction n at 545 nm for the main green emission of Tb ions, E_g and E_U values obtained after fitting procedures depicted in Figure 5.8. The reported errors for A_0 and A_1 are retrieved from the fits. Errors associated with the thickness are around 1 to 2 nm due to the employed fitting method, equations and additional film inhomogeneities [178].

content found in the composition. As the temperature is increased, the crystalline characteristics of the sample are boost, for example with the increase of XRD intensity peaks. This increase of structural organization in preferred orientation planes can lead to a reduction of localized defect levels and consequently increases the optical bandgap values. The Tauc plot data confirms that the bandgap energy of the film increases when the temperature is increased. At 600°C the Urbach energy of films treated with RTA decreases until it reaches a disorder equivalent to that obtained using substrate heating (see Table 5.2). This suggests that along with high temperature the film reaches a structure that allows to diminish the local fluctuations responsible for band tail states.

This work reports the observation of room temperature CL and PL spectra and PL decay times of Tb^{3+} doped AlN, to explore the suitability of this material for visible optoelectronic devices. It has been well established that the visible green and blue emission from both PL and CL, are a strong function of the Tb concentration. In general, all RE doped host material evidence a practical limit in RE concentration beyond which the light emission intensity starts to decrease. The RE solid solubility of the host material is the endmost doping limit, because if the concentration is higher than the solid solubility, it may cause the formation of second phase materials such as RE oxides and RE clusterization, which results in deterioration of the optical and electronic properties of the host material. Another doping limit is the concentration quenching effect on the RE luminescence intensity, which has been extensively studied in literature, and in particular an optimal 1.0 - 1.5 at.% Tb concentration has been reported for the enhancement of Tb^{3+} related light emission intensity in AlN thin films [178].

In order to assess the optimal Tb concentration, some sputtering deposition trials were done by varying the number of Tb flakes placed on the Al target. As a result, three different Tb concentrations of 2, 4 and 7 at.% were produced. Although the Tb concentration is slightly higher than the suggested

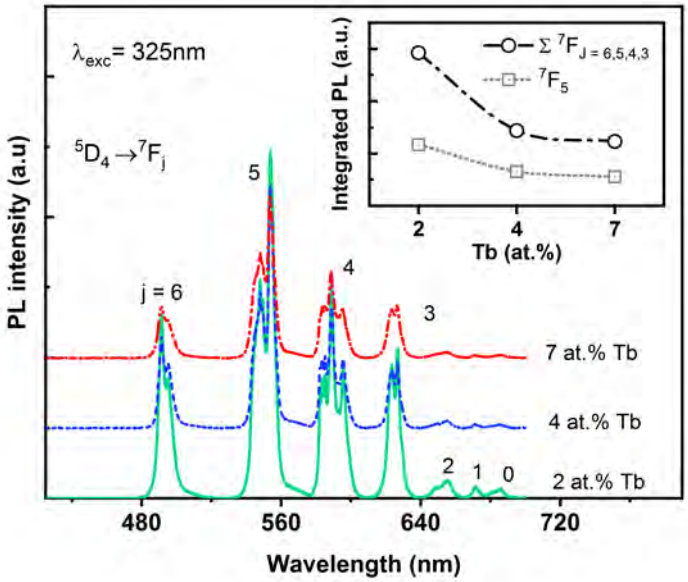

Figure 5.9: PL emission spectra of Tb^{3+} doped AlN thin films with various Tb concentrations. Inset shows comparison of main peak intensities $^7F_5$ and the sum of maximum peak intensities $^7F_{J\,=\,6,5,4,3}$ versus the Tb concentrations.

value of 1.0 - 1.5 at.% Tb [178], an evident enhancement of the PL intensity of Tb^{3+} doped AlN samples was observed at 2 at.% Tb, compared with the others 4 and 7 at.% Tb concentrations, as seen in Figure 5.9. Onwards, the sputtering set up for the lowest atomic percentage of Tb was used in further production of samples.

The PL and CL emission spectra of AlN:Tb^{3+} samples are plotted in Figure 5.10. The samples analyzed were treated with RTA processing after deposition at different temperatures. The obtained CL is nearly identical to the PL, with linewidths ∼20 – 25 nm, in both the emission shows richly structured spectra attributed to Tb^{3+} ions, with the characteristics $^5D_4 \rightarrow ^7F_J$ (J = 0, 1, 2, 3, 4, 5, 6) transitions in the spectral range from 400 to 700 nm without any signature of the broadband emission related to the AlN host. Such host related PL superimposed on Tb^{3+} emission peaks have been reported by Guerra et al. [246], under low temperature and for the resonant 488 nm excitation wavelength. It must be recalled that this broad band emission has been associated with defect related electronic states in the AlN host lattice. As claimed by Guerra et al. [246], at room temperature these defects can transfer the excitation energy to nearby Tb^{3+} ions via phonon-assisted energy transfer process. However, in low temperature conditions, the number of phonons decreases, the efficiency of the phonon-assisted energy transfer is strongly reduced and the defect induced host emission increases.

To study the effect of RTA on the Tb^{3+} CL and PL intensity, the four most intense $^5D_4 \rightarrow ^7F_J$ transition bands were chosen to represent the Tb^{3+} emission in the films. The inset graphs in Figure 5.10 show the integrated intensity of this transition bands as a function of annealing temperature. The PL emission shows an optimal annealing temperature at 700°C, above which the induced thermal changes becomes detrimental for the emission intensity. Whilst, for the CL emission the intensity continues to increase at 900°C, beyond the optimal temperature observed in PL experiments. As a matter of

fact, the optimal annealing temperature not only depends on the excitation source, but also on many factors such as the annealing conditions and the actual AlN:Tb^{3+} film composition [246, 299]. It can be noted that the overall effect of annealing is an improvement of the Tb^{3+} emission intensity by up to a factor of 2. Previous studies have reported similar increase in the Tb^{3+} emission intensity after annealing when embedded in AlN and other different hosts [246, 23, 59, 190]. However, a quantitative comparison among the effect of post growth treatment and the substrate temperature effect on the luminescent properties of the AlN:Tb^{3+} films have not been reported yet.

To compare the two different heat treatments, the PL spectra of the AlN:Tb^{3+} films grown with substrate temperature and AlN:Tb^{3+} films subjected to post deposition RTA processes are plotted in Figure 5.11. For an accurate comparison, only films with an uniform thickness around 150 nm have been studied. It can be seen that, as the substrate temperature increases from 300°C to 600°C, the Tb^{3+} intensity increases monotonically. A similar rise with temperature occurs in the samples subjected to post deposition annealing, but the intensity (counts) was significantly increased compared with in situ heating. To understand this behavior it is important to recall that in fact, the increase in Tb^{3+} intensity is a consequence of more optically active Tb ions. In a first stage, this can be realized by varying the Tb concentration. But, when embedded in the AlN matrix, not every Tb^{3+} ion is an active center possibly due to adverse conditions in the environment around the ion. In this scenario, the thermal treatments are intended to promote the formation of more optically active centers in the AlN matrix. This activation of Tb^{3+} ions leads to an increasing population of emitting Tb^{3+} sites in the AlN matrix due to underlying mechanism. These mechanisms are typically associated to the electronic enhancement of the material by the quench of non-radiative path ways. Also, they can be attributed to the reordering of atoms in the local structure surrounding the Tb^{3+} ion, thus triggering the activation by changing the symmetry properties governing the electronic transitions in the 4f orbital.

To compare the two different heat treatments, the PL spectra of the AlN:Tb^{3+} films deposited under different substrate temperatures, and the PL spectra of the AlN:Tb^{3+} films deposited at room temperature with further post deposition RTA processing are plotted in Figure 5.11. For an accurate comparison, only films with an uniform thickness around 150 nm have been studied. It can be seen that, as the substrate temperature increases from 300°C to 600°C, the Tb^{3+} intensity increases monotonically. A similar increase with temperature occurs in the samples subjected to post deposition annealing, but the intensity (counts) were significantly increased compared with the previous case. To understand this behavior it is important to recall that in fact, the increase in Tb^{3+} intensity is a consequence of more optically active Tb^{3+} ions. In a first stage, this can be realized by varying the Tb concentration. But, when embedded in the AlN matrix, not every Tb^{3+} ion is an active center possibly due to adverse conditions in the environment around the ion. In this scenario, the thermal treatments are intended to promote the formation of more optically active centers in the AlN matrix.

Sputtering with in situ heating means the possibility of surface rearrangement during the growth of the film in order to prevent defects that otherwise could not be annihilated. Oxygen can be considered

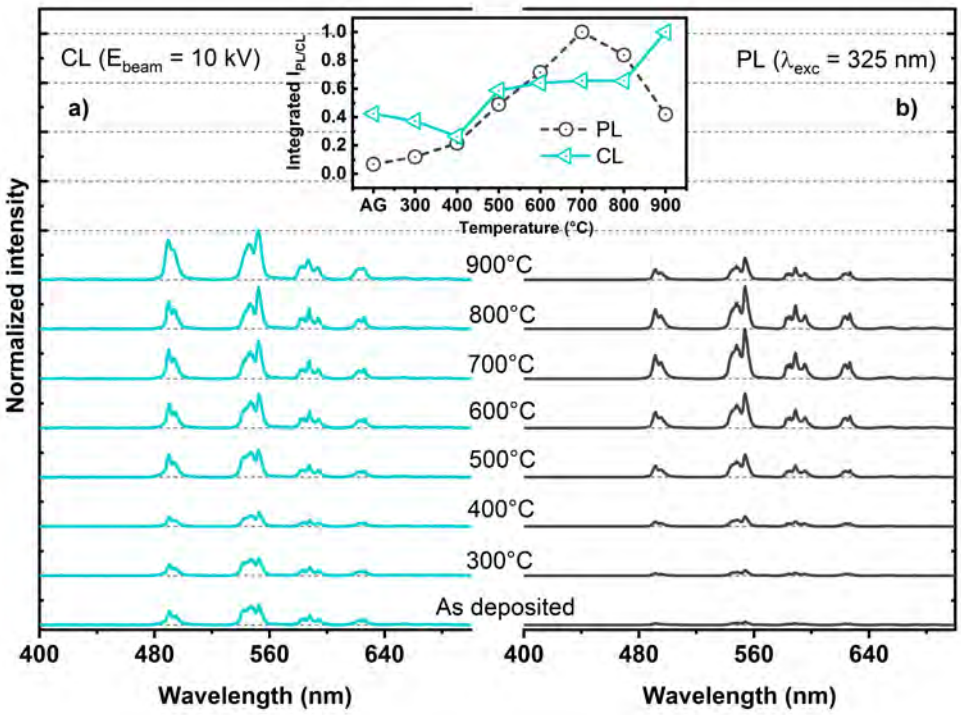

Figure 5.10: Normalized (a) CL and (b) PL spectra of AlN:Tb3+ samples with post deposition RTA treatments at different temperatures. The inset graph shows the integrated intensity of most intense peaks $^7F_{J\,=\,6,5,4,3}$ in the respective CL and PL spectra, as a function of the temperature.

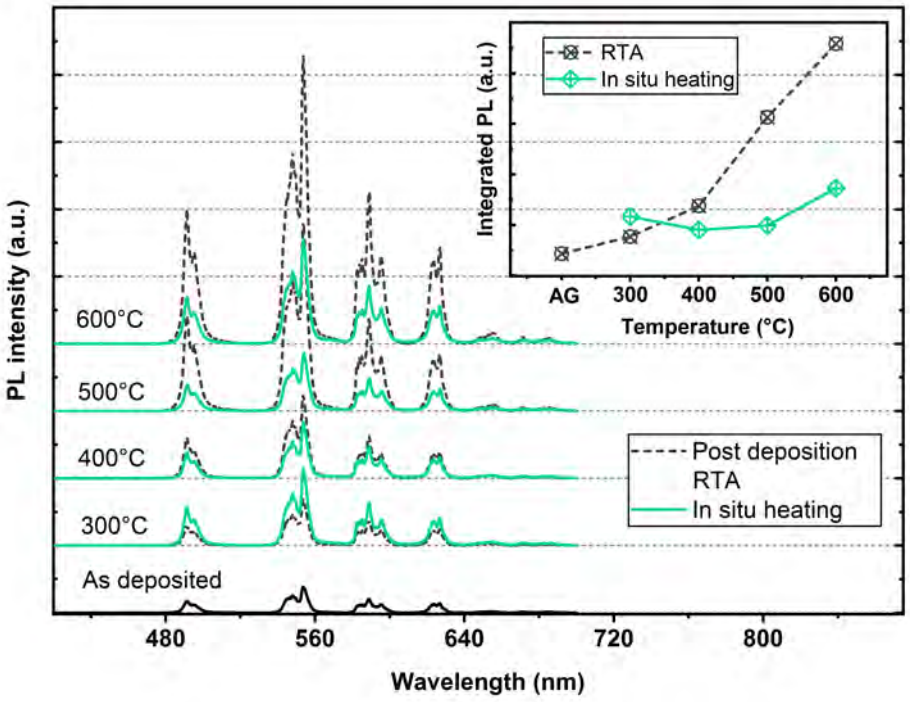

Figure 5.11: Comparison between the PL spectra of Tb^{3+} doped AlN samples subjected to two types of thermal treatments: grown with in situ heating and post deposition annealing at different temperatures. The inset shows the integrated intensity of the most intense peaks $^7F_{J\,=\,6,5,4,3}$ in the PL spectra as a function of temperature.

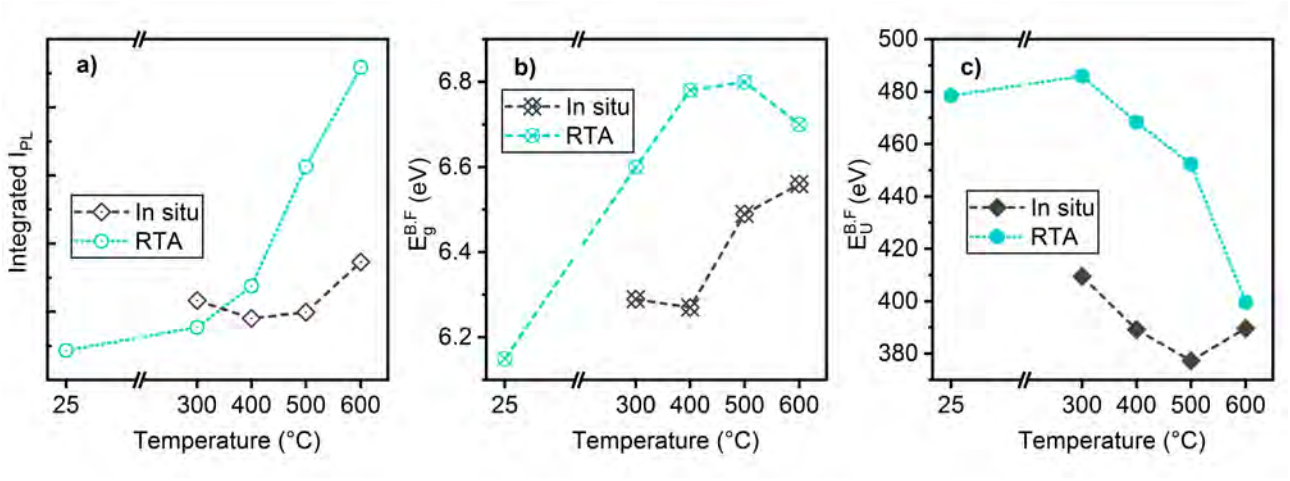

Figure 5.12: (a) Normalized integrated PL intensities, (b) optical band gap and (c) Urbach energy of the of AlN:Tb^{3+} thin films.

as a point defect created during the film production or afterwards, and which may ultimately diffuse and form complexes. From the compositional and structural analysis of the prepared AlN:Tb^{3+} films, higher substrate temperature lowers the oxygen concentration, change the preferred orientation peaks of wurtzite AlN, and smooth the film surface. In contrast, post deposition annealing at higher temperature leads to a slight increase of oxygen concentration and a better degree of crystallinity without further change in orientation planes.

The reason for the observed PL intensity behavior in Figure 5.11 could be linked to the variation of the optical bandgap and Urbach energy of the AlN:Tb^{3+} samples at different annealing temperatures. With the increase in temperature, the optical bandgap increases and the Urbach energy decreases in both types of heat treatments. According to Guerra et al [23], in the low doping regime, the reduction of electronic defects, measured by the Urbach energy, should enhance the light emission by the quench of non radiative paths. Note that for samples grown with in situ annealing, the optical bandgap and Urbach energy are lower than the values for samples annealed with RTA processes. If the reduction of electronic defects were the only factor for a higher PL intensity, the opposite behavior should be expected. However, the explanation why the higher PL intensity occurs in samples annealed after deposition is not trivial because several parameters must be taken into account. First, it is well accepted that the Tb^{3+} ions are optically activated by the presence of Tb-O complexes that appears after annealing treatments. In fact, EDS analysis has found a slightly higher oxygen content in samples treated with RTA after deposition. The increase of Tb^{3+} related PL can partially be explained by its coordination with oxygen atoms [300]. Another important factor is the effective Tb^{3+} cross section related to the number of clusters and the Tb^{3+} sites in the host crystalline structure. Since no Tb^{3+} related phases are identified in the XRD patters, this means that Tb^{3+} ions could be mostly embedded in the grain and at the grain boundaries of the AlN host, probably taking the substitutional Al site of the wurtzite AlN lattice. Thus, the Tb^{3+} ion site should be influenced by the local symmetry structure of the host lattice, perhaps related to the variation of the crystallographic planes (0002) or $(10\bar{1}1)$ in the AlN host lattice.

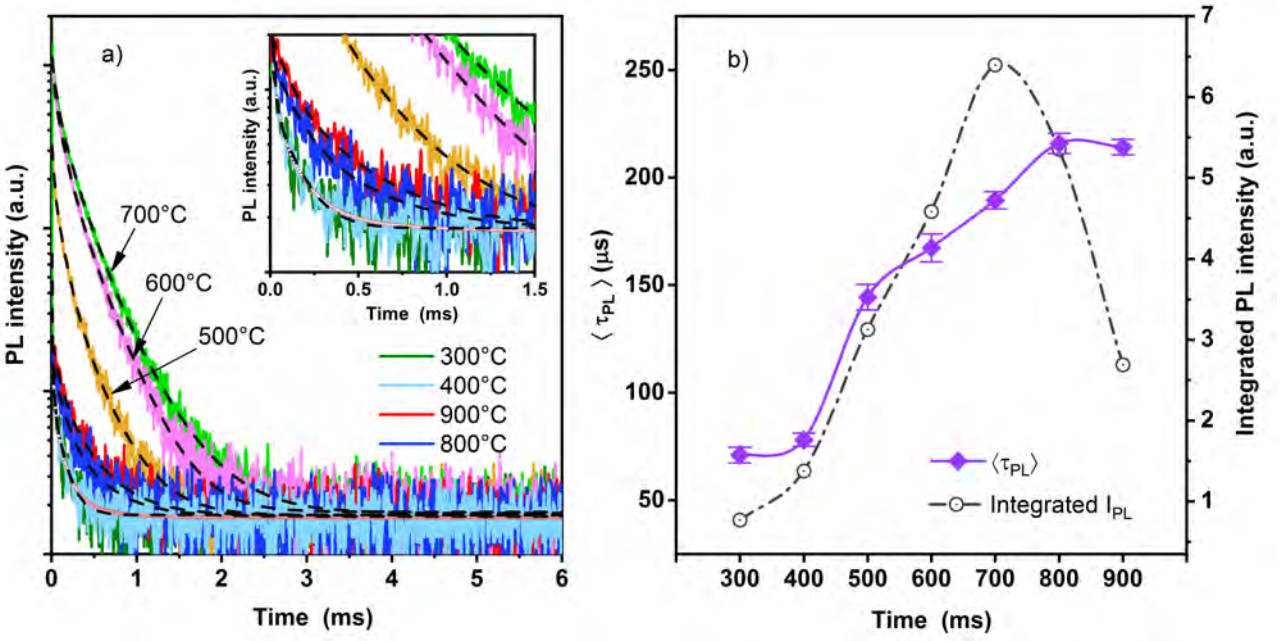

Figure 5.13: (a) Room temperature time resolved PL decay curves (plotted in a logarithmic scale) of the main emission peak of Tb^{3+} doped AlN samples after annealing at different temperatures. Smooth dashed lines are the fitting curves with a double-exponential decay function. (b) PL integrated intensity and average decay time measured as a function of the annealing temperature. The dashed lines are only a guide to the eye.

With the aim to produce a TFEL device, high intensity emitting light materials are required as active layer. The AlN:Tb^{3+} film has shown the highest PL emission intensities after heating with RTA process at 700°C. To study the annealing temperature effects in more detail, measurements of PL decay were conducted for each sample. Figure 5.13 shows the PL decays for the most intense $^5D_4 \rightarrow ^7F_5$ PL band ($\lambda = 545\,nm$), for samples annealed from 300°C to 900°C. In general, all measured PL decays were non single exponential and were fitted with double exponential decay function given by:

$$I_{PL}(t) = A_1 exp\left(\frac{-t}{\tau_1}\right) + A_2 exp\left(\frac{-t}{\tau_2}\right) \tag{5.1}$$

Herein $I_{PL}(t)$ denotes total PL intensity at time t, τ_1 and τ_2 are the PL decay lifetimes and A_1, A_2 are contributing intensity amplitudes. The double exponential character of the PL decay has been early reported for the emission of Tb^{3+} ions embedded in SiN_x[301] and SiO_2[302] film matrices and it was tentatively attributed to the presence of Tb^{3+} ions at several different sites in the SiN_x matrix. From the fitting parameters, the average PL decay times were calculated for each sample using $< \tau_{PL} >= (A_1\tau_1 + A_2\tau_2) / (A_1 + A_2)$ [303]. Here, it should be emphasized that the single exponential decay function $I_{PL}(t) = Aexp(-t/\tau_{PL})$ was also performed but resulted in a lower fit quality at the end of the decay curves. However, the difference between $< \tau_{PL} >$ and τ_{PL} calculated from the fit with double and single exponential decay function respectively, does not exceed 5%. Since no physical model is used to improve the fit quality, any physical meaning can be assigned to τ_1 and τ_2 separately. On the other hand, the average PL lifetime definition is the amount of time which Tb^{3+} ions spend in

their excited $^5D_4$ state [304]. In an ideal case, only radiative recombination process relax the excited Tb^{3+} ion and the PL decays are single exponential. This will shorter the PL decay lifetime, which would mean a higher luminescence efficiency in this ideal case. However, for real semiconductors, defects and impurities inevitably exist inside the host lattice, and with so much dopant concentration and multiphonon relaxation, conditions are far from ideal. In a simple realistic case, the rate of radiative recombination is comparable with the rate of non radiative recombination. As a result, the decay curve of the PL intensity is not singly exponential. This behavior will also shorter lifetime but it does not certainly mean higher luminescence efficiency. Finally, if the rate of non radiative recombination from the $^5D_4$ state by far exceeds the radiative recombination rate, a considerable population of Tb^{3+} ions becomes non luminescent. Hence, $< \tau_{PL} >$ remain steady and weak or no PL signal is observed.

Figure 5.13(b) shows the dependence on the annealing temperature of the PL intensity and the average lifetime for all samples. Based on this results, it is possible to discuss more in detail the effect of annealing temperature on the non-radiative recombination process. Up to 700°C, clearly both the PL decay lifetime and the integrated PL intensity gradually increase with annealing temperature. If the PL intensity and the $< \tau_{PL} >$ follow similar trends during thermal annealing, it can be assumed that the changes in the PL intensity arise mainly from the changes in the PL lifetime. Herein, the integrated intensity increases by a factor of 8.0 upon annealing, whereas the lifetime increases only by a factor of 3.0. Since the change between the PL intensity and the lifetime is not proportional, it suggests that the fraction of the active Tb^{3+} ions has increased upon annealing. As early explained, the effect of thermal annealing is to raise the number of optically active centers and thus, the population of excited Tb^{3+} ions N^*_{Tb} , given that $I_{PL} = k_R N^*_{Tb}$. After 700°C, the lifetime stops the steep increase, while the integrated PL intensity decreases with increasing annealing temperature. This behavior suggests that nonradiative processes play an important role on the PL intensity.

The measured average lifetimes of the RE ions are regarded to be a function of the natural radiative lifetime of the central ion and the sum of non radiative deactivation processes according to:

$$< \tau_{PL} >= \frac{1}{k_r + k_{nr}} \tag{5.2}$$

Where k_r is the rate constant for radiative transitions and k_{nr} is the sum of rate constants for all the non radiative transitions. By definition,$\tau_{rad} = 1/k_r$ is the radiative lifetime or the time it takes to the electrons in the excited $^5D_4$ state of Tb^{3+} to decay by emitting a photon. In contrast with $< \tau_{PL} >$ the measured , τ_{rad} does not accounts for the non radiative losses. In practice the overall quantum yield or eficiency (QE) of a RE doped material is a function of the measured and radiative lifetimes, $QE = k_r/(k_r + k_{nr}) =< \tau_{PL} > /\tau_{rad}$. In order to estimate the QE, τ_{rad} has to be calculated. The radiative transitions within the 4f configuration of the Tb^{3+} ion should be analyzed by using the Judd-Ofelt theory [35, 34], which describes the intensities of transitions of Tb^{3+} ions embedded in the solid matrix using the so called Judd-Ofelt parameters $(\Omega_2, \Omega_4, \Omega_6)$ to characterize the local structure and

T_A(°C)	JO (10^{-24} cm^2)			Lifetime (ms)		QE (%)	$^5D_4$ to	β_{cal}	β_{exp}	A (s^{-1})	A^{ED}(s^{-1})	A^{MD}(s^{-1})
	Ω_2	Ω_4	Ω_6	τ_{rad}	τ_{PL}							
300	0.37	1.27	7.69	1.56	0.07	4.5	$^7F_3$	0.12	0.11	76.9	76.9	0
							$^7F_4$	0.17	0.18	112.4	112.4	0
							$^7F_5$	0.46	0.46	295.3	262.4	32.8
							$^7F_6$	0.24	0.23	154.8	140.2	14.6
400	0.29	0.13	8.54	1.64	0.08	4.8	$^7F_3$	0.11	0.10	66.6	66.6	-
							$^7F_4$	0.17	0.22	105.2	105.2	-
							$^7F_5$	0.46	0.46	285.1	262.7	22.4
							$^7F_6$	0.23	0.20	152.2	132.2	20.1
500	0.18	0.12	7.5	2.0	0.14	7.0	$^7F_3$	0.10	0.10	51.2	51.2	-
							$^7F_4$	0.19	0.21	91.2	91.1	-
							$^7F_5$	0.47	0.47	237.5	220.4	17.1
							$^7F_6$	0.23	0.21	120.6	114.2	6.4
600	0.21	0.24	5.33	2.45	0.16	6.5	$^7F_3$	0.11	0.11	45.4	45.4	-
							$^7F_4$	0.17	0.22	68.1	68.1	-
							$^7F_5$	0.47	0.47	191.1	169.9	21.2
							$^7F_6$	0.23	0.19	102.3	85.5	16.8
700	0.17	0.11	4.99	2.74	0.19	6.9	$^7F_3$	0.11	0.10	39.5	39.5	-
							$^7F_4$	0.18	0.21	62.1	62.1	-
							$^7F_5$	0.47	0.47	172.9	154.5	18.5
							$^7F_6$	0.25	0.25	90.3	77.9	12.4
800	0.17	0.73	3.68	3.11	0.21	6.7	$^7F_3$	0.12	0.11	37.5	37.5	-
							$^7F_4$	0.18	0.22	55.7	55.7	-
							$^7F_5$	0.45	0.45	147.0	126.8	20.2
							$^7F_6$	0.23	0.19	81.1	69.3	11.8
900	0.11	0.61	3.14	3.70	0.21	5.6	$^7F_3$	0.11	0.10	28.5	28.5	-
							$^7F_4$	0.18	0.21	47.3	47.3	-
							$^7F_5$	0.46	0.46	124.8	102.9	21.9
							$^7F_6$0.46	0.25		68.9	58.6	10.3

Table 5.3: Judd-Ofelt (JO) intensity parameters, calculated and measured lifetimes of the $^5D_4$ level of Tb^{3+} in the AlN thin films annealed at different temperatures. Calculated and experimental branching ratios and the radiative transition rates for electric dipole (ED) and magnetic dipole (MD) contributions of the $^5D_4 \rightarrow {}^7F_J$ emission transitions.

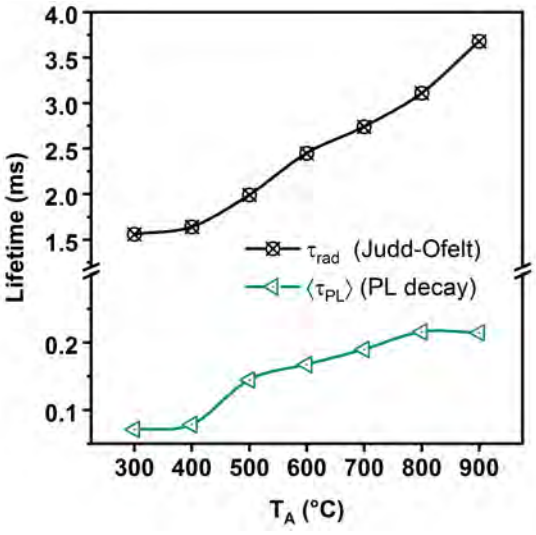

Figure 5.14: Measured and calculated PL lifetimes for Tb^{3+} doped AlN thin films upon annealing treatments.

bonding around the Tb^{3+} ion. Table 5.3 lists the Judd-Ofelt intensity parameters, the spontaneous emission probability of the electric and magnetic dipole contributions and the radiative lifetime for each AlN:Tb^{3+} sample annealed from 300°C to 900°C. For more details concerning this method and the performed calculations please consult Appendix A.1 and A.2.

For most materials, the reported radiative lifetime τ_{rad} of the $^5D_4$ state of Tb^{3+} ion is very long, at least of the order of several millisecond [305, 306]. The non radiative decay process occurs on a shorter time scale depending on the defect structure of the material. When the excited $^5D_4$ state of Tb^{3+} ion interacts with non radiative recombination centers, such as defects, the non radiative decay competes with the emission of photons. In the case of strong coupling to defects, the rate of non radiative recombination is much higher than the rate of radiative recombination, therefore the Tb^{3+} emission quenches and the PL spectra or PL decay measurements are undetectable. This is not the case in this work, and the non radiative coupling to defect states can be regarded as intermediate/weak since the Tb^{3+} emission takes place but with a decreased QE (see Table 5.3). Finally, note that even though the calculated radiative lifetime is 10^1 order of magnitud higher than the measured lifetime $< \tau_{PL} >$, both parameters follow parallel trends during thermal annealing, as shown in Figure 5.14.

I-V curves of AlN:Tb^{3+} based TFEL devices

To investigate the resistive switching properties of the AlN:Tb^{3+} thin film samples, a customized DC voltage was applied to the DC-TFEL devices via top electrodes of ITO, and to the AC-TFEL devices via a bottom Mo electrode and a top ITO electrode. The electric pulse amplitude was 1 V, and the current is detected as a function of the applied voltage. Nonetheless for DC-TFEL devices no electrical response was obtained. Figure 5.15 shows the several I-V curves obtained for the AC-TFEL devices. The thickness of the AlN:Tb^{3+} films was adjusted around the same 150 nm to compare the samples. Some curves show a linear response, indicating ohmic behavior of the Tb^{3+} doped AlN film. This has occurred especially in the case of non thermally treated sample and after annealing at 300°C. Only by RTA treatments higher than 300°C, was the ohmic behavior be turned into non ohmic. In

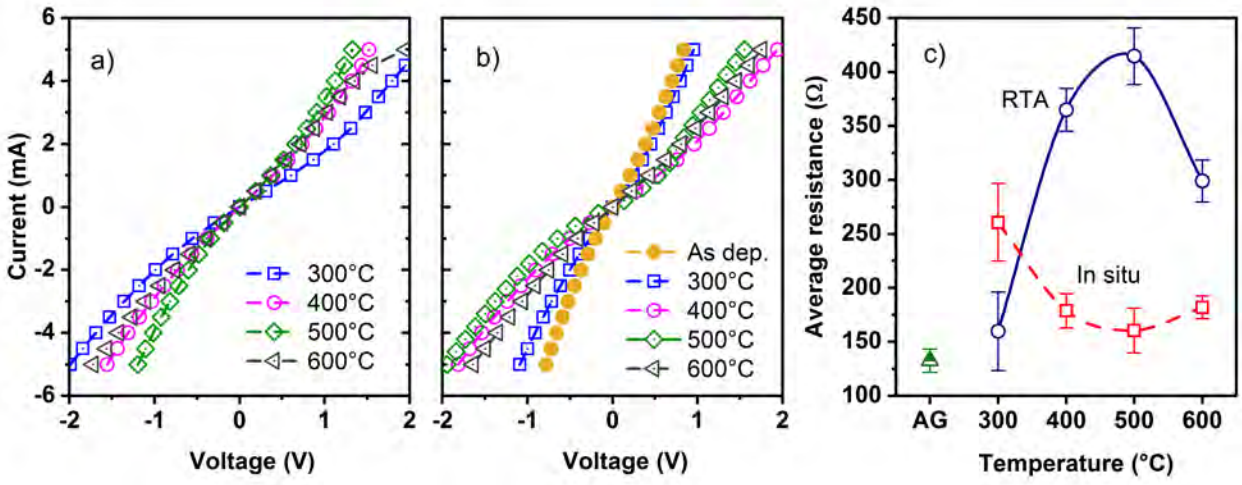

Figure 5.15: Current - voltage curves obtained from Tb doped AlN films prepared at (a) in situ substrate heating and subjected to (b) post deposition RTA. (c) Average resistance characteristics plotted versus temperature for the two types of thermal treatments applied to the samples.

the case of samples grown at different substrate temperatures, the majority of the curves show a non linear response and demonstrates Schottky contact with poor contact characteristics.

Figure 5.15(c) shows temperature dependent characterizations of resistance from 300°C to 600°C, to investigate ohmic contact formation mechanism. In samples with RTA process, resistance increases which might be an effect of the composition, more over at the interface contact - active layer[307, 308]. While in samples with in situ heating, it can be seen that resistance slightly decreases with the increasing substrate temperature. It might occur also due to the doping of the AlN due to the diffusion of In or Sn ions from the ITO. At the end, the current flow through the active layer was so poor that no light emission has been observed. Although it is not part of this thesis, it can be suggested for future work to try conventional the interfacial properties, band offset and work function differences in the case of the DC-TFEL devices; also the poor electrical transport and quantum efficiencies of the AlN:Tb^{3+} layers in the case of AC-TFEL devices. The latter factor is closely related to non-radiative transitions and cross-relaxation through the defect states that can extinguish the light emission.

5.4 Conclusions

Experiments were designed to investigate the properties of AlN:Tb^{3+} thin films grown by dc reactive magnetron sputtering using small Tb flakes added on top of the Al target in mixed argon and nitrogen atmosphere. Two types of thermal treatments were carried out to enhance the light emission intensity of Tb^{3+} ions: in situ substrate heating and post deposition rapid thermal annealing, at temperatures ranging from 300 to 600°C. For a proper comparison of their structural, optical and luminescent properties, the sputtering setup and conditions were optimized in order to achieve film thicknesses around 150 nm with small variation in their elemental composition. Undoped AlN with closer stoichiometric composition was obtained for comparison. In the case of Tb^{3+} doped AlN samples, a nearly constant Tb concentration around 2 at.%, Al/N ratios between 0.64 and 0.69 and oxygen concentrations <

10 at.% were verified in all samples by EDS analysis. The XRD results show that in both processes the films exhibit a polycrystalline wurtzite structure with (0002), (10$\bar{1}$1) and (10$\bar{1}$0) crystal plane peaks. Post deposition annealing increases the crystalline quality without changing the relative intensities of the diffraction peaks. The increase of the (0002) peak intensity using in situ heating has been attributed to the decrease of the Al-N bond length in the growth film. SEM images revealed the grainy morphology of the films. Complementary, the smooth surface of the films were confirmed via AFM measurements with RMS surface roughness of few nanometer order.

The optical properties of AlN:Tb^{3+} thin films were studied upon both thermal processes at different temperatures. Post deposition annealing caused a slight increment of oxygen content in the AlN:Tb^{3+} films, and induced the increase of the bandgap from 6.1 to 6.8 eV. Whereas, substrate temperature allowed a lower oxygen content in the films which result in bandgaps ranging from 6.2 to 6.5 eV. Similarly, the Urbach energies reported for films grown upon increasing substrate temperature indicate lower disorder in the structure attributable to the higher surface mobility of the adatoms. In both thermal treatments, as temperature increased some changes of the PL spectra have been observed. The PL spectra of Tb^{3+} doped films under both thermal treatments have shown prominent green emission from the $^5D_4$ excited state. Also, the intensity of films subjected to post annealing treatments has been found to be almost three times higher than in the case of films grown with substrate temperature. It has been well established that the effect of thermal treatments is to rise the population of optically active Tb^{3+} sites. The mechanisms behind this activation can be tentatively attributed to the coordination of Tb^{3+} ions with nearby oxygen atoms, due to the slight increment of oxygen concentration with annealing temperature. Also, the variation of the crystallographic planes in the host structure exerts an influence on the local symmetry structure around the Tb^{3+} ions. To study the annealing temperature effects in more detail, rapid thermal annealing was carried out from 300 to 900°C in steps of 100°C at the same annealing conditions. The optimal annealing temperature for CL or PL emission occurs at 900°C and 700°C, respectively. Besides, it was found that annealing enhances the photoluminescence intensity of Tb^{3+} ions and increases the PL intensity of the average PL decay time measured for the main $^5D_4 \rightarrow ^7F_5$ transition peak (545 nm) of Tb^{3+} ions. The latter can be explained by decrease of the non radiative recombination rate and increase of the population of excited Tb^{3+} ions upon annealing. For the calculation of the quantum efficiency, a modified Judd-Ofelt method using only the emission spectra has been applied to estimate the radiative lifetimes of each film. The quantum efficiencies obtained ranges from 4.5 to 7.0 %.

Finally, the deposition of Tb^{3+} doped AlN thin films by dc-sputtering, then subjected to rapid thermal annealing at 700°C has shown the advantage of higher emission intensity with respect to substrate temperature during film deposition up to 600°C. The films characterized were implemented in DC- and AC-TFEL devices as active layers. The I-V curves showed ohmic behavior of the as deposited AlN:Tb^{3+} film. With increasing temperature, the ohmic behavior was turned into non ohmic electrical transport. No electroluminescent emission has been obtained from the AlN:Tb^{3+} devices yet. This work points out that possible reasons for the non emitting TFEL device has to do with their small quantum efficiency and the poor contact characteristics from the measured I-V curves, which allows

for many electrical leakage paths. It is concluded that post deposition annealing treatments are much more effective than film growth using substrate temperature to produces an AlN:Tb^{3+} active layer with strong emission intensity.

Chapter 6

General conclusions

This thesis focused on the study the optical and luminescent properties of a rare earth doped AlO_xN_y and AlN thin films prepared by magnetron sputtering for optoelectronic applications. Rare earth doped group III nitrides, and more particularly AlO_xN_y and AlN , have gained attention due to their wide optical bandgap in the range 6 to 7 eV, forming a good host material for rare earth ion emission in the ultraviolet to visible range. Additionally, these materials possess high thermal conductivity, low thermal expansion coefficient, good dielectric properties and strong chemical resistance. All these features enable the integration of the studied thin film materials in devices working at high power operation. Analyzed were singly doped Tb^{3+} and Yb^{3+} as well as co-doped Tb^{3+}/Yb^{3+} ions as sensitizer, along with the use of AlO_xN_y as an amorphous host to study the influence of the doping concentration, the co-doping as well as the oxygen to nitrogen ratio and the thermal activation. Another studied system consist of Tb ions embedded in a polycrystalline AlN host. Below are outlined relevant aspects from each system analyzed in this work, in order to review main points.

With the purpose to investigate a down conversion process between $Tb^{3+}$and Yb^{3+} ions in an a-AlO_xN_y matrix, combinatorial thin film libraries of undoped a-AlO_xN_y, Tb^{3+}doped a-AlO_xN_y, Yb^{3+} doped a-AlO_xN_y and Tb^{3+}/Yb^{3+} codoped a-AlO_xN_y thin film libraries were prepared by radio frequency magnetron co-sputtering of Al, Tb and/or Yb targets. As a result, large area samples containing a composition gradient of the dopants and the matrix elements have been obtained and further analyzed by extensive PL and EDS measurements, complemented with UV-VIS, PLE, XRD and AFM characterizations. Green and NIR emissions were obtained using 325 nm excitation of Tb^{3+} and Yb^{3+} ions, respectively. The high Yb^{3+} related emission could be tailored by controlling the appropriate $Yb^{3+}$and Tb^{3+}concentration as well as the O:N ratio in the matrix. Nonetheless, both Tb^{3+} and Yb^{3+} related emissions are also governed by energy back transfer process between matrix and rare earth ions. The absence of a intermediate energy level of the Tb^{3+} ions prevents energy back transfer from the Yb^{3+} ions. Post deposition annealing treatments up to 850°C have been found to reduce the undoped matrix related emission intensity while increasing the Yb^{3+} related emission. Moreover, in the codoped sample, the Tb^{3+} related emission intensity diminishes in favor of Yb^{3+} emission, leading to a Yb^{3+} emission intensity ∼2 times higher than that obtained in the Yb^{3+} singly doped sample. The highest Yb related intensity ocurred for a concentration ratio Tb:Yb ∼ 1/2, thus suggesting a possible cooperative energy transfer from one Tb^{3+} ion to two Yb^{3+} ions. Larger

concentrations of both Tb^{3+} and Yb^{3+} produce luminescent quenching because of energy migrations due to inter-ionic cluster interaction. This process reduces the energy transfer efficiency which in turn could reduce the down conversion emission. The role of oxygen concentration on the Tb^{3+} and Yb^{3+} PL emission intensities has been studied through the evolution of the O:N ratio with annealing temperature. At O:N = 2, the oxygen concentration was beneficial for the Yb^{3+} emission intensity which quenches at lower and higher oxygen content. In contrast, the singly doped Tb^{3+} emission intensity monotonically increases with increasing oxygen content. Through Arrhenius plots, the activation energy associated to the thermal activation process have been determined for different O:N ratios. As oxygen increases in Tb^{3+} doped a-AlO_xN_y matrix, the energy required to activate Tb^{3+} emission decreases. The underlying mechanisms for this behavior are tentatively attributed to the formation of Tb oxide clusters or nanocrystals in the host structure. This idea is supported by the opposite behavior of the bandgap and Urbach energy of the undoped AlO_xN_y and Tb^{3+}/Yb^{3+} codoped film. In the former, the bandgap increases and the Urbach energy decreases with increasing anneling temperature. Meanwhile, in the latter, the bandgap reduces and the Urbach energy increases with temperature. Since the rare earth oxides are known to posses lower bandgap values, the observed bandgap reduction could be associated to the clusterization these systems. Besides, it has been found that in the case of singly doped AlO_xN_y:Yb^{3+} samples, the energy required to activate Yb^{3+} ions for light emission is higher than in the codoped AlO_xN_y. Thus, evidencing the sensitizer role of Tb^{3+} in favor of Yb^{3+} in the codoped AlO_xN_ythin films. Finally, by comparing the activation energies for oxygen and nitrogen diffusion in AlN and Al_2O_3 layers, the thermal activation could be attributed to possible nitrogen diffusion or the reordering of atoms in the surrounding environment of the rare earth ions, with sufficient low symmetry to enhance the optical transitions and/or the electronic enhancement of the material reducing the number of possible non radiative pathways intensity of light emitted.

Polycrystalline Tb^{3+} doped AlN thin films, were prepared using DC reactive magnetron sputtering, and their stoichiometric, structural, morphological, optical and luminescent properties were studied in an effort to develop AlN:Tb^{3+} based TFEL devices. The prepared samples have been subjected to two different thermal treatments in order to enhance the light emission intensity of Tb^{3+}: in situ heating during the deposition process and post deposition rapid thermal annealing. The crystalline structure of the prepared samples and their compositions have been examined by XRD, EDS, SEM and AFM analyses. The samples showed an uniform Tb concentration around 2 at.%, almost stoichiometric Al/N ratio between 0.64 and 0.69, and oxygen content below 10 at.%. Post deposition annealing has slightly increased the oxygen content from 6 to 8 at.% with increasing temperature. This oxygen increment is reflected in large bandgaps values ranging from 6.1 to 6.8 eV. Contrastingly, in situ deposition substrate heating lowers the oxygen content leading to bandgap values between 6.2 to 6.5 eV. The substrate temperature affects the mobility of the adatom, which is a key factor that control the structure evolution. Consistent changes are observed in the bandgap and Urbach energy with annealing and substrate temperature and are a measure of the structural disorder in the films. According to XRD measurements, the polycrystalline wurtzite structure of the films has preferred orientations $(10\bar{1}0)$, $(10\bar{1}1)$ and (0002). Substrate heating above 500°C has induced a change in the intensity of the reflected peaks, and more particularly the increase of the (0002) plane with respect

to the other planes. This means the shortening of the Al-N bond length due to the formation of the more compact (0002) planes that is attributed to the high adatom mobility with increasing substrate temperature. Whereas, post deposition annealing treatment has maintained the relative intensities between the peaks, only increasing the degree of crystallinity with increasing annealing temperature. The films present a smooth grainy morphology of the surface, with an RMS roughness of few nanometer order. The highest Tb^{3+}PL emission intensity obtained for films with post deposition annealing at 600°C is three times higher than that obtained for the films grown using substrate heating. Annealing at high temperatures is typically associated with clustering, and along with the presence of oxygen are a key for sensitizing the Tb^{3+} photoluminescence. The optimal annealing temperature for the highest PL intensity of AlN:Tb^{3+} films happens at 700°C. The strong relation between the average PL decay time, measured for the main $^5D_4$ to$^7F_5$ transition peak of Tb^{3+}, and the PL emission with annealing temperature suggest that annealing raise the number of optically active Tb^{3+} centers which in turn increase the population of excited Tb^{3+} ions upon annealing. Although annealing plays a role to induce more optically active Tb^{3+} ions, larger concentrations of oxygen and clusterization induced with higher temperatures might produce luminescent quenching due to the enhancement of non radiative recombination paths such as energy migrations by inter ionic cluster interactions. Finally, a modified Judd-Ofelt method to determine the Judd-Ofelt intensity parameters only from the emission spectra has been applied to calculate the radiative lifetimes of the films upon annealing. The highest quantum efficiency obtained is 7.0 % which means the films produced have very low PL quantum yield. Regarding the production of TFEL devices, in the DC-TFEL devices the ITO electrode was in direct contact with the active layer and no other carrier injecting layer has been considered to reduce the band offsets between AlN:Tb and ITO. This could be the reason why there was no current flowing through the active layer and no I-V curve of this device could be measured. Whereas, the AC-TFEL device do not depend on the work function and band offsets since the injection of charges is directly from the interfaces insulator/active layer. However, most of the I-V curves measured show a non linear response and non ohmic electrical transport with poor contact characteristics. This insufficient current flow through the active layer and the low PL quantum yield found for these films can explain why no light emission was observed, when the current was applied to the devices.

Appendix

A. Transitions between 4f electronic states: the Judd–Ofelt theory

The Judd-Ofelt (J-O) theory [35, 34] describes intensities of 4f electron transitions of rare earths in solids and solutions, in contrast the Judd-Ofelt parameters characterize local structure and bonding in the vicinity of rare earth ions. The remarkable success of this theory relies on simple approximations to find electric dipole matrix elements between mixed parity states for manifold to manifold transitions. This theory has shown to be a powerful tool for an analysis of the 4f-4f absorption spectra of trivalent rare earth ions, and provides information about emission probabilities, radiative lifetime, and branching ratios of the emission transitions.

The interaction between the electromagnetic field and the electrons of an atom is generally dominated by electric-dipole (ED) interactions and to a lesser extent by magnetic-dipole (MD) interactions. The ED operator has ungerade (u) inversion symmetry and the 4f wavefunctions have also ungerade (u) inversion symmetry, therefore for an ED induced 4f-4f transition, the direct product u⊗u⊗u = u is also ungerade. According to the Laporte selection rule, the transition probability is non zero only if the product of the 4f wavefunctions with the dipole moment operator is symmetric or gerade (g) with respect to the center of symmetry. Thus, for an ED induced 4f - 4f transition to occur, some admixture of the states with opposite gerade parity into the ungerade 4f wavefunctions is required. Such admixtures can be mediated by odd-parity crystal field components. This is the fundamental premise of the J-O theory, which uses an odd-parity crystal field to obtain a new wavefunction $|\psi\rangle$ of admixing even-parity states $|\varphi\rangle$ into the 4f wavefunction $|4f^nSLJ\rangle$.

$$|\psi\rangle = \frac{|4f^nSLJ\rangle + \sum_\varphi \langle(\langle 4f^nSLJ\,|V|\,\varphi\rangle)\text{—}\varphi\rangle}{E(4f^nSLJ\,|V|) - E(\varphi)} \tag{6.1}$$

Herein $E(4f^nSLJ\,|V|) - E(\varphi)$ are the energy differences between the 4f state and the perturbing even parity states φ, with V as the crystal field interaction operator. For the trivalent RE ions, the even parity $\left|4f^{n-1}5d\right\rangle$ states are strongly admixed into the $|4f^n\rangle$ states due to small separation of energies. Whereas in the divalent RE ions the energy separation is much smaller, and thereby the $|4f^n\rangle \rightarrow \left|4f^{n-1}5d\right\rangle$ transitions tends to mask the weak $|4f^n\rangle \rightarrow |4f^n\rangle$ transitions. In the latter case, the J-O theory can not describe the $|4f^n\rangle \rightarrow |4f^n\rangle$ transitions, which means that the perturbation approach equation 6.1 can not be used.

For a $|4f^n\rangle \rightarrow |4f^n\rangle$ transition, the admixed wavefunctions are given by equation 6.1 and the matrix element of the ED moment $D_{k,q}$ is provided by [35]:

$$\langle \psi | D_{k,q} | \psi' \rangle = \sum_{\varphi} \left\{ \frac{\langle 4f^n SLJ | V | \varphi \rangle \langle 4f^n S'L'J' | D_{k,q} | \varphi \rangle}{E(4f^n SLJ) - E(\varphi)} + \frac{\langle 4f^n S'L'J' | V | \varphi \rangle \langle 4f^n SLJ | D_{k,q} | \varphi \rangle}{E(4f^n S'L'J') - E(\varphi)} \right\} \tag{6.2}$$

According to J-O theory, to solve the equation 6.2 it must be assumed that all sublevels of a the even parity state φ are degenerate. Secondly, it is assumed that $E(4f^n SLJ) - E(\varphi) = E(4f^n S'L'J') - E(\varphi)$. Both assumptions are rough because the separation between $4f^n$- $4f^{n-1}5d$ states is higher than the tipical $4f^n - 4f^n$ transition energies. Nonetheless, these assumptions make it possible to combine the sums in equation 6.2 and to simplify the matrix element of the ED moment to a sum of only three terms.

According to the J-O theory, the theoretical expression for the oscillator strength of an induced ED transition from the ground state to an excited state (absorption) is given by:

$$f_{ED}^{abs} = \frac{8\pi^2 m_e c}{3h\bar{\lambda}(2J+1)} \frac{\chi_{ED}^{abs}}{n} \sum_{i=2,4,6} \Omega_i \left| \left\langle l^N SLJ \left\| U^i \right\| l^N S'L'J' \right\rangle \right|^2 \tag{6.3}$$

Where the fundamental constants are given in SI units. Herein, $\bar{\lambda}$ is the mean wavelength of the transition $\left|l^N SLJ\right\rangle \rightarrow \left|l^N S'L'J'\right\rangle$, h is the Planck constant ($4.135 \times 10^{-15} eV.s$), $2J+1$ is the degeneracy of the initial state, n is the refractive index, $\Omega_{2,4,6}$ are the three Judd-Ofelt parameters and $\left\langle l^N SLJ \left\| U^i \right\| l^N S'L'J' \right\rangle$ terms are the dimensionless double reduced matrix elements of unit tensor operator U whose values does not depend of the local environment around the RE ion. The factor X represents the local electric field correction, which is given by $\chi_{ED}^{abs} = \left(\left(n^2+2\right)/3\right)^2$ for an oscillator strength proportional to the square of the electric field. A more detailed description of the local electric field correction can be found in [169]. Kaminskii [309] and Morrison [310, 311] have computed the reduced matrix elements between all of the intermediate-coupled wavefunctions for the multiplets of the $4f^N$ electronic configuration of the free ion. Note that the ED trasnition strength is expandend as the sum of three even ranked tensors. Whereas, the oscillator strength for a MD absorption transition given by equation 6.4 only depends on one reduced matrix element $\left\langle l^N SLJ \left\| L + gS \right\| l^N S'L'J' \right\rangle$.

$$f_{MD}^{abs} = \frac{h}{6m_e \bar{\lambda} c(2J+1)} n \left| \left\langle l^N SLJ \left\| L + gS \right\| l^N S'L'J' \right\rangle \right|^2 \tag{6.4}$$

The tensor $L + gS$ is the magnetic dipole operator and $g = 2.002319304362$ is the electron factor [169]. Some transitions have both ED and MD contributions, therefore the total oscillator strength is given by $f^{abs} = f_{ED}^{abs} + f_{MD}^{abs}$. In the J-O theory, the radiative transition probability (emission) $A_{J \rightarrow J'}^{emi}$, is related to the ED and MD oscillator strengths according to the following equation:

$$
\begin{aligned}
A^{emi}_{J\to J'} &= \frac{16\pi^3 e^2}{3\varepsilon_0 h\bar{\lambda}^3(2J+1)}\frac{\chi^{emi}_{ED}}{n}\left[S_{ED}+n^3 S_{MD}\right] \\
S_{ED} &= \textstyle\sum_{i=2,4,6}\Omega_i\left|\left\langle l^N SLJ\left\|U^i\right\|l^N S'L'J'\right\rangle\right|^2 \\
S_{MD} &= \frac{h}{\left(4\pi m_e\right)^2 c^5}\left|\left\langle l^N SLJ\left\|L+gS\right\|l^N S'L'J'\right\rangle\right|^2
\end{aligned}
\tag{6.5}
$$

Where S_{ED} and S_{MD} are the electric and magnetic dipole strengths, respectively. Equation 6.5 is the spontaneous radiative emission probability for a transition from an excited state $\left|l^N SLJ\right\rangle$, to a lower energy state $\left|l^N S'L'J'\right\rangle$. However, in most cases an excited state can decay to several lower energy final states. Thus, the total radiative emission probability is the sum of all radiative decay rates from the excited state to each of the lower energy states. The relative contribution of one transition channel (or branch) to the total spontaneous emission is given by the emission branching ratio:

$$
\beta_{J\to J'} = \frac{A^{emi}_{J\to J'}}{\sum_{J'} A^{emi}_{J\to J'}} \tag{6.6}
$$

The branching ratio can be directly calculated in an experiment using the relative intensities of the various emissions transition bands in a photoluminescence spectrum. The resulting radiative lifetime of the excited state is given by:

$$
\tau^{rad} = \frac{1}{\sum_{J'} A^{emi}_{J\to J'}} \tag{6.7}
$$

$$
\eta = \frac{\sum A_{rad}}{\sum\left(A_{nrad}+A_{rad}\right)} = \frac{\tau_{tot}}{\tau^{rad}} \tag{6.8}
$$

It should be pointed out that equation 6.7 accounts only for radiative contributions to the decay of an excited state. Nonetheless, non radiative decay transitions can also take place via multiphonon relaxation, cross relaxation and several energy migration mechanisms. If one considers both the radiative and non radiative decay processes, the result is an overall shorter lifetime compared with the purely radiative lifetime calculated by equation 6.7. In fact, the radiative emission probability can be further used to calculate the non radiative probability A_{nrad} and the emission quantum efficiency η. The latter quantity gives the ratio between the number of photons emitted by the RE ion to the number of those absorbed. It is a very important parameter used to evaluate the quality of a light emitting system.

B. Judd-Ofelt parameters calculation from emission spectrum

For the rare earth doped thin film materials, the absorption bands do not have the well resolved peak features that are seen in the emission spectrum. A method has been proposed to determine the Judd-Ofelt parameters and derived quantities using only the emission spectrum [312]. Here, a succinct description of the method proposed is presented.

According to [145], the intensity of spontaneous light emission $I_{J\to J'}$, of a decay transition $\left|l^N SLJ\right\rangle \to \left|l^N S'L'J'\right\rangle$, is proportional to the energy of the emitted photon $hv_{J\to J'}$, multiplied by the spontaneous transition probability $A_{J\to J'}$:

$$I(v_{J\to J'}) \propto hv_{J\to J'} A_{J\to J'} \tag{6.9}$$

From the emission spectra, the total spontaneous emission probability $A_{J\to J'}$ of each transition band is calculated by integrating the area below the peak, divided by the energy of the emitted photon:

$$A_{J\to J'} \propto \int_{v_{min}}^{v_{max}} I_{JJ'}(v)(hv_{JJ'})^{-1} dv \tag{6.10}$$

Using equation 6.10, the experimental branching ratios can be calculated for each transition band according to equation 6.11. From the experimental banching ratio, the radiative lifetime can be examined as follows:

$$\beta^{exp}_{J\to J'} = \frac{A_{J\to J'}}{\sum_{J'} A_{J\to J'}} = A_{J\to J'}\tau_{rad} \tag{6.11}$$

Considering the ED and MD components of the spontaneous emission probability, the experimental branching ratio can be expressed in terms of the Judd-Ofelt parameters.

$$\frac{\beta^{exp}_{J\to J'}}{\tau_{rad}} = A^{oe}_{J\to J'} \left(\sum_{i=2,4,6} \Omega_i \left| \left\langle U^i_{J\to J'} \right\rangle \right|^2 \right) + A^{MD}_{J\to J'} \tag{6.12}$$

$$A^{oe}_{J\to J'} = \frac{16\pi^3 e^2}{3\varepsilon_0 h \bar{\lambda}^3 (2J+1)} \frac{n^2(n^2+2)^2}{9}$$

In order to avoid meaningless negative values for the Judd-Ofelt parameters, equation 6.12 can be rewritten in a matrix form as given by equation 6.13. Herein the squared matrix elements of the MD

terms are represented by $k_{JJ'}$ for each $J \rightarrow J'$ transition and the radiative lifetime is represented by y.

$$\begin{gathered}\left(\sum_i A^{oe}_{J\rightarrow J'} \left|\left\langle U^i_{J\rightarrow J'}\right\rangle\right|^2\right)\Omega_i = \frac{\beta^{exp}_{J\rightarrow J'}}{y} - A^{MD}_{J\rightarrow J'}(k_{JJ'}) \\ M\hat{\Omega} = b\end{gathered} \tag{6.13}$$

where $M = \begin{bmatrix} A^{oe}_1 \left|\left\langle U^2_1\right\rangle\right|^2 & A^{oe}_1 \left|\left\langle U^4_1\right\rangle\right|^2 & A^{oe}_1 \left|\left\langle U^6_1\right\rangle\right|^2 \\ A^{oe}_2 \left|\left\langle U^2_2\right\rangle\right|^2 & A^{oe}_2 \left|\left\langle U^4_2\right\rangle\right|^2 & A^{oe}_2 \left|\left\langle U^6_2\right\rangle\right|^2 \\ \vdots & \vdots & \vdots \\ A^{oe}_N \left|\left\langle U^2_N\right\rangle\right|^2 & A^{oe}_N \left|\left\langle U^4_N\right\rangle\right|^2 & A^{oe}_N \left|\left\langle U^6_N\right\rangle\right|^2 \end{bmatrix} \quad J \rightarrow J' = 1, 2, 3...N$

and $b = \begin{bmatrix} \beta^{exp}_1/y - A^{MD}_1(k_1) \\ \beta^{exp}_2/y - A^{MD}_2(k_2) \\ \vdots \\ \beta^{exp}_N/y - A^{MD}_N(k_N) \end{bmatrix}$

Herein $k_{JJ'}$ and y are minimizing parameters. The matrix $\hat{\Omega}$ is the matrix of the least squares estimates Judd-Ofelt parameters given by 6.14, and whose expresions are now function of the minizing parameters.

$$\begin{gathered}\hat{\Omega} = \left(M^T M\right)^{-1} M^T b \\ \hat{\Omega} = \hat{\Omega}\left(y,\, k_1,\, k_2...k_N\right)\end{gathered} \tag{6.14}$$

According to the definition of the radiative lifetime, $\tau = 1/\sum_{J'} A_{J\rightarrow J'}$, it can now be expressed in terms of the Judd-Ofelt parameter expressions derived from the least square matrix $\hat{\Omega}\left(y,\, k_1,\, k_2...k_N\right)$ elements.

$$\tau_{rad} = \sum_{J'} \left(A^{oe}_{J\rightarrow J'} \left(\sum_{i=2,4,6} \Omega_i(y,\, k_1,\, k_2...k_N) \left|\left\langle U^i_{J\rightarrow J'}\right\rangle\right|^2 \right) + A^{MD}_{J\rightarrow J'} \right) \tag{6.15}$$

Since the radiative lifetime itself is a minimizing parameter represented by y, the problem is reduced to find the parameters y, k_1, ..., k_N that minimize the estimator χ^2 given by:

$$\chi^2 = \left(y - \frac{1}{\sum_{J'} A_{J\rightarrow J'}(y,\, k_1,\, k_2...k_N)} \right)^2 \tag{6.16}$$

Because of the complexity of equation 6.16 and the multiple solutions for the minimizing parameters that do not necessarily have a physical meaning, it is required to use appropriate conditions to avoid meaningless solutions for y and k_i . The conditions are twofold: (1) the parameters themselves must be positive values (or $y > 0$ and $k_i > 0$) since they represent the radiative lifetime and the squared matrix elements of the MD contribution; and (2) the values of y and k_i when replaced in equation 6.14 shall give positive Judd-Ofelt parameter values. Moreover, the error in the calculation of the Judd-Ofelt parameters is given by the product of the square root of the respective diagonal matrix element of the matrix $\left(M^T M\right)^{-1}$ and the RMS deviation as follows:

$$RMS = \left[\sum_{J'} (\beta^{exp}_{J \to J'} - \beta^{cal}_{J \to J'})^2 / (N - m) \right]^{1/2} \tag{6.17}$$

where N is the number of transitions and m is the number of parameters used in the minimizing procedure. The proposed method has been implemented in Mathematica 11.0 to perform the complex calculations and find the variables y, k_1, ..., k_N that minimize the value of the χ^2 estimator. This method requires three input information: the experimental branching ratios calculated from the peak areas of the emission spectrum band transitions, the mean wavelength $\bar{\lambda}$ calculated for each transition peak and the refractive index n of the host material. The validity of the proposed method has been tested by comparing the results obtained with the ones reported in literature data. For instance, the calculated radiative lifetimes with the proposed method have a relative error less than 2% with the reported values. More details and guidelines for the validation and verification of the proposed method can be found in [312].

Bibliography

[1] S. Belmokhtar, A. Bouajaj, M. R. Britel, S. Normani, C. Armellini, M. Ferrari, F. Enrichi, A. Lukowiak, B. Boulard, F. Enrichi, F. Belluomo, and A. Di Stefano Meridionale. Enhancing photovoltaic performance of silicon solar cells by rare earth doped glass ceramic. In *2015 3rd International Renewable and Sustainable Energy Conference (IRSEC)*, pages 1–5, Dec 2015.

[2] Lin Min, Zhao Ying, Wang Shuqi, Liu Ming, Duan Zhenfeng, Chen Yongmei, Li Fei, Xu Feng, and Lu Tian. Recent advances in synthesis and surface modification of lanthanide-doped upconversion nanoparticles for biomedical applications. *Biotechnology advances*, 30:1551–61, 04 2012.

[3] Anthony Kenyon. Recent developments in rare-earth doped materials for optoelectronics progress. *Progress in Quantum Electronics*, 26:225–284, 12 2002.

[4] Dahal Rajendra, Lin Joung-Yol, X. Jiang H, and J Zavada. *Er-Doped GaN and InxGa1-xN for Optical Communications*, volume 124, pages 115–157. 06 2010.

[5] Wakahara A., Takemoto K., Oikawa F., Okada H., Ohshima T., and Itoh H. Investigation of Tb-related green emission in group-III nitrides by time-resolved photoluminescence measurement. *physica status solidi (a)*, 205(1):56–59, 2008.

[6] Richardson H. H., Van Patten P. G., Richardson D. R., and Kordesch M. E. Thin-film electroluminescent devices grown on plastic substrates using an amorphous AlN:Tb3+ phosphor. *Applied Physics Letters*, 80(12):2207–2209, 2002.

[7] El Ouafi Mariem, Belmokhtar Saloua, Bouajai A, Britel Mohammed Reda, Enrichi Francesco, Armellini C, Chiappini A, Meneghet M, Ngoc TranThi, Zur Lidia, Belluomo F, and Ferrari Maurizio. Rare earth ions doped down-conversion materials for third generation photovoltaic solar cells. pages 1–4, 12 2017.

[8] Alombert Goget Guillaume, Ristic Davor, Chiasera Alessandro, Varas S, Ferrari Maurizio, Righini Giancarlo, Dieudonne Belto, and Boulard Brigitte. Down-converter based on rare earth doped fluoride glass to improve Si-based solar cell efficiency. *Proceedings of SPIE*, 8069, 05 2011.

[9] Taguchi Akihito, Takahei Kenichiro, and Horikoshi Yoshiji. Multiphonon assisted energy transfer between Yb 4f shell and InP host. *Journal of Applied Physics*, 76(11):7288–7295, 1994.

[10] Neuhalfen A. J. and Wessels B. W. Thermal quenching of Er3+ related luminescence in In1-xGaxP. *Applied Physics Letters*, 60(21):2657–2659, 1992.

[11] P. N. Favennec, H. L'Haridon, M. Salvi, D. Moutonnet, and Y. Le Guillou. Luminescence of erbium implanted in various semiconductors: IV, III-V and II-VI materials. *Electronics Letters*, 25(11):718–719, May 1989.

[12] Zanatta A. R. Photoluminescence quenching in Er-doped compounds. *Applied Physics Letters*, 82(9):1395–1397, 2003.

[13] Wang Y. Q. and Steckl A. J. Three-color integration on rare-earth-doped GaN electroluminescent thin films. *Applied Physics Letters*, 82(4):502–504, 2003.

[14] Ananta Acharya. Group iii-nitride semiconductors: Preeminent materials for modern electronic and optoelectronic applications. *Himalayan Physics*, 5:22–26, Jun. 2015.

[15] Stan George, Pasuk Iuliana, Galca Aurelian, and Dinescu A. Highly textured (001) AlN nanostructured thin films synthesized by reactive magnetron sputtering for saw and fbar applications. *Digest Journal of Nanomaterials and Biostructures*, 5:1041–1054, 10 2010.

[16] Deniz D., Karabacak T., and Harper J. M. E. Competitive growth mechanisms of aluminum nitride thin films deposited by off-normal reactive magnetron sputtering. *Journal of Applied Physics*, 103(8):083553, 2008.

[17] Roy Gordon, Umar Riaz, and David M. Hoffman. Chemical vapor deposition of aluminum nitride thin films. *Journal of Materials Research*, 7:1679 – 1684, 07 1992.

[18] M Ishihara, K Yamamoto, F Kokai, and Y Koga. Aluminum nitride thin films prepared by radical-assisted pulsed laser deposition. *Vacuum*, 59(2):649 – 656, 2000. Proceedings of the Fifth International Symposium on Sputtering and Plasma Processes.

[19] Patrick Kung. Chapter 2. the rise of III-nitrides: An introduction. In M. Razeghi and M. Henini, editors, *Optoelectronic Devices: III Nitrides*, pages 9 – 22. Elsevier, Oxford, 2005.

[20] Schubert E.F. *Light-Emitting Diodes*. Cambridge University Press, 2006.

[21] Janotta A., Schmidt M., Janssen R., Stutzmann M., and Buchal Ch. Photoluminescence of er^{3+} implanted amorphous hydrogenated silicon suboxides. *Phys. Rev. B*, 68:165207, Oct 2003.

[22] A R Zanatta. Effect of thermal annealing treatments on the optical properties of rare-earth-doped AlN films. *Journal of Physics D: Applied Physics*, 42(2):025109, 2009.

[23] J. A Guerra, F. Benz, A. R. Zanatta, H. P Strunk, A. Winnacker, and R. Weingartner. Concentration quenching and thermal activation of the luminescence from terbium-doped a-SiC:H and c-AlN thin films. *physica status solidi c*, 10(1):68–71, 2013.

[24] S Abedrabbo, B Lahlouh, and A T Fiory. Analytical study of thermal annealing behaviour of erbium emission in Er2O3 sol gel silica films. *Journal of Physics D: Applied Physics*, 44(31):315401, 2011.

[25] N. Azema, J. Durand, R. Berjoan, C. Dupuy, and L. Cot. Oxidation stages of aluminium nitride thin films obtained by plasma-enhanced chemical vapour deposition (PECVD). *Journal of the European Ceramic Society*, 8(5):291 – 298, 1991.

[26] Masashi Yamashita, Yukichi Sasaki, Hiroki Ito, Hitoshi Ohsato, and Noriyoshi Shibata. Fabrication of aluminum nitride thin film and its oxidation behavior. *Journal of the Society of Materials Science, Japan*, 55(8):785–789, 2006.

[27] Svedberg Lynne M., Arndt Kenneth C., and Cima Michael J. Corrosion of aluminum nitride (AlN) in aqueous cleaning solutions. *Journal of the American Ceramic Society*, 83(1):41–46, 2000.

[28] Barbara Mitchell, D. Timmerman, Jonathan D. Poplawsky, Weiguang Zhu, Donghoon Lee, Rika Wakamatsu, J. Takatsu, Masami Matsuda, Wei Guo, K. Lorenz, E. Alves, Asuka Koizumi, Volkmar Dierolf, and Yuichiro Fujiwara. Utilization of native oxygen in Eu(RE)-doped GaN for enabling device compatibility in optoelectronic applications. In *Scientific reports*, 2016.

[29] L. G. van Uitert and S. Iida. Quenching interactions between rare-earth ions. *Chemical Physics*, 37:986–992, 09 1962.

[30] Hideomi Koinuma and Ichiro Takeuchi. Combinatorial solid-state chemistry of inorganic materials. *Nature materials*, 3:429–38, 2004.

[31] Potyrailo Radislav, Rajan Krishna, Stoewe Klaus, Takeuchi Ichiro, Chisholm Bret, and Lam Hubert. Combinatorial and high-throughput screening of materials libraries: Review of state of the art. *ACS Combinatorial Science*, 13(6):579–633, 2011. PMID: 21644562.

[32] Danielson Earl, H. Golden Josh, W. McFarland Eric, M. Reaves Casper, Henry Weinberg W, and Di Wu Xin. A combinatorial approach to the discovery and optimization of luminescent materials. *Nature*, 389:944–948, 10 1997.

[33] Walsh Brian M. Judd-ofelt theory: principles and practices. In Baldassare Di Bartolo and Ottavio Forte, editors, *Advances in Spectroscopy for Lasers and Sensing*, pages 403–433, Dordrecht, 2006. Springer Netherlands.

[34] Ofelt G. S. Intensities of crystal spectra of rare earth ions. *The Journal of Chemical Physics*, 37(3):511–520, 1962.

[35] B. R. Judd. Optical intensities of rare-earth ions. *Physical Review*, 127:750–761, 08 1962.

[36] Arturas Zukauskas, Shur Michael, and Gaska Remis. *Introduction to Solid-State Light*, volume 1. 01 2002.

[37] P. Kathirgamanathan, L. M. Bushby, M. Kumaraverl, S. Ravichandran, and S. Surendrakumar. Electroluminescent organic and quantum dot LEDs: The state of the art. *Journal of Display Technology*, 11(5):480–493, May 2015.

[38] H. J. Round. A note on carborundum. *Electrical World*, 49:309, 1907.

[39] Holonyak Nick and Bevacqua S. F. Coherent (visible) light emission from Ga(As1-1xPx)junctions. *Applied Physics Letters*, 1(4):82–83, 1962.

[40] Patrick Mottier. *LEDs for lighting applications*. Wiley, 2009.

[41] Alexey N. Krasnov. Electroluminescent displays: history and lessons learned. *Displays*, 24(2):73–79, 2003.

[42] Sebastien Cueff, Christophe Labbe, Olivier Jambois, Yonder Berencen, Anthony J. Kenyon, Blas Garrido, and Richard Rizk. Structural factors impacting carrier transport and electroluminescence from Si nanocluster-sensitized Er ions. *Opt. Express*, 20(20):22490–22502, Sep 2012.

[43] Faiz Rahman. Solid-state lighting with wide band gap semiconductors. *MRS Energy and Sustainability*, 1:E6, 2014.

[44] Lee D. S. and Steckl A. J. Enhanced blue and green emission in rare-earth-doped GaN electroluminescent devices by optical photopumping. *Applied Physics Letters*, 81(13):2331–2333, 2002.

[45] Kryshtab T, Khomchenko V.S., Adame Andraca, Zavyalova L.V., Roshchina N.N., Rodionov V.E., and Khachatryan V.B. Preparation and properties of thin ZnS:Cu films phosphors. *Thin Solid Films*, 515:513–516, 10 2006.

[46] Vlasenko N A and Popkov I A. Study of the electroluminescence of a sublimed ZnS-Mn phosphor. *Optics and Spectroscopy*, 8(39), 1960.

[47] Adrian Tikai. *Principles of Solar Cells, LEDs and Diodes: The role of the PN junction*, chapter 5, pages 215–252. John Wiley and Sons, Ltd, 2011.

[48] Bailey P., Carkner D., and Wu X. Trailing edge light emission from ZnS:Mn and ZnS:Tb, F in a thick dielectric electroluminescent display. *Journal of Applied Physics*, 81(2):931–936, 1997.

[49] Bringuier E. Impact excitation in ZnS-type electroluminescence. *Journal of Applied Physics*, 70(8):4505–4512, 1991.

[50] John A. Edmond, Hua-Shuang Kong, and Calvin H. Carter. Blue LEDs, UV photodiodes and high-temperature rectifiers in 6H-SiC. In Chris G. Van de Walle, editor, *Wide Band Gap Semiconductors*, pages 453–460. Elsevier, Amsterdam, 1993.

[51] Potter Ralph M., Blank John M., and Addamiano Arrigo. Silicon carbide light emitting diodes. *Journal of Applied Physics*, 40(5):2253–2257, 1969.

[52] J.I. Pankove, E.A. Miller, D. Richman, and J.E. Berkeyheiser. Electroluminescence in GaN. *Journal of Luminescence*, 4(1):63 – 66, 1971.

[53] J.I. Pankove, E.A. Miller, and J.E. Berkeyheiser. GaN blue light-emitting diodes. *Journal of Luminescence*, 5(1):84 – 86, 1972.

[54] Nakamura Shuji, Mukai Takashi, and Senoh Masayuki. Candela class high brightness InGaN/AlGaN double heterostructure blue light emitting diodes. *Applied Physics Letters*, 64(13):1687–1689, 1994.

[55] A.J. Steckl, J. Heikenfeld, D.S. Lee, and M. Garter. Multiple color capability from rare earth-doped gallium nitride. *Materials Science and Engineering: B*, 81(1):97 – 101, 2001.

[56] Wang Cai-Feng, Li Qing-Shan, Wang Ji-Suo, Zhao Feng-Zhou, and Zhang Li-Chun. White light emission from ZnS:Mn thin films deposited on GaN substrates by pulsed laser deposition. *Chinese Physics Letters*, 33:076802, 07 2016.

[57] James D. Patterson and Bernard C. Bailey. *Solid-State Physics: Introduction to the Theory*. Springer-Verlag Berlin Heidelberg, 2007.

[58] *Physics of Nanostructured Solid State Devices*. New York: Springer, 2012.

[59] Harald Ibach and Hans Luth. *Solid-State Physics: An Introduction to Principles of Materials Science*. Berlin: Springer-Verlag, 4th Edition, 2009.

[60] Joshua Owolabi Adeyemi, Onimisi Muhammad, Abdu Sadiq, and Olowomofe Olawale. Determination of band structure of gallium-arsenide and aluminium-arsenide using density functional theory. *Computational Chemistry*, 04:73–82, 01 2016.

[61] M.G. Craford, S.A. Stockman, M.J. Peanasky, and F.A. Kish. Chapter 1 visible light-emitting diodes. In Gerd Mueller, editor, *Electroluminescence I*, volume 64 of *Semiconductors and Semimetals*, pages 1 – 47. Elsevier, 1999.

[62] P. W. Anderson. Absence of diffusion in certain random lattices. *Phys. Rev.*, 109:1492–1505, Mar 1958.

[63] R. A. Street. *Hydrogenated Amorphous Silicon*. Cambridge Solid State Science Series. Cambridge University Press, 1991.

[64] M. Stutzmann. The defect density in amorphous silicon. *Philosophical Magazine B*, 60(4):531–546, 1989.

[65] Morigaki K. *Physics of Amorphous Semiconductors*. London: World Scientific Publishing Company, 1999.

[66] Adachi Sadao. *Optical properties of crystalline and amorphous semiconductors : materials and fundamental principles*. Boston : Kluwer Academic Publishers, 1999. Includes bibliographical references and index.

[67] J. Singh and K. Shimakawa. *Advance of Amorphous Semiconductors*. London: CRC Press, 2003.

[68] *Fundamentals of Semiconductors: Physics and Materials properties*. Springer 3rd Edition, 2005.

[69] Freeman Eva C. and Paul William. Optical constants of rf sputtered hydrogenated amorphous Si. *Phys. Rev. B*, 20:716–728, Jul 1979.

[70] A P Sokolov, A P Shebanin, O A Golikova, and M M Mezdrogina. Structural disorder and optical gap fluctuations in amorphous silicon. *Journal of Physics: Condensed Matter*, 3(49):9887–9894, dec 1991.

[71] Franz Urbach. The long-wavelength edge of photographic sensitivity and of the electronic absorption of solids. *Phys. Rev.*, 92:1324–1324, Dec 1953.

[72] J. A. Guerra, L. M. Montanez, F. De Zela, and A. Winnacker R. Weingartner. On the origin of the urbach rule and the urbach focus. *MRS Proceedings*, 1536:139–145, 01 2013.

[73] Zhang Fangqing, Xue Hua, Song Zhizhong, Guo Yongping, and Chen Guanghua. Effect of high-temperature annealing on the optical absorption edge of hydrogenated amorphous silicon-carbon films. *Phys. Rev. B*, 46:4590–4594, Aug 1992.

[74] L. M. Montanez, J. A. Guerra, K. Zegarra, S. Kreppel, F. De Zela, A. Winnacker, and R. Weingartner. Optical bandgap enhancement of a-SiC through hydrogen incorporation and thermal annealing treatments. *Proc.SPIE*, 8785:8780–8785, 2013.

[75] J. A. Guerra, Liz Montanez, O Erlenbach, Gonzalo Galvez de la Puente, Francisco De Zela, A Winnacker, and R. Weingartner. Determination of the optical bandgap and disorder energies of thin amorphous SiC and AlN films produced by radio frequency magnetron sputtering. *Journal of Physics: Conference Series*, 274, 2011.

[76] Dow John D. and Redfield David. Theory of exponential absorption edges in ionic and covalent solids. *Phys. Rev. Lett.*, 26:762–764, Mar 1971.

[77] N F Mott and E A Davis. *Electronic Processes in Non-Crystalline Materials*. Oxford: Clarendon Press 2nd Edition, 1979.

[78] Sajeev John, Costas Soukoulis, Morrel H. Cohen, and E. N. Economou. Theory of electron band tails and the urbach optical-absorption edge. *Phys. Rev. Lett.*, 57:2877–2877, Dec 1986.

[79] O'Leary Stephen K., Zukotynski Stefan, and Perz John M. Optical absorption in amorphous semiconductors. *Phys. Rev. B*, 52:7795–7797, Sep 1995.

[80] Moseley Leslie and Lukes T. A simplified derivation of the kubo-greenwood formula. *American Journal of Physics*, 46:676–677, 06 1978.

[81] J. A. Guerra, J. R. Angulo, S. Gomez, J. Llamoza, L. M. Montanez, A. Tejada, J. A. Töfflinger, A. Winnacker, and R. Weingärtner. The urbach focus and optical properties of amorphous hydrogenated SiC thin films. *Journal of Physics D: Applied Physics*, 49(19):195102, apr 2016.

[82] J. A. Guerra, A. Tejada, L. Korte, L. Kegelmann, J. A. Tofflinger, S. Albrecht, B. Rech, and R. Weingartner. Determination of the complex refractive index and optical bandgap of CH3NH3PbI3 thin films. *Journal of Applied Physics*, 121(17):173104, 2017.

[83] J. A. Guerra, A. Tejada, J. A. Tofflinger, R. Grieseler, and L. Korte. Band-fluctuations model for the fundamental absorption of crystalline and amorphous semiconductors. a dimensionless joint density of states analysis. *Journal of Physics D Applied Physics*, 52(10):105303, 2019.

[84] Deutsch T. Sunlight. Water and III-V Nitrides for Fueling the Future. *PhD Thesis, Boulder, Colorado*, 98, 2006.

[85] Yuichi Oshima, Takeshi Eri, Masatomo Shibata, Haruo Sunakawa, Kenji Kobayashi, Toshinari Ichihashi, and Akira Usui. Preparation of freestanding gan wafers by hydride vapor phase epitaxy with void-assisted separation. *Japanese Journal of Applied Physics*, 42(Part 2, No.1A/B):L1–L3, jan 2003.

[86] Vurgaftman I. and Meyer J. R. Band parameters for nitrogen-containing semiconductors. *Journal of Applied Physics*, 94(6):3675–3696, 2003.

[87] Y Goldberg, Michael Levinshtein, and Sergey Rumyantsev. Properties of advanced semiconductor materials: GaN, AIN, InN, BN, SiC, SiGe. *SciTech Book News*, 25:93–146, 01 2001.

[88] G. A. Jeffrey and G. S. Parry. Crystal structure of aluminum nitride. *The Journal of Chemical Physics*, 23(2):406–406, 1955.

[89] A. Stolz, A. Soltani, B. Abdallah, J. Charrier, D. Deresmes, P.Y. Jouan, M.A. Djouadi, E. Dogheche, and J.C. De Jaeger. Optical properties of aluminum nitride thin films grown by direct-current magnetron sputtering close to epitaxy. *Thin Solid Films*, 534:442–445, 2013.

[90] Gillinger M, Schneider M, Bittner A, Nicolay P, and Schmid U. Impact of annealing temperature on the mechanical and electrical properties of sputtered aluminum nitride thin films. *Journal of Applied Physics*, 117(6):065303, 2015.

[91] Aleksej Majkić, Uroš Puc, Alexander Franke, Ronny Kirste, Ramón Collazo, Zlatko Sitar, and Marko Zgonik. Optical properties of aluminum nitride single crystals in the THz region. *Opt. Mater. Express*, 5(10):2106–2111, Oct 2015.

[92] H. Altuntas, C. Ozgit-Akgun, I. Donmez, and N. Biyikli. Effect of film thickness on the electrical properties of AlN films prepared by plasma-enhanced atomic layer deposition. *IEEE Transactions on Electron Devices*, 62(11):3627–3632, Nov 2015.

[93] Zhenghua An, Chuanling Men, Zhengkui Xu, Paul K. Chu, and Chenglu Lin. Electrical properties of AlN thin films prepared by ion beam enhanced deposition. *Surface and Coatings Technology*, 196(1):130–134, 2005. 13th International Conference on surface modification of materials by ion beams.

[94] C. Morosanu, T. A. Stoica, T. F. Stoica, D. Necsoiu, and M. Popescu. Optical, electrical and structural properties of AlN thin films. In *1995 International Semiconductor Conference. CAS '95 Proceedings*, pages 183–186, Oct 1995.

[95] D. Liufu and K. C. Kao. Piezoelectric, dielectric and interfacial properties of aluminum nitride films. *Journal of Vacuum Science and Technology A*, 16(4):2360–2366, 1998.

[96] M.A. Signore, A. Taurino, D. Valerini, A. Rizzo, I. Farella, M. Catalano, F. Quaranta, and P. Siciliano. Role of oxygen contaminant on the physical properties of sputtered AlN thin films. *Journal of Alloys and Compounds*, 649:1267–1272, 2015.

[97] J. Garcia, J. A. Gomez, J. Ferron, E. Gautron, J. Manuel, B. Abdallahand A. Djouadi, J. Feugeas, and P. Y. Jouan. Aln thin films deposited by DC reactive magnetron sputtering. effect of oxygen on film growth. *The European Physical Journal Applied Physics*, 64, 10 2013.

[98] J. A. Edmond, D. C. Waltz, S. Brueckne, H. S. Kong, I. W. Palmour, and C. H. Carter Jr. High temperature rectifiers in 6h-silicon carbide. *Trans. 1st Int. High Temp. Elec. Conf*, page 207, 1991.

[99] Konorova E.A., Kuznetsov Yu.A., Sergienko V.F., Tkachenko S.D., Tsikunov A.V., Spitsyn A.V., and Danyushevskii Yu.Z. Impact ionization in semiconductor structures made of ion-implanted diamond. *Soviet physics. Semiconductors*, 17:146–149, 02 1983.

[100] Bogdanov A. V. Investigation of microplasma breakdown at a contact between a metal and a semiconducting diamond. *Sov. Phys. Semicond.*, 16:720, 1982.

[101] M. N. Yoder. Wide bandgap semiconductor materials and devices. *IEEE Transactions on Electron Devices*, 43(10):1633–1636, Oct 1996.

[102] Yamanaka T., Morimoto S., and Kanda H. Influence of the isotope ratio on the lattice constant of diamond. *Phys. Rev. B*, 49:9341–9343, Apr 1994.

[103] Michael E. Thomas and William J. Tropf. Optical properties of diamond, 1994.

[104] P. T. B. Shaffer. Refractive index, dispersion, and birefringence of silicon carbide polytypes. *Appl. Opt.*, 10(5):1034–1036, May 1971.

[105] Wang Shunchong, Zhan Minjie, Wang Gang, Xuan Hongwen, Zhang Wei, Liu Chunjun, Xu Chunhua, Liu Yu, Wei Zhiyi, and Chen Xiaolong. 4H-SiC: a new nonlinear material for midinfrared lasers. *Laser & Photonics Reviews*, 7(5):831–838, 2013.

[106] Giorgio Turri, Scott Webster, Ying Chen, Benjamin Wickham, Andrew Bennett, and Michael Bass. Index of refraction from the near-ultraviolet to the near-infrared from a single crystal microwave-assisted cvd diamond. *Opt. Mater. Express*, 7(3):855–859, Mar 2017.

[107] Long X.C., Myers R. A., Brueck S. R. J., Ramer R., Zheng K., and Hersee S. D. GaN linear electro-optic effect. *Applied Physics Letters*, 67(10):1349–1351, 1995.

[108] Barker A. S. and Ilegems M. Infrared lattice vibrations and free-electron dispersion in GaN. *Phys. Rev. B*, 7:743–750, Jan 1973.

[109] Green Martin A. and Keevers Mark J. Optical properties of intrinsic silicon at 300 k. *Progress in Photovoltaics: Research and Applications*, 3(3):189–192, 1995.

[110] Pierce D. T. and Spicer W. E. Electronic structure of amorphous si from photoemission and optical studies. *Phys. Rev. B*, 5:3017–3029, Apr 1972.

[111] Takahashi K., Yoshikawa A., and Sandhu A. *Wide Bandgap Semiconductors. Fundamental Properties and Modern Photonic and Electronic Devices.* Springer Berlin Heidelberg, 2007.

[112] Ahmad I., Holtz M., Faleev N. N., and Temkin H. Dependence of the stress-temperature coefficient on dislocation density in epitaxial GaN grown on a-Al2O3 and 6H-SiC substrates. *Journal of Applied Physics*, 95(4):1692–1697, 2004.

[113] Kucheyev S. O., Bradby J. E., Williams J. S., Jagadish C., Toth M., Phillips M. R., and Swain M. V. Nanoindentation of epitaxial gan films. *Applied Physics Letters*, 77(21):3373–3375, 2000.

[114] Matsumoto Tsubasa, Nishizawa Shin Ichi, and Yamasaki Satoshi. Calculation of lattice constant of 4h-sic as a function of impurity concentration. In *Silicon Carbide and Related Materials 2009*, volume 645 of *Materials Science Forum*, pages 247–250. Trans Tech Publications, 7 2010.

[115] Morkoc H. *Handbook of Nitride Semiconductors and Devices, Materials Properties, Physics and Growth*. Handbook of Nitride Semiconductors and Devices. Wiley, 2009.

[116] V Cimalla, Joerg Pezoldt, and Oliver Ambacher. Group iii nitride and SiC based MEMS and NEMS: Materials properties, technology and applications. *J. Phys. D: Appl. Phys*, 40:6386–6434, 10 2007.

[117] Kimoto T. and Cooper J.A. *Fundamentals of Silicon Carbide Technology: Growth, Characterization, Devices and Applications*. Wiley - IEEE. Wiley, 2014.

[118] M. Bhatnagar and B. J. Baliga. Comparison of 6H-SiC, 3C-SiC, and Si for power devices. *IEEE Transactions on Electron Devices*, 40(3):645–655, March 1993.

[119] Francesco Bertazzi, Michele Moresco, and Enrico Bellotti. Theory of high field carrier transport and impact ionization in wurtzite GaN. part i: A full band monte carlo model. *Journal of Applied Physics*, 106(6):063718, 2009.

[120] B Benbakhti, M Rousseau, A Soltani, and J. C De Jaeger. Electron transport properties of gallium nitride for microscopic power device modelling. *Journal of Physics: Conference Series*, 193:012005, nov 2009.

[121] O'Leary Stephen K., Foutz Brian E., Shur Michael S., and Eastman Lester F. Steady-state electron transport in the iii-v nitride semiconductors: A sensitivity analysis. *Journal of Electronic Materials*, 32(5):327–334, May 2003.

[122] Jun Wu, Hiroyuki Yaguchi, Kentaro Onabe, Yasuhiro Shiraki, and Ryoichi Ito. Metalorganic vapor phase epitaxy growth of high quality cubic GaN on GaAs (100) substrates. *Japanese Journal of Applied Physics*, 37(Part 1, No. 3B):1440–1442, mar 1998.

[123] S. Yoshida, H. Okumura, S. Misawa, and E. Sakuma. Hetero-epitaxial growth of cubic GaN on GaAs by gas-source molecular beam epitaxy. *Surface Science*, 267(1):50 – 53, 1992.

[124] Sverdlov B. N., Martin G. A., Morkoc H., and Smith David J. Formation of threading defects in GaN wurtzite films grown on nonisomorphic substrates. *Applied Physics Letters*, 67(14):2063–2065, 1995.

[125] Kozawa T., Kachi T., Kano H., Nagase H., Koide N., and Manabe K. Thermal stress in GaN epitaxial layers grown on sapphire substrates. *Journal of Applied Physics*, 77(9):4389–4392, 1995.

[126] Matthew H. Kane and Nazmul Arefin. Gallium nitride GaN on silicon substrates for LEDs. In Jian Jang Huang, Hao-Chung Kuo, and Shyh-Chiang Shen, editors, *Nitride Semiconductor Light-Emitting Diodes (LEDs) (Second Edition)*, Woodhead Publishing Series in Electronic and Optical Materials, pages 79–121. Woodhead Publishing, second edition edition, 2018.

[127] E. Salmani, A. Marjaoui, O. Mounkachi, M. Ben Ali, H. El Moussaoui, H. Ez-Zahraouy, M. Hamedoun, M. Benaissa, and A. Benyoussef. Band gap engineering of (InGaN) for photovoltaic application. In *2014 International Renewable and Sustainable Energy Conference (IRSEC)*, pages 602–607, Oct 2014.

[128] Theodore D. Moustakas. Ultraviolet optoelectronic devices based on AlGaN alloys grown by molecular beam epitaxy. *MRS Communications*, 6(3):247–269, 2016.

[129] Ray-Hua Horng, Dong-Sing Wuu, Chia-Feng Lin, and Chun-Feng Lai. Recent development of fabrication technologies of nitride leds for performance improvement. In JianJang Huang, Hao-Chung Kuo, and Shyh-Chiang Shen, editors, *Nitride Semiconductor Light-Emitting Diodes (LEDs) (Second Edition)*, Woodhead Publishing Series in Electronic and Optical Materials, pages 209–241. Woodhead Publishing, second edition edition, 2018.

[130] Persson C. and Lindefelt U. Detailed band structure for 3C-, 2H-, 4H-, 6H-SiC, and Si around the fundamental band gap. *Phys. Rev. B*, 54:10257–10260, Oct 1996.

[131] H M. Jennings, B J. Dalgleish, and P L. Pratt. Reactions between silicon and nitrogen. *Journal of Materials Science*, 23:2573–2583, 07 1988.

[132] Madelung O., von der Osten W., and U. Rössler. *Intrinsic Properties of Group IV Elements and III-V, II-VI and I-VII Compounds*. Condensed Matter. Springer, 1986.

[133] Pan L.S. and Kania D.R. *Diamond. Electronic Properties and Applications*. Electronic Materials: Science & Technology. Springer US, 2013.

[134] Asmussen J. and Reinhard D. *Diamond Films Handbook*. Taylor and Francis, 2002.

[135] A.M. Zaitsev. *Optical Properties of Diamond. A Data Handbook*. Springer Berlin Heidelberg, 2013.

[136] Hirohiko Katayama, Shunri Oda, and Hiroshi Kukimoto. Zns blue light emitting diodes with an external quantum efficiency of 5x10-4. *Applied Physics Letters*, 27:697 – 699, 01 1976.

[137] H. Cheng and J. M. DePuydt. ZnSe-based blue/green light emitting diodes. In *LEOS 1991 Summer Topical Meetings on Epitaxial Materials and In-Situ Processing for Optoelectronic Devices. Photonics and Optoelectronics*, pages 29–29, July 1991.

[138] Eason David, Yu Zhengtian, C. Hughes W, H. Roland W, Boney C, J. W. Cook Jr, J F. Schetzin, Cantwell G, and C. Harsch W. High-brightness blue and green light-emitting diodes. *Applied Physics Letters*, 66:115–117, 01 1995.

[139] Jagadish C. and Pearton S.J. *Zinc Oxide Bulk, Thin Films and Nanostructures: Processing, Properties, and Applications*. Elsevier Science, 2011.

[140] Kim Sung-Kyu, Jeong Se-Young, and Cho Chae-Ryong. Structural reconstruction of hexagonal to cubic ZnO films on Pt/Ti/SiO2/Si substrate by annealing. *Applied Physics Letters*, 82(4):562–564, 2003.

[141] Bates C H, White W B, and Roy R. New high-pressure polymorph of zinc oxide. *Science*, 137:993, sep 1962.

[142] R. Thangavel, M. Rajagopalan, and J. Kumar. Theoretical investigations on ZnCdO2 and ZnMgO2 alloys. a first principle study. *Solid State Communications*, 137(9):507 – 511, 2006.

[143] K. Ogata, K. Koike, T. Tanite, T. Komuro, F. Yan, S. Sasa, M. Inoue, and M. Yano. ZnO and ZnMgO growth on a-plane sapphire by molecular beam epitaxy. *Journal of Crystal Growth*, 251(1):623 – 627, 2003. Proceedings of the Twelfth International Conference on Molecular Beam Epitaxy.

[144] Sadofev S., Sch/"afer P., Fan Y. H., Blumstengel S., Henneberger F., Schulz D., and Klimm D. Radical-source molecular beam epitaxy of ZnMgO and ZnCdO alloys on ZnO substrates. *Applied Physics Letters*, 91(20):201923, 2007.

[145] Shionoya S., Yen W.M., and Yamamoto H. *Phosphor Handbook*. CRC Press laser and optical science and technology series. CRC Press, 2018.

[146] Smith F. Graham, King Terry A., and Wilkins Dan. *Optics and Photonics: An Introduction*. England: Wiley, 2nd Edition, 2007.

[147] Martin R. M. *Reciprocity between emission and absorption for rare earth ions in glass*. PhD thesis, Worcester Polytechnic Institute, 2006.

[148] Becquerel J. Theorie des phenomenes magneto-optiques dans les cristaux. *Le Radium*, 4:107–118, 1907.

[149] Van Vleck J. H. On the anisotropy of cubic ferromagnetic crystals. *Phys. Rev.*, 52:1178–1198, Dec 1937.

[150] Condon E.U. and Shortley G.H. *The Theory of Atomic Spectra*. Cambridge Univ.Pr.209. Cambridge University Press, 1951.

[151] Racah Giulio. Theory of complex spectra. i. *Phys. Rev.*, 61:186–197, Feb 1942.

[152] Racah Giulio. Theory of complex spectra. ii. *Phys. Rev.*, 62:438–462, Nov 1942.

[153] Racah Giulio. Theory of complex spectra. iii. *Phys. Rev.*, 63:367–382, May 1943.

[154] Racah Giulio. Theory of complex spectra. iv. *Phys. Rev.*, 76:1352–1365, Nov 1949.

[155] Robert D. Cowan. The theory of rare earth eaergy levels and spectra. *Nuclear Instruments and Methods*, 110:173–182, 1973.

[156] Zipora B. Goldschmidt. Chapter 1 atomic properties (free atom). In *Metals*, volume 1 of *Handbook on the Physics and Chemistry of Rare Earths*, pages 1–171. Elsevier, 1978.

[157] M. Goeppert Mayer. Rare-earth and transuranic elements. *Phys. Rev.*, 60:184–187, Aug 1941.

[158] Judd B.R. *Operator Techniques in Atomic Spectroscopy.* Advanced physics monograph series. McGraw-Hill, 1963.

[159] B. G. Wybourne. *Spectroscopic properties of rare earths.* Wiley-Interscience. New York: Wiley, 1965.

[160] S. Hufner. *Optical Spectra of Transparent Rare Earth Compounds.* Elsevier Science, 2012.

[161] Jean-Claude Bunzli and Svetlana Eliseeva. *Basics of Lanthanide Photophysics*, volume 7, pages 1–45. 07 2010.

[162] C. G. Ma, M.G. Brik, D.X. Liu, B. Feng, Ya Tian, and A. Suchocki. Energy level schemes of fn electronic configurations for the di-, tri-, and tetravalent lanthanides and actinides in a free state. *Journal of Luminescence*, 170:369–374, 2016.

[163] G. van der Laan, E. Arenholz, Z. Hu, A. Bauer, E. Weschke, Ch. Schussler-Langeheine, E. Navas, A. Muhlig, G. Kaindl, J. B. Goedkoop, and N. B. Brookes. Magnetic circular dichroism in tb 3d4f resonant photoemission. *Phys. Rev. B*, 59:8835–8843, Apr 1999.

[164] G. van der Laan and B. T. Thole. Strong magnetic x-ray dichroism in 2p absorption spectra of 3d transition metal ions. *Phys. Rev. B*, 43:13401–13411, Jun 1991.

[165] H. Dieke Gerhard. *Spectra and Energy Levels of Rare Earth Ions in Crystals*, volume 38. 1968.

[166] W T. Carnall and H Crosswhite. Energy level structure and transition probabilities in the spectra of the trivalent lanthanides in laf3. *Argonne Natl. Lab. Rept.*, ANL78XX95, 01 1977.

[167] Peijzel P.S., Meijerink Andries, Wegh Rene, Reid Michael, and Burdick Gary. A complete energy level diagram for all trivalent lanthanide ions. *Journal of Solid State Chemistry*, 178:448–453, 02 2005.

[168] C.H. Huang. *Rare Earth Coordination Chemistry: Fundamentals and Applications.* Wiley, 2011.

[169] Markus P. Hehlen, Mikhail G. Brik, and Karl W. Kramer. 50th anniversary of the judd-ofelt theory: An experimentalist view of the formalism and its application. *Journal of Luminescence*, 136:221–239, 2013.

[170] B. Henderson and G.F. Imbusch. *Optical Spectroscopy of Inorganic Solids.* Monographs on the physics and chemistry of materials. Clarendon Press, 2006.

[171] Th. Förster. Zwischenmolekulare energiewanderung und fluoreszenz. *Annalen der Physik*, 437(1-2):55–75, 1948.

[172] T. Förster. *Fluoreszenz organischer Verbindungen*. Göttingen, Vandenhoeck and Ruprecht, 1951.

[173] D. L Dexter. A theory of sensitized luminescence in solids. *The Journal of Chemical Physics*, 21(5):836–850, 1953.

[174] Vij D R. *Handbook of Applied Solid State Spectroscopy*. Springer US, 2007.

[175] Axe J. D. and Weller P. F. Fluorescence and energy transfer in y2o3-eu3+. *The Journal of Chemical Physics*, 40(10):3066–3069, 1964.

[176] J B. Gallivan, J S. Brinen, and J G. Koren. Absorption and polarized phosphorescence spectra of substituted s-triazines. *Journal of Molecular Spectroscopy*, 26:24–35, 05 1968.

[177] Naoto Yamada, Shigeo Shionoya, and Takashi Kushida. Phonon-assisted energy transfer between trivalent rare earth ions. *Journal of The Physical Society of Japan*, 32:1577–1586, 06 1972.

[178] J. A. Guerra. *Optical characterization and thermal activation of Tb doped amorphous SiC, AlN and SiN thin films*. PhD thesis, Pontificia Universidad Católica del Perú and Friedrich-Alexander Universität Erlangen-Nürnberg, 2017.

[179] F.M. Penning. Coating by cathode disintegration. US Patent 2146025, 1939.

[180] J.S. Chapin. Sputtering process and apparatuse. US Patent 4166018, 1979.

[181] Kostas Sarakinos, J Alami, and Stephanos Konstantinidis. High power pulsed magnetron sputtering: A review on scientific and engineering state of the art. *Surface and Coatings Technology*, 204:1661–1684, 02 2010.

[182] M. Ohring. *Materials Science of Thin Films*. Elsevier Science, 2001.

[183] Davood Raoufi and Atefeh Tahernia. The effect of substrate temperature on the microstructural, electrical and optical properties of Sn-doped indium oxide thin films. *The European Physical Journal Applied Physics*, 70, 05 2015.

[184] Zhang Song, Wang Tingting, Zhang Ziyu, Li Jun, Tu Rong, Shen Qiang, Wang Chuanbin, Luo Guoqiang, and Zhang Lianmeng. Microstructure and oxidation behavior of metal v films deposited by magnetron sputtering. *Materials*, 12(3), 2019.

[185] J. A. Thornton. High rate thick film growth. *Annual Review of Materials Science*, 7(1):239–260, 1977.

[186] Movchan B.A. and Demchishin A.V. Structure and properties of thick condensates of nickel, titanium, tungsten, aluminum oxides and zirconium dioxide in vacuum. *Fiz. Metal. Metalloved*, 28:653–660, 1969.

[187] Thornton John A. Influence of apparatus geometry and deposition conditions on the structure and topography of thick sputtered coatings. *Journal of Vacuum Science and Technology*, 11(4):666–670, 1974.

[188] R. Grieseler. *Untersuchung der Eigenschaften sowie der Anwendung von reaktiven Mehrschichtsystemen in der Aufbau und Verbindungstechnik*. PhD thesis, Universitatsverlag Ilmenau, 2015.

[189] Bickermann M., Epelbaum B. M., and Winnacker A. PVT growth of bulk AlN crystals with low oxygen contamination. *Physica Status Solidi (c)*, 0(7):1993–1996, 2003.

[190] K. Tucto, L. Flores, J. A. Guerra, R. Grieseler, T. Kups, J. Pezoldt, A. Osvet, M. Batentschuk, and R. Weingärtner. Effect of post-annealing treatment on the structure and luminescence properties of AIN:Tb3+ thin films prepared by radio frequency magnetron sputtering. In *Material Science and Engineering Technology V*, volume 890 of *Materials Science Forum*, pages 299–302. Trans Tech Publications Ltd, 4 2017.

[191] Scalese S, Franzo Giorgia, Mirabella Salvo, M Re, Terrasi Antonio, F Priolo, Rimini Emanuele, A Camera, and Mirabella Salvo. Siero layers grown by molecular beam epitaxy. structural, electrical and optical properties. *Materials Science and Engineering B - Solid State Materials for advanced technoly*, 81:62–66, 04 2001.

[192] Juntao Li, Othman Zalloum, Tyler Roschuk, C.L. Heng, Wojcik J, and Peter Mascher. Light emission from rare-earth doped silicon nanostructures. *Advances in Optical Technologies*, 2008, 04 2008.

[193] A Lourenco M, M Milosevic M, Gorin Arnaud, M Gwilliam R, and P Homewood K. Superenhancement of 1.54 ÎŒm emission from erbium codoped with oxygen in silicon-on-insulator. *Scientific Reports*, 5:37501, 11 2016.

[194] K. Tucto, W. Aponte, J. Dulanto, J. A. Tofflinger, J. A. Guerra, and R. Grieseler. Combinatorial approach towards optimization of the light emission intensity of AlOxNy:Yb3+ thin films. *Applied Optics*, 58:3097–3103, 04 2019.

[195] Hemant Raut, Anand Ganesh Venkatesan, Sreekumaran Nair, and Seeram Ramakrishna. Antireflective coatings: A critical, in-depth review. *Energy Environ. Sci.*, 4, 01 2011.

[196] Review of physical vapor deposited (pvd) spectrally selective coatings for mid- and high-temperature solar thermal applications. *Solar Energy Materials and Solar Cells*, 98:1–23, 2012.

[197] Oxide semiconductors in photoelectrochemical conversion of solar energy. *Solar Energy*, 25(1):41–54, 1980.

[198] Hirosaki Naoto, Xie Rong-Jun, Kimoto Koji, Sekiguchi Takashi, Yamamoto Yoshinobu, Suehiro Takayuki, and Mitomo Mamoru. Characterization and properties of green-emitting beta-sialon:eu2+ powder phosphors for white light-emitting diodes. *Applied Physics Letters*, 86:211905–211905, 05 2005.

[199] Ish-Shalom Moshe. Formation of aluminum oxynitride by carbothermil reduction of aluminum oxide in nitrogen. *Journal of Materials Science Letters*, 1:147–149, 04 1982.

[200] Wende Xiao and Xin Jiang. Optical and mechanical properties of nanocrystalline aluminum oxynitride films prepared by electron cyclotron resonance plasma enhanced chemical vapor deposition. *Journal of Crystal Growth*, 264:165–171, 03 2004.

[201] Lin Yung-Hsin, Hsu Jin-Cherng, Ding Yi, and Wang Paul. Optical properties of high transmittance aluminum oxynitride thin films for spectral range from near ultraviolet to visible. *Optical Review*, 16:400–403, 05 2009.

[202] Vergeer P., Vlugt T. J. H., Kox M. H. F., den Hertog M. I., van der Eerden J. P. J. M., and Meijerink A. Quantum cutting by cooperative energy transfer in ybxy1-xpo4tb3+. *Phys. Rev. B*, 71:014119, Jan 2005.

[203] Near-infrared quantum cutting in ce3+ yb3+ co-doped ybo3 phosphors by cooperative energy transfer. *Optical Materials*, 32(9):998–1001, 2010.

[204] Chen Daqin, Yu Yunlong, Wang Yuansheng, Huang Ping, and Weng Fangyi. Cooperative energy transfer upconversion and quantum cutting dow conversion in Yb3+ TbF3 nanocrystals embedded glass ceramics. *Journal of Physical Chemistry C*, 113:6406–6410, 04 2009.

[205] Zhang Q. Y., Yang C. H., Jiang Z. H., and Ji X. H. Concentration dependent near infrared quantum cutting in GdBO3.Tb3+Yb3+ nanophosphors. *Applied Physics Letters*, 90(6):061914, 2007.

[206] Song Ye, Bin Zhu, Jin Luo, Jingxin Chen, Gandham Lakshminarayana, and Jianrong Qiu. Enhanced cooperative quantum cutting in tm3+ yb3+ codoped glass ceramics containing laf3 nanocrystals. *Optical Express*, 16(12):8989–8994, Jun 2008.

[207] Yu Dechao, Ballato John, and Riman R.E. The temperature dependence of multiphonon relaxation of rare earth ions in solid state hosts. *The Journal of Physical Chemistry C*, 120, 04 2016.

[208] Renata Reisfeld and M Eyal. Possible ways of relaxation for excited states of rare earth ions in amorphous media. *http://dx.doi.org/10.1051/jphyscol:1985763*, 46, 10 1985.

[209] L. Aarts, S. Jaeqx, B.M. van der Ende, and A. Meijerink. Downconversion for the er3+ and yb3+ couple in kpb2cl5-a low phonon frequency host. *Journal of Luminescence*, 131(4):608–613, 2011.

[210] C Carlone, K M. Lakin, and H R. Shanks. Optical phonons of aluminum nitride. *Journal of Applied Physics*, 55:4010–4014, 07 1984.

[211] Wei Shih Cheng and Chin Albert. New material transistor with record-high field-effect mobility among wide-band-gap semiconductors. *ACS Applied Materials and Interfaces*, 8:19187–19191, 08 2016.

[212] A. Tarafder, A.R. Molla, and B. Karmakar. Chapter 13 - advanced glass-ceramic nanocomposites for structural, photonic, and optoelectronic applications. In Basudeb Karmakar, Klaus Rademann, and Andrey L. Stepanov, editors, *Glass Nanocomposites*, pages 299–338. William Andrew Publishing, Boston, 2016.

[213] Viehmann W. Influence of charge compensation on uv excitation of rare-earth fluorescence. *The Journal of Chemical Physics*, 47:875–883, 1967.

[214] Helena Cristina Vasconcelos and Afonso Silva Pinto. Chapter 5: Fluorescence properties of rare-earth-doped sol-gel glasses. *Recent Applications in Sol-Gel Synthesis. Intech*, 2017.

[215] Samuel S. Mao and Paul E. Burrows. Combinatorial screening of thin film materials. an overview". *Journal of Materiomics*, 1(2):85–91, 2015.

[216] X. D. Xiang, Xiaodong Sun, Gabriel Briceño, Yulin Lou, Kai-An Wang, Hauyee Chang, William G. Wallace-Freedman, Sung-Wei Chen, and Peter G. Schultz. A combinatorial approach to materials discovery. *Science*, 268(5218):1738–1740, 1995.

[217] J. A. Guerra. Determination of the optical bandgap of thin amorphous (SiC)1-x (AIN)x films produced by radio frequency dual magnetron sputtering. Master's thesis, Pontificia Universidad Católica del Perú, 2010.

[218] A. Tejada, L. Montanez, C. Torres, P. Llontop, L. Flores, F. De Zela, A. Winnacker, and J. A. Guerra. Determination of the fundamental absorption and optical bandgap of dielectric thin films from single optical transmittance measurements. *Applied Optics*, 58(35):9585–9594, 2019.

[219] R. Swanepoel. Determination of the thickness and optical constants of amorphous silicon. *Journal of Physics E: Scientific Instruments*, 16(12):1214–1222, dec 1983.

[220] Chambouleyron I, Martinez J.M., Moretti A.C., and Mulato M. Optical constants of thin films by means of a pointwise constrained optimization approach. *Thin Solid Films*, 317:133–136, 04 1998.

[221] MacLeod H.A. *Thin Film Optical Filters*. Series in Optics and Optoelectronics. CRC Press, 2001.

[222] J. A. Guerra, J. R. Angulo, S. Gomez, J. Llamoza, L. M. Montanez, A. Tejada, J. A. Tofflinger, A. Winnacker, and R. Weingartner. The urbach focus and optical properties of amorphous hydrogenated sic thin films. *Journal of Physics D: Applied Physics*, 49(19):195102, apr 2016.

[223] M Roberts and D J Dunstan. A theory of bandgap fluctuations in amorphous semiconductors. *Journal of Physics C: Solid State Physics*, 18(28):5429–5433, oct 1985.

[224] D J Dunstan. New evidence for a fluctuating band-gap in amorphous semiconductors. *Journal of Physics C: Solid State Physics*, 16(17):L567–L571, jun 1983.

[225] Wagh Akshatha, Mahato K. K., Lakshmikanth R., Rajaramakrishna R., and Kamath Sudha D. Optical properties of eu2o3 doped lead fluoroborate glass. *AIP Conference Proceedings*, 1447(1):537–538, 2012.

[226] Olson J. K., Li Heng, Ju T., Viner J. M., and Taylor P. C. Optical properties of amorphous gete, sb2te3, and ge2sb2te5. the role of oxygen. *Journal of Applied Physics*, 99(10):103508, 2006.

[227] Palik E.D. *Handbook of Optical Constants of Solids, Five-Volume Set. Handbook of Thermo-Optic Coefficients of Optical Materials with Applications*. Elsevier Science, 1997.

[228] Oliver A Dicks, Jonathon Cottom, Alexander L Shluger, and Valeri V Afanasev. The origin of negative charging in amorphous al2o3 films: the role of native defects. *Nanotechnology*, 30(20):205201, mar 2019.

[229] Mustafa Alevli, Ozgit Cagla, Donmez Inci, and Biyikli Necmi. Optical properties of aln thin films grown by plasma enhanced atomic layer deposition. *Journal of Vacuum Science and Technology A*, 30(2):021506, 2012.

[230] Yuan Zang, Li Lianbi, Ren Zhanqiang, Cao Ling, and Zhang Yan. Characterization of AlN thin film prepared by reactive sputtering. *Surface and Interface Analysis*, 48(10):1029–1032, 2016.

[231] Ifa Jlassi, Habib Elhouichet, and Mokhtar Ferid. Thermal and optical properties of tellurite glasses doped erbium. *Journal of Materials Science*, 46:806–812, 02 2011.

[232] Sushama Damayanthy and P Predeep. Thermal and optical studies of rare earth doped tungston tellurite glasses. *International Journal of Applied Physics and Mathematics*, 4:139–143, 01 2014.

[233] Yasser B. Saddeek, I.S. Yahia, K.A. Aly, and W. Dobrowolski. Spectroscopic, mechanical and magnetic characterization of some bismuth borate glasses containing gadolinium ions. *Solid State Sciences*, 12(8):1426–1434, 2010.

[234] Street R.A. *Hydrogenated Amorphous Silicon*. Cambridge Solid State Science Series. Cambridge University Press, 2005.

[235] Adachi G., Imanaka N., and Kang Z.C. *Binary Rare Earth Oxides*. Springer Netherlands, 2006.

[236] Soares G. V., Bastos K. P., Pezzi R. P., Miotti L., Driemeier C., Baumvol I. J. R., Hinkle C., and Lucovsky G. Nitrogen bonding, stability, and transport in alon films on si. *Applied Physics Letters*, 84(24):4992–4994, 2004.

[237] Nazarov Alexei, Tiagulskyi Stanislav, P. Tyagulskyy I, Lysenko V, Rebohle L, Lehmann J, Prucnal Slawomir, Voelskow Matthias, and Skorupa W. The effect of rare-earth clustering on charge trapping and electroluminescence in rare-earth implanted metal-oxide-semiconductor light-emitting devices. *Journal of Applied Physics*, 107:123112 – 123112, 07 2010.

[238] C Labbe, Y-T An, G Zatryb, X Portier, A Podhorodecki, P Marie, C Frilay, J Cardin, and F Gourbilleau. Structural and emission properties of tb3+ doped nitrogen rich silicon oxynitride films. *Nanotechnology*, 28(11):115710, 2017.

[239] Ding Wu-Chang, Liu Yan, Zhang Yun, Guo Jian-Chuan, Zuo Yu-Hua, Cheng Bu-Wen, Yu Jin-Zhong, and Wang Qi-Ming. A comparison of silicon oxide and nitride as host matrices on the photoluminescence from er3+ ions. *Chinese Physics B*, 18(7):3044–3048, 2009.

[240] Horoz S., Simsek S., Palaz, S., and Mamedov A. Electronic and optical properties of rare earth oxides. ab initio calculation. *World Journal of Condensed Matter Physics*, 5:78–85, 2015.

[241] Silva Filho C. I., Oliveira A. L., Pereira S. C. F., de Sa Gilberto F., da Luz L. L., and Alves S. Bright thermal blackbody emission of visible light from LnO2 (Ln = Pr3+ Tb3+) photoinduced by a NIR 980 nm laser. *Dalton Trans.*, 48:2574–2581, 2019.

[242] Ohmi Shun-ichiro, Kobayashi C, Kashiwagi I, Ohshima C, Ishiwara Hiroshi, and Iwai H. Characterization of la2o3 and yb2o3 thin films for high-k gate insulator application. *Journal of The Electrochemical Society*, 7, 2003.

[243] Lee Moon-Sook and Bent Stacey F. Temperature effects in the hot wire chemical vapor deposition of amorphous hydrogenated silicon carbon alloy. *Journal of Applied Physics*, 87(9):4600–4610, 2000.

[244] I.V Kityk, A Kassiba, K Plucinski, and J Berdowski. Band structure of large-sized sic nanocomposites. *Physics Letters A*, 265(5):403 – 410, 2000.

[245] Rajagopalan T., Wang X., Lahlouh B., Ramkumar C., Dutta Partha, and Gangopadhyay S. Low temperature deposition of nanocrystalline silicon carbide films by plasma enhanced chemical vapor deposition and their structural and optical characterization. *Journal of Applied Physics*, 94(8):5252–5260, 2003.

[246] J. A. Guerra, L. M. Montanez, A. Winnacker, F. De Zela, and R. Weingartner. Thermal activation and temperature dependent PL and CL of Tb doped amorphous AlN and SiN thin films. *Physica Status Solidi C*, 12(8):1183–1186, 2015.

[247] Jamalaiah B.C., Vijaya Kumar M.V., and Rama Gopal K. Investigation on luminescence and energy transfer in tb3+ doped lead telluroborate glasses. *Physica B Condensed Matter*, 406:2871–2875, 2011.

[248] Weingartner R., Erlenbach O., Winnacker A., Welte A., Brauer I., Mendel H., Strunk H.P., Ribeiro C. T. M., and Zanatta A. R. Thermal activation cathodo and photoluminescence measurements of rare earth doped (tm, tb, dy, eu, sm, yb) amorphous/nanocrystalline aln thin films prepared by reactive rf-sputtering. *Optical Materials*, 28:790–793, 2006.

[249] Benz Felix and Strunk Horst P. Rare earth luminescence. a way to overcome concentration quenching. *AIP Advances*, 2(4):042115, 2012.

[250] Benz Felix, Strunk Horst, Schaab Jakob, Kunecke Ulrike, and Wellmann Peter. Tuning the emission colour by manipulating terbium-terbium interactions. terbium doped aluminum nitride as an example system. *Journal of Applied Physics*, 114(7):073518, 2013.

[251] Zhang Bingye, Ying Shitian, Han Lu, Zhang Jinsu, and Chen Baojiu. Color-tunable phosphor of Sr3YNa(PO4)3F-Tb3+ via interionic cross-relaxation energy transfer. *RSC Adv*, 8:25373–25386, 2018.

[252] Nyk M., Kudrawiec R., Strek W., and Misiewicz J. Synthesis and optical properties of eu3+ and tb3+ doped gan nanocrystallite powders. *Optical Materials*, 28:767–770, 2006.

[253] Blasse G. The influence of charge-transfer and rydberg states on the luminescence properties of lanthanides and actinides. In *Spectra and Chemical Interactions*, pages 43–79", 1976.

[254] P. Dorenbos. Systematic behaviour in trivalent lanthanide charge transfer energies. *Journal of Physics: Condensed Matter*, 15(49):8417–8434, 2003.

[255] Dorenbos P. and Bos A.J.J. Lanthanide level location and related thermoluminescence phenomena. *Radiation Measurements*, 43:139–145, 2008.

[256] Zolin V.F. Spectroscopy of europium and terbium pyridine carboxylates. *Journal of Alloys and Compounds*, 05 2004.

[257] Lozykowski H. J. and Jadwisienczak W. M. Thermal quenching of luminescence and isovalent trap model for rare earth ion doped aln. *Physica Status Solidi B*, 244(6):2109–2126, 2007.

[258] Kik P. G., de Dood M. J. A., Kikoin K., and Polman A. Excitation and deexcitation of Er3+ in crystalline silicon. *Applied Physics Letters*, 70(13):1721–1723, 1997.

[259] Priolo Francesco, Franzo Giorgia, Coffa Salvatore, and Carnera Alberto. Excitation and nonradiative deexcitation processes of Er3+ in crystalline Si. *Phys. Rev. B*, 57:4443–4455, Feb 1998.

[260] Borzone G, Raggio Riccardo, and Ferro Riccardo. Thermochemistry and reactivity of rare earth metals. *Physical Chemistry Chemical Physics*, 1:1487–1500, 04 1999.

[261] Akashev Lev, A. Popov N, Yarmoshenko Yuri, V. Druzhinin A, and G. Shevchenko V. Effect of atmospheric nitrogen on the oxidation mechanism of aluminum alloys with rare-earth metals. *Russian Journal of Applied Chemistry*, 88:1913–1919, 12 2015.

[262] C. Fitzgibbon George and E. Holley Charles. Enthalpies of solution and of formation of several terbium oxides. *Journal of Chemical and Engineering Data*, 13:63–65, 01 1968.

[263] Akhmadullina N. S., Lysenkov A. S., Ashmarin A. A., Kargin Yu. F., Ishchenko A. V., Yagodin V. V., and Shul'gin B. V. Effect of dopant concentration on the phase composition and luminescence properties of Eu2+- and Ce3+-doped AlONs. *Inorganic Materials*, 51(5):473–481, 2015.

[264] Thyago Santos Braga, Marcos Massi, Diego Alexandre Duarte, Argemiro Soares Silva Sobrinho, Guilherme Wellington Alves Cardoso, Fabiano Pinto Pereira, JoÃ£o Paulo Barros Machado, and Choyu Otani. Effect of the thermal annealing on the properties of RF sputtered Mo-AlNxOy composite thin films. *Vacuum*, 129:115–121, 2016.

[265] Konings Rudy J. M., Benes Ondrej, Kovacs Attila, Manara Dario, Sedmidubsky David, Gorokhov Lev, Iorish Vladimir S., Yungman Vladimir, Shenyavskaya E., and Osina E. The thermodynamic properties of the f-elements and their compounds. part 2. the lanthanide and actinide oxides. *Journal of Physical and Chemical Reference Data*, 43(1):013101, 2014.

[266] L. R. Tessler. Erbium in a-Si:H. *Brazilian Journal of Physics*, 29:616–622, 12 1999.

[267] L. Flores, K. Tucto, J. A. Guerra, J. A. Tofflinger, E. Serquen, A. Winnacker, R. Grieseler, and R. Weingartner. Luminescence properties of Yb3+ Tb3+ co-doped amorphous silicon oxycarbide thin films. *Optical Materials*, 92:16–21, 04 2019.

[268] Talbot Etienne, Larde Rodrigue, Pareige Philippe, Khomenkova L, Hijazi Khalil, and Gourbilleau Fabrice. Nanoscale evidence of erbium clustering in er-doped silicon-rich silica. *Nanoscale research letters*, 8:39, 01 2013.

[269] Muhammad Maqbool, Martin E. Kordesch, and A. Kayani. Enhanced cathodoluminescence from an amorphous aln:ho phosphor by co-doped gd+3 for optical devices applications. *J. Opt. Soc. Am. B*, 26(5):998–1001, May 2009.

[270] L. Caldwell Meghan, Van Patten Greg, E. Kordesch Martin, and Richardson Hugh. Visible luminescent activation of amorphous aln:eu thin-film phosphors with oxygen. *Mrs Internet Journal Of Nitride Semiconductor Research*, 6:1–8, 01 2001.

[271] Solmon Heiene, Robinson David, and Dieckmann Rudiger. Oxygen transport in aluminum nitride substrates. *Journal of the American Ceramic Society*, 77(11):2841–2848, 1994.

[272] J. Reed David and J. Wuensch B. Ion probe measurement of oxygen self-diffusion in single crystalline Al2O3. *Journal of the American Ceramic Society*, 63:88–92, 06 2006.

[273] Oishi Y. and Kingery W. D. Self-diffusion of oxygen in single crystal and polycrystalline aluminum oxide. *The Journal of Chemical Physics*, 33(2):480–486, 1960.

[274] Zheng Qingjun and Reddy Ramana G. Kinetics of in-situ formation of AlN in Al alloy melts by bubbling ammonia gas. *Metallurgical and Materials Transactions B*, 34(6):793–804, 2003.

[275] Novikov Yuriy, Vishnyakov A, Gritsenko V.A., Nasyrov K.A., and Wong Hei. Modeling the charge transport mechanism in amorphous Al2O3 with multiphonon trap ionization effect. *Microelectronics Reliability*, 50:207–210, 02 2010.

[276] Liehr M., Thiry P. A., Pireaux J. J., and Caudano R. High resolution electron energy loss spectroscopy of an anisotropic insulator surface: A test for the dielectric theory. *Journal of Vacuum Science and Technology A*, 2(2):1079–1082, 1984.

[277] Yoshimasa A. Ono. *Electroluminescent displays*. River Edge NJe: World Scientific, 1995.

[278] M.J. Russ and D.I. Kennedy. The effects of double insulating layers on the electroluminescence of evaporated ZnS:Mn films. *Journal of the Electrochemical Society*, 114:1066–1072, 1967.

[279] J. Heikenfeld, D. S. Lee, M. Garter, R. Birkhahn, and A. J. Steckl. Low-voltage GaN:Er green electroluminescent devices. *Applied Physics Letters*, 76:1365–1367, 2000.

[280] Inoguchi T. Retrospect and prospect on research and development of electroluminescent panels. In Shionoya Shigeo and Kobayashi Hiroshi, editors, *Electroluminescence*, pages 2–7, Berlin, Heidelberg, 1989. Springer Berlin Heidelberg.

[281] Lu F., Carius R., Alam A., Heuken M., and Buchal Ch. Green electroluminescence from a Tb-doped AlN thin-film device on Si. *Journal of Applied Physics*, 92(5):2457–2460, 2002.

[282] Dimitrova V.I, Van Patten Greg, Richardson Hugh, and Kordesch M.E. Photo-, cathodo-, and electroluminescence studies of sputter deposited aln:er thin films. *Applied Surface Science*, 175-176:480–483, 05 2001.

[283] Ohnishi Hideomi, Yoshino Hirofumi, Sakuma Naoshi, and Ieyasu Kenzo. Green emitting thin film DC EL devices with low threshold voltage. *Proceedings of the 3rd International Display Research Conference*, 25:88–91, 01 1983.

[284] S. Ohta. Dc electroluminescence of Au/ZnS:Mn/n-Si devices. *Proceedings of the 3rd International Display Research Conference*, 25:566–569, 1983.

[285] I. Abdalla Mohamed, Thomas Jacques, Brenac Alain, and Noblanc J.P. Performance of DC EL coevaporated ZnS:Mn Cu low voltage devices. *Electron Devices, IEEE Transactions on*, 28:694–697, 1981.

[286] Jacobson Dean L. and Campbell Albert E. Molybdenum work function determined by electron emission microscopy. *Metallurgical and Materials Transactions B*, 2(11):3063–3066, Nov 1971.

[287] Farhan Mansour S., Zalnezhad Erfan, Bushroa Abdul Razak, and Sarhan Ahmed Aly Diaa. Electrical and optical properties of indium-tin oxide (ITO) films by ion-assisted deposition (IAD) at room temperature. *International Journal of Precision Engineering and Manufacturing*, 14(8):1465–1469, Aug 2013.

[288] Christensen N. E. and Gorczyca I. Optical and structural properties of iii-v nitrides under pressure. *Phys. Rev. B*, 50:4397–4415, Aug 1994.

[289] Dimitrova V. I., Van Patten P. G., Richardson H. H., and Kordesch M. E. Visible emission from electroluminescent devices using an amorphous AlN:Er3+ thin-film phosphor. *Applied Physics Letters*, 77(4):478–479, 2000.

[290] Kim Min Ju and Kim Tae Geun. Fabrication of metal-deposited indium tin oxides: Its applications to 385 nm light-emitting diodes. *ACS Applied Materials and Interfaces*, 8(8):5453–5457, 2016. PMID: 26859604.

[291] Lee Jae, Woo Kie Young, Kim Kyeong Heon, Kim Hee-Dong, and Geun Kim Tae. ITO/Ag/ITO multilayer-based transparent conductive electrodes for ultraviolet light emitting diodes. *Optics letters*, 38:5055–5058, 12 2013.

[292] Hasan Musarrat, Park Hokyong, Lee Joon-Myoung, and Hwang Hyunsang. Dual metal gate work function by controlling metal gate thickness and composition. *Electrochemical and Solid-State Letters*, 11(5):124–126, 2008.

[293] Hao-Long Chen, Yang-Ming Lu, Jun-Yi Wu, and Weng-Sing Hwang. Effects of substrate temperature and oxygen pressure on crystallographic orientations of sputtered nickel oxide films. *Materials Transactions*, 46(11):2530–2535, 2005.

[294] Marinov G, Strijkova Velichka, Vasileva Marina, Madjarova Violeta, Malinowski Nikola, and Babeva Tsvetanka. Effect of substrate temperature on the microstructural, morphological, and optical properties of electrosprayed ZnO thin films. *Advances in Condensed Matter Physics*, 2018:1–7, 05 2018.

[295] Ocal Tuna, Yusuf Selamet, Gulnur Aygun, and Lutfi Ozyuzer. High quality ITO thin films grown by dc and rf sputtering without oxygen. *Journal of Physics D: Applied Physics*, 43(5):055402, jan 2010.

[296] X. H. Xu, H.S. Wu, C.J. Zhang, and Z.H. Jin. Morphological properties of AlN piezoelectric thin films deposited by DC reactive magnetron sputtering. *Thin Solid Films*, 388:62–67, 2001.

[297] Li J., Nam K. B., Nakarmi M. L., Lin J. Y., Jiang H. X., Carrier Pierre, and Wei Su-Huai. Band structure and fundamental optical transitions in wurtzite AlN. *Applied Physics Letters*, 83(25):5163–5165, 2003.

[298] Qixin Guo and Akira Yoshida. Temperature dependence of band gap change in InN and AlN. *Japanese Journal of Applied Physics*, 33(Part 1 No. 5A):2453–2456, 1994.

[299] J. A. Guerra, F. De Zela, K. Tucto, L. M. Montanez, J. A. Tofflinger, A. Winnacker, and R. Weingartner. Effect of thermal annealing treatments on the optical activation of tb doped amorphous sich thin films. *Journal of Physics D Applied Physics*, 49(37):375104, 2016.

[300] Priolo F., Coffa S., Franzo G., Spinella C., Carnera A., and Bellani V. Electrical and optical characterization of er implanted si: The role of impurities and defects. *Journal of Applied Physics*, 74(8):4936–4942, 1993.

[301] Klak Michal, Zatryb Grzegorz, Golacki Lukasz, Benzo Patrizio, Labbe C, Cardin Julien, Misiewicz Jan, Gourbilleau Fabrice, and Podhorodecki Artur. Influence of rapid thermal annealing temperature on the photoluminescence of tb ions embedded in silicon nitride films. *Thin Solid Films*, 675, 02 2019.

[302] Blazquez Oriol, Julian Lopez-Vidrier, Lopez-Conesa Lluis, Busquets Maso Marti, Estrade Sonia, Peiro F, Hernandez Sergi, and Garrido Blas. Structural and optical properties of al-tb-sio2 multilayers fabricated by electron beam evaporation. *Journal of Applied Physics*, 120:135302, 10 2016.

[303] Sillen Alain and Engelborghs Yves. The correct use of average fluorescence parameters. *Photochemistry and Photobiology*, 67(5):475–486, 1998.

[304] Lakowicz Joseph. *Principles of Fluorescence Spectroscopy*, volume 1. 01 2006.

[305] G. Zatryb, A. Podhorodecki, M. Banski, J. Misiewicz, and N.V. Gaponenko. Influence of annealing temperature on the electron-lattice coupling strength in terbium doped yttrium alumina perovskite xerogels embedded in nano-porous anodic alumina. *Optical Materials*, 35(6):1230–1235, 2013.

[306] L. Zur, J. Pisarska, and W.A. Pisarski. Terbium doped heavy metal glasses for green luminescence. *Journal of Rare Earths*, 29(12):1198–1200, 2011.

[307] Tigran T Mnatsakanov, Michael E Levinshtein, Lubov I Pomortseva, Sergey N Yurkov, Grigory S Simin, and M Asif Khan. Carrier mobility model for gan. *Solid State Electronics*, 47(1):111–115, 2003.

[308] L. Zhang, Z. Liu, S. Zhao, M. Lin, and P. Wang. Low-temperature ohmic contact formation in AlN/GaN HEMT using microwave annealing. *IEEE Transactions on Electron Devices*, 64(3):1385–1389, 2017.

[309] Kaminskii A. *Crystalline Lasers Physical Processes and Operating Schemes*. Laser and Optical Science and Technology. Taylor and Francis, 1996.

[310] Morrison C. A. and Leavitt R. P. Crystal field analysis of triply ionized rare earth ions in lanthanum trifluoride. *The Journal of Chemical Physics*, 71(6):2366–2374, 1979.

[311] Leavitt R. P. and Morrison C. A. Crystal field analysis of triply ionized rare earth ions in lanthanum trifluoride. II. Intensity calculations. *The Journal of Chemical Physics*, 73(2):749–757, 1980.

[312] K. Tucto Salinas. Structural, luminescence and judd-ofelt analysis to study the influence of post-annealing treatment on the AIN:Tb thin films prepared by radiofrequency magnetron sputtering. Master's thesis, Pontificia Universidad Católica del Perú and Technische Universität Ilmenau, 2016.

Karem Y. Tucto Salinas

Email: karemy.tucto@pucp.pe

Education

1. Doctorate in Physics. From August 2016 - to August 2019. Physics Section, Escuela de Posgrado, Pontificia Universidad Católica del Perú Lima, Perú.

2. Master of Materials Science and Engineering. From March 2014 to February 2016. Escuela de Posgrado, Pontificia Universidad Católica del Perú and Technische Universität Ilmenau. A double degree master program from the academic cooperation between Perú and Germany.

3. Bachelor and Licentiate in Physics. From March 2006 to December 2012. Physics Section, Pontificia Universidad Católica del Perú Lima, Perú.

Publications

1. ***K. Tucto***,W. Aponte, J. Dulanto, J. Töfflinger, J. Guerra, R. Grieseler. "Combinatorial approach towards optimization of the light emission intensity of AlOxNy:Yb^{3+} thin films" Applied Optics, Vol. 58, Iss.12 (2019) pp.3097-3103 DOI:10.1364/AO.58.003097

2. ***K. Tucto***, L. Flores, J. Guerra, J. Töfflinger, J. Dulanto, R. Grieseler, A. Osvet, M. Batentschuk and R. Weingärtner. "Co-Activated AlON Thin Films for Down Conversion Applications in Photovoltaic Cells" MRS Advances, Vol. 2, Iss. 52 (2017) pp.299-302 DOI:10.1557/adv.2017.478

3. ***K. Y. Tucto Salinas***, L. F. Flores Escalante, J. A. Guerra Torres, R. Grieseler, T. Kups, J. Pezoldt, A. Osvet, M. Batentschuk and R. Weingärtner. "Effect of post-annealing treatment on the structure and luminescence properties of AlN:Tb3+ thin films prepared by radio frequency magnetron sputtering" Material Science Forum, Vol. 890 (2017) pp.299-302 DOI:10.4028/www.scientific.net/MSF.890.299

4. J. A. Guerra, F. De Zela, ***K. Tucto***, L. Montañez, J. A. Töfflinger, A.Winnacker and R.Weingärtner "Effect of thermal annealing treatments on the optical activation of Tb3+ -doped amorphous SiC:H thin films" Journal of Physics D: Applied Physics, Vol. 29, Iss. 37 375104 (2016) DOI:10.1088/0022-3727/49/37/375104

5. J. A. Guerra, ***K. Tucto***, L. M. Montañez, F. De Zela, J. A. Töfflinger, A. Winnaker, R. Weingärtner. "Analytical Study of the Thermal Activation of Tb Doped Amorphous SiC:H Thin Films" MRS Advances, Vol. 1, Iss. 38 (2016) pp. 2689-2694 DOI:10.1557/adv.2016.464

6. J. A. Guerra, L. M. Montañez, ***K. Tucto***, J. Angulo, J. A. Töfflinger, A. Winnaker, R. Weingärtner. "Bandgap Engineering of Amorphous Hydrogenated Silicon Carbide" MRS Advances, Vol. 1, Iss. 49 (2016) pp. 2929-2934 DOI:10.1557/adv.2016.422

Conference Presentations

1. XVI Brazilean Material Research Society Meeting. September 2017, Gramado - RS, Brasil. "Thermally activated luminescence in AlON:Tb^{3+}:Yb^{3+} thin films for third generation photovoltaic solar cells". Authors: K. Tucto, L. Flores, J. Dulanto, J. Guerra, J. Töfflinger, R. Grieseler, A. Osvet, M. Batentschuk and R. Weingärtner. Poster presentation.

2. 18th International Conference on Luminescence. August 2017, Joao Pessoa - PB, Brasil. "Thermally activated luminescence in AlON:Tb^{3+}:Yb^{3+} thin films for third generation photovoltaic solar cells". Authors: K. Tucto, L. Flores, J. Dulanto, J. Guerra, J. Töfflinger, R. Grieseler, A. Osvet, M. Batentschuk and R. Weingärtner. Oral presentation.

3. 2017 Material Research Society Spring Meeting & Exhibit. April 2017, Phoenix - AZ, USA. "Production and Characterization of Tb^{3+}/Yb^{3+} Co-activated AlN Thin Films for Down-Conversion Applications in Photovoltaic Cells". Authors: K. Tucto, L. Flores, J. Dulanto, J. Guerra, J. Töfflinger, J. Dulanto, R. Grieseler, A. Osvet, M. Batentschuk and R. Weingärtner. Poster presentation.

4. 5th International Conference on Material Science and Engineering Technology. October 2016, Tokyo, Japan. "Effect of post-annealing treatment on the structure and luminescent properties of AlN:Tb^{3+} thin films prepared by radiofrequency magnetron sputtering". Authors: K. Tucto, L. F. Flores Escalante, J. A. Guerra Torres, R. Grieseler, T. Kups, J. Pezoldt, A. Osvet, M. Batentschuk and R. Weingärtner. Oral presentation.

5. XXIII International Materials Research Congress. August 2014, Cancún, México. "Determination of the Judd-Ofelt parameters of Tb-doped a-SiC:H, AlN and SiN thin films". Authors: K. Tucto, J. A. Guerra Torres, R.Weingärtner. Oral presentation.

Awards and Fundings

1. Winner, Programas de Apoyo a la Investigación para Estudiantes (PAIP - doctoral category) of the PUCP, September 2017

2. Doctoral Scholarship, Peruvian National Fund for Scientific and Technological Development (FONDECYT) 236-2015, August 2016 - July 2019

3. Master Scholarship, FONDECYT 012-2013, March 2014 - February 2016